

**Deciphering  
glacial-interglacial  
Southern Ocean dynamics  
with deep-sea corals**

**Torben Struve**

**Imperial College London, Department of Earth Science and Engineering**

**A thesis submitted for the degree of Doctor of Philosophy (Ph.D) 2015**

## **Declaration of Originality**

I herewith declare that this thesis and the research presented here are of my own work and that any ideas and work from others are fully acknowledged and referenced.

A handwritten signature in black ink, consisting of the letters 'T', 'S', and 'e' in a stylized, cursive script.

Torben Struve

‘The copyright of this thesis rests with the author and is made available under a Creative Commons Attribution Non-Commercial No Derivatives licence. Researchers are free to copy, distribute or transmit the thesis on the condition that they attribute it, that they do not use it for commercial purposes and that they do not alter, transform or build upon it. For any reuse or redistribution, researchers must make clear to others the licence terms of this work’

## **Acknowledgements**

The work presented here is the result of my four years at Imperial College London. This would not have been possible without the guidance and support I received from my supervisor, Tina. Her generosity with her time and her enthusiasm for the research I conducted cannot be appreciated enough, and I truly thank you!

Thanks also to the entire MAGIC group providing such excellent working environment. In particular, Barry and Katharina are thanked for keeping the labs and machines running and providing good advice whenever needed. Along those lines, I owe Kirsty big thanks for giving me the necessary tools to analyse my coral samples. Myriam is acknowledged for pioneering in trouble-shooting and David for the fruitful discussions on past ocean circulation.

I would also like to acknowledge Laura, Jess, Andrea and Sophie for providing coral sample material, uranium-series dates and radiocarbon analyses making this project an exciting international multi-proxy collaboration. The Nd isotope work presented in this thesis would not have been possible without this collaboration. The collective expertise in this project is phenomenal and I am looking forward to the discussions to come! Laura is particularly thanked for her helpful comments on my research and for giving me the opportunity to join her research cruise JC094 across the tropical Atlantic, during which I learned more about corals and deep-sea life than any lecture could convey.

The Grantham Institute for Climate Change is acknowledged for funding and support during my time at Imperial.

I appreciate that Prof. Mark Rehkämper and Dr. Alexander Piotrowski agreed to read this piece of work and I am looking forward to the upcoming discussion.

During the last four years numerous people have helped in various ways to get me to the point of finishing this project, on campus and off campus. Many thanks to my parents for hosting me while I was writing up which helped significantly to keep my focus. All friends and family, in the UK, Germany and elsewhere, distracting and supporting me during the past years – this was much appreciated and I owe you! Sofia, you are particularly thanked for your endless patience and support during the process of finishing this!

Having made experience with life's ugly face before I moved to the UK I also want to thank everyone who provided support during a time when I learned that most problems in life are minor. This experience provided, however, the stamina to face any challenge thereafter.

# Abstract

Recent observations and past reconstructions have highlighted the significance of the Southern Ocean for modern and past ocean circulation patterns. Deep wind-induced upwelling renders the Southern Ocean unique, such that deep waters are brought directly to the surface where they can exchange with the atmosphere. Moreover, the Antarctic Circumpolar Current (ACC) is the dominant feature of Southern Ocean circulation linking all ocean basins and facilitating the inter-basin exchange of ocean properties. Hence, Southern Ocean dynamics act to (partly) moderate both, zonal and meridional transports, and both were shown to be sensitive to atmospheric forcing on different time scales. However, due to the remoteness and harsh conditions, direct evidence of past Southern Ocean circulation is scarce.

This work uses neodymium (Nd) isotopes extracted from the aragonitic skeletons of deep-sea corals collected in the Drake Passage and at the Tasmanian margin. The fidelity of the skeletal Nd isotope signature was tested in a calibration effort and the nature of Nd in coralline aragonite was explored. Based on the promising results, the approach was then confidently applied to uranium-series dated deep-sea corals in order to decipher Southern Ocean water mass mixing across intervals of past climate perturbations. The results show that Drake Passage and Tasmanian margin corals record complimentary features of Southern Ocean circulation. Intervals of high sampling resolution reveal unexpectedly dynamic and abrupt changes of water mass mixing oscillating on millennial to (sub) centennial time scales during the past ~40,000 years.

This thesis explores the nature of the recorded signal in the light of available literature, focusing on phases of abrupt change and fitting the processes considered to drive the Southern Ocean Nd isotope signal into a global framework.

| <b>Table of Contents</b>  |    |
|---|----|
| <b>List of Figures</b>  | 9  |
| <b>List of Tables</b>   | 10 |
| <b>Glossary</b>   | 11 |
| <b>Chapter 1 Introduction</b>   | 12 |
| 1.1. The Southern Ocean's role in the global overturning circulation  | 13 |
| 1.2. The Southern Ocean's role in ocean-atmosphere exchange of carbon   | 16 |
| 1.3. The marine neodymium isotope system and its application to palaeoceanography   | 18 |
| 1.4. Deep-sea corals as palaeoceanographic archives   | 20 |
| 1.5. Thesis structure   | 24 |
| <b>Chapter 2 Neodymium isotope analyses after combined extraction of actinide and lanthanide elements from seawater and deep-sea coral aragonite</b>            | 25 |
| Abstract  | 26 |
| 2.1. Introduction   | 27 |
| 2.2. Methodology  | 28 |
| 2.2.1. Seawater sample preparation and anion exchange chemistry: the neodymium fraction during protactinium – thorium separation                                | 28 |
| 2.2.2. Carbonate sample preparation and anion exchange chemistry: the neodymium fraction during uranium – thorium separation                                    | 28 |
| 2.2.3. Two-stage neodymium purification for TIMS NdO <sup>+</sup> analysis  | 29 |
| 2.2.3.1. Step 1 - Cation exchange chemistry or TRU spec <sup>®</sup> /RE spec <sup>®</sup> chemistry: separating the rare earth elements from the sample matrix | 30 |
| 2.2.3.2. Step 2 - Ln spec <sup>®</sup> chemistry: neodymium purification  | 31 |
| 2.2.4. Synthesising a TaF <sub>5</sub> activator for TIMS NdO <sup>+</sup> analyses   | 31 |
| 2.2.5. Thermal Ionisation Mass Spectrometry   | 32 |
| 2.3. Application: seawater and carbonates   | 33 |
| 2.3.1. Intercomparison of results for Nd extraction from seawater   | 33 |
| 2.3.2. Intercomparison of results for Nd extraction from aragonitic deep-sea coral skeletons  | 34 |
| 2.4. Summary and concluding remarks   | 36 |
| <b>Chapter 3 Neodymium isotopes and concentrations in aragonitic deep-sea corals - modern calibration and evaluation of palaeo-applications</b>                 | 37 |
| Abstract  | 38 |
| 3.1. Introduction   | 39 |
| 3.2. Samples  | 41 |

|   |           |
|---|-----------|
| 3.3. Analytical procedures  | 45        |
| 3.3.1. Sample preparation for Nd isotope analyses   | 45        |
| 3.3.2. Neodymium isotope analyses   | 46        |
| 3.3.3. Major and trace element analyses on modern and fossil corals and sediments   | 47        |
| 3.4. Results  | 48        |
| 3.4.1. Seawater Nd isotope data   | 48        |
| 3.4.2. Sediment data  | 49        |
| 3.4.3. Deep-sea coral data  | 49        |
| 3.4.3.1. Modern Calibration   | 49        |
| 3.4.3.2. Trace Metal Systematics  | 53        |
| 3.5. Discussion   | 59        |
| 3.5.1. Calibration of modern deep-sea corals against ambient seawater   | 59        |
| 3.5.1.1. Drake Passage seawater data  | 59        |
| 3.5.1.2. Calibrating modern deep-sea corals with seawater neodymium isotope data  | 60        |
| 3.5.2. In search for the Nd carrier phases in coralline aragonite   | 63        |
| 3.5.2.1. Lithogenic and FeMn oxyhydroxide phases as Nd carrier in coral skeletons   | 64        |
| 3.5.2.2. Rare earth element case for a seawater origin  | 66        |
| 3.5.2.3. Organic phases as potential Nd carrier in coral skeletons  | 67        |
| 3.5.2.4. Phosphate phases as Nd carrier in coral skeletons  | 69        |
| 3.6. Conclusions  | 71        |
| <br>  |           |
| <b>Chapter 4     The deglacial Southern Ocean: centennial-scale circulation changes recorded in deep-sea coral skeletons?</b> | <b>72</b> |
| Abstract  | 73        |
| 4.1. Introduction   | 74        |
| 4.2. Material and Methods   | 77        |
| 4.2.1. Drake Passage coral samples  | 78        |
| 4.2.2. Deep-sea corals from south of Tasmania   | 79        |
| 4.2.3. Sample preparation and analytical procedures   | 79        |
| 4.3. Results  | 80        |
| 4.3.1. Drake Passage deep-sea coral data  | 80        |
| 4.3.2. Deep-sea coral data from south of Tasmania   | 84        |
| 4.3.3. Significance of the Nd isotope signal recorded in Southern Ocean deep-sea corals                                       | 84        |
| 4.3.4. Generating a time series from individual corals  | 84        |
| 4.4. Discussion   | 86        |
| 4.4.1. Processes influencing the recorded seawater Nd isotope signal  | 86        |
| 4.4.2. Millennial-scale evolution of glacial and deglacial Southern Ocean water mass mixing                                   | 88        |
| 4.4.2.1. Water mass mixing south of Tasmania: evidence for ventilation from the North Pacific                                 | 89        |
| 4.4.2.2. Glacial water mass mixing in the Drake Passage and implications for the overturning circulation                      | 91        |
| 4.4.3. Transition into the interglacial Southern Ocean between 18 and 14 kyr BP   | 97        |

|  |            |
|--|------------|
| 4.4.3.1. Overturning circulation and ocean ventilation: the 15.8 to 14.7 kyr BP interval   | 97         |
| 4.4.3.2. The role of Southern Ocean mid-depth circulation in atmospheric CO <sub>2</sub> rise                                    | 103        |
| 4.5. Summary and conclusions   | 104        |
| <br>   |            |
| <b>Chapter 5 Mid-depth ocean circulation during MIS 2 and MIS 3: neodymium isotope evidence for interhemispheric coupling</b>    | <b>106</b> |
| Abstract   | 107        |
| 5.1. Introduction  | 108        |
| 5.2. Material and Methods  | 111        |
| 5.2.1. Deep-sea coral samples  | 111        |
| 5.2.1.1. North Atlantic  | 111        |
| 5.2.1.2. Drake Passage   | 112        |
| 5.2.1.3. South of Tasmania   | 112        |
| 5.2.2. Sample preparation and analytical procedures  | 114        |
| 5.3. Results   | 115        |
| 5.3.1. North Atlantic  | 115        |
| 5.3.2. Drake Passage   | 115        |
| 5.3.3. South of Tasmania   | 116        |
| 5.4. Discussion  | 119        |
| 5.4.1. The significance of local inputs for the Nd isotope signature of ambient water masses                                     | 119        |
| 5.4.2. The North Atlantic: composition of exported northern sourced water during MIS 3 and 2                                     | 122        |
| 5.4.3. Unmixing the Nd isotope signal south of Tasmania: identifying dominant source water masses                                | 126        |
| 5.4.4. Southern Ocean water mass mixing and implications for ocean circulation during MIS 3 and MIS 2                            | 127        |
| 5.4.5. A Southern Hemisphere driver of North Atlantic Heinrich events?   | 129        |
| 5.5. Conclusions   | 135        |
| <br>   |            |
| <b>Chapter 6 Holocene changes in Southern Ocean circulation in response to atmospheric forcing inferred from deep-sea corals</b> | <b>137</b> |
| Abstract   | 138        |
| 6.1. Introduction  | 139        |
| 6.2. Material and Methods  | 143        |
| 6.2.1. Deep-sea corals samples   | 143        |
| 6.2.2. Sample preparation and analytical procedures  | 143        |
| 6.3. Results   | 144        |
| 6.4. Discussion  | 146        |
| 6.4.1. Significance of the neodymium isotope signal recorded in deep-sea corals  | 146        |
| 6.4.2. Formation of Antarctic Intermediate Water during the Holocene   | 147        |

|  |     |
|--|-----|
| 6.4.3. Deep stratification of the Holocene Southern Ocean - implications<br>for the global overturning circulation | 152 |
| 6.5. Conclusions   | 157 |
| <b>Chapter 7 Summary and general conclusions</b>   | 159 |
| <b>Bibliography</b>  | 165 |
| <b>Appendix</b> Additional Nd isotope data from Galapagos, Interim seamount and<br>Reykjanes Ridge                 | 195 |

## List of Figures

|  |     |
|--|-----|
| <b>Fig. 1.1:</b> Schematic of a three dimensional view on the modern global overturning circulation.                                       | 13  |
| <b>Fig. 1.2:</b> Pathways of Nd from the sources to the sinks.   | 19  |
| <b>Fig. 1.3:</b> Global distribution of deep-sea corals.   | 21  |
| <b>Fig. 1.4:</b> Sub-fossil skeleton of <i>Desmophyllum dianthus</i> collected during NBP0805.   | 21  |
| <b>Fig. 1.5:</b> Global calibration for Nd isotopes in deep-sea coral aragonitic skeletons.  | 22  |
| <b>Fig. 2.1:</b> Working scheme of combined Pa-Th-Nd and U-Th-Nd chemical procedures.  | 29  |
| <b>Fig. 2.2:</b> Neodymium isotope results on BATS seawater Pa-Th intercalibration samples.  | 33  |
| <b>Fig. 2.3:</b> Results of in-house coral reference material Nd isotope analyses.   | 35  |
| <b>Fig. 3.1:</b> Global locations of modern deep-sea corals calibrations.  | 41  |
| <b>Fig. 3.2:</b> Seawater, sediment and coral sampling locations in the Drake Passage.   | 42  |
| <b>Fig. 3.3:</b> Alive and sub-fossil deep-sea coral specimens.  | 43  |
| <b>Fig. 3.4:</b> Sample location on Reykjanes Ridge in the North Atlantic.   | 44  |
| <b>Fig. 3.5:</b> Seawater Nd isotope results.  | 60  |
| <b>Fig. 3.6:</b> Global calibration of deep-sea coral Nd isotope data against modern seawater.   | 61  |
| <b>Fig. 3.7:</b> Drake Passage deep-sea coral trace metal data.  | 64  |
| <b>Fig. 3.8:</b> REE patterns of sediments, FeMn coating, coral skeletons and seawater.  | 67  |
| <b>Fig. 3.9:</b> Trace metal results of different sub-samples of the same coral.   | 70  |
| <b>Fig. 4.1:</b> Global map with simplified sub-surface ocean circulation pattern superimposed.  | 76  |
| <b>Fig. 4.2:</b> Latitudinal section of oxygen concentration across the Drake Passage.   | 78  |
| <b>Fig. 4.3:</b> Latitudinal section of oxygen concentration from the Tasman Sea toward Antarctica.  | 79  |
| <b>Fig. 4.4:</b> Results of Drake Passage and Tasmanian deep-sea coral Nd isotope analyses.  | 85  |
| <b>Fig. 4.5:</b> The Southern Ocean deep-sea coral time series in the context of relevant proxy records between 26 and 11 kyr BP.          | 90  |
| <b>Fig. 4.6:</b> Drake Passage and Tasmanian deep-sea coral data in radiocarbon-Nd isotope space.  | 93  |
| <b>Fig. 4.7:</b> The Southern Ocean deep-sea coral time series during the transition to interglacial circulation between 18 and 14 kyr BP. | 100 |
| <b>Fig. 5.1:</b> Global map with simplified sub-surface ocean circulation pattern superimposed.  | 110 |
| <b>Fig. 5.2:</b> Deep-sea coral Nd isotope data from MIS 5 to 2 compared to modern seawater.   | 113 |
| <b>Fig. 5.3:</b> Deep-sea coral Nd isotope data analysed for latest MIS 5 to MIS 2.  | 116 |
| <b>Fig. 5.4:</b> Time series of deep-sea coral Nd isotope data compared to tracers for local input.  | 120 |
| <b>Fig. 5.5:</b> Comparison of deep-sea coral Nd isotope data with literature data for MIS 4 to 2.   | 125 |
| <b>Fig. 5.6:</b> Schematic of Tasman Sea circulation (modern and peak glacial).  | 129 |
| <b>Fig. 5.7:</b> Time interval from 32 to 30 kyr BP covering Heinrich stadial 3.   | 131 |
| <b>Fig. 6.1:</b> Global map of sub-surface ocean circulation, sampling sites and oxygen section across the Drake Passage.                  | 141 |
| <b>Fig. 6.2:</b> Time series of Nd isotope results and tracers of local input.   | 147 |
| <b>Fig. 6.3:</b> Holocene Southern Hemisphere atmosphere and ocean dynamics and their role in AAIW formation.                              | 149 |
| <b>Fig. 6.4:</b> Drake Passage deep-sea coral data in radiocarbon-Nd-isotope space.  | 153 |
| <b>Fig. 6.5:</b> Global picture of overturning circulation changes during the Holocene.  | 154 |
| <b>Fig. 7.1:</b> Summary of the new deep-sea coral Nd isotope data.  | 160 |
| <b>Fig. 7.2:</b> Schematic of modern and proposed peak glacial mid-depth circulation.  | 162 |

**List of Tables**

|   |     |
|---|-----|
| <b>Table 2.1:</b> Neodymium isotope results for BATS seawater and a deep-sea coral standard   | 34  |
| <b>Table 3.1:</b> Neodymium isotope results for Drake Passage seawater  | 48  |
| <b>Table 3.2:</b> Neodymium isotope results for Drake Passage sediment samples  | 51  |
| <b>Table 3.3:</b> ICP-MS major and trace metal data of Drake Passage sediment samples   | 51  |
| <b>Table 3.4:</b> Neodymium isotopic compositions and U-Th dating of modern coral specimens from the Drake Passage and the North Atlantic | 52  |
| <b>Table 3.5:</b> Major and trace element data for 17 deep-sea coral samples from the Drake Passage                                       | 55  |
| <b>Table 3.6:</b> Nd concentration results from U-Th dating chemistry cuts  | 56  |
| <b>Table 4.1:</b> Neodymium isotope and concentration results of glacial-deglacial deep-sea corals collected in the Drake Passage         | 81  |
| <b>Table 4.2:</b> Neodymium isotope and concentration results of glacial-deglacial deep-sea corals collected south of Tasmania            | 83  |
| <b>Table 5.1:</b> North Atlantic and Southern Ocean deep-sea coral data from the last glacial   | 117 |
| <b>Table 6.1:</b> Holocene deep-sea coral data  | 145 |
| <b>Appendix:</b> Deep-sea coral results from Galapagos, Interim seamount and Reykjanes Ridge.   | 196 |

## Glossary of commonly used and re-occurring abbreviations

|   |   |
|---|---|
| <b>AABW:</b> Antarctic Bottom Water   | <b>MIS:</b> Marine Isotope Stage                            |
| <b>AAIW:</b> Antarctic Intermediate Water   | <b>MLD:</b> Mixed layer depth                               |
| <b>ACC:</b> Antarctic Circumpolar Current   | <b>MOC:</b> Meridional Overturning Circulation              |
| <b>ACR:</b> Antarctic Cold Reversal   | <b>MOW:</b> Mediterranean Outflow Water                     |
| <b>AMOC:</b> Atlantic Meridional Overturning Circulation                                    | <b>MS:</b> Magnetic susceptibility                          |
| <b>B-A:</b> Bølling-Allerød   | <b>NACW:</b> North Atlantic Central Waters                  |
| <b>BATS:</b> Bermuda Atlantic Time Series   | <b>NADW:</b> North Atlantic Deep Water                      |
| <b>BP:</b> Before present, i.e. before 1950 and commonly used<br>in thousand years (kyr) BP | <b>NES:</b> New England Seamounts                           |
| <b>CDW:</b> Circumpolar Deep Water (prefix U/L:<br>upper/lower)                             | <b>NPIW:</b> North Pacific Intermediate Water               |
| <b>CHUR:</b> Chondritic Uniform Reservoir   | <b>PAAS:</b> Post-Archean Australian Shale                  |
| <b>CO<sub>2</sub>:</b> Carbon dioxide   | <b>PDW:</b> Pacific Deep Water                              |
| <b>COC:</b> Centre of calcification   | <b>PF:</b> Polar Front                                      |
| <b>CTD:</b> Conductivity, Temperature, Depth sensor   | <b>REE:</b> Rare Earth Element (prefix L/H:<br>light/heavy) |
| <b>D/O cycle:</b> Dansgaard-Oeschger cycle  | <b>SACC:</b> Southern ACC front                             |
| <b>DSOW:</b> Denmark Strait Overflow Water  | <b>SAF:</b> Subantarctic Front                              |
| <b>GNAIW:</b> Glacial North Atlantic Intermediate Water                                     | <b>SAM:</b> Southern Annular Mode                           |
| <b>GNPIW:</b> Glacial North Pacific Intermediate Water                                      | <b>SAMW:</b> Subantarctic Mode Water                        |
| <b>HS:</b> Heinrich Stadial   | <b>SD:</b> Standard deviation                               |
| <b>IDW:</b> Indian Deep Water   | <b>SE:</b> Standard error                                   |
| <b>IRD:</b> Ice-rafted detritus   | <b>SFZ:</b> Shackleton Fracture Zone                        |
| <b>ISOW:</b> Iceland-Scotland-Overflow Water  | <b>SPDW:</b> South Pacific Deep Water                       |
| <b>ITCZ:</b> Intertropical Convergence Zone   | <b>SPMW:</b> Subpolar Mode Water                            |
| <b>LGM:</b> Last Glacial Maximum  | <b>SST:</b> Sea Surface Temperature                         |
| <b>LOD:</b> Limit of detection  | <b>STF:</b> Subtropical Front                               |
| <b>LSW:</b> Labrador Seawater   | <b>SWW:</b> Southern Hemisphere westerly winds              |
| <b>MAR:</b> Mid-Atlantic Ridge  | <b>TIMS:</b> Thermal ionisation mass spectrometry           |
| <b>(MC-)ICP-MS:</b> (Multi-collector) inductively coupled<br>plasma mass spectrometry       | <b>WAIS:</b> West Antarctic Ice Sheet                       |
|   | <b>WAP:</b> Westantarctic Peninsula                         |
|   | <b>WSDW:</b> Weddel Sea Deep Water                          |

# **Chapter 1**

# **Introduction**

### 1.1. The Southern Ocean's role in the global overturning circulation

The modern type of ocean circulation and heat transport evolved with the opening of the Tasman Gateway and the Drake Passage during the Cenozoic (e.g., Kennett, 1977; Broecker, 1991; Lawver and Gahagan, 2003; Sijp and England, 2004; Lagabrielle et al., 2009). This modern deep circulation is characterised by the central role of the Southern Ocean and vigorous formation of deep water masses in the North Atlantic Ocean (e.g., Talley, 2013; Fig. 1.1). From an Atlantic perspective the deep circulation pattern is referred to as Atlantic Meridional Overturning Circulation AMOC, which is, according to Marshall and Speer (2012), organised in “two global-scale counter-rotating meridional cells”.

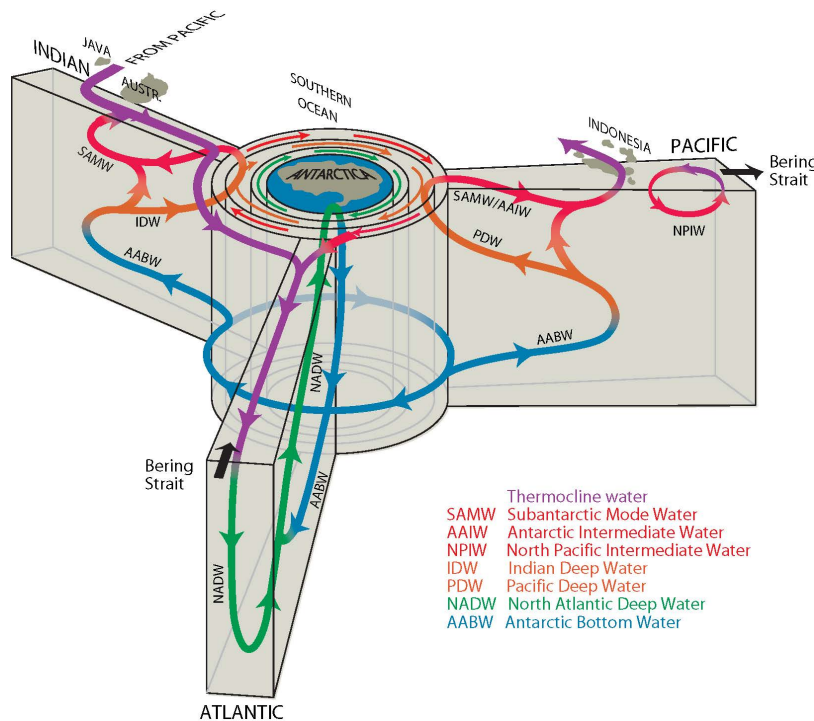


**Figure 1.1:** Schematic of a three dimensional view on the modern global overturning circulation, from Talley (2013). Note the outcropping of NADW close to the Antarctic continent and PDW/IDW supplying mode and intermediate water formation to the north of the ACC polar front. The isolated, shallow and weak overturning cell associated with NPIW is indicated in the North Pacific.

The ventilation of the upper cell is closely linked to the formation of North Atlantic Deep Water (NADW) sourced from deep convection of originally (sub) tropical surface waters into the deeper water column through extensive heat loss in the marginal seas of the North Atlantic (Gascard, 1978; Schlitzer et al., 1991; Lilly et al., 1999; Ronski and Budéus, 2005). The NADW product is then exported southwards into the zonal flow of the Antarctic Circumpolar Current (ACC) in the Southern Ocean (Fig. 1.1). The eastward ACC flow of  $\sim 130 - 140$  Sv (i.e.  $10^6$  m<sup>3</sup>/s) is largely bound to two zonal jets, i.e. the Subantarctic Front (SAF) and the Polar Front (PF) extending through the entire water column and steered by wind and topography (Orsi et al., 1995; Cunningham et al., 2003). Based on its apparent uniformity, Sverdrup (1940) termed this circumpolar water mass Circumpolar Deep Water (CDW). This was later revisited due to the fact that the core of NADW joins the ACC at lower depths reflected in water mass properties of Lower Circumpolar Deep Water (LCDW), e.g., relatively high salinity and oxygen contents (Reid and Lynn, 1971; Callahan, 1972). In contrast, Upper

Circumpolar Deep Water (UCDW) shows a strong influence from Pacific Deep Water (PDW) and Indian Deep Water (IDW), and is therefore characterised by lower salinity and reduced oxygen content compared to LCDW (Reid and Lynn, 1971; Callahan, 1972). Both water masses can roughly be divided by the neutral density surface (isoneutral)  $\gamma^n = 28.0 \text{ kg/m}^{-3}$  (e. g., Sudre et al., 2011).

The deep wind-induced upwelling of UCDW ( $28.0 \text{ kg/m}^{-3} > \gamma^n > 27.6 \text{ kg/m}^{-3}$ ) into the surface mixed layer of the ACC is associated with buoyancy gain from positive fresh water and heat fluxes (e.g., Marshall and Speer, 2012). As such, UCDW is the major upwelling component feeding into the formation of Subantarctic Mode Water (SAMW) and Antarctic Intermediate Water (AAIW), both of which are subducted into the ocean interior north of the PF (Piola and Georgi, 1982; Bostock et al., 2013; Talley, 2013; Fig. 1.1). Poleward of the PF, upwelling of NADW-spiked LCDW ( $28.2 \text{ kg/m}^{-3} > \gamma^n > 28.0 \text{ kg/m}^{-3}$ ) takes part in the circumpolar formation of Antarctic Bottom Water (AABW). In detail, high density shelf bottom water masses are formed from upwelling CDW which mixes with very cold shelf waters ( $T < 0^\circ\text{C}$ ) upon supercooling below ice-shelves, heat loss to the atmosphere and/or brine rejection during sea ice formation (Orsi et al., 1999). Subsequently, such shelf bottom water masses flow over the shelf edge into the abyss of the adjacent basins, thereby entraining ambient LCDW (Orsi et al., 1999; Stramma and England, 1999). During northward penetration, AABW mixes into overlying water masses (i.e. NADW, PDW and IDW), thus closing the lower global meridional overturning circulation (MOC) cell (Marshall and Speer, 2012; Talley, 2013; Fig. 1.1). This subsurface part of the global overturning circulation can be summarised by the southward export of deep water masses balanced by the northward return flow of SAMW/AAIW and AABW (Talley, 2013; Fig. 1.1). In the modern Atlantic Ocean, an additional effect occurs due to the vigorous formation of NADW leading to unique cross-equatorial flow of (sub) tropical surface waters supplying the formation of NADW source waters (e.g., Marshall and Speer, 2012; Fig. 1.1).

Although the central role of the ACC in this global overturning circulation system and associated oceanographic features are well-known, there is an ongoing debate on the dominating return path of deep water masses from the ocean interior to the surface and the processes driving this deep-water return (e.g., Kuhlbrodt et al., 2007; Marshall and Speer, 2012). Early work by Stommel (1958), Wyrski (1961) and Munk (1966) suggested that diapycnal mixing (i.e. mixing across neutral density surfaces) is balanced by downward mixing of heat which, in slightly refined form, led later studies to propose that large scale diapycnal mixing is the dominant driver of the MOC (e.g., Bryan, 1987; Munk and Wunsch, 1998). More recent work identified a differentiated picture of non-uniform diapycnal mixing in the ocean interior (e.g., Polzin et al., 1997; Saenko, 2006; Decloedt and Luther, 2010; Watson et al., 2013). But also the role of surface winds inducing deep mixing has been considered e.g., by Munk and Wunsch (1998). In a series of model studies by Toggweiler and Samuels (1993, 1995, 1998), and more recently by e.g., Marini et al. (2011) and Sheen et al. (2014), Southern Hemisphere wind forcing has been directly coupled with deep circulation. As summarised by Marshall

and Speer (2012) both, wind-induced upwelling and diapycnal mixing in the ocean interior are involved in driving the MOC.

The wind-induced upwelling is closely linked to the Southern Hemisphere westerly winds (SWW) comprising a major component of the insolation-driven global atmospheric circulation. Specifically, the SWW result from the dynamic pressure gradient of the low and mid-latitudes to the high latitudes, described by the Southern Annular Mode (SAM; Limpasuvan and Hartmann, 1999). On a first order, atmospheric surface pressure gradients result from the surface distribution of heat so that the SAM is the dominant pattern of a “nearly zonally symmetric, [latitudinal] movement of momentum and mass” (Limpasuvan and Hartmann, 1999). Or in other words: the latitudinal movement of the westerly wind belt. Following this, fluctuations of the SAM/SWW occur roughly in response to changes in heat distribution, recorded on various time scales, i.e. from sub-annual (e.g., Baldwin, 2001) to (multi-) millennial (e.g., Anderson et al., 2009; Lamy et al., 2010; Kohfeld et al., 2013). Such mid-latitude atmospheric variability projects (asymmetrically: Sallée et al., 2008, 2010) on the (sub-) surface ocean across a similar range of time scales thus influencing the structure (e.g., Gille, 2008; Anderson et al., 2009) and transport rate (e.g., Hall and Visbeck, 2002; Hughes et al., 2003; Lamy et al., 2015) of circumpolar flow.

The early studies of Toggweiler and Samuels (1993, 1995, 1998) suggested a strong sensitivity of the overturning strength to the intensity of the Southern Hemisphere westerly winds (SWW). Marshall and Radko (2003) showed, however, that wind- and buoyancy-induced meridional Eulerian mean transport of the ACC is widely compensated by eddy-induced transport, leaving the MOC as relatively insensitive residual flow. This effect has been found frequently in recent fine resolution model simulations and is referred to as “eddy compensation” (e.g., Viebahn and Eden, 2010; Meredith et al., 2012; Zhai and Munday, 2014). But the degree of compensation seems to relate to the intensity of applied wind stress over the ACC (e.g., Viebahn and Eden, 2010; Munday et al., 2013) and to surface restoring conditions, i.e. interactive buoyancy forcing and whether or not the isoneutrals are free to move (e.g., Abernathey et al., 2011; Zhai and Munday, 2014). Similarly, the wind-induced zonal flow of the ACC is balanced by effective eddy transport, termed eddy saturation (see e.g., Munday et al., 2013), but was shown to be sensitive to variable atmospheric forcing (e.g., Hall and Visbeck, 2002; Hughes et al., 2003). This highlights that the direct response of both, the (residual) meridional and zonal transport to wind forcing, are (partially) compensated by enhanced eddy fields. The degree of sensitivity of meridional and zonal ACC transport to changes in wind stress is however subject to debate (e.g., Marshall and Radko, 2003; Meredith et al., 2012; Munday et al., 2013; Ferrari et al., 2014; Sheen et al., 2014; Langlais et al., 2015). Nonetheless, past work suggested that SWW forcing seems to critically influence the structure of the overturning circulation (e.g., Saenko et al., 2004; Toggweiler et al., 2006; Anderson et al., 2009; Sijp and England, 2009; Meredith et al., 2012; Sheen et al., 2014) and the transport rate of the ACC (e.g., Hughes et al., 2003; Lamy et al., 2015).

Therefore, the controls on structure, flow and (trans-) formation of Southern Ocean water masses are complex. These considerations are important for understanding the coupled ocean-atmosphere dynamics in the Southern Hemisphere mid- to high latitudes and their link with the global ocean circulation.

## 1.2. The Southern Ocean's role in ocean-atmosphere exchange of carbon

The unique characteristic of the Southern Ocean in the global overturning circulation system provides a direct link between deep ocean waters and the atmosphere through upwelling highlighting its central role in the global re-distribution of key parameters such as heat, freshwater and carbon (Marshall and Speer, 2012). A particularly important parameter in the modern climate system is carbon dioxide (CO<sub>2</sub>) due to its potential of enhancing global warming trends (IPCC, 2013). Naturally, the Southern Ocean acts as a net source of CO<sub>2</sub> resulting from upwelling of old deep waters, whereas during the past decades, the Southern Ocean acted as a net sink of anthropogenic carbon from the atmosphere (Sabine et al., 2004). Recent changes in the structure and dynamics of the SWW, attributed to anthropogenic global warming, act to reduce Southern Ocean CO<sub>2</sub> uptake (Le Quéré et al., 2007). Similarly, the dynamics of the ACC change in response to atmospheric forcing, and as such, the nature of ocean-atmosphere exchange is sensitive to changes of the wind fields and ocean circulation (e.g., Gille, 2002, 2008; Böning et al., 2008; Sallée et al., 2010).

From reconstructions of deglacial climate states it was concluded that millennial-scale exchange between the large deep oceanic carbon reservoir and the atmosphere was moderated through wind-induced Southern Ocean upwelling intensity (Anderson et al., 2009; Burke and Robinson, 2012). Alongside, there is a rapid decrease in atmospheric radiocarbon (<sup>14</sup>C) activity associated with the two-step 100 ppm deglacial rise in atmospheric CO<sub>2</sub> content (Reimer et al., 2013; Marcott et al., 2014). This can only partly be explained by elevated <sup>14</sup>C production in the contemporaneous atmosphere (Laj et al., 2002, Muscheler et al., 2004; Broecker and Barker, 2007). It has been proposed that changes in the distribution of carbon between the deep ocean and the atmosphere can provide a reasonable mechanism explaining the deglacial carbon cycle disruptions (e.g., Broecker et al., 1982; Sigman et al., 2010). Therefore, an isolated deep ocean carbon reservoir was suggested to have accumulated during glaciations contributing to the postglacial rise in atmospheric CO<sub>2</sub> through outgassing. Such an isolated carbon reservoir is evident from radiocarbon-depleted glacial Southern Ocean water masses (e.g., Sikes et al., 2000; Skinner et al., 2010; 2015; Burke and Robinson, 2012). The application of radiocarbon is based on the basic principle of gas exchange between a given reservoir (here: the ocean, or an oceanic water mass) and the atmosphere where the <sup>14</sup>C is produced from <sup>14</sup>N ( $^{14}\text{N} + n \rightarrow ^{14}\text{C} + p$ ). The production rate in the atmosphere depends on the intensity of cosmic rays and solar activity modulated by geomagnetic field intensity (Masarik and Beer, 1999). Along with internal changes in the carbon cycle, e.g., reduced exchange between reservoirs, these parameters determine the variability of atmospheric <sup>14</sup>C content through time (Laj et al., 2002; Muscheler et al., 2004; Reimer et al., 2013).

Reducing the exchange between the ocean and the atmosphere, for instance, by reducing the intensity of deep ocean circulation and/or mixing (i.e. more sluggish) may cause a quasi-isolated reservoir where  $^{14}\text{C}$  is decaying away (with a half-life of  $5730 \pm 40$  years), resulting in significant radiocarbon depletion (e.g., Adkins and Boyle, 1997; Sikes et al., 2000; Skinner et al., 2010, 2015; Burke and Robinson, 2012). On the one hand, this gives rise to a major uncertainty when using radiocarbon dating to produce age models for palaeoclimatic records which require the calibration of  $^{14}\text{C}$ -derived ages against absolute ages apart from simple decay (Reimer et al., 2013). On the other hand, if the age of a sample/record can be determined independently, e.g., by uranium-series (U-series) dating,  $^{14}\text{C}$  is free to calculate reservoir ages. The reservoir age is the difference between the  $^{14}\text{C}$  age (measured in relation to stable  $^{12}\text{C}$ , normalised to Vienna Pee Dee Belemnite reference material and expressed as  $\Delta^{14}\text{C}$  in per mil) and the absolute U-series age of a given sample which can then be compared to the contemporaneous atmospheric  $^{14}\text{C}$  content as compiled by Reimer et al. (2013). The difference between these two reservoirs at a given time can be expressed as  $\Delta\Delta^{14}\text{C}$ .

In the modern ocean, the radiocarbon content of oceanic water masses has proven to be a useful proxy to identify the age of respective water masses (Matsumoto, 2007). The reconstruction of past  $\Delta\Delta^{14}\text{C}$  was approached by paired foraminifer records (e.g., Broecker et al., 1988; Shackleton et al., 1988; Adkins et al., 1997; Sikes et al., 2000) and deep-sea corals (e.g., Adkins et al., 1998; Goldstein et al. 2001; Robinson et al., 2005) in order to trace potential changes in deep ocean reservoir ages. During the Last Glacial Maximum (LGM), the equivalent of modern NADW was restricted to depths above  $\sim 2500$  m (e.g., Sarnthein et al., 1994; Curry and Oppo, 2005). In contrast, Southern Ocean water masses, such as AABW and AAIW, expanded vertically and likely also laterally into the North Atlantic Ocean (e.g., Sarnthein et al., 1994; Curry and Oppo, 2005; Pahnke et al., 2008, Roberts et al. 2010). This shoaling of the NADW-AABW interface is believed to have efficiently reduced mixing between the upper and lower circulation cell, leaving the lower cell poorly ventilated (e.g., Ferrari et al., 2014). This scenario is consistent with the glacial to deglacial distribution of radiocarbon-depleted water masses found in the North Atlantic (Robinson et al., 2005; Thornalley et al., 2011, 2015; Skinner et al., 2014), Arabian Sea (Bryan et al., 2010), in the intermediate (Mangini et al., 2010) and deep South Atlantic (Barker et al., 2010; Skinner et al., 2010), the Drake Passage (Goldstein et al., 2001; Burke and Robinson, 2012), as well as in the Western (Sikes et al., 2000; Skinner et al., 2015) and Eastern Pacific Ocean (Marchitto et al., 2007, Stott et al., 2009). Burke and Robinson (2012) presented direct evidence that upwelling of water masses from a radiocarbon-depleted deep ocean reservoir through the Southern Ocean water column contributed to the deglacial rise in atmospheric  $\text{CO}_2$  (e.g., Marcott et al., 2014). Mechanistically, such intensified upwelling is considered to be related to strengthening of the SWW over the ACC in concert with retreating Southern Ocean sea ice cover (Anderson et al., 2009).

However, along the western margin of South America no evidence for  $\Delta^{14}\text{C}$ -depleted water masses was found (De Pol-Holz et al., 2010) and wide areas of the deep Pacific show glacial  $\Delta^{14}\text{C}$

depletions not significantly different to modern values (e.g., Shackleton et al., 1988; Broecker et al., 2007). Hence, it is necessary to apply an independent proxy to decipher the nature of water mass mixing and reservoir ages. From section 1.1 follows that modern ocean circulation is inferred mainly from conservative seawater properties. The reconstruction of past oceanic salinity and temperature distribution is challenging and does not contain water mass provenance information. A promising proxy preserved in the geological record, are neodymium (Nd) isotopes.

### 1.3. The marine neodymium isotope system and its application to palaeoceanography

Radiogenic isotope systems, such as Nd, are powerful tools for the reconstruction of water mass mixing on different time scales (e.g., Frank, 2002; Goldstein and Hemming, 2003; van de Flierdt and Frank, 2010).

Neodymium has seven stable isotopes of which the radiogenic  $^{143}\text{Nd}$  is of particular interest to isotope geochemical applications. The ingrowth of radiogenic  $^{143}\text{Nd}$  over time results from  $\alpha$ -decay of  $^{147}\text{Sm}$  (Samarium-147) with a half-life of 106 billion years. Chemical fractionation of parent and daughter elements, Sm and Nd, during crustal extraction (e.g., O’Nions et al., 1979; Allègre et al., 1980; DePaolo, 1980) resulted in higher Sm/Nd, and thus higher  $^{143}\text{Nd}/^{144}\text{Nd}$  ratios in the Earth’s mantle. Hence, young mantle-derived rocks show distinct Nd isotopic compositions compared to old continental crust (e.g., Jeandel et al., 2007).

Since variations in natural  $^{143}\text{Nd}/^{144}\text{Nd}$  ratios are very small, i.e. on the order of  $10^{-4}$  to  $10^{-5}$ , Nd isotopes are typically expressed in the  $\epsilon_{\text{Nd}}$ -notation:

$$\epsilon_{\text{Nd}} = \left( \frac{(^{143}\text{Nd}/^{144}\text{Nd})_{\text{sample}}}{(^{143}\text{Nd}/^{144}\text{Nd})_{\text{CHUR}}} - 1 \right) \times 10^4$$

CHUR refers to the Chondritic Uniform Reservoir describing the primordial bulk earth isotopic composition derived from chondritic meteorites providing a reference frame of Earth’s isotopic evolution. According to Jacobsen and Wasserburg (1980) the present day  $^{143}\text{Nd}/^{144}\text{Nd}$  of CHUR is 0.512638.

In the ocean, the particulate phase of Nd represents only 5 to 10% of the total budget; the rest is in dissolved phase (Jeandel et al. 1995). The global oceanic budget of dissolved Nd is controlled by the input of weathering products and their partial dissolution (Figure 1.2), and as such, dominated by continental inputs (e.g., Frank, 2002; Fig. 1.2), whereas hydrothermal inputs of Nd are removed immediately very close to or within the hydrothermal sources (German et al., 1990; Halliday et al., 1992). Neodymium has an average global residence time of 400 to 2000 years (Tachikawa et al., 1999, 2003), although more recent studies suggest a residence time being at the lower end of that range (Siddall et al., 2008; Arsouze et al., 2009).

The main sources contributing to the dissolved oceanic Nd budget are dust (Goldstein et al., 1984; Greaves et al., 1999), rivers (Goldstein and Jacobsen, 1988) and boundary exchange (Lacan and

Jeandel, 2004, 2005a). Although dust input was generally considered a significant source to the dissolved marine Nd budget through partial dissolution (Goldstein et al., 1984; Greaves et al. 1999; Tachikawa et al., 1997, 1999) its influence on the deep ocean seems limited (cf. Jones et al., 1994; Stichel et al., 2015). Most of the dissolved Nd supplied to the ocean via rivers in dissolved or colloidal form is removed upon contact with seawater (e.g., Goldstein and Jacobsen, 1988; Elderfield et al., 1990). Recent work showed, however, that a significant amount of Nd can be released from sediments in the mid- to high-salinity zone of an estuary, a process that could dominate the global Nd fluxes to the ocean (Rousseau et al., 2015). Along these lines of sediment-seawater interaction, another important source of rare earth elements to the ocean is boundary exchange, i.e. the exchange of a moving water mass with bathymetric features (e.g., Lacan and Jeandel, 2005a; Wilson et al., 2012). Lacan and Jeandel (2005a) showed that this process can significantly alter the Nd isotopic composition and/or the Nd concentration of seawater at the margins of all ocean basins. Taken together, these fluxes imprint the Nd isotopic composition of terrestrial sources on seawater in vicinity to the continents (e.g., Jeandel et al., 2007; Lacan et al., 2012).

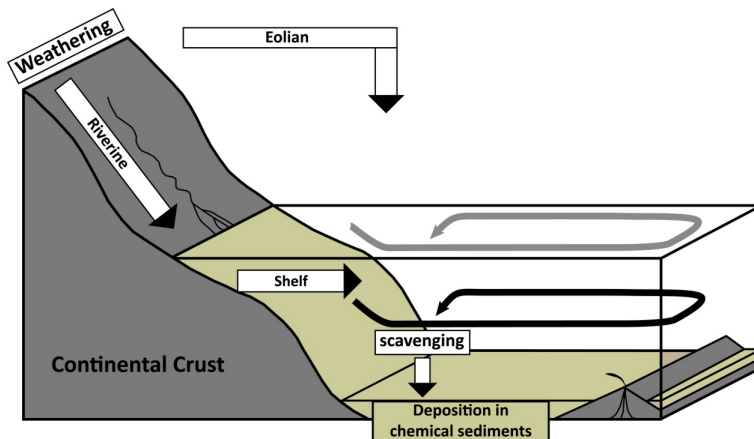


**Figure 1.2:** Pathways of Nd from the sources to the sinks. The major inputs are: riverine, eolian, hydrothermal and release from shelf sediments. The solid lines and arrows mark ocean circulation which causes mixing of the dissolved Nd (modified, from Frank, 2002).

This is reflected in the unradiogenic Nd isotope imprint on North Atlantic Deep Water (i.e. contributions from the old cratonic areas around the North Atlantic; NADW:  $\epsilon_{Nd}$  values of  $\sim -13.5$ , Piepgras and Wasserburg, 1987; Lacan and Jeandel, 2005b), and a radiogenic imprint on Pacific seawater (i.e. from young, mantle-derived rocks around the Pacific;  $\epsilon_{Nd}$  values of  $\sim -4$ ; Piepgras and Jacobsen, 1988; Amakawa et al., 2009).

The Southern Ocean links these two global Nd isotope source regions through the vigorous mixing of water masses in the ACC. Therefore, circumpolar water masses are characterised by a rather homogenous Nd isotopic composition  $\epsilon_{Nd} \approx -8$  with a small degree of inter-basin variability resulting from mainly conservative mixing between NADW and PDW (Piepgras and Wasserburg, 1982; Carter et al., 2012; Stichel et al., 2012; Garcia-Solsona et al., 2014; Rickli et al., 2014; Basak et al., 2015). In contrast, AABW shows clear provinciality, dependent on the Antarctic source rocks in the formation areas, ranging from  $\epsilon_{Nd}$  values of  $-9$  in the Atlantic sector and  $-10$  in the Australian-Antarctic basin to -

7 in the Pacific sector (van de Flierdt et al., 2006a; Carter et al., 2012; Stichel et al., 2012; Rickli et al., 2014; Basak et al., 2015).

Given that ocean circulation is sensitive to changing climate conditions, deciphering changes in water mass mixing during extreme climate transitions, such as the last deglaciation, is highly relevant, in particular with respect to key regions like the Southern Ocean (e.g., Robinson and van de Flierdt, 2009). Neodymium isotopes are advantageous over other conventional tracers of ocean circulation, such as stable carbon isotopes as they, most notably, do not fractionate significantly during biological processes or evaporation. Even if fractionation would occur, such effect is removed through the correction for mass bias during mass spectrometric analyses (Chapter 2). Likewise important for the application as a water mass tracer is the observation that Nd isotopes act as a quasi-conservative tracer in deep waters as reflected in the close correlation with salinity and silicate (e.g., Elderfield and Greaves, 1982; De Baar et al., 1985; von Blanckenburg, 1999; Siddall et al., 2008; Arsouze et al., 2009; Stichel et al., 2012; Lambelet et al., accepted; see also discussion in Goldstein and Hemming, 2003). Past Nd isotopic compositions of seawater are incorporated and preserved in authigenic (= seawater-derived) precipitates, such as ferromanganese coatings on sediments (e.g., Piotrowski et al., 2005; Gutjahr et al., 2007), foraminiferal calcite (e.g., Vance and Burton, 1999; Burton and Vance, 2000), fossil fish teeth (e.g., Martin and Scher, 2004), ferromanganese crusts (e.g., Burton et al., 1997; Foster and Vance, 2006), and the skeletons of aragonitic deep-sea corals (van de Flierdt et al., 2006b, 2010; Copard et al., 2010, 2011).

#### 1.4. Deep-sea corals as palaeoceanographic archives

In the Southern Ocean, traditional palaeoceanographic archives such as foraminifera are difficult to use due to poor calcite preservation. Furthermore, strong bottom currents make many areas deficient of continuous sediment records. Hence, novel archives are needed to reconstruct past Southern Ocean water mass properties. Deep-sea corals are such new archive, and, with respect to palaeoceanographic investigations, a particularly promising one.

Deep-sea corals are of the phylum cnidaria, and are divided into black corals (Antipatharia), hydrocorals (Stylasteridae), soft corals (Octocorallia) and stony corals (Scleractinia) (Roberts et al., 2006). Whereas some colonial species build reef structures (e.g., *Lophelia pertusa*) similar to shallow-water corals, other deep-sea corals are solitary (e.g., *Desmophyllum dianthus*) (Freiwald et al., 2004).

In contrast to shallow water corals (zooxanthellate), deep-sea corals (azooxanthellate) are able to grow in the absence of sunlight. Their distribution is global (Fig. 1.3), i.e. they can be found in all major ocean basins between 0 and >6000 m water depth (Keller 1976; Freiwald et al., 2004), with a preference for mid-depths (e.g., Roberts et al., 2006). Knowledge about temperature and salinity ranges for deep-sea coral habitats is incomplete, but observed temperatures span from <0 to >20 °C (Keller, 1976; Stanley and Cairns, 1988), with an apparent preference for temperatures between 4 and 12 °C (Roberts et al., 2006). Similarly, salinities for deep-sea coral habitats show a wide range from

~32 % in Norwegian Fjords up to 38.8 % in the Ionian Sea (Freiwald et al., 2004).

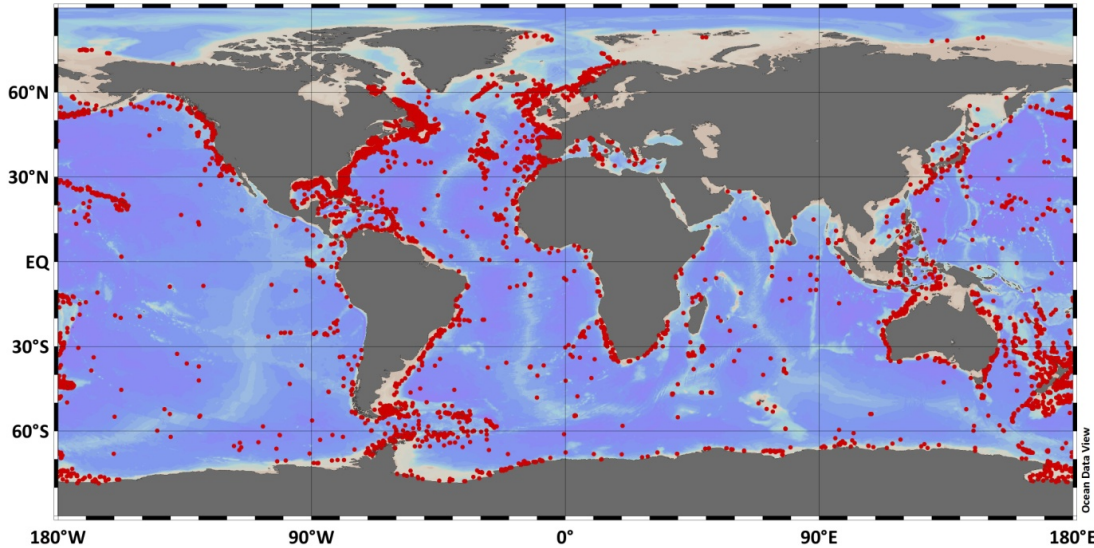


**Figure 1.3:** Summarised distribution of Antipatharia, Stylasteridae, Octocorallia and Scleractinia in the global ocean (below 100 m water depth). Coral data from OBIS (2015). Map generated with ODV software (Schlitzer, 2012).

Due to their fast growth rates from 0.5-2 mm/year (*Desmophyllum dianthus*; Fig. 1.4) up to 4-26 mm/year (*Lophelia Pertusa*) (Risk et al., 2002; Adkins et al., 2004) the skeletons of aragonitic scleractinian deep-sea corals provide high resolution palaeoceanographic archives, which can be dated accurately by U-series disequilibrium (e.g., Cheng et al., 2000; Robinson et al., 2006; Andersen et al., 2008). Dating reveals that deep-sea coral populations vary through space and time, indicating a potential link between ocean circulation (i.e. environmental) changes and coral growth (e.g., Roberts et al., 2006; Robinson et al., 2007; Burke et al., 2010; Thiagarajan et al., 2013; Henry et al., 2014; Margolin et al., 2014). In the Southern Ocean, deep-sea coral populations seem to have changed dramatically in vertical and lateral direction on climatic time scales in genus-specific response to changes in productivity, oxygen and carbonate ion concentrations (Robinson et al., 2007; Thiagarajan et al., 2013; Margolin et al., 2014). For instance, *D. dianthus* populations appear to expand during phases of rapid change whereas climatically more stable intervals are associated with retreating populations (Thiagarajan et al., 2013). These ecological observations on coral populations have been facilitated by efficient age screening methods, and in particular new radiocarbon-based dating techniques (Burke et al., 2010; McIntyre et al., 2011). Moreover, such age surveys are the most important initial step in using deep-sea coral collections for palaeoceanographic studies (Burke et al., 2010,



**Figure 1.4:** Sub-fossil skeleton of *Desmophyllum dianthus* collected during NBP0805. Scale in centimetre. Photo: Dann Blackwood.

McIntyre et al., 2011). Reconnaissance type radiocarbon dating is less precise than common  $^{14}\text{C}$  analyses, but provides a valuable approach for screening large numbers of samples for age surveys and selection for precise U-series dating and further proxy applications (Burke et al., 2010, Burke and Robinson, 2012; Robinson et al., 2014).

Probably the single most successful tracer extracted from the skeletons of deep-sea corals (Fig. 1.4) over the past 15 years is radiocarbon (e.g., Adkins et al., 1998; Goldstein et al. 2001; Frank et al., 2004; Robinson et al., 2005; Burke and Robinson, 2012). As outlined above, atmospheric radiocarbon content is variable through time (Laj et al., 2002; Muscheler et al., 2004; Reimer et al., 2013) resulting from (1) changes in the production rate (Masarik and Beer, 1999) and (2) internal changes in the carbon cycle like reduced exchange between reservoirs. The data extracted from deep-sea coral skeletons contributed significantly to constrain glacial-interglacial variability in carbon exchange between reservoirs. In particular, variability of carbon exchange between the atmosphere and the ocean could be resolved by application of U-series dating and  $\Delta^{14}\text{C}$  analyses to deep-sea corals (e.g., Adkins et al., 1998; Robinson et al., 2005; Mangini et al., 2010; Burke and Robinson, 2012). However, radiocarbon analyses alone cannot determine water mass origin and/or mixing. Therefore, it is crucial to obtain an independent handle on water mass mixing. This can be achieved by using Nd isotopes along with U-Th dating and  $\Delta^{14}\text{C}$  analyses (e.g., Basak et al., 2010).

This PhD project focused on the extraction of Nd isotopes from the aragonitic skeletons of deep-sea corals and the application as a palaeoceanographic tool in order to obtain an independent constraint on past water mass mixing in the Southern Ocean. Calibration work of van de Flierdt et al. (2006b, 2010) and Copard et al. (2010) demonstrated that the seawater Nd isotope signal is recorded faithfully in the aragonitic skeletons of deep-sea corals across a wide range of Nd isotope signatures (Fig. 1.5). Based on this successful calibration work, Nd isotopes extracted from deep-sea corals were applied to trace glacial to Holocene water mass mixing in the Northwest and Northeast Atlantic Ocean (van de Flierdt et al., 2006b; Colin et al., 2010; Copard et al., 2011, 2012; López Correa et al., 2012; Montero-Serrano et al., 2011, 2013; Wilson et al., 2014).

In the Southern Ocean, a single fossil, *D. dianthus*, from Sars Seamount in the Drake Passage has been U-series dated to an age of 16.7 kyr, and analysed for radiocarbon and Nd isotopes (Goldstein et al., 2001; Robinson and van de Flierdt, 2009). The results have been interpreted to reflect reduced NADW influence in the Drake Passage during

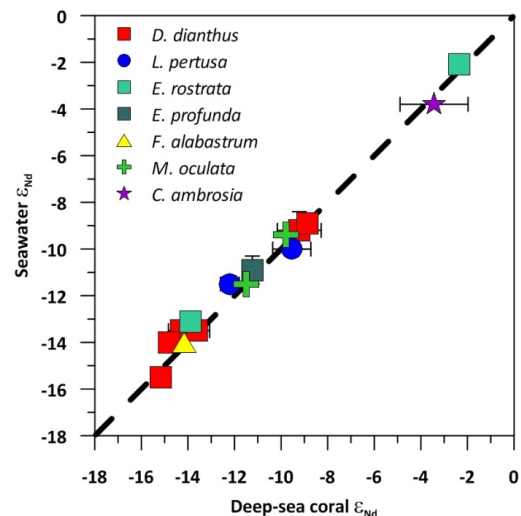


**Figure 1.5:** Global calibration for Nd isotopes in deep-sea coral aragonitic skeletons. Reproduced from Robinson et al. (2014) including data from Copard et al., (2010) and van de Flierdt et al. (2010).

Heinrich Stadial 1 (HS1), expressed by a  $\sim 2.5$  epsilon unit shift in Nd isotopes, and a  $\sim 50$  ‰ shift in  $\Delta^{14}\text{C}$  compared to today. This finding and the fact that the Southern Ocean is drastically undersampled with respect to palaeoclimatic investigations, was the motivation to collect deep-sea corals in the Drake Passage and south of Tasmania during targeted ship-board expeditions (NBP0850, NBP1103, TN-228). The coral samples were subsequently processed in a collaborative effort extracting multiple proxies from the same coral of which the Nd isotope work is presented in this thesis.

## 1.5. Thesis structure

This work uses Nd isotopes to tackle the question of how the Southern Ocean water mass mixing changed during the past ~70,000 years, with a particular focus on the past ~40,000 years. Therefore, the thesis is structured as follows:

**Chapter 1** (*Introduction*) provides a general introduction to the relevant topics.

**Chapter 2** (*Neodymium isotope analyses after combined extraction of actinide and lanthanide elements from seawater and deep-sea coral aragonite*) contains the methodological approach of applied chemical multi-element separation and discusses the fidelity of Nd isotope results extracted from seawater and aragonitic matrices.

**Chapter 3** (*Neodymium isotopes and concentrations in aragonitic deep-sea corals - modern calibration and evaluation of palaeo-applications*) extends previous calibration work and discusses the nature of Nd in deep-sea coral skeletons.

**Chapter 4** (*The deglacial Southern Ocean: centennial-scale circulation changes recorded in deep-sea coral skeletons?*) evaluates the newly obtained high resolution deep-sea coral Nd isotope data in the context of deglacial climate perturbations focusing on the oceanic response to abrupt change.

**Chapter 5** (*Mid-depth ocean circulation during MIS 3 and MIS 2: neodymium isotope evidence for interhemispheric coupling*) covers a time interval of significant swings of the climate system and establishes an interhemispheric link between Southern Ocean circulation and Northern Hemisphere abrupt change.

**Chapter 6** (*Holocene changes in Southern Ocean mid-depth ocean circulation in response to atmospheric forcing inferred from deep-sea corals*) explores the significance of Southern Ocean dynamics for the global overturning system under similar-to-modern boundary conditions.

**Chapter 7** (*Summary and general conclusions*) comprises an illustrated summary of the data presented in the individual chapters and general conclusions drawn from the work presented here, including an outlook for future research.

## **Chapter 2**

# **Neodymium isotope analyses after combined extraction of actinide and lanthanide elements from seawater and deep-sea coral aragonite**

**This chapter is prepared for publication as T. Struve, T. van de Flierdt, L. F. Robinson, L. I. Bradtmiller, S. K. Hines, J. F. Adkins, M. Lambelet, K. C. Crocket, K. Kreissig, B. Coles, and M. E. Auro: Neodymium isotope analyses after combined extraction of actinide and lanthanide elements from seawater and deep-sea coral aragonite, ‘Technical Reports: Methods’ in *Geochemistry, Geophysics, Geosystems*.**

**Abstract**

Isotopes of the actinide elements protactinium (Pa), thorium (Th) and uranium (U), and the lanthanide element neodymium (Nd) are often used as complementary tracers of modern and past oceanic processes. The extraction of such elements from low abundance matrices, such as seawater and carbonate, is however labor-intensive and requires significant amounts of sample material. We here present a combined method for the extraction of Pa, Th and Nd from 5 to 10 L seawater samples, and of U, Th and Nd from <1 g carbonate samples. Rare earth elements, and hence Nd, are collected in the respective wash fractions of Pa-Th and U-Th anion exchange chromatographies. Regardless of the original sample matrix, Nd is extracted during a two-stage ion chromatography, followed by thermal ionization mass spectrometry (TIMS) analysis as  $\text{NdO}^+$ . Using this combined procedure, we obtained results for Nd isotopic compositions on two GEOTRACES consensus samples from Bermuda Atlantic Time Series (BATS), which are within error identical to results for separately sampled and processed dedicated Nd samples ( $\epsilon_{\text{Nd}} = -9.20 \pm 0.21$  and  $-13.11 \pm 0.21$  for 15 and 2000 m water depth, respectively; intercalibration results from 14 laboratories:  $\epsilon_{\text{Nd}} = -9.19 \pm 0.57$  and  $-13.14 \pm 0.57$ ). Furthermore, Nd isotope results for an in-house coral reference material are identical within analytical uncertainty for dedicated Nd chemistry and after collection of Nd from U-Th anion exchange chromatography. Our procedure does not require major adaptations to independently used ion exchange chromatographies for U-Pa-Th and Nd, and can hence be readily implemented for a wide range of applications.

## 2.1. Introduction

The isotopes of the radionuclides protactinium (Pa), thorium (Th), uranium (U) and of the rare earth element (REE) neodymium (Nd) are invaluable tools for studying modern ocean biogeochemistry and past ocean conditions (e.g., Goldstein and Hemming, 2003; Henderson and Anderson, 2003). Even though our understanding of their modern biogeochemical cycles is still relatively poor  $^{230}\text{Th}$ ,  $^{232}\text{Th}$ ,  $^{231}\text{Pa}$ , and Nd isotopes ( $^{143}\text{Nd}/^{144}\text{Nd}$  ratio, expressed as  $\epsilon_{\text{Nd}} = ((^{143}\text{Nd}/^{144}\text{Nd}_{\text{sample}})/(^{143}\text{Nd}/^{144}\text{Nd}_{\text{CHUR}}) - 1) \times 10,000$ ; CHUR: chondritic uniform reservoir; Jacobsen and Wasserburg, 1980) are frequently used as proxies to reconstruct past ocean chemistry and dynamics (e.g., van de Flierdt et al., 2012; Anderson et al., 2012). This situation is currently being rectified in the context of the international GEOTRACES program (SCOR Working Group, 2007) where  $^{230}\text{Th}$ ,  $^{231}\text{Pa}$ , and Nd isotopes are ‘key parameters’, which have to be measured on all planned and completed GEOTRACES section cruises. However, accurate and precise analysis of these nuclides in seawater requires relatively large sample volumes (5 to 10 L) (van de Flierdt et al., 2012; Anderson et al., 2012). Although recent analytical advances allow some laboratories to target sample volumes of less than 5 L, shipping large volumes of water to home laboratories is nevertheless an expensive endeavor. In order to reduce shipping costs and sample processing time, a combined extraction method for  $^{231}\text{Pa}$ ,  $^{230}\text{Th}$  and Nd isotopes, which are typically analysed by different groups, would be desirable (e.g., Jeandel et al., 2011).

Similarly in palaeo-archives such as deep-sea corals, sample material could be saved and time consuming sample preparation could be reduced by simultaneous separation of U, Th and Nd. The aragonitic skeleton of corals allows for accurate age control by U-series dating (e.g., Cheng et al., 2000), and Nd isotopes have been shown to present a promising tracer to reconstruct past water mass properties (e.g., van de Flierdt et al., 2006b, 2010; Copard et al., 2010). Deep-sea corals are increasingly targeted as a palaeoceanographic archive, as they are found in areas where other traditional archives (e.g., foraminiferal carbonate) tend to be scarce, such as the Southern Ocean, or in water depths which are undersampled by sediment cores (e.g., intermediate waters) (see Robinson et al., 2014 for a recent summary). Moreover, such combined extraction approaches could ensure that the data obtained are from exactly the same sample thus facilitating optimal comparison between different geochemical parameters.

Here we demonstrate accurate Nd isotope results obtained from a combined extraction scheme of Pa, Th and Nd from seawater and U, Th and Nd from coralline aragonite. The method is easy to adapt, as it merely requires collecting elution fractions from anion exchange columns set up for separating U-Th-Pa (e.g., Auro et al., 2012; Edwards et al., 1987), which normally would go to waste, and subsequent processing through standard ion exchange chromatography for Nd isotope analyses (e.g., van de Flierdt et al., 2006b, 2012). Our Nd isotope intercalibration results for the combined chemistries are in excellent agreement with results from seawater and coral samples processed for Nd only.

## 2.2. Methodology

### 2.2.1. Seawater sample preparation and anion exchange chemistry: the neodymium fraction during protactinium – thorium separation

A refined methodology to extract protactinium and thorium from large volume seawater samples was recently published by Auro et al. (2012). We here briefly summarise the key features of the method (Fig. 2.1). Acidified seawater samples of 10 L volume were spiked ( $^{229}\text{Th}$  and  $^{233}\text{Pa}$ ) and left to equilibrate. In order to remove the trace metals of interest from the sample matrix, 100 mg of purified Fe were added per sample as  $\text{FeCl}_3$ . Purification of Fe was achieved by repeated isopropyl ether extraction, and the rather high amount of Fe was chosen to quantitatively precipitate Pa (Auro et al., 2012). The trace metals were isolated from solution by adjusting the pH to between 7.5 and 8.0 through addition of ammonium hydroxide to precipitate  $\text{Fe}(\text{OH})_3$ . The precipitate was subsequently transferred into 50 ml Teflon<sup>®</sup> centrifuge tubes in which the precipitate was washed four times with pH-adjusted Milli-Q<sup>®</sup>  $\text{H}_2\text{O}$  (pH = 8) and then dissolved in 12 M HCl for a three stage anion exchange chromatography (Auro et al., 2012; Fig. 2.1). Samples were loaded onto the first column (Eichrom<sup>®</sup> prefilter resin + 1X-8, 100-200 mesh resin) in 12 M HCl, followed by Th and REE elution in 12 M HCl, and Pa elution in 12 M HCl + 0.13 M HF. The prefilter resin hereby served to remove organic compounds from the sample solution (Auro et al., 2012). The second stage targeted a purification of the Pa fraction, by repeating the first column (Eichrom<sup>®</sup> prefilter resin + 1X-8, 100-200 mesh). During the third stage Th and REE were separated from each other by loading the REE/Th elute from the first column in 8 M  $\text{HNO}_3$ , eluting the REE in the same acid, and collecting Th in 12 M HCl (resin: Eichrom<sup>®</sup> prefilter resin + 1X-8, 100-200 mesh; Fig. 2.1) (Auro et al., 2012).

### 2.2.2. Carbonate sample preparation and anion exchange chemistry: the neodymium fraction during uranium – thorium separation

Uranium-series dating of deep-sea coral aragonite (<1 g) requires thorough removal of contaminating phases prior to ion exchange chromatography and mass spectrometry. This is typically achieved by rigorous physical cleaning with a Dremel<sup>®</sup> tool and subsequent oxidative and reductive chemical cleaning (e.g., Cheng et al., 2000; Robinson et al., 2005; van de Fliedert et al., 2010). Sample dissolution was achieved in nitric acid to which a mixed  $^{236}\text{U}$ - $^{229}\text{Th}$  spike was added (Edwards et al., 1987; Hines et al., 2015). The samples were evaporated, then dissolved in 2 M HCl and ~3-5 mg of purified Fe were added as  $\text{FeCl}_3$ , followed by addition of ammonium hydroxide to co-precipitate trace metals at pH = 7-9, whereas most high-abundance matrix elements, and in particular Ca, are not precipitated (e.g., Dulski, 1996). It should be noted that this  $\text{FeCl}_3$  precipitation step would not be required for processing coral samples for Nd isotopes alone (e.g., Crocket et al., 2014; Wilson et al., 2014). After a MQ rinse, samples were re-dissolved in 8 M  $\text{HNO}_3$  for U and Th separation during two-stage anion exchange chemistry based on the recipe of Edwards et al. (1987). In brief, samples were loaded in 8 M  $\text{HNO}_3$  on Biorad<sup>®</sup> AG1-X8 (100-200 mesh) anion exchange resin, followed by

matrix elution in 8 M HNO<sub>3</sub>, which is the fraction containing the REE. Thorium is subsequently stripped off the column using 6 M HCl, evaporated to dryness and then converted to nitric form for MC-ICP-MS analyses. The U fraction was the last to be eluted from the first column using 18.2 MΩ Milli-Q<sup>®</sup> (hereafter: MQ) (Fig. 1; Hines et al., 2015).

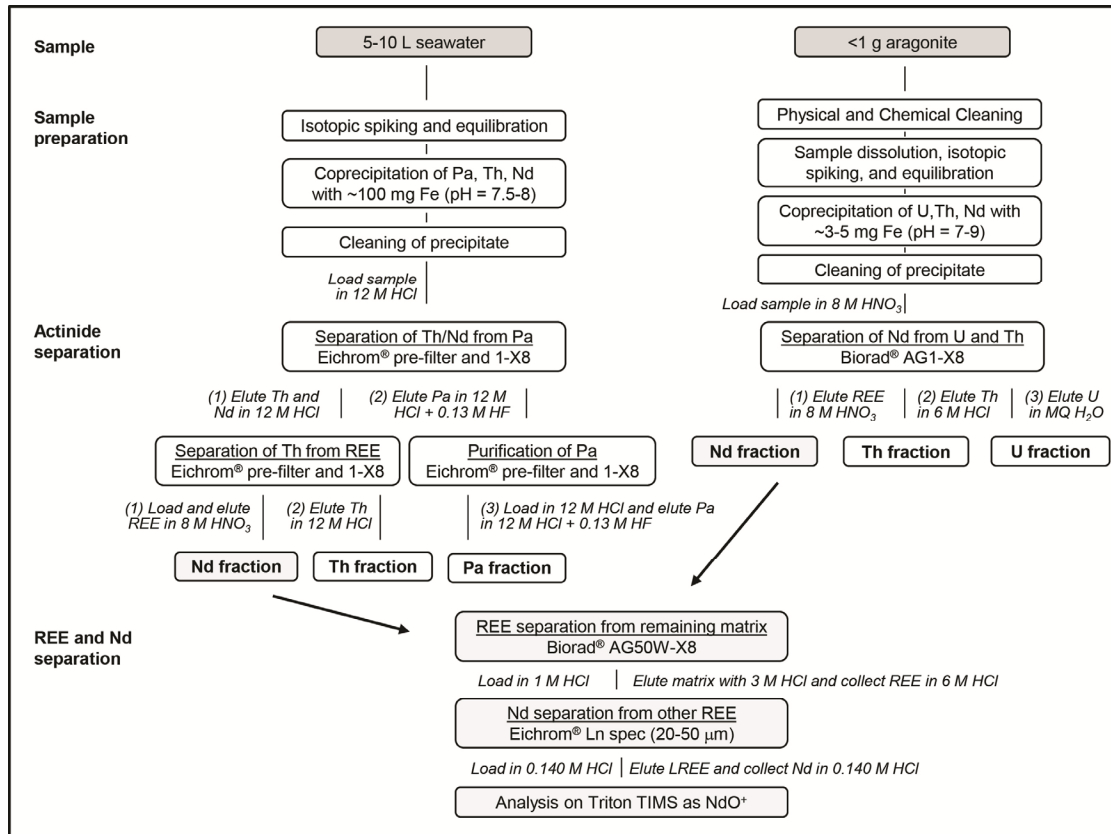


**Figure 2.1:** Working scheme of combined Pa-Th-Nd and U-Th-Nd chemical procedures towards Nd isotope analyses. Purified U, Pa and Th fractions were analysed by MC-ICP-MS (Anderson et al., 2012; Auro et al., 2012; Hines et al., 2015). Note that some laboratories apply a second Th purification step during U-Th separation (cf. Burke and Robinson, 2012). It is also noted that isotopic spiking is not yet tested for the combined method in seawater and corals. It has however successfully been achieved for combined Pa-Th-Nd chemistry of marine particulate samples (Kretschmer, Lambelet et al., pers. comm.). Finally, our preferred method for REE separation after Fe coprecipitation and actinide extraction is the traditional cation exchange chemistry, as the application of strong oxidising agents to combat leaking organics from such resins can be avoided (e.g., Lambelet et al., accepted).

### 2.2.3. Two-stage neodymium purification for TIMS NdO<sup>+</sup> analysis

The method for ion chromatography in preparation for TIMS NdO<sup>+</sup> analysis as performed in the MAGIC laboratories at Imperial College London was recently published by Crocket et al. (2014). Here, we briefly summarise the key points with a focus on amendments to the published procedure. We note that for this study all Nd cuts from U-Th and Pa-Th separation were doped with <sup>150</sup>Nd after anion exchange chromatography to determine minimum Nd concentrations (Nd<sub>min</sub>) omitting Nd loss during sample preparation and U-Th and Pa-Th anion exchange chromatographies. It is however

recommended for future work to add a mixed spike that contains Nd at an earlier stage (Fig. 2.1) to obtain accurate Nd concentration measurements on all samples.

Dried Nd cuts from U-Th and Pa-Th chemistries were oxidised with aqua regia at 200°C, followed by a 1:1 mixture of concentrated HNO<sub>3</sub> and 30% H<sub>2</sub>O<sub>2</sub> prior to Nd extraction to break down potential residual organics. Such residual organics may be sourced either from sample matrix or from anion exchange chromatography as observed by Auro et al. (2012) for Pa-Th separation. Subsequently, samples were converted to chloride form and redissolved in 1 ml 1 M HCl for cation exchange chromatography or to nitrate form for RE spec<sup>®</sup> chemistry.

### **2.2.3.1. Step 1 - Cation exchange chemistry or TRU spec<sup>®</sup>/RE spec<sup>®</sup> chemistry: separating the rare earth elements from the sample matrix**

The procedure to isolate REE from sample matrix was designed to accommodate high Fe content of up to ~10 mg, and was then used for REE separation from anion exchange wash fractions collected from both, Pa-Th and U-Th chemistries. In order to pre-concentrate trace metals ~100 mg Fe were added to each seawater sample and ~5 mg to each coral sample rendering REE separation from Fe a major concern. During the first step of Pa-Th separation Fe is expected to be retained by the anion exchange resin (Fig. 2.1). This is based on the fact that Fe<sup>3+</sup> has a high distribution constant ( $K_D$ ; see IUPAC, 2014) with strong-base anion exchange resin in hydrochloric acid (Kraus et al., 1956), which should inhibit Fe elution with the Th/REE fraction during Pa separation (Fig. 2.1). In practice, small amounts of Fe are however eluted into the REE fraction. During the first step of U-Th separation on the other hand, nitric acid is used to achieve efficient separation of U and Th from Fe (no adsorption of Fe in 0.1 to 14 M HNO<sub>3</sub> with anion exchange resin; Faris and Buchanan, 1964). Hence, the ~5 mg of Fe added to coral samples will be eluted together with the REE during matrix elution so that the REE fraction contains a significant Fe matrix (Fig. 2.1). Therefore, we initially applied a modified version of the RE spec<sup>®</sup> (cf. Huff and Huff, 1993) chemistry published by Crocket et al. (2014). More specifically, we added 1 ml of 0.9 M ascorbic acid to 2 ml 1.5 M HNO<sub>3</sub> in order to reduce Fe and obtain minimal adsorption onto the resin (e.g., Horwitz et al., 1993). While efficient in removing Fe (tested for up to 50 mg of Fe), leaking organics from TRU/RE spec<sup>®</sup> resins require strong sample oxidation after REE separation (e.g., Gault-Ringold and Stirling, 2012; Crocket et al., 2014; Murphy et al., 2015; Lambelet et al., accepted). We therefore substituted the RE spec<sup>®</sup> chemistry by traditional cation exchange chromatography (e.g., Cohen et al., 1988), using 1.4 ml of pre-cleaned Biorad<sup>®</sup> AG50 W-X8 resin (200-400 mesh) in hand-packed Biorad<sup>®</sup> Poly-Prep columns. Cleaning of resin and columns was done with 10 ml 6 M HCl, followed by resin conditioning with 1 + 0.5 ml 1 M HCl. Samples were loaded in 0.5 + 0.5 ml 1 M HCl and subsequently washed in with 0.5 + 0.5 ml 1 M HCl. Sample matrix was eluted with 1 + 6 ml 3 M HCl and 0.5 ml 6 M HCl, after which the REE fraction was stripped off using 7 ml 6 M HCl. We chose 3 M HCl for Fe elution rather than ~3.7 M HCl (i.e. the minimum  $K_D$  of Fe on AG50W-X8 resin; Strelow, 1960; Nelson et al., 1964) to

avoid REE loss during Fe elution. As the resin in the columns was re-used, a final wash was carried out with 10 ml 6 M HCl, followed by 1 + 1 ml MQ for storage in 0.5 M HCl. Most elements of relevance, and in particular barium, have  $K_{DS}$  in 6 M HCl on AG50W-X8 (Nelson et al., 1964) similar to or lower than REE so that the extensive 6 M HCl wash is considered sufficient to avoid cation build-up on negatively charged resin exchange spaces. It is however noted that a nitric acid wash may be desirable to add (cf. Strelow et al., 1965).

#### 2.2.3.2. Step 2 - Ln spec<sup>®</sup> chemistry: neodymium purification

Separation of neodymium (Nd) from the light rare earth elements (LREE), and in particular from praseodymium (Pr) is crucial for analysis as  $NdO^+$ . We followed the method by Crocket et al. (2014) and packed Savillex<sup>®</sup> columns (4 cm long, 3.2 mm inner diameter, 20  $\mu$ m frits) with  $\sim 320$   $\mu$ l Eichrom Ln spec<sup>®</sup> resin (20-50  $\mu$ m) (see also Pin and Zalduogui, 1997). The calibration with 0.140 M HCl yielded  $>75\%$  Nd and less than 5% Pr contribution to the Nd fraction, but it is noted that Nd yields on different columns can be variable. Different to the published method (Crocket et al., 2014), we left the Ln spec<sup>®</sup> resin in the columns between procedural batches. Re-suspension of the resin in the column was achieved in MQ water with acid cleaned 8.3 cm long Corning<sup>®</sup> gel-loading pipette tips (1-200  $\mu$ l) in order to avoid resin compaction, which could affect the precisely calibrated elution scheme, and to keep the flow rates between  $\sim 0.55$  and 0.6 ml/hr. After a washing step in 6 M HCl and addition of MQ water, the resin was pre-conditioned with 0.140 M HCl and samples were loaded and later on collected in the same acid (Crocket et al., 2014). The resin was re-used until degradation of separation efficiency of Nd and Pr was observed. In order to pool the Nd fraction in one spot during evaporation for subsequent TIMS  $NdO^+$  analyses, 10  $\mu$ l 0.001 M  $H_3PO_4$  were added to the Nd fraction after Ln spec<sup>®</sup> chemistry.

#### 2.2.4. Synthesising a TaF<sub>5</sub> activator for TIMS $NdO^+$ analyses

As detailed in Crocket et al. (2014), samples were loaded in 2 x 0.5  $\mu$ l 2.5 M HCl between two layers of 0.5  $\mu$ l TaF<sub>5</sub> activator on degassed single W filaments in smallest possible increments in order to reduce domain mixing effects (e.g., Andreasen and Sharma, 2009). During sample loading the current was set to 0.9 A and afterwards increased slowly to  $\sim 2.0$  A (over a time period of 4 minutes). For this study, TaF<sub>5</sub> was prepared from Ta<sub>2</sub>O<sub>5</sub> powder, which was fluxed in 28 M HF at 80 °C for 7 days in an acid clean Teflon beaker (10 ml 28 M HF for 250 mg Ta<sub>2</sub>O<sub>5</sub>) (Charlier et al., 2006), after which the solution was evaporated to dryness at 130°C. Per 150 mg of TaF<sub>5</sub> we used 0.178 ml 28 M HF, 7.98 ml MQ water, 1.025 ml 3 M HNO<sub>3</sub> and 0.169 ml 14.8 M H<sub>3</sub>PO<sub>4</sub>, which is a modified version of the recipe used by Charlier et al. (2006). It is important to add the aliquot of 28 M HF first in order to dissolve the crystals either upon contact or leave until fully dissolved, otherwise the crystals remain un-dissolved once the remaining reagents are added. The combined activator and loading Nd blank was  $<0.2$  pg. The performance of the activator was variable, similar to results

reported in detail by Crocket et al. (2014) and Lambelet et al. (accepted). We found that purification of the activator solution by  $\text{NH}_4\text{OH}$  coprecipitation, described in the literature (e.g., Charlier et al., 2006) to reduce the loading blank, was not improving Nd blank levels and sometimes compromised beam intensity and stability and was hence omitted.

### 2.2.5. Thermal Ionisation Mass Spectrometry

All Nd isotope analyses were carried out on a Thermo Triton TIMS at the Department of Earth Science and Engineering, Imperial College London, closely following the analytical protocol of Crocket et al. (2014). Samples were routinely analysed in nine blocks comprising 20 cycles using a peak integration time of 8.4 s at temperatures between 1520°C and 1580°C. Isobaric interferences were corrected by routinely monitoring  $^{140}\text{Ce}^{16}\text{O}$ ,  $^{141}\text{Pr}^{16}\text{O}$  and  $^{147}\text{Sm}^{16}\text{O}$  whereas La and in particular Ba were monitored manually. Residual Ba was however negligible in all our samples. Interference and mass bias corrections were applied as outlined by Crocket et al. (2014) using  $^{17}\text{O}/^{16}\text{O} = 0.000390$ ,  $^{18}\text{O}/^{16}\text{O} = 0.002073$  and  $^{146}\text{Nd}/^{144}\text{Nd} = 0.7219$ , respectively. A slightly higher  $^{146}\text{Nd}/^{144}\text{Nd}$  was applied to spiked samples (Crocket et al., 2014 and references therein).

Over a period of 26 months 5 and 15 ng loads of pure JNdi-1 were analysed ( $^{143}\text{Nd}/^{144}\text{Nd} = 0.512105 \pm 0.000009$ , 2SD,  $n = 110$ ) to monitor instrumental offset and normalise mass bias corrected  $^{143}\text{Nd}/^{144}\text{Nd}$  ratios of samples to the reference ratio of  $^{143}\text{Nd}/^{144}\text{Nd} = 0.512115 \pm 0.000007$  (Tanaka et al., 2000). Repeated analyses of 10, 20 and 30 ng Nd loads of the USGS BCR-2 reference material yielded  $^{143}\text{Nd}/^{144}\text{Nd}$  results of  $0.512637 \pm 0.000011$  (2SD,  $n = 32$ ) and 10 and 30 ng loads of our in-house coral reference material resulted in  $^{143}\text{Nd}/^{144}\text{Nd}$  ratios of  $0.512336 \pm 0.000009$  (2SD,  $n = 23$ ), both of which are in excellent agreement with previously published values (Weis et al., 2006; Crocket et al., 2014). The observed raw ratios of major interfering masses for column-processed BCR-2 material and our in-house coral reference material were  $^{147}\text{Sm}^{16}\text{O}/^{144}\text{Nd}^{16}\text{O} < 0.0012$ ,  $^{140}\text{Ce}^{16}\text{O}/^{144}\text{Nd}^{16}\text{O} < 0.024$  and  $^{141}\text{Pr}^{16}\text{O}/^{144}\text{Nd}^{16}\text{O} < 0.46$  and hence within the suggested limits presented by Crocket et al. (2014). Blank levels of Nd chemistry alone were mostly  $< 5$  pg, regardless of the procedure used for REE isolation. The first batch of samples processed through cation exchange chemistry showed however slightly elevated Nd blanks of 7 and 17 pg for unresolved reasons.

Full procedural blanks of combined U, Th and Nd separation from deep-sea corals ranged from 2 to 35 pg Nd, averaging at 11 pg ( $n = 31$ ) and contributed  $< 1\%$  to the analysed sample Nd. This shows that procedural Nd blank is low in the combined method although no efforts were made to specifically reduce Nd blank during sample preparation and actinide separation (Fig. 2.1). Full procedural Nd blanks of combined Pa, Th and Nd separation on seawater samples reported in this study were 140 and 160 pg. The reasons for these abnormally high blanks are discussed below in more detail and are related to initial problems in the Pa-Th chemistry described by Auro et al. (2012).

### 2.3. Application: seawater and carbonates

#### 2.3.1. Intercomparison of results for Nd extraction from seawater

We tested our combined Pa, Th and Nd separation procedure on filtered and acidified seawater samples collected at 15 and 2000 m water depth at Bermuda Atlantic Time Series (BATS) station (31°50' N, 64°10' W) from the GEOTRACES Pa-Th intercalibration (Anderson et al., 2012). The Nd isotope results generated for these samples are compared to GEOTRACES Nd intercalibration results from samples collected independently from the same water depth on the same expedition (KNR193-6/2) (van de Flierdt et al., 2012) (Table 2.1). The Nd isotope GEOTRACES intercalibration results for seawater from 15 m depth are  $\epsilon_{Nd} = -9.19 \pm 0.57$  and  $\epsilon_{Nd} = -13.14 \pm 0.57$  for 2000 m water depth (van de Flierdt et al., 2012; Table 2.1). These values are indicated by the dashed line in Figure 2.2 (representing the consensus values, i.e.  $\Delta\epsilon_{Nd} = 0$ ). Our newly obtained Nd isotope data from the Pa-Th chemistry wash fractions are reported in Table 2.1 and plotted as deviation from the reported consensus values for 15 and 2000 m water depth, respectively (Fig. 2.2). The maximum offset of  $\Delta\epsilon_{Nd}$  is 0.06 epsilon units and demonstrates the excellent agreement between samples processed for Nd only and samples processed through the combined methodology (Fig. 2.1).

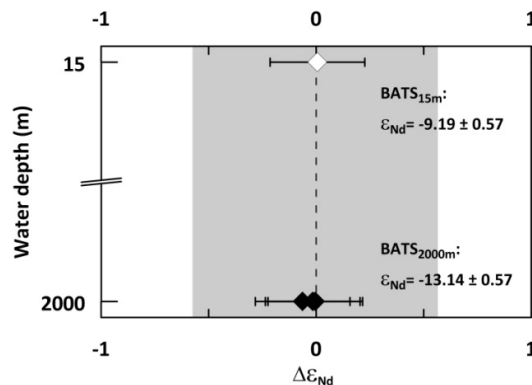


**Figure 2.2:** Neodymium isotope results obtained for wash fractions from anion exchange chemistry further processed for Nd separation on GEOTRACES BATS seawater Pa-Th intercalibration samples. Data are presented as  $\Delta\epsilon_{Nd}$  deviation from GEOTRACES Nd intercalibration results from 14 laboratories (dashed line) (van de Flierdt et al., 2012). Numbers represent consensus values and the grey shading indicates the 2SD.

We should however note that the Nd data presented here were generated by the “initial method” reported by Auro et al. (2012). This method suffered from procedural problems during column chemistry and sample preparation (i.e. with resin, frits and Fe solution used for coprecipitation) resulting in higher Th blanks and lower Th yields (see Auro et al., 2012 for details). Neodymium and Th are eluted from the same column (Fig. 2.1), and we can see this reflected in elevated Nd blanks of up to ~2%, paired with estimated sample loss of up to 72% (Table 2.1) when compared to expected seawater Nd concentrations from published Nd results (van de Flierdt et al., 2012). As our TIMS NdO<sup>+</sup> method allows for analyses of sub-nanogram levels of Nd, we were however able to isotopically constrain the Nd blank from these samples, i.e. 0.14 ng Nd with  $\epsilon_{Nd} = -19.31 \pm 0.78$  and 0.16 ng Nd with  $\epsilon_{Nd} = -10.49 \pm 0.69$ . These values are used for a mixing calculation to assess the significance of blank contamination to our BATS seawater Nd results.

$$IC_{\text{sample}} = \frac{IC_{\text{final}} \times ([Nd]_{\text{sample}} \times f_{\text{sample}} + [Nd]_{\text{blank}} \times f_{\text{blank}}) - IC_{\text{blank}} \times [Nd]_{\text{blank}} \times f_{\text{blank}}}{([Nd]_{\text{sample}} \times f_{\text{sample}})}$$

IC stands for the isotopic composition, [Nd] for the Nd concentration, and f for the fraction. Following above mixing equation we can calculate that the maximum Nd blank contribution of 160 pg would shift the sample Nd isotopic composition by 0.01 epsilon units. Such blank contribution is considered negligible, supported by the accurate results we report for the Nd isotopic compositions from Pa-Th wash fractions (Table 2.1, Fig. 2.2).

| Sample   | $^{143}\text{Nd}/^{144}\text{Nd}^{\text{a}}$ | 2SE <sup>b</sup> | $\epsilon_{\text{Nd}}^{\text{c}}$ | 2SE  | 2SD <sup>d</sup> | Nd in wash fraction (ng) | Pre-chemistry Nd (ng) |
|--|--|------------------|-----------------------------------|------|------------------|--------------------------|-----------------------|
| <b>Seawater samples (this study)</b>   |  |                  |                                   |      |                  |                          |                       |
| KNR193-6-Th-720 (BATS 15 m)  | 0.512167                                     | 0.000006         | -9.20                             | 0.13 | 0.21             | 7.5                      | 20.7                  |
| KNR193-6-Th-648 (BATS 2000 m)  | 0.511965                                     | 0.000007         | -13.12                            | 0.13 | 0.21             | 8.0                      | 25.9                  |
| KNR193-6-Th-649 (BATS 2000 m)  | 0.511965                                     | 0.000010         | -13.14                            | 0.20 | 0.21             | 9.2                      | 25.9                  |
| KNR193-6-Th-650 (BATS 2000 m)  | 0.511968                                     | 0.000008         | -13.08                            | 0.16 | 0.21             | 7.3                      | 25.9                  |
| <b>Seawater samples of published consensus values from 14 laboratories (van de Flierdt et al., 2012)</b> |  |                  |                                   |      |                  |                          |                       |
| GEOTRACES BATS 15 m  | 0.512167                                     | 0.000029         | -9.19                             |      | 0.57             |                          |                       |
| GEOTRACES BATS 2000 m  | 0.511964                                     | 0.000029         | -13.14                            |      | 0.57             |                          |                       |
| <b>In house deep-sea coral reference material (this study)</b>   |  |                  |                                   |      |                  |                          |                       |
| Coral Ref 1 (U-Th fraction)  | 0.512337                                     | 0.000004         | -5.87                             | 0.08 | 0.18             | 26.68                    | 29.72                 |
| Coral Ref 2 (U-Th fraction)  | 0.512332                                     | 0.000004         | -5.97                             | 0.07 | 0.18             | 26.64                    | 29.81                 |
| Coral Ref 3 (U-Th fraction)  | 0.512336                                     | 0.000004         | -5.89                             | 0.08 | 0.18             | 26.23                    | 29.77                 |
| Coral Ref RE spec <sup>®</sup> (n = 11)  | 0.512337                                     | 0.000009         | -5.89                             |      | 0.19             |                          |                       |
| Coral Ref AG50W-X8 (n = 9)   | 0.512335                                     | 0.000009         | -5.90                             |      | 0.18             |                          |                       |
| <b>In house deep-sea coral reference material (Crocket et al., 2014)</b>                                 |  |                  |                                   |      |                  |                          |                       |
| Coral Ref (n = 13)   | 0.512338                                     | 0.000008         | -5.86                             |      | 0.16             |                          |                       |

(a)  $^{143}\text{Nd}/^{144}\text{Nd}$  ratios were corrected for the offset of the measured JNdi-1 ratio of  $0.512105 \pm 0.000009$  (n = 110) from the published value of  $0.512115 \pm 0.000007$  (Tanaka et al., 2000)

(b) 2SE is the analytical 2 $\sigma$  standard error. 2SE for Nd concentrations is  $\leq 0.005$ .

(c)  $\epsilon_{\text{Nd}}$  was calculated using the present day CHUR value of  $^{143}\text{Nd}/^{144}\text{Nd} = 0.512638$  (Jacobsen and Wasserburg, 1980).

(d) 2SD refers to the 2 $\sigma$  standard deviation derived from the longterm reproducibility of respective reference material (see text).

GEOTRACES 2SD represents the 2 $\sigma$  standard deviation of the 14 laboratories involved in the respective measurements (van de Flierdt et al., 2012).

**Table 2.1:** Neodymium isotope results for BATS seawater and a deep-sea coral reference material grouped by chemical procedure applied. Neodymium isotope results for Pa-Th anion exchange chemistry wash fractions are based on BATS GEOTRACES Pa-Th intercalibration samples (KNR193-6-Th). ‘Neodymium in wash fraction’ refers to the amount of Nd in the respective anion exchange chemistry wash fractions, determined by  $^{150}\text{Nd}$  doping after collection. The pre-chemistry Nd content is estimated based on the  $[Nd]_{\text{seawater}}$  at BATS from van de Flierdt et al. (2012). Neodymium results on our in-house coral reference material, processed through combined U-Th-Nd chemistry, are listed individually (n = 3); REE were isolated using cation exchange chemistry. Pre-chemistry Nd amounts were determined by weighing of an aliquot of dissolved in-house coral reference material of known Nd concentration. Results for in-house coral reference material are grouped according to chemical procedures applied, i.e. RE spec<sup>®</sup> chemistry (n = 11) and cation exchange chemistry with Biorad<sup>®</sup> AG50W-X8 resin (n = 9). All in-house coral reference material aliquots were taken from the original solution prepared from homogenised deep-sea coral powder by Crocket et al. (2014). Literature GEOTRACES and coral reference material data taken from van de Flierdt et al. (2012) and Crocket et al. (2014).

### 2.3.2. Intercomparison of results for Nd extraction from aragonitic deep-sea coral skeletons

The application of combined uranium, thorium and neodymium extraction from aragonitic sample matrices was tested on a coral reference material created from a homogenised mixture of *Desmophyllum dianthus* deep-sea corals from the Southern Ocean (in-house coral reference material)

(see Crocket et al., 2014 for details). Neodymium yields for the Fe coprecipitation and U-Th anion exchange chromatography were found to be nearly quantitative at 88-90% during three individual batches of chemistry, consistent with ‘slight adsorption’ of Nd on anion exchange resins in HNO<sub>3</sub> (Faris and Buchanan, 1964). Such Nd yields are likely representative for the Pa-Th separation as well, considering that there is no adsorption of Nd on strong-base anion exchange resins in HCl minimising Nd loss on the first column (Kraus and Nelson, 1958) (Fig. 2.1). Hence, the matrix elution with HNO<sub>3</sub> on the second column of Pa-Th separation is considered to be the only place where minimal loss of Nd could occur, resulting in similar quantitative Nd yields for both anion exchange based chemistries, i.e. U-Th and Pa-Th separation (cf. Kraus and Nelson, 1958; Faris and Buchanan, 1964).

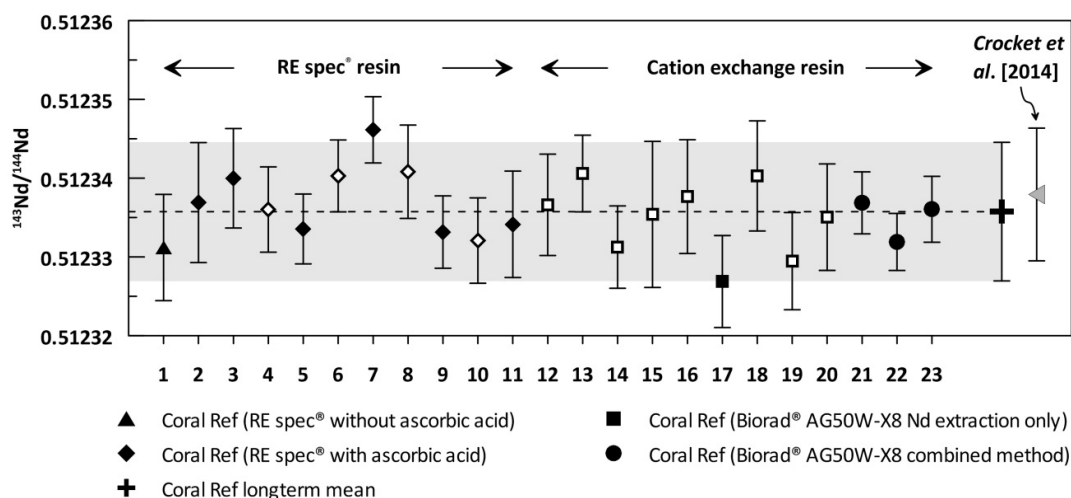


**Figure 2.3:** Results of in-house coral reference material Nd isotope analyses of sample loads containing 10 and 30 ng Nd, measured over a period of 26 months. Error bars of individual measurements are given as internal 2SE. Sample loads containing 10 ng of Nd are indicated by white symbols with black outline. The first 20 results (diamonds and squares) were obtained for samples processed through Nd isotope chemistry only, using Eichrom RE spec<sup>®</sup> resin (with and without addition of ascorbic acid) and cation exchange chemistry respectively to isolate REE from the sample matrix. Black circles mark results obtained by processing the same coral reference material through Fe coprecipitation and U-Th anion exchange chemistry followed by Nd isotope separation (i.e. the combined method). The long-term average of all results is  $^{143}\text{Nd}/^{144}\text{Nd} = 0.512336 \pm 0.000009$  ( $n = 23$ ) and the grey shading marks the 2SD. The grey triangle marks the results previously published by Crocket et al. (2014) on the same in-house coral reference material.

In order to test our combined U-Th-Nd separation for accuracy of Nd isotopes, we report results on 20 repeats of our in-house coral reference material (10 and 30 ng Nd aliquots) processed individually through RE spec<sup>®</sup> chemistry ( $n = 11$ ) and cation exchange chemistry ( $n = 9$ ) (Table 2.1; Fig. 2.3). These results are compared to Nd isotope data obtained from three coral reference material aliquots (30 ng Nd each; Table 2.1) processed individually through Fe coprecipitation and U-Th anion exchange chromatography. The results document excellent reproducibility of coral reference material aliquots regardless of the applied procedure. In particular, results are consistent between samples collected from U-Th chemistry wash fractions, those loaded directly onto the respective first column

of Nd extraction, and previously published coral reference material Nd isotope data (Crocket et al., 2014) (Fig. 2.3, Table 2.1). Together with previous work (cf. Jeandel et al., 2011), these results highlight the benefit of combined procedures to separate different elements from the same sample, and moreover, show the potential to extend the range of extracted elements.

#### 2.4. Summary and concluding remarks

We here presented intercalibration Nd isotope results of combined separation procedures for Pa, Th and Nd from seawater, and U, Th and Nd from aragonitic sample matrices. The method was designed with minor modifications to existing protocols used in separate laboratories carrying out U-Th-Pa analyses and Nd isotope analyses as it utilises wash fractions from U-Th and Pa-Th anion exchange chemistries that are then further processed for Nd separation. The method significantly reduces the workload and sample consumption for common applications in low temperature geochemistry and is easy to implement between different laboratories.

We tested the combined methodology for Nd isotope accuracy and obtained excellent results compared to previously published data for Nd isotope processing alone. Future optimisation of our combined approach can be obtained by separation of additional elements from the same samples and inclusion of a mixed Nd-Th-Pa and/or Nd-U-Th spike prior to Fe coprecipitation in order to generate quantitative Nd concentration data from the same samples.

**Acknowledgements:** We thank the team on the 2nd leg of the first GEOTRACES intercalibration cruise for sample collection, Joanne Goudreau, Kuo Fang Huang, Jurek Bluztajn for help at the WHOI Plasma facility, Martin Fleisher and Sven Kretschmer for discussion, and Derek Vance for sharing his  $^{150}\text{Nd}$  spike. Torben Stichel is acknowledged for help during column calibration. All data presented in this manuscript can be found in the table included in the main body of the text. Funding that supported this work was received from the National Science Foundation (NSF 0752402), the Leverhulme Trust (RPG-398), the Natural Environmental Research Council (NE/J021636/1 and NE/N003861/1), the European Research Council (278705) and the Grantham Institute for Climate Change.

**Declaration:** This work was completed as part of a collaborative effort to which I contributed the seawater and coral Nd isotope and concentration analyses. Specifically, Kirsty C. Crocket instructed me in the work with low concentration Nd isotope analyses and Myriam Lambelet determined oxygen isotope ratios and helped during column calibration and method refinement. Barry Coles and Katharina Kreissig provided support and guidance for mass spectrometry and clean laboratory work, respectively. All U-Th and Pa-Th related work as described in the text was performed by Laura F. Robinson, Louisa I. Bradtmiller, Sophie K. Hines, Jess F. Adkins and Maureen E. Auro.

## **Chapter 3**

# **Neodymium isotopes and concentrations in aragonitic deep-sea corals - modern calibration and evaluation of palaeo-applications**

**This chapter is prepared for publication as T. Struve, T. van de Flierdt, A. Burke, L. F. Robinson, S. Hammond, L. I. Bradtmiller, M. E. Auro, and K. M. Falcon: Neodymium isotopes and concentrations in aragonitic scleractinian deep-sea corals - modern calibration and evaluation of palaeo-applications in *Geochimica et Cosmochimica Acta*.**

## Abstract

Deep-sea corals are a unique archive of intermediate to deep ocean chemistry. They can be accurately dated and their fast growth rates allow producing records of high temporal resolution. Among the geochemical tools preserved in the aragonitic skeletons of deep-sea corals, Nd isotopes have been shown to reliably record ambient seawater signatures. Recent studies using fossil deep-sea corals however reported elevated Nd concentrations in coral skeletons, up to two orders of magnitude higher than expected from Nd-aragonite coprecipitation experiments. The source of this excess Nd is still poorly constrained as is its significance for the reliability as deep-sea coral aragonite for seawater Nd isotope reconstructions.

We here present new results that refine the calibration of modern scleractinian deep-sea coral specimens by analysing three seawater profiles from the Drake Passage and nine modern corals of the species *Desmophyllum dianthus* (n = 3), *Balanophyllia malouinensis* (n = 4), *Flabellum curvatum* (n = 1) and *Madropora oculata* from across the Drake Passage and the North Atlantic. All species were either collected alive or U-series dated to be less than 500 years old. Seawater analyses yield Nd isotopic compositions consistent with previously published values, revealing small vertical and lateral Nd isotope gradients in modern Drake Passage water masses. Most of the modern corals (n = 5) agree with ambient seawater values within analytical uncertainty. Two samples of the species *Balanophyllia malouinensis* however deviate by up to 0.6  $\epsilon_{Nd}$  from ambient seawater and one specimen has to be omitted due to an open system U-series age. This species should hence be treated with caution for palaeoceanographic reconstructions of seawater using Nd isotopes.

An additional set of 71 fossil deep-sea corals was analysed for Nd concentrations to complement existing U and Th concentrations. The observed Nd concentrations range from 7.3 to 964.5 ng/g of which specimens of the species *D. dianthus* and *Caryophyllia spp.* show minor covariation with Th serving as an indicator for lithogenic contamination. Strong covariation is however observed in the previously unstudied species *B. malouinensis* and *G. antarctica*. Furthermore, 16 corals were re-sampled and analysed for their rare earth element (REE) content, as well as major and trace element geochemistry in order to constrain the source and nature of excess Nd in the aragonitic skeletons of deep-sea corals. These data provided supporting evidence that lithogenic contamination is minor as indicated by low Al, Mn, Ti and Fe. Moreover, mass balance calculations and seawater-like REE patterns seem to rule out lithogenic contamination as a major contributor to elevated Nd concentrations in coral aragonite. Paired with poor reproducibility of Nd concentrations in replicate samples these observations point to a heterogeneously distributed seawater-derived Nd carrier phase in deep-sea coral skeletons. Here we suggest authigenic phosphate phases as carrier of excess skeletal Nd concentrations, lending more confidence to using Nd isotopes in fossil deep-sea corals as a powerful tracer for palaeoclimatic studies.

### 3.1. Introduction

Deep-sea corals are a promising archive for the reconstruction of past ocean properties (see Robinson et al., 2014 for a review). It is generally differentiated between species building proteinaceous axes and species secreting calcium carbonate skeletons (Cairns, 2007). The skeletons of calcium carbonate secreting species provide an archive which is advantageous over other marine archives of which aragonitic scleractinian deep-sea corals can be dated accurately by uranium-series disequilibrium (e.g., Cheng et al., 2000; Robinson et al., 2006). Moreover, fast growth rates from 0.5-2 mm/year in *Desmophyllum dianthus* (Risk et al., 2002; Adkins et al., 2004) up to 26 mm/year in *Lophelia pertusa* (Gass and Roberts, 2006) provide high resolution archives in regions where other palaeoceanographic archives are scarce, such as the Southern Ocean (e.g., Thiagarajan et al., 2013; Margolin et al., 2014).

In contrast to shallow water corals (zooxanthellate), deep-sea corals (azooxanthellate) are able to grow in the absence of sunlight, and can be found in all major ocean basins between 0 and >6000 m water depth (Keller 1976; Freiwald et al., 2004). Knowledge about temperature and salinity ranges for deep-sea coral habitats is incomplete, but observed temperatures range from <0 to >20°C (Keller, 1976; Stanley and Cairns, 1988), with an apparent preference for temperatures between 4 and 12°C (Roberts et al., 2006). Similarly, salinities for deep-sea coral habitats span a wide range from ~32‰ in Norwegian Fjords up to 38.8‰ in the Ionian Sea (Freiwald et al., 2004). The highest deep-sea coral abundance is however found at intermediate water depths where populations change when favourable habitat conditions change (e.g., Burke et al., 2010; Thiagarajan et al., 2013; Henry et al., 2014; Margolin et al., 2014), a yet undersampled depth interval of the past oceanic water column due to the lack of sedimentary archives away from the continental margins. The intermediate ocean is particularly interesting due to its dynamic role in modulating carbon exchange with the atmosphere (e.g., Anderson et al., 2009; Burke and Robinson, 2012). The role of intermediate ocean circulation changes during phases of transient climate change is however still poorly constrained, in particular in the Southern Hemisphere (e.g., Pahnke et al., 2008; Robinson and van de Flierdt, 2009).

A powerful proxy to better constrain past water mass variability is neodymium (Nd) isotopes which have been extracted from various marine archives (e.g., van de Flierdt and Frank, 2010). Neodymium isotopes in deep-sea corals have been successfully used as a proxy to reconstruct past water mass properties, with a particular focus on water mass provenance and water mass mixing (van de Flierdt et al., 2006b; Robinson and van de Flierdt, 2009; Colin et al., 2010; Copard et al., 2011, 2012; López Correa et al., 2012; Montero-Serrano et al., 2011, 2013; Wilson et al., 2014). While the proxy has been calibrated successfully in both, modern colonial (reef - building) and solitary corals (van de Flierdt et al., 2006b; Copard et al., 2010, van de Flierdt et al., 2010), there are a number of issues that still need addressing. Firstly, the calibration study by van de Flierdt et al. (2010) worked with museum specimens, which were U-Th dated to be between 0 and 377 years old, with two ages however ranging back to the middle and early Holocene. While the younger ages offer a good

possibility that some of these corals may have been collected alive, we can not be certain about this point. Furthermore, Nd isotope results from the corals from the Smithsonian were compared to the most proximal site in the ocean where seawater results were published from the same water mass bathing the coral sampling locations. In some cases, this was up to 2000 km away from the site of coral collection. A more direct calibration was performed by Copard et al. (2010), who analysed 13 corals collected alive for their Nd isotopic composition, five of which were directly comparable to nearby seawater measurements. It is however desirable to compare live coral Nd isotopic composition to seawater collected at the same site.

Another point that needs revisiting for the application of Nd isotopes in deep-sea corals as a palaeo water mass proxy is the observation of elevated Nd concentrations in thoroughly cleaned fossil coral skeletons. Previous studies showed that Nd concentrations in modern deep-sea coral specimens of  $\leq 110.1$  ng/g (Copard et al., 2010, 2011, 2012; van de Flierdt et al., 2010) are similar to observations in shallow-water corals, i.e.  $\leq 55.5$  ng/g (Shaw and Wasserburg, 1985; Sholkovitz and Shen, 1995; Akagi et al., 2004; Wyndham et al., 2004). Moreover, Copard et al. (2010) showed a weak dependence of Nd concentrations with water depth, qualitatively in agreement with the behavior of dissolved Nd in seawater. Comparison to fossil specimens however showed that Nd concentrations were significantly elevated ( $[Nd] = 772$  ng/g; Wilson et al., 2014), which has been speculated to result from incomplete removal of contaminant phases (Copard et al., 2010; Crocket et al., 2014; Wilson et al., 2014). Colin et al. (2012) ruled out sedimentary contributions based on the lack of systematic relationship between sediment and coral Nd isotopic compositions. Recently, Crocket et al. (2014) presented a dataset of fossil solitary deep-sea corals from the New England seamounts including specimens with Nd concentrations of up to 612 ng/g. Mass balance calculations, however, showed that only a maximum of 27% of the coral-bound Nd could be explained by contamination from ferromanganese oxyhydroxide phases coated around the outer skeleton of fossil deep-sea corals (Crocket et al., 2014). The effect of contamination from such FeMn phases on coral Nd isotopic composition was shown to be minor (Crocket et al., 2014). However, as most modern and fossil deep-sea corals show Nd concentrations in excess of what is predicted from inorganic aragonite precipitation experiments (Terakado and Masuda, 1988;  $\sim 6 - 11$  ng/g) it is vital to identify the nature of coral-bound Nd in order to use Nd isotopes from coral skeletons as a robust proxy for past ocean conditions.

In this paper we present (i) a new Nd isotope calibration of seawater and live deep-sea corals from the Drake Passage and a location close to Iceland (Fig. 3.1), and (ii) a multi-element investigation into the nature of elevated Nd concentrations in fossil deep-sea corals. Taken together our results greatly add to the robustness of the palaeo Nd isotope signal extracted from aragonitic samples.

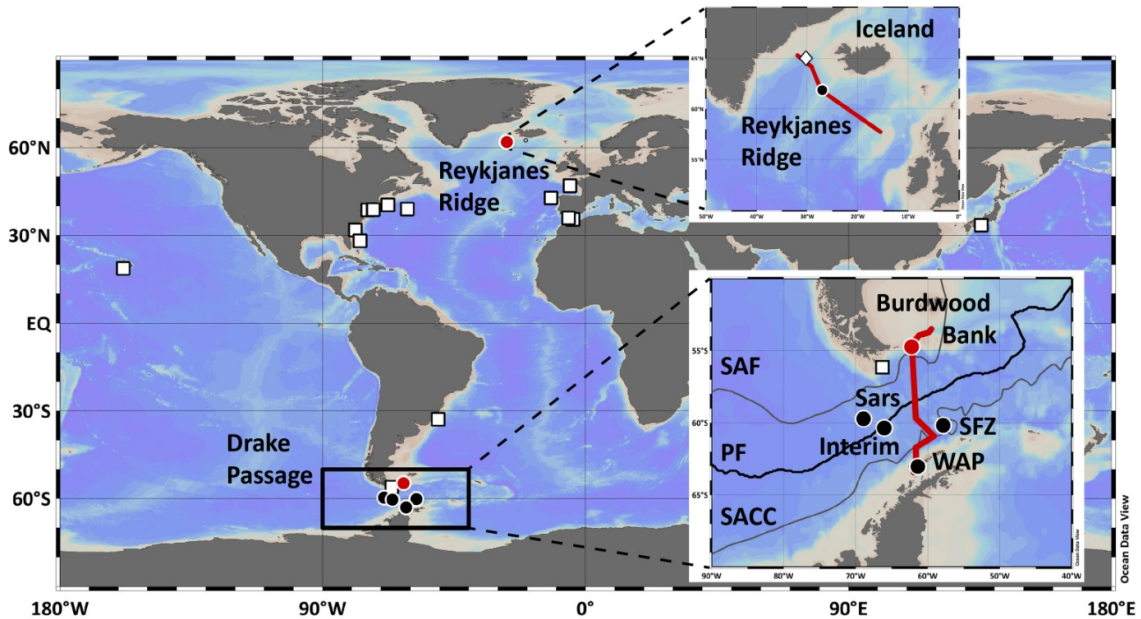


**Figure 3.1:** Global locations of modern deep-sea corals calibrated against seawater for their Nd isotopic composition. White squares indicate sample locations of previous studies (Copard et al., 2010; van de Flierdt et al., 2010). Black dots with white outlines denote sample locations for this study. Red dots highlight the locations of Burdwood Bank and Reykjanes Ridge, i.e. places where modern coral specimens are calibrated against seawater. Red line indicates the trajectory of oxygen (Drake Passage) and potential temperature (Reykjanes Ridge) sections presented in Figures 3.2 and 3.4. White diamond represents location of Northeast Atlantic seawater shown in Fig. 3.4. Maps generated with ODV software; Schlitzer, 2012). Positions of Southern Ocean fronts from Orsi et al. (1995). SAF: Sub-Antarctic Front; PF: Polar Front; and SACC: southern ACC front. SFZ: Shackleton Fracture Zone; WAP: West Antarctic Peninsula.

### 3.2. Samples

In order to compare coral data to ambient seawater three seawater profiles were collected for 10 to 12 depths each during NBP0805 (April to May 2008) on the *R/V Nathaniel B. Palmer* using the shipboard CTD system equipped with PVC Niskin bottles (Fig. 3.1 and Table 3.1). Samples were transferred from Niskin bottles into acid cleaned cubitainers using Tygon<sup>®</sup> tubing. Unfiltered 10L samples were acidified to  $\text{pH} < 2$  onboard using high purity HCl. Sampling stations were located in deep waters off Burdwood Bank (north of the Polar Front), off the southern end of the Shackleton Fracture Zone (south of the Polar Front), and inbetween Sars and Interim Seamount (near the Polar Front) (Figs. 3.1 and 3.2). All major water masses were sampled: surface mixed layer, Subantarctic Mode Water (SAMW), Antarctic Intermediate Water (AAIW), Upper Circumpolar Deep Water (UCDW) and Lower Circumpolar Deep Water (LCDW) (Fig. 3.2).

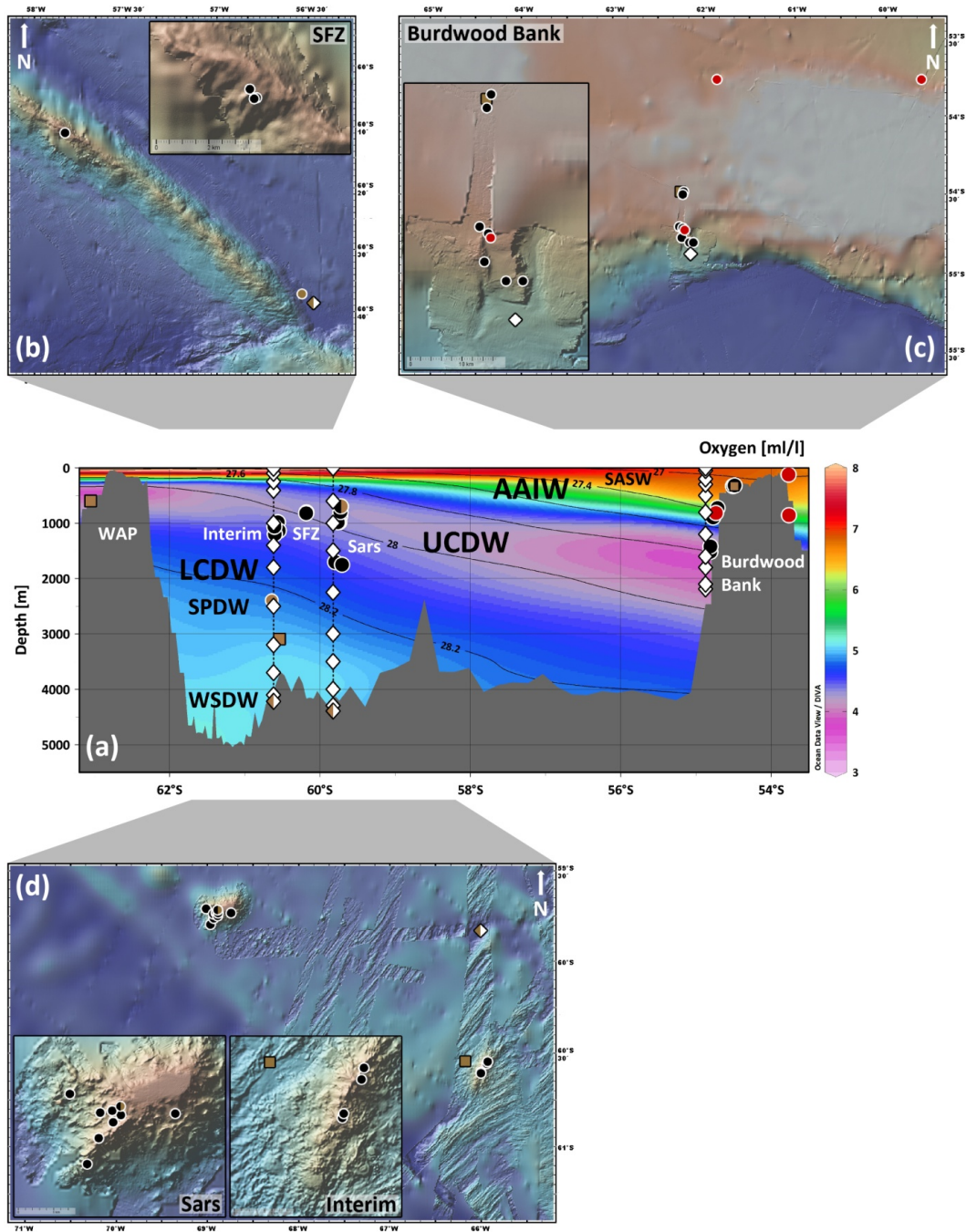


**Figure 3.2:** Seawater, sediment and coral sampling locations in the Drake Passage. (a) Oxygen section across the Drake Passage (red line in Figure 3.1; WOA13: Garcia et al., 2013; generated with ODV software; Schlitzer, 2012). White diamonds: seawater profiles; black circles: fossil deep-sea corals; red circles: modern deep-sea corals; brown colour: locations for sediment collection, with symbol indicating the sampling device; box or Kasten cores (squares), dredges (dots), minicorer attached to CTD (diamond). Shared symbols indicate multiple samples collected with same device at respective location. Thin black lines indicate surfaces of neutral density anomaly  $\gamma^n$  (Jackett and McDougall, 1997; in  $\text{kg/m}^3$ ). SASW: Sub-Antarctic Surface Water, AAIW: Antarctic Intermediate Water, UCDW: Upper Circumpolar Deep Water, LCDW: Lower Circumpolar Deep Water, SPDW: South Pacific Deep Water, WSDW: Weddell Sea Deep Water (after Sievers and Nowlin, 1984; Orsi et al., 1999, Sudre et al., 2011) (b) to (d) Detailed bathymetric maps for (b) Shackleton Fracture Zone, (c) Burdwood Bank, and (d) Sars and Interim seamounts. Maps were generated with Geomapapp (<http://www.geomapapp.org>) with GMRT (Ryan et al., 2009) and high resolution data from NBP0805 and NBP1103 bathymetric surveys (Hoy et al., 2015).

Furthermore we report results from sediment samples ( $n = 7$ ), which were collected during NBP0805 and NBP1103 (May to June 2011) from water depths between 333 to 4395 m water depth across the Drake Passage, i.e. at Burdwood Bank, Shackleton Fracture Zone (SFZ), Sars and Interim seamounts and at the margin of the Westantarctic Peninsula (WAP) (Figs. 3.1 and 3.2, Table 3.2). Sediment recovery is notoriously difficult due to prevailing strong currents in the Drake Passage. However, coring was successful during NBP1103 at Burdwood Bank (Kasten core KC 63, 333 m water depth), Interim seamount (Kasten core KC77, 3095 m) and at the WAP margin (Box core BC63, 597 m water depth). During NBP0805 small amounts of sediment samples were collected using a minicorer attached to the CTD to recover sediments from 4221 and 4395 m water depth near Sars and at SFZ, respectively. Additional gravel was collected from two dredges (DR18 and DR35; Table 3.3) at SFZ (2392m) and Sars seamount (695 m) (Figs. 3.1 and 3.2, Table 3.2). Samples were taken from respective top sections where possible (i.e. not applicable to dredge samples) (Table 3.2). The lithology of the different samples was very heterogeneous reflecting the different depositional environments, but also different sampling methods; for example dredged sediment samples contained rock fragments scraped off the bedrock. KC08 is characterised as quartz sand, including some darker minerals with an overall slightly green (mouldy) appearance. Sediment samples from Sars (DR35 and CTD04 minicore) and Interim (KC077) seamounts were dominated by light-brown and grey colours indicating unusually high carbonate contents. Sediments from SFZ (DR18 and CTD03 minicore) were muddy to sandy, dominated by grey to brown colours. BC63 sediments from the WAP are a grey-brown mixture of various grain sizes in the range of mud to sand.

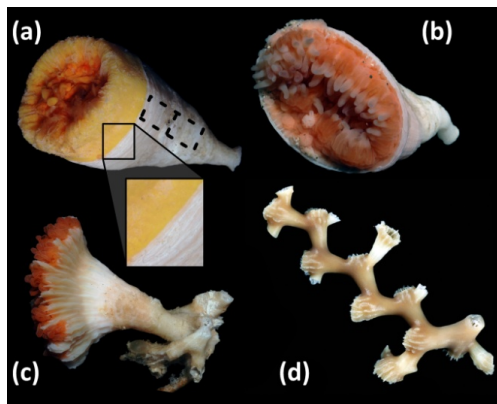


**Figure 3.3:** Alive specimens of (a) *B. malouinensis*, (b) *F. curvatum*, (c) *D. dianthus* collected in the Drake Passage during NBP0805 (photo credit: Dann Blackwood) and (d) sub-fossil *M. oculata* (Cairns and Kitahara, 2012). Alive specimens are characterised by their organic tissue which is strongly coloured (purple, red, orange) in all specimens. For *B. malouinensis* the coral skeleton is only solid in the lower parts and becomes porous at the top, as overgrown by organic tissue (see enlargement of the interface between the two parts of the skeleton). The stippled rectangle in (a) illustrates subsampling areas for upper and lower parts of a fossil *B. malouinensis* skeleton (for their trace metal content: Table 3.5; NBP1103 DH16 Bc-2).

Modern solitary coral specimen of *Desmophyllum dianthus* ( $n = 3$ ), *Balanophyllia malouinensis* ( $n = 4$ ) and *Flabellum curvatum* ( $n = 1$ ) (Fig. 3.3) were collected on Burdwood Bank by dredging and trawling during NBP0805 ( $n = 6$ ; all from one Blake Trawl at 816 m water depth) and LMG0605 on the *R/V Laurence M. Gould* ( $n = 2$ ; both *B. malouinensis*; one from 120 m water depth and one from 854 m water depth) (Figs. 3.2 and 3.3; Table 3.4). It should be noted that ‘modern samples’ in this case includes specimens collected alive ( $n = 3$ ) and specimens to be less than 467

years old as confirmed by U-series dating (Table 3.4; Burke and Robinson, 2012 and Burke et al., unpubl. data). The shallowest sample from 120 m water depth (*B. malouinensis*) was bathed in subsurface waters of the mixed layer, whereas the samples from 816 m (southern slope of Burdwood Bank) and 854 m (northern slope of Burdwood Bank) were bathed in AAIW (Fig. 3.2; Table 3.4). *B. malouinensis* (Fig. 3.3) is a species that is very abundant in the Drake Passage, but has not yet been calibrated for Nd isotope work.

We also include here one specimen of the colonial coral *Madrepora oculata* (Figs. 3.3 and 3.4), dredged during cruise CE0806 in the North Atlantic at 768 m water depth on the Reykjanes Ridge (61.87°N, 27.01°W) (Burke, 2012). This coral was bathed in a mixture of Subpolar Mode Waters (SPMW), its densest representative Labrador Seawater (LSW), Iceland-Scotland-Overflow Water (ISOW) and North Atlantic Central Waters (NACW; Talley and McCartney, 1982; Lacan and Jeandel, 2004a,b, 2005a; Yashayaev et al., 2007; Fig. 3.4, Table 3.4).

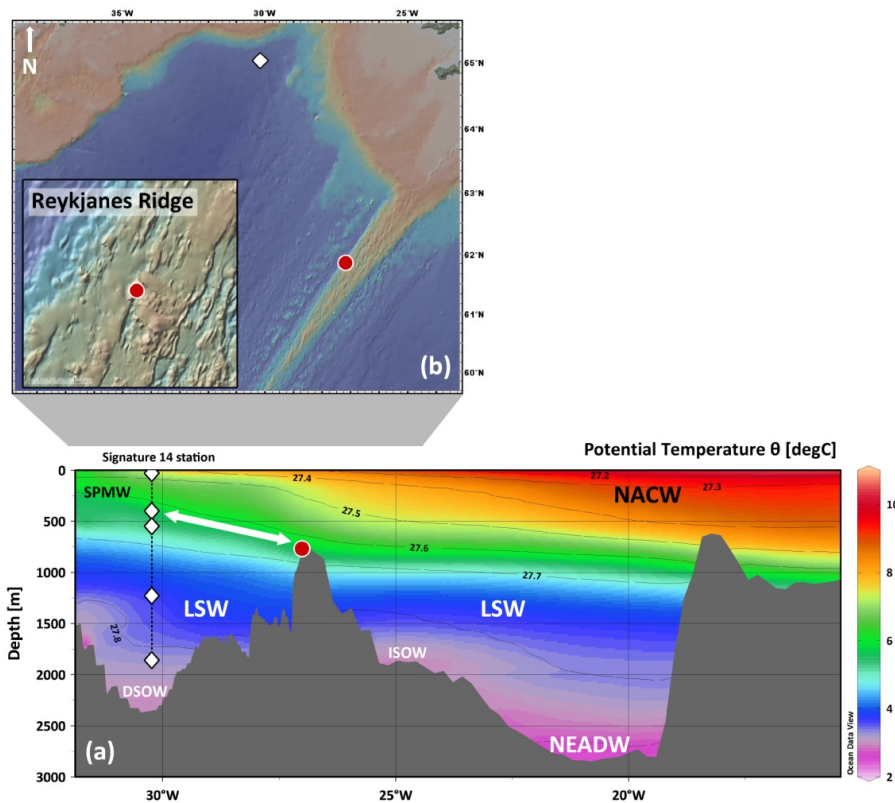


**Figure 3.4:** Sample location on Reykjanes Ridge in the North Atlantic. Red circle indicates modern deep-sea coral sample location used for Nd isotope calibration. White diamonds indicate seawater measurements at signature station 14 from Lacan and Jeandel (2004a, 2005b). (a) Section of potential temperature across the Northeast Atlantic (red line in Fig. 3.1; WOA13; Locarnini et al., 2013; generated with ODV software; Schlitzer, 2012). Thin black lines indicate surfaces of neutral density anomaly  $\gamma^n$  (Jackett and McDougall, 1997; in  $\text{kg/m}^3$ ). Black stippled line with arrowheads indicates mixing along  $\gamma^n = 27.74 \text{ kg/m}^3$ . NACW: North Atlantic Central Water, SPMW: Subpolar Mode Water, LSW: Labrador Sea Water, NEADW: Northeast Atlantic Deep Water, ISOW: Iceland Scotland Overflow Water, DSOW: Denmark Strait Overflow Water. Water masses after Talley and McCartney (1982), Lacan and Jeandel (2004a, 2005b) and Yashayaev et al. (2007). (b) Reykjanes Ridge bathymetry map generated with GeoMapApp (<http://www.geomapp.org>) with GMRT (Ryan et al., 2009).

In order to investigate the integrity of the Nd isotope signal in fossil deep-sea coral aragonite, we selected an additional 71 fossil specimens from the Drake Passage. The sample set includes the species *Desmophyllum dianthus* (n = 55), *Balanophyllia malouinensis* (n = 8), *Flabellum curvatum* (n = 3), *Gardineria antarctica* (n = 3) and *Caryophyllia spp.* (n = 2) and was collected by dredging or trawling during cruises NBP0805, NBP1103 and LMG0605 at Burdwood Bank (318 to 1515.5 m), Sars Seamount Seamount (695 to 1750 m), Interim Seamount (982.5 to 1195.5 m), and the Shackleton Fracture Zone (SFZ) (Figs. 3.1 and 3.2, Tables 3.5 and 3.6). A subset of re-sampled corals (n = 17) was investigated for major and trace metal content, not including U-series dating on individual subsamples (Table 3.5). All remaining fossil deep-sea coral samples presented here have been U-series dated (Burke and Robinson, 2012; Chen et al., 2015; Burke et al., unpubl. data) and ages range from 1.1 to 226 kyrs. Full chemical replicate analyses were carried out on *D. dianthus* (n = 14), *Caryophyllia spp.* (n = 1) and *G. antarctica* (n = 1), twelve of which were re-sampled pieces of the same coral. The remaining four replicates were generated from two separate aliquots from a crushed, but still inhomogenous coral sample (Table 3.6).

### 3.3. Analytical procedures

#### 3.3.1. Sample preparation for Nd isotope analyses

Seven sediment samples from across the Drake Passage were selected for analyses (Table 3.2). Available sample size was in some cases limited to sub-gram levels, for example for the top sections of CTD minicorer samples, dredged samples and box core samples (Table 3.2); homogenisation may be imperfect in such sediments. Sediment samples were exposed to a sequential leaching and digestion procedure following Cook et al. (2013). Briefly, this procedure involved carbonate removal with buffered acetic acid and removal of FeMn oxyhydroxide phases in a mixture of acetic acid and hydroxylamine hydrochloride. No step was performed to remove biogenic opal. Sub-samples of ~50 mg sediment (NBP0805 DR35, < 300  $\mu\text{m}$  fraction: ~8 mg) were exposed to aqua regia (3 : 1 mixture of concentrated HCl and HNO<sub>3</sub>, respectively) to remove organics, followed by silicate digestion in a mixture of 16 M HNO<sub>3</sub>, 28 M HF and 12 M HClO<sub>4</sub> in 1 : 2 : 0.6 proportion, after which the samples were converted to chloride form in 1 M HCl. An aliquot containing ~5 - 6 mg dissolved detritus (~22 mg of sand sample NBP1103 KC08, 0 - 5 cm) was then spiked with <sup>150</sup>Nd spike and used for subsequent cation exchange chromatography using Biorad<sup>®</sup> AG50W-X8 resin (200 - 400 mesh) following Chapter 2. Separation of Nd from other REEs followed the procedure of Cook et al. (2013) and was achieved using Eichrom Ln spec<sup>®</sup> resin (50 - 100  $\mu\text{m}$  bead size, modified after Pin and Zalduegui, 1997).

Deep-sea coral data were generated from ~0.1 to 1.3 g subsamples, either from wash fractions collected at WHOI during uranium-thorium separation (Chapter 2) or from re-sampled pieces of the same coral specimens used for U-series dating (Tables 3.4, 3.5 and 3.6). Cleaning of re-sampled specimens and those utilised for combined U-Th-Nd extraction followed similar procedures (e.g.,

Cheng et al., 2000; van de Flierdt et al., 2010; Burke and Robinson, 2012; Crocket et al. 2014). All coral and seawater samples were oxidised with aqua regia, followed by a 1:1 mixture of 16 M HNO<sub>3</sub> and 30% H<sub>2</sub>O<sub>2</sub> prior to REE separation in order to remove any residual organics from previous columns and/or initial digestion in 8 M HNO<sub>3</sub>. All samples from wash fractions processed for Nd isotope analyses were doped with a <sup>150</sup>Nd spike after collection to monitor Nd concentrations. This procedure produces a minimum concentration estimate (Nd<sub>min</sub>), which may underestimate true Nd concentrations in coralline aragonite by up to ~12% (Tables 3.4 and 3.6; Chapter 2). Coral samples processed for Nd isotope analyses only were spiked after initial digestion in 8 M HNO<sub>3</sub>.

10 L seawater samples were initially processed by Fe coprecipitation and anion exchange chromatography for Pa-Th separation at WHOI. Wash fractions from this procedure were subjected to the same ion exchange chromatography as coral samples (Chapter 2), which is outlined in brief below.

Samples processed for Nd isotope analyses before April 2014 were dissolved in 1 M HNO<sub>3</sub> and 0.9 M ascorbic acid mixture for REE separation with Eichrom RE spec<sup>®</sup> resin (100 - 150 μm). Due to the strong oxidation required after RE spec<sup>®</sup> chemistry (Crocket et al., 2014) we changed in April 2014 to REE-matrix separation using Biorad<sup>®</sup> AG50W-X8 resin (200 - 400 mesh). In both cases seawater and coral Nd purification was achieved on a second column using Eichrom Ln spec<sup>®</sup> resin (20 - 50 μm) (Crocket et al., 2014).

### 3.3.2. Neodymium isotope analyses

Neodymium isotope analyses were carried out on a ThermoFinnigan Triton TIMS in the MAGIC laboratories at Imperial College London. Seawater and coral samples, analysed in NdO<sup>+</sup> mode, were loaded in 2 x 0.5 μl 2.5 M HCl on degassed single W filaments between two layers of 0.5 μl TaF<sub>5</sub> activator (Crocket et al., 2014). Sediment Nd isotope analyses, performed in Nd<sup>+</sup> mode, were loaded in 2 x 0.5 μl 2.5 M HCl sandwiched between two layers of 0.5 μl 0.01 M H<sub>3</sub>PO<sub>4</sub> on degassed Re filaments in a double filament assembly (e.g., Andreasen and Sharma, 2009). After correcting for isobaric interferences, the instrumental mass bias was corrected for by normalisation to <sup>146</sup>Nd/<sup>144</sup>Nd = 0.7219 using an exponential law, and slightly higher <sup>146</sup>Nd/<sup>144</sup>Nd for spiked samples following Crocket et al. (2014). Barium was monitored manually, but no significant interference was found for the critical mass range of isobaric BaF and BaO. Pure JNdi-1 loads of 5 and 15 ng were analysed in NdO<sup>+</sup> mode (n = 110) and 60 and 100 ng loads in Nd<sup>+</sup> mode (n = 5) over a period of 26 months (<sup>143</sup>Nd/<sup>144</sup>Nd = 0.512104 ± 0.000010, n = 115) to monitor instrumental offset and normalise mass bias corrected <sup>143</sup>Nd/<sup>144</sup>Nd ratios of samples to the reference ratio of <sup>143</sup>Nd/<sup>144</sup>Nd = 0.512115 ± 0.000007 (Tanaka et al., 2000). 2σ external reproducibility of 10 and 30 ng Nd BCR-2 rock reference material analysed as NdO<sup>+</sup> was <sup>143</sup>Nd/<sup>144</sup>Nd = 0.512637 ± 0.000011 (n = 32). One additional ~80 ng Nd BCR-2 load was analysed with the sediment samples as Nd<sup>+</sup>. Overall, the reproducibility of reference materials analysed in NdO<sup>+</sup> and Nd<sup>+</sup> mode gave similar results so that altogether 33 BCR-2 analyses yielded

$^{143}\text{Nd}/^{144}\text{Nd} = 0.512637 \pm 0.000010$ , i.e. 20 ppm. Our in-house coral standard yielded a similar precision for 10 and 30 ng Nd loads ( $^{143}\text{Nd}/^{144}\text{Nd} = 0.512336 \pm 0.000009$ ;  $n = 23$ ).

Full procedural blanks of combined U, Th and Nd separation from aragonite matrix ranged from 2 to 27 pg Nd ( $n = 20$ ). Full procedural blanks of combined Pa, Th and Nd separation from seawater matrix were significantly higher at 0.24 and 0.48 ng Nd due to blank problems induced by sample processing (Auro et al., 2012), which were rectified during the later part of our study (e.g., after processing of the seawater samples reported here). Contribution of Nd chemistry to this elevated blank was monitored and found to be below 17 pg Nd ( $n = 7$ ). The Nd isotopic composition of the 0.48 ng full procedural blank was  $^{143}\text{Nd}/^{144}\text{Nd} = 0.512225 \pm 0.000029$  (2SE). Even though blanks contributed up to 25% of the analysed natural sample Nd, blank corrections were found to contribute less than 0.04 epsilon units and hence no correction was applied. The full procedural Nd blank of the sediment protocol was 13 pg ( $n = 1$ ).

### 3.3.3. Major and trace element analyses on modern and fossil corals and sediments

Major and trace element analyses on 17 re-sampled and cleaned fossil and modern coral samples and seven sediment samples were carried out on an Agilent 7500s ICP-MS at CEP SAR, Open University. Analyses of coral and sediment samples were carried out on unspiked aliquots taken from the fully dissolved samples prior to ion chromatography. In order to optimise results of low-abundance lanthanide series elements, aliquots of dissolved coral samples were diluted to ~1000 ppm Ca for elemental masses < 89 and to ~2000 ppm Ca for elemental masses  $\geq 89$ . Coral samples were analysed in a matrix of 2% nitric acid in four separate runs over two analytical sessions (Table 3.5). Sample concentrations were calculated using an in-house multi-element standard doped with Ca to match sample contents. Machine drift was monitored with an in-house multi-element standard and a deep-sea coral standard (Crocket et al., 2014). BCR-2 was measured as an unknown for additional quality control in the beginning and at the end of each analytical session. Limestone reference material JLS-1 was used to monitor reproducibility during 1000 ppm Ca sessions. Aliquots of dissolved sediment samples were diluted to ~5 ng/g Nd as Nd concentrations were already known from TIMS isotope dilution measurements (see 3.3.1 and Table 3.2). All sediment samples were analysed during one analytical session, containing rock reference material BCR-2 and a deep-sea coral standard (Crocket et al., 2014) for additional quality control. Full procedural blank levels were negligible for all elements of interest and BCR-2 ( $n = 6$ ) yielded REE results within 5% RSD of certified values and within 20% for most other elements (Al, Ca, Sc, Ti, Y, Th and U). Exceptions were Fe (51% RSD) and Mn (53% RSD). Coral standard ( $n = 9$ ) RSDs were below 8% for most REE and U, whereas low abundance heavy REE (HREE) reproduced less well (Tm: 31%, Yb: 11.4% and Lu: 11.8%). Typical reproducibilities for selected elements in our coral standard were as follows: Th: 14.5%, Al: 19.6%, Ca: 7.0%, Ti: 8.4%, Mn: 27.3% and Fe: 13.3% RSD. Limestone reference material JLS-1 ( $n = 8$ ) reproduced better than 7% for most elements, except Ti: 16.2% (omitting one flyer), Sm: 12.4%, Tb:

15.3%, Tm: 13.0% (n = 4, below limit of detection during second run), Yb: 8.4% and Th: 12.6% (Table 3.5).

Four out of the 17 re-sampled corals have furthermore been processed for Nd concentrations by TIMS isotope dilution allowing for intercomparison with ICP-MS data (Tables 3.4 and 3.6).

### 3.4. Results

#### 3.4.1. Seawater Nd isotope data

The Nd isotopic composition of seawater from three Drake Passage depth profiles falls in a narrow  $\epsilon_{Nd}$  range between -7.6 and -8.6 (Table 3.1, Fig. 3.5; ( $\epsilon_{Nd} = ((^{143}Nd/^{144}Nd_{sample})/(^{143}Nd/^{144}Nd_{CHUR}) - 1) \times 10,000$ ; CHUR: chondritic uniform reservoir, see Jacobsen and Wasserburg, 1980), indicating a relatively homogenous water column across the Drake Passage.

| Sample       | Lat     | Long    | Water depth (m) | Location            | $^{143}Nd/^{144}Nd^a$ | 2SE <sup>b</sup> | $\epsilon_{Nd}^c$ | 2SE  | 2SD <sup>d</sup> |
|--------------|---------|---------|-----------------|---------------------|-----------------------|------------------|-------------------|------|------------------|
| CTD2_R-2-1   | -54.872 | -62.140 | 2190            | Burdwood Bank       | 0.512229              | 0.000008         | -7.97             | 0.16 | 0.20             |
| CTD2_R-4-2   | -54.872 | -62.140 | 2100            | Burdwood Bank       | 0.512243              | 0.000016         | -7.70             | 0.32 | 0.32             |
| CTD2_R-6-3   | -54.872 | -62.140 | 1800            | Burdwood Bank       | 0.512245              | 0.000014         | -7.66             | 0.26 | 0.26             |
| CTD2_R-12-6  | -54.872 | -62.140 | 1200            | Burdwood Bank       | 0.512229              | 0.000009         | -7.97             | 0.18 | 0.20             |
| CTD2_R-14-7  | -54.872 | -62.140 | 805             | Burdwood Bank       | 0.512220              | 0.000020         | -8.16             | 0.40 | 0.40             |
| CTD2_R-16-8  | -54.872 | -62.140 | 500             | Burdwood Bank       | 0.512235              | 0.000015         | -7.86             | 0.30 | 0.30             |
| CTD2_R-18-9  | -54.872 | -62.140 | 300             | Burdwood Bank       | 0.512211              | 0.000010         | -8.33             | 0.19 | 0.20             |
| CTD2_R-20-10 | -54.872 | -62.140 | 200             | Burdwood Bank       | 0.512213              | 0.000014         | -8.28             | 0.28 | 0.28             |
| CTD2_R-21-11 | -54.872 | -62.140 | 49              | Burdwood Bank       | 0.512210              | 0.000020         | -8.35             | 0.39 | 0.39             |
| CTD2_R-24-12 | -54.872 | -62.140 | 0               | Burdwood Bank       | 0.512203              | 0.000022         | -8.48             | 0.43 | 0.43             |
| CTD3_R-2-1   | -60.617 | -56.535 | 4221            | Shackl. Fract. Zone | 0.512249              | 0.000006         | -7.60             | 0.11 | 0.20             |
| CTD3_R-4-2   | -60.617 | -56.535 | 4105            | Shackl. Fract. Zone | 0.512245              | 0.000004         | -7.67             | 0.08 | 0.20             |
| CTD3_R-6-3   | -60.617 | -56.535 | 3700            | Shackl. Fract. Zone | 0.512232              | 0.000005         | -7.92             | 0.10 | 0.20             |
| CTD3_R-8-4   | -60.617 | -56.535 | 3200            | Shackl. Fract. Zone | 0.512218              | 0.000005         | -8.19             | 0.11 | 0.20             |
| CTD3_R-10-5  | -60.617 | -56.535 | 2500            | Shackl. Fract. Zone | 0.512225              | 0.000005         | -8.05             | 0.10 | 0.20             |
| CTD3_R-12-6  | -60.617 | -56.535 | 1800            | Shackl. Fract. Zone | 0.512209              | 0.000005         | -8.36             | 0.10 | 0.20             |
| CTD3_R-14-7  | -60.617 | -56.535 | 1400            | Shackl. Fract. Zone | 0.512204              | 0.000006         | -8.46             | 0.11 | 0.20             |
| CTD3_R-16-8  | -60.617 | -56.535 | 1000            | Shackl. Fract. Zone | 0.512197              | 0.000006         | -8.61             | 0.12 | 0.20             |
| CTD3_R-18-9  | -60.617 | -56.535 | 410             | Shackl. Fract. Zone | 0.512213              | 0.000006         | -8.29             | 0.12 | 0.20             |
| CTD3_R-20-10 | -60.617 | -56.535 | 249             | Shackl. Fract. Zone | 0.512215              | 0.000006         | -8.26             | 0.12 | 0.20             |
| CTD3_R-21-11 | -60.617 | -56.535 | 100             | Shackl. Fract. Zone | 0.512228              | 0.000006         | -7.99             | 0.11 | 0.20             |
| CTD3_R-24-12 | -60.617 | -56.535 | 8.8             | Shackl. Fract. Zone | 0.512233              | 0.000007         | -7.90             | 0.13 | 0.20             |
| CTD4_R-2-1   | -59.823 | -66.003 | 4395            | Near Sars Seamount  | 0.512245              | 0.000007         | -7.66             | 0.14 | 0.20             |
| CTD4_R-4-2   | -59.823 | -66.003 | 4295            | Near Sars Seamount  | 0.512237              | 0.000006         | -7.81             | 0.11 | 0.20             |
| CTD4_R-6-3   | -59.823 | -66.003 | 4000            | Near Sars Seamount  | 0.512249              | 0.000006         | -7.60             | 0.12 | 0.20             |
| CTD4_R-8-4   | -59.823 | -66.003 | 3500            | Near Sars Seamount  | 0.512240              | 0.000007         | -7.77             | 0.14 | 0.20             |
| CTD4_R-10-5  | -59.823 | -66.003 | 2999            | Near Sars Seamount  | 0.512221              | 0.000006         | -8.13             | 0.12 | 0.20             |
| CTD4_R-12-6  | -59.823 | -66.003 | 2250            | Near Sars Seamount  | 0.512214              | 0.000007         | -8.28             | 0.13 | 0.20             |
| CTD4_R-14-7  | -59.823 | -66.003 | 1499            | Near Sars Seamount  | 0.512208              | 0.000013         | -8.24             | 0.25 | 0.25             |
| CTD4_R-16-8  | -59.823 | -66.003 | 1000            | Near Sars Seamount  | 0.512204              | 0.000017         | -8.46             | 0.32 | 0.32             |
| CTD4_R-18-9  | -59.823 | -66.003 | 600             | Near Sars Seamount  | 0.512236              | 0.000015         | -7.84             | 0.29 | 0.29             |
| CTD4_R-24-12 | -59.823 | -66.003 | 0               | Near Sars Seamount  | 0.512223              | 0.000008         | -8.09             | 0.15 | 0.20             |

(a)  $^{143}Nd/^{144}Nd$  ratios were corrected for the offset of the measured JNdi-1 ratio of  $0.512104 \pm 0.000010$  (n = 115) from the published value of  $0.512115 \pm 0.000007$  (Tanaka et al., 2000)

(b) 2SE is the analytical 2 $\sigma$  standard error.

(c)  $\epsilon_{Nd}$  was calculated using the present day CHUR value of  $^{143}Nd/^{144}Nd = 0.512638$  (Jacobsen and Wasserburg, 1980).

(d) 2SD refers to the 2 $\sigma$  standard deviation derived from the longterm reproducibility of BCR-2 standards over a 26 months period (see text). If the internal 2 $\sigma$  SE was larger than the external one, the internal error is reported.

**Table 3.1:** Neodymium isotope results for three seawater stations sampled during expedition NBP0805 on the Nathaniel B. Palmer in the Drake Passage. Note that samples were not filtered and that Nd chemistry was performed on chemistry cuts from Pa-Th chemistry, yielding to poor yields in places (see Auro et al., 2012, for details). Shackl. Fract. Zone = Shackleton Fracture Zone.

In detail, the two seawater profiles from Sars seamount and the SFZ reveal identical  $\epsilon_{\text{Nd}}$  values within error. Both profiles are characterised by slightly more radiogenic values in surface and bottom waters ( $\epsilon_{\text{Nd}} (<100\text{m}) = -8.0 \pm 0.2$ ,  $n = 3$ ;  $\epsilon_{\text{Nd}} (>4000\text{m}) = -7.7 \pm 0.2$ ,  $n = 5$ ) compared to intermediate water depth ( $\epsilon_{\text{Nd}} (1000\text{m}) = -8.5$  to  $-8.6$ ). While the seawater profile from the slope off Burdwood Bank reveals the same overall range in Nd isotopic compositions, the most radiogenic values are observed in 1800 to 2190 m water depth ( $\epsilon_{\text{Nd}}$  of  $-7.8 \pm 0.3$ ,  $n = 3$ ) and the least radiogenic values are found in the uppermost 300 m of the water column ( $\epsilon_{\text{Nd}} = -8.4 \pm 0.2$ ,  $n = 4$ ). Figure 3.5 furthermore illustrates that our new seawater Nd isotope results are in excellent agreement with previously published seawater profiles from the Drake Passage, omitting a small apparent deviation in deep waters from south of the polar front (Stichel et al., 2012).

### 3.4.2. Sediment data

Major and trace element data as well as Nd isotopic compositions of detrital sediments collected from across the Drake Passage are reported in Tables 3.2 and 3.3. Radiogenic Nd isotope values ranging from  $\epsilon_{\text{Nd}} = 2.5 \pm 0.2$  to  $\epsilon_{\text{Nd}} = -6.5 \pm 0.2$ , as well as positive Eu anomalies ( $\text{Eu}/\text{Eu}^* = 2 \times \text{Eu}/(\text{Sm} + \text{Gd}) = 1.1$  to  $1.9$ ) indicate a significant volcanogenic component in the lithogenic fraction. Neodymium concentrations are relatively low ( $[\text{Nd}] = 11.6$  to  $21.2 \mu\text{g/g}$ ) compared to upper continental crust values ( $[\text{Nd}] = 27 \mu\text{g/g}$ ; Taylor and McLennan, 1985), but within the range of local basalts from the Antarctic Peninsula and the southern tip of Chile (GEOROC database). The two most positive results in  $\epsilon_{\text{Nd}}$  stem from two samples (DR35 and BC63; Table 3.2), which were potentially contaminated and are hence omitted from further discussion and mass balance calculations (see Table 3.2 and caption for details).

### 3.4.3. Deep-sea coral data

#### 3.4.3.1. Modern Calibration

The modern North Atlantic specimen of *M. oculata* from 768 m water depth was dated to be no older than 30 years and yielded an  $\epsilon_{\text{Nd}}$  of  $-13.1 \pm 0.2$ , which is the least radiogenic Nd isotopic composition obtained during this study and in line with other analyses of deep-sea corals in the North Atlantic. As such it shows excellent agreement with the nearby seawater from West off Iceland (Fig. 3.6), following the neutral density anomaly  $\gamma^n = 27.74 \text{ kg/m}^3$  ( $\epsilon_{\text{Nd}} = -13.2 \pm 0.2$  at 401 m water depth; Station 14, Lacan and Jeandel, 2004a; Figs. 3.1 and 3.4). Results for modern specimens of *F. curvatum* (collected alive;  $n = 1$ ), *B. malouinensis* (collected alive and dated to be up to 330 years old;  $n = 4$ ), and *D. dianthus* (up to 467 years old;  $n = 3$ ) span a range of  $\epsilon_{\text{Nd}}$  values from  $-7.0$  to  $-7.6$  (Table 3.4; Fig. 3.6). A complete replicate of sample Big Beauty yielded excellent agreement in Nd isotopic composition. Overall, most of the specimens investigated show Nd isotopic compositions consistent with ambient seawater. In detail, two *D. dianthus*, one *F. curvatum*, and one *B. malouinensis* yield

values within error of seawater at 805 m at Burdwood Bank ( $\epsilon_{Nd} = -8.2 \pm 0.4$ ; Fig. 3.6) (Table 3.4, Fig. 3.6). One *D. dianthus* specimen (TB04 Dp-A-02) and two alive-collected specimens of *B. malouinensis* (Mod. Balano-1/-2) from the same location however deviate from this value.

One additional *B. malouinensis* (LMG06-05/3-1) collected from the northern flank of Burdwood Bank at 120 m water depth ( $\epsilon_{Nd} = -7.2 \pm 0.2$ ) is also offset from seawater measured at 200 m water depth on the southern flank of Burdwood Bank ( $\epsilon_{Nd} = -8.3 \pm 0.3$ ; Tables 3.1 and 3.4, Figs. 3.2 and 3.6). The latter is however the only specimen in this collection showing an offset from seawater  $\delta^{234}U = 146.8 \pm 0.1\%$  ( $2\sigma$ ,  $n = 19$ ; Andersen et al., 2010), i.e. initial coral  $\delta^{234}U = 111.6 \pm 0.5\%$  indicates open system behaviour (see caption of Table 3.6 for details) and is hence omitted from Figure 3.6 and further discussion.

| Cruise  | Event | Device       | Lat     | Long    | Water depth (m) | Sample size (g) | Location              | Depth bsf | $^{143}\text{Nd}/^{144}\text{Nd}^{\text{d}}$ | $2\text{SE}^{\text{b}}$ | $\epsilon_{\text{Nd}}^{\text{c}}$ | $2\text{SE}$ | $2\text{SD}^{\text{d}}$ | Nd ( $\mu\text{g}/\text{g}$ ) | $2\text{SE}(\text{ep})^{\text{e}}$ |
|---------|-------|--------------|---------|---------|-----------------|-----------------|-----------------------|-----------|--|-------------------------|-----------------------------------|--------------|-------------------------|-------------------------------|------------------------------------|
| NBP1103 | KC08  | Kasten corer | -54.486 | -62.230 | 333             | 6.19            | Burdwood Bank         | 0-5 cm    | 0.512381                                     | 0.000004                | -5.02                             | 0.08         | 0.20                    | 15.82                         | 0.000003                           |
| NBP0805 | DR35* | Dredge       | -59.723 | -68.881 | 695             | 0.84            | Sars seamount         | <300um    | 0.512658                                     | 0.000010                | 0.38                              | 0.19         | 0.20                    | 7.49                          | 0.000002                           |
| NBP0805 | CTD04 | Minicorer    | -59.823 | -66.003 | 4395            | 0.07            | Near Sars             | 0-3 cm    | 0.512488                                     | 0.000006                | -2.92                             | 0.13         | 0.20                    | 11.60                         | 0.000012                           |
| NBP1103 | KC077 | Kasten corer | -60.544 | -66.177 | 3095            | 3.26            | Interim               | 0-5 cm    | 0.512469                                     | 0.000007                | -3.29                             | 0.13         | 0.20                    | 11.89                         | 0.000009                           |
| NBP0805 | DR18  | Dredge       | -60.643 | -56.472 | 2392            | 1.63            | SFZ surface scrapings | coretop   | 0.512304                                     | 0.000006                | -6.52                             | 0.11         | 0.20                    | 21.23                         | 0.000003                           |
| NBP0805 | CTD03 | Minicorer    | -60.617 | -56.535 | 4221            | 0.79            | SFZ                   | coretop   | 0.512584                                     | 0.000007                | -1.06                             | 0.14         | 0.20                    | 15.61                         | 0.000005                           |
| NBP1103 | BC63* | Boxcorer     | -63.054 | -61.592 | 597             | 0.32            | WAP                   | 0-1 cm    | 0.512764                                     | 0.000006                | 2.46                              | 0.13         | 0.20                    | 12.81                         | 0.000004                           |

(a)  $^{143}\text{Nd}/^{144}\text{Nd}$  ratios were corrected for the offset of the measured JNdI-1 ratio of  $0.512104 \pm 0.000010$  ( $n = 115$ ) from the published value of  $0.512115 \pm 0.000007$  (Tanaka et al., 2000).

(b)  $2\text{SE}$  is the analytical  $2\sigma$  standard error.

(c)  $\epsilon_{\text{Nd}}$  was calculated using the present day CHUR value of  $^{143}\text{Nd}/^{144}\text{Nd} = 0.512638$  (Jacobsen and Wasserburg, 1980).

(d)  $2\text{SD}$  refers to the  $2\sigma$  standard deviation derived from the longterm reproducibility of BCR-2 standards over a 26 months period (see text). If the internal  $2\sigma$  SE was larger than the external one, the internal error is reported.

(e)  $2\text{SE}(\text{ep})$  is the propagated  $2\sigma$  standard error of Nd concentrations determined by isotope dilution.

**Table 3.2:** Neodymium isotope results for sediment samples collected during two cruises on the Nathaniel B. Palmer, NBP1103 and NBP0805, at Burdwood Bank, Sars and Interim seamounts, Shackleton Fracture Zone (SFZ) and the Westantarctic Peninsula (WAP). Samples were analysed as  $\text{Nd}^+$  by TIMS at Imperial College London and were spiked with  $^{150}\text{Nd}$  after digestion to obtain accurate Nd concentration data by isotope dilution. Asterisks indicate potentially contaminated samples and therefore omitted. After digestion blue pieces of rubber were found in sample DR35 and in sample BC63 a non-detrital soft component appearing during digestion procedure could not be classified.

| Sample ID                         | Al (%) | Ca (%) | Ti (%) | Mn ( $\mu\text{g}/\text{g}$ ) | La ( $\mu\text{g}/\text{g}$ ) | Ce ( $\mu\text{g}/\text{g}$ ) | Pr ( $\mu\text{g}/\text{g}$ ) | Nd ( $\mu\text{g}/\text{g}$ ) | Sm ( $\mu\text{g}/\text{g}$ ) | Eu ( $\mu\text{g}/\text{g}$ ) | Gd ( $\mu\text{g}/\text{g}$ ) | Tb ( $\mu\text{g}/\text{g}$ ) | Dy ( $\mu\text{g}/\text{g}$ ) | Ho ( $\mu\text{g}/\text{g}$ ) | Er ( $\mu\text{g}/\text{g}$ ) | Yb ( $\mu\text{g}/\text{g}$ ) | Lu ( $\mu\text{g}/\text{g}$ ) | Th ( $\mu\text{g}/\text{g}$ ) | U ( $\mu\text{g}/\text{g}$ ) | Ce/Ce* | Gd/Gd* | Eu/Eu* |
|-----------------------------------|--------|--------|--------|-------------------------------|-------------------------------|-------------------------------|-------------------------------|-------------------------------|-------------------------------|-------------------------------|-------------------------------|-------------------------------|-------------------------------|-------------------------------|-------------------------------|-------------------------------|-------------------------------|-------------------------------|------------------------------|--------|--------|--------|
| KC08                              | 5.8    | 0.5    | 0.3    | 247                           | 16.8                          | 38.9                          | 4.4                           | 16.6                          | 3.5                           | 0.8                           | 2.9                           | 0.5                           | 2.5                           | 0.5                           | 1.6                           | 1.6                           | 0.2                           | 5.7                           | 1.9                          | 1.04   | 0.91   | 1.22   |
| DR35*                             | 3.5    | 1.9    | 0.5    | 354                           | 7.7                           | 27.3                          | 1.9                           | 7.6                           | 1.6                           | 0.6                           | 1.5                           | 0.2                           | 1.3                           | 0.3                           | 0.7                           | 0.7                           | 0.1                           | 2.8                           | 0.7                          | 1.62   | 0.75   | 1.85   |
| CTD04                             | 6.5    | 1.4    | 0.4    | 538                           | 12.6                          | 26.4                          | 3.2                           | 12.0                          | 2.6                           | 0.7                           | 2.2                           | 0.4                           | 2.2                           | 0.5                           | 1.4                           | 1.5                           | 0.2                           | 4.0                           | 1.0                          | 0.95   | 0.83   | 1.40   |
| KC77                              | 5.3    | 1.4    | 0.3    | 368                           | 15.2                          | 30.9                          | 3.4                           | 12.4                          | 2.5                           | 0.8                           | 2.1                           | 0.4                           | 2.1                           | 0.5                           | 1.4                           | 1.3                           | 0.2                           | 3.9                           | 1.0                          | 0.99   | 0.77   | 1.55   |
| DR18                              | 5.4    | 1.2    | 0.5    | 448                           | 22.9                          | 52.0                          | 5.9                           | 22.6                          | 4.6                           | 1.0                           | 4.2                           | 0.7                           | 3.8                           | 0.8                           | 2.3                           | 2.3                           | 0.3                           | 8.0                           | 1.4                          | 1.03   | 0.99   | 1.06   |
| CTD03                             | 7.0    | 2.1    | 0.5    | 779                           | 15.0                          | 32.1                          | 4.1                           | 16.5                          | 4.0                           | 1.1                           | 3.7                           | 0.6                           | 3.8                           | 0.8                           | 2.4                           | 2.3                           | 0.4                           | 4.3                           | 1.4                          | 0.94   | 0.85   | 1.37   |
| BC63*                             | 8.1    | 3.7    | 0.6    | 1041                          | 11.2                          | 24.1                          | 3.3                           | 14.1                          | 3.6                           | 1.2                           | 3.9                           | 0.7                           | 4.2                           | 0.9                           | 2.7                           | 2.5                           | 0.4                           | 2.8                           | 0.9                          | 0.90   | 0.85   | 1.45   |
| BCR-2 (session certified value)   | 7.1    | 5.2    | 1.3    | 1434                          | 25.6                          | 53.4                          | 7.0                           | 29.2                          | 6.7                           | 2.1                           | 6.8                           | 1.1                           | 6.0                           | 1.3                           | 3.7                           | 3.6                           | 0.5                           | 5.8                           | 1.6                          | -      | -      | -      |
| RSD                               | 0.1    | 0.08   | 0.03   | 60                            | 1.0                           | 2.0                           | 0.3                           | 2.0                           | 0.3                           | 0.1                           | 0.3                           | 0.0                           | -                             | 1.3                           | -                             | 3.5                           | 0.5                           | 6.2                           | -                            | -      | -      | -      |
| Difference to certified value (%) | 0.8    | -1.2   | 3.5    | 5.6                           | -2.3                          | -0.8                          | -2.7                          | -4.3                          | -0.7                          | -6.4                          | 0.5                           | -1.0                          | -                             | 0.9                           | -                             | -1.8                          | -2.8                          | 6.6                           | -                            | -      | -      | -      |

**Table 3.3:** ICP-MS major and trace metal data of Drake Passage sediment samples generated at the Open University (see Table 3.2 for sample details). Last three columns denote Ce, Gd and Eu anomalies, calculated using PAAS-normalised values (Taylor and McLennan, 1985):  $\text{Ce}/\text{Ce}^* = 2 \times \text{Ce}/(\text{La} + \text{Pr})$ ,  $\text{Gd}/\text{Gd}^* = 2 \times \text{Gd}/(\text{Eu} + \text{Tb})$  and  $\text{Eu}/\text{Eu}^* = 2 \times \text{Eu}/(\text{Sm} + \text{Gd})$ . The results of one USGS BCR-2 rock standard analysis are reported and compared to the certified values.



### 3.4.3.2. Trace Metal Systematics

For a total of 9 modern and 87 fossil deep sea coral samples from the Drake Passage Nd, U and Th concentrations are available from isotope dilution during combined coral dating (MC-ICP-MS; Burke and Robinson, 2012; Chen et al., 2015; Burke et al., unpubl. data) and Nd isotope analyses (TIMS; mostly  $[\text{Nd}_{\text{min}}]$ ; see also Chapter 2). In modern coral specimens,  $^{232}\text{Th}$  concentrations are generally low, but vary by one order of magnitude (43 to 377 pg/g; Table 3.4). Neodymium concentrations are typically higher, but less variable with values between ~5 and 27 ng/g (with the exception of modern *F. curvatum* with 152.2 ng/g; mostly  $[\text{Nd}_{\text{min}}]$  estimates only, see Table 3.4). It is worth noting that, among modern coral samples, *D. dianthus* specimen Dp-A-02 and *B. malouinensis* specimen Mod. Balano-1 show the highest  $^{232}\text{Th}$  concentrations of 344 pg/g and 377 pg/g, respectively. Of the remaining modern corals *B. malouinensis* specimens show slightly elevated  $^{232}\text{Th}$  concentrations relative to *D. dianthus*, *F. curvatum* and *M. oculata* (Table 3.4).

The fossil coral data set consists of 87 coral samples including 13 replicates analysed as wash fractions from U-Th dating (i.e.  $[\text{Nd}_{\text{min}}]$  estimates) and 3 re-sampled corals analysed for their Nd only. Minimum Nd concentrations in fossil coral specimens range from 7.3 ng/g to 964.5 ng/g and  $^{232}\text{Th}$  concentrations range from 20 to 3500 pg/g (Table 3.6, Fig. 3.7). The entire coral  $[\text{Nd}_{\text{min}}]$  and  $^{232}\text{Th}$  concentration dataset obtained from isotope dilution (including modern coral samples) shows a weak correlation of  $R^2 = 0.48$  ( $n = 91$ ; Fig. 3.7). Significantly higher covariations are displayed for the species *B. malouinensis* ( $R^2 = 0.96$ ,  $n = 11$ ) and *G. antarctica* ( $R^2 = 1$ ,  $n = 4$ ) (Fig. 3.7).

The subset of modern and fossil samples ( $n = 17$ ) analysed for major and trace element concentrations yielded the following results:  $[\text{Al}] < 9.2 \mu\text{g/g}$ ,  $[\text{Ti}] < 0.54 \mu\text{g/g}$ ,  $[\text{Mn}] < 0.38 \mu\text{g/g}$  and  $[\text{Fe}] < 14 \mu\text{g/g}$  (omitting one result) (Table 3.5). These concentrations are several orders of magnitude lower than in lithogenic and FeMn oxyhydroxide phases (Tables 3.3 and 3.5, Fig. 3.7; Crocket et al., 2014). Despite the large range of Nd concentrations observed in modern and fossil coral specimens their shale-normalised rare earth element patterns show three distinct features: (i) negative Ce anomalies ( $\text{Ce}/\text{Ce}^* = 2 \times \text{Ce}/(\text{La} + \text{Nd})$  ranging from 0.03 to 0.09), (ii) enrichment of heavy over light rare earth elements ( $\text{HREE}/\text{LREE} = (\text{Er} + \text{Yb})/(\text{La} + \text{Nd}) = 1.1$  to 10), and (iii) positive Gd anomalies ( $\text{Gd}/\text{Gd}^* = 2 \times \text{Gd}/(\text{Eu} + \text{Tb}) = 1$  to 1.3, except for sample NBP0805 DR35 Dc-D002, which shows a negative Gd anomaly (Table 3.5, Fig. 3.8). These observations are consistent on intra- and interspecies level, i.e. the REE data set includes *D. dianthus*, *G. antarctica* and *B. malouinensis*.

One fossil specimen of *B. malouinensis* was furthermore sub-sampled at the upper and lower part of its skeleton (Fig. 3.3) in order to investigate potential geochemical gradients. The lower part contains about 6 times higher concentrations of lithogenic elements such as Al and Ti, slight enrichment in Nd (38.4 ng/g in the upper part and 52.6 ng/g in the lower parts), and rather similar concentrations in Fe (Table 3.5).

Another coral specimen that has not been studied for palaeo work so far is *G. antarctica*. We note that even though REE concentrations seem elevated the PAAS-normalised pattern (Taylor and McLennan, 1985) looks like modern seawater (Table 3.5, Fig. 3.8).

The reproducibility of trace metal concentrations in re-sampled corals is reflected in replicate U, Th and  $\text{Nd}_{\text{min}}$  concentration results obtained from isotope dilution. Excluding one respective outlier resampled  $[\text{Nd}_{\text{min}}]_{\text{coral}}$  shows only weak correlation ( $R^2 = 0.35$ ;  $n = 15$ ) whereas  $[\text{U}]_{\text{coral}}$  ( $R^2 = 0.76$ ;  $n = 12$ ) and  $[\text{}^{232}\text{Th}]_{\text{coral}}$  ( $R^2 = 0.63$ ;  $n = 12$ ) reproduce better between different parts of the same coral (Table 3.6, Fig. 3.9). This observation is moreover manifested in comparison of  $[\text{Nd}_{\text{min}}]_{\text{coral}}$  and  $[\text{U}]_{\text{coral}}$  obtained from isotope dilution (Tables 3.4 and 3.6) with the respective results of the 17 re-sampled coral samples analysed by ICP-MS (Table 3.5). Excluding two outliers, the Nd results indicate poor reproducibility represented by  $R^2$  of 0.28 whereas U concentrations show  $R^2 = 0.71$  between different parts of the same coral analysed by different methods thus echoing the results of the isotope dilution replicate data. The  $^{232}\text{Th}$  LOD of the ICP-MS limits a similar comparison with isotope dilution MC-ICP-MS data (Table 3.5).

However, trace metal concentrations obtained using isotope dilution and by ICP-MS from the same sample solution show consistent trends indicating that the trends are not an analytical artifact. The integrity of data obtained from different methods is further demonstrated by comparison of Nd concentrations obtained by TIMS isotope dilution with ICP-MS analyses. Both analyses were carried out with aliquots from the same sample solution of four resampled corals. The results show good agreement between different analytical methods, i.e. within 6.1% ( $n = 3$ ) and 25.9% for sample NBP0805 TB04 Big Beauty, which shows however low [Nd] so that the absolute difference between 5.4 and 4.0 ng/g is small (Tables 3.4, 3.5 and 3.6).

| Cruise  | Event | Sample          | Sample mass (g) | Al (µg/g) | Ca (%) | Ti (µg/g) | Mn (µg/g) | Fe (µg/g) | La (ng/g) | Ce (ng/g) | Pr (ng/g) | Nd (ng/g) | Sm (ng/g) | Eu (ng/g) | Gd (ng/g) | Tb (ng/g) | Dy (ng/g) | Ho (ng/g) | Er (ng/g) | Tm (ng/g) | Vb (ng/g) | Lu (ng/g) | Th (ng/g) | U (ng/g) | Ce/Ce | Gd/Gd | Eu/Eu | HREE/LREE |      |      |  |  |  |
|---|-------|-----------------|-----------------|-----------|--------|-----------|-----------|-----------|-----------|-----------|-----------|-----------|-----------|-----------|-----------|-----------|-----------|-----------|-----------|-----------|-----------|-----------|-----------|----------|-------|-------|-------|-----------|------|------|--|--|--|
| <b>Run 1</b>                                  |       |                 |                 |           |        |           |           |           |           |           |           |           |           |           |           |           |           |           |           |           |           |           |           |          |       |       |       |           |      |      |  |  |  |
| NBP0805                                       | TB04  | Big Beauty      | 0.3039          | <LOD      | 36.74  | 0.03      | <LOD      | 7.2       | 8.3       | <LOD      | 0.9       | 4.0       | <LOD      | 1.0       | <LOD      | <LOD      | 2.1       | 0.1       | 1.8       | <LOD      | 1.8       | <LOD      | 1.1       | 4056     | -     | -     | -     | -         | 3.75 |      |  |  |  |
| NBP0805                                       | TB04  | modern Balamo-2 | 0.2010          | 7.5       | 37.21  | 0.54      | <LOD      | 9.5       | 43.8      | <LOD      | 5.6       | 26.0      | 4.4       | 1.6       | 7.5       | 1.0       | 7.5       | 1.2       | 4.9       | <LOD      | <LOD      | 4.7       | 0.4       | <LOD     | 4142  | -     | -     | -         | -    | 1.72 |  |  |  |
| NBP0805                                       | DR35  | Dc-A-2c         | 0.0260          | 0.3       | 37.12  | 0.06      | <LOD      | 7.8       | 78.1      | <LOD      | 8.2       | 36.7      | 7.4       | 2.9       | 14.9      | 1.7       | 14.0      | 3.1       | 12.0      | <LOD      | 11.2      | 1.1       | <LOD      | 3329     | -     | -     | -     | -         | 2.55 |      |  |  |  |
| NBP1103                                       | DH16  | Bc-2 (up)       | 0.0334          | 1.5       | 37.74  | 0.08      | <LOD      | 10.9      | 59.6      | <LOD      | 8.0       | 38.4      | 8.5       | 2.7       | 13.3      | 1.3       | 13.5      | 2.4       | 9.1       | <LOD      | 8.2       | 0.7       | <LOD      | 4811     | -     | -     | -     | -         | 2.19 |      |  |  |  |
| NBP1103                                       | DH74  | Gc-2            | 0.0484          | <LOD      | 38.14  | 0.30      | <LOD      | 9.1       | 581.0     | 27.5      | 76.2      | 350.3     | 68.4      | 18.5      | 93.7      | 11.4      | 74.7      | 15.9      | 44.0      | 4.5       | 34.4      | 4.5       | 1.5       | 4496     | 0.03  | 1.26  | 1.05  | 1.05      | 1.50 |      |  |  |  |
| NBP0805                                       | DR35  | Dc-D4           | 0.1065          | <LOD      | 37.75  | 0.08      | <LOD      | 9.4       | 93.1      | <LOD      | 10.1      | 46.9      | 8.5       | 2.7       | 12.3      | 1.6       | 11.6      | 2.3       | 9.1       | 0.2       | 7.8       | 0.7       | <LOD      | 3467     | -     | -     | -     | -         | 1.86 |      |  |  |  |
| NBP0805                                       | DR35  | Dc-E1           | 0.7371          | <LOD      | 36.75  | 0.13      | <LOD      | 7.9       | 78.7      | <LOD      | 9.4       | 39.9      | 7.1       | 2.2       | 10.6      | 1.1       | 10.7      | 2.1       | 9.4       | <LOD      | 8.2       | 0.9       | 4.1       | 4304     | -     | -     | -     | -         | 1.86 |      |  |  |  |
| NBP0805                                       | DR38  | Dc-A1           | 0.3478          | 0.3       | 37.00  | 0.09      | <LOD      | 10.3      | 99.4      | <LOD      | 13.1      | 55.4      | 8.3       | 3.2       | 13.0      | 1.6       | 12.5      | 2.5       | 9.6       | <LOD      | 9.0       | 0.9       | <LOD      | 5181     | -     | -     | -     | -         | 1.50 |      |  |  |  |
| <b>Run 1 LOD (ng/g)</b>                       |       |                 |                 |           |        |           |           |           |           |           |           |           |           |           |           |           |           |           |           |           |           |           |           |          |       |       |       |           |      |      |  |  |  |
|   |       |                 |                 | 0.3       | -      | 0.04      | 58.0      | -         | 1.6       | 3.8       | 0.5       | 2.0       | 1.8       | 0.5       | 2.2       | 0.4       | 1.8       | 0.6       | 0.3       | 0.6       | 0.6       | 0.8       | 0.5       | 0.4      | 3.2   |       |       |           |      |      |  |  |  |
| <b>Run 2</b>                                  |       |                 |                 |           |        |           |           |           |           |           |           |           |           |           |           |           |           |           |           |           |           |           |           |          |       |       |       |           |      |      |  |  |  |
| NBP0805                                       | DR35  | Dc-D02          | 0.5604          | 0.5       | 35.31  | 0.06      | <LOD      | 1.4       | 90.9      | 6.0       | 9.7       | 43.4      | 7.7       | 3.2       | 8.8       | 1.5       | 10.6      | 2.4       | 8.6       | 2.3       | 6.1       | 0.7       | <LOD      | 3217     | 0.04  | 0.78  | 1.77  | 1.37      | 1.40 |      |  |  |  |
| NBP0805                                       | DR36  | Dc-A2           | 0.1311          | <LOD      | 36.74  | 0.08      | <LOD      | 4.5       | 131.4     | <LOD      | 15.3      | 75.5      | 12.0      | 4.8       | 19.8      | 2.4       | 18.1      | 4.1       | 13.9      | 1.6       | 9.4       | 1.1       | <LOD      | 3180     | -     | -     | -     | -         | 1.39 |      |  |  |  |
| NBP1103                                       | DH16  | Bc-2 (lp)       | 0.0418          | 9.2       | 36.93  | 0.51      | <LOD      | 11.0      | 94.5      | 4.7       | 11.2      | 52.6      | 12.3      | 3.5       | 18.6      | 2.6       | 23.5      | 4.2       | 13.9      | 1.4       | 10.1      | 0.7       | 1.4       | 3795     | 0.03  | 1.20  | 1.04  | 2.03      | 2.03 |      |  |  |  |
| NBP0805                                       | DR35  | Dc-A-2a         | 0.2039          | <LOD      | 37.00  | 0.02      | <LOD      | 5.9       | 48.2      | <LOD      | 5.1       | 23.9      | 4.4       | 1.8       | 6.8       | 0.8       | 7.0       | 1.4       | 7.2       | 0.8       | 5.8       | 0.4       | <LOD      | 3350     | -     | -     | -     | -         | 2.25 |      |  |  |  |
| NBP0805                                       | DR23  | Dc-A2           | 0.1522          | <LOD      | 36.37  | 0.18      | 0.38      | 13.8      | 554.5     | 26.2      | 75.0      | 342.8     | 61.1      | 14.8      | 67.3      | 8.6       | 52.6      | 10.7      | 30.6      | 3.2       | 22.6      | 2.4       | <LOD      | 4358     | 0.03  | 1.17  | 1.07  | 0.74      | 2.25 |      |  |  |  |
| NBP0805                                       | DR23  | Dc-A6           | 0.0447          | 0.6       | 39.43  | 0.29      | <LOD      | 10.8      | 86.0      | <LOD      | 10.0      | 58.0      | 18.9      | 9.5       | 63.4      | 9.6       | 75.4      | 19.1      | 63.2      | 8.2       | 52.4      | 7.9       | <LOD      | 3619     | -     | -     | -     | -         | 9.94 |      |  |  |  |
| NBP1103                                       | DH117 | Dc-29           | 0.7930          | <LOD      | 37.36  | 0.11      | <LOD      | 9.4       | 105.9     | <LOD      | 12.8      | 60.9      | 11.3      | 3.3       | 13.4      | 2.0       | 15.4      | 2.7       | 12.3      | 1.3       | 10.3      | 1.1       | <LOD      | 3541     | -     | -     | -     | -         | 1.69 |      |  |  |  |
| NBP0805                                       | DR35  | Dc-A1           | 0.0667          | <LOD      | 37.04  | <LOD      | <LOD      | 9.2       | 10.6      | <LOD      | 0.9       | 4.7       | <LOD      | <LOD     | <LOD  | <LOD  | <LOD  | <LOD      | 4.29 |      |  |  |  |
| NBP0805                                       | TB04  | Dn-A10          | 0.1082          | 8.1       | 38.39  | 0.39      | <LOD      | 33.1      | 128.1     | 18.6      | 15.8      | 77.4      | 17.0      | 6.8       | 40.1      | 5.9       | 43.4      | 10.2      | 35.4      | 4.5       | 28.6      | 3.7       | 0.7       | 2681     | 0.09  | 1.24  | 1.07  | 3.87      | 3.87 |      |  |  |  |
| <b>Run 2 LOD (ng/g)</b>                       |       |                 |                 |           |        |           |           |           |           |           |           |           |           |           |           |           |           |           |           |           |           |           |           |          |       |       |       |           |      |      |  |  |  |
|   |       |                 |                 | 0.2       | -      | 0.06      | 0.09      | -         | 1.46      | 3.46      | 0.43      | 1.80      | 1.63      | 0.49      | 2.02      | 0.33      | 1.65      | 0.52      | 0.66      | 0.52      | 0.71      | 0.46      | 0.40      | 2.92     |       |       |       |           |      |      |  |  |  |
| <b>Reproducibility of reference materials</b> |       |                 |                 |           |        |           |           |           |           |           |           |           |           |           |           |           |           |           |           |           |           |           |           |          |       |       |       |           |      |      |  |  |  |
| <b>Coral standard</b>                         |       |                 |                 |           |        |           |           |           |           |           |           |           |           |           |           |           |           |           |           |           |           |           |           |          |       |       |       |           |      |      |  |  |  |
| average                                       |       |                 | 14.0            | 20.7      | 0.57   | 0.66      | 24.2      | 447.3     | 88.2      | 56.9      | 248.5     | 32.9      | 6.6       | 31.0      | 3.2       | 19.4      | 3.8       | 11.7      | 1.1       | 8.9       | 1.1       | 8.9       | 1.1       | 3.9      | 2014  |       |       |           |      |      |  |  |  |
| RSD   |       |                 | 2.7             | 1.4       | 0.05   | 0.18      | 3.2       | 16.9      | 3.2       | 1.6       | 6.8       | 2.0       | 0.5       | 2.1       | 0.2       | 1.3       | 0.3       | 0.8       | 0.3       | 0.8       | 0.3       | 1.0       | 0.1       | 0.6      | 88    |       |       |           |      |      |  |  |  |
| RSD (%)                                       |       |                 | 20              | 7         | 8      | 2.7       | 13        | 3.8       | 3.6       | 2.8       | 2.7       | 6.0       | 8.0       | 6.9       | 5.7       | 6.7       | 7.8       | 6.5       | 30.5      | 11.4      | 11.8      | 14.5      | 4.4       | 4.4      | 4.4   |       |       |           |      |      |  |  |  |
| <b>JLS-1</b>                                  |       |                 |                 |           |        |           |           |           |           |           |           |           |           |           |           |           |           |           |           |           |           |           |           |          |       |       |       |           |      |      |  |  |  |
| average                                       |       |                 | 67.8            | 33.7      | 1.90   | 13.01     | 85.7      | 82.1      | 137.5     | 18.9      | 76.1      | 17.3      | 23.6      | 20.2      | 2.6       | 17.4      | 2.9       | 11.3      | 1.7       | 10.9      | 1.5       | 15.0      | 1356      |          |       |       |       |           |      |      |  |  |  |
| RSD   |       |                 | 2.3             | 0.9       | 1.17   | 0.86      | 3.3       | 2.7       | 5.9       | 0.7       | 2.5       | 2.1       | 1.3       | 1.2       | 0.4       | 0.8       | 0.2       | 0.8       | 0.2       | 0.8       | 0.2       | 0.9       | 0.2       | 1.9      | 24.3  |       |       |           |      |      |  |  |  |
| RSD (%)                                       |       |                 | 3               | 3         | 16.2   | 7         | 4         | 3.3       | 4.3       | 3.7       | 3.4       | 12.4      | 5.4       | 6.0       | 15.3      | 4.8       | 6.3       | 6.9       | 13.0      | 8.4       | 15.8      | 12.6      | 1.8       | 1.8      | 1.8   |       |       |           |      |      |  |  |  |
| <b>BCR-2</b>                                  |       |                 |                 |           |        |           |           |           |           |           |           |           |           |           |           |           |           |           |           |           |           |           |           |          |       |       |       |           |      |      |  |  |  |
| average                                       |       |                 | 5.7             | 4.9       | 1.2    | 0.2       | 11.0      | 25.0      | 53.6      | 6.8       | 28.7      | 6.6       | 2.0       | 7.0       | 1.0       | 6.4       | 1.3       | 3.8       | 0.5       | 3.5       | 0.5       | 3.5       | 0.5       | 6.6      | 1.2   |       |       |           |      |      |  |  |  |
| RSD   |       |                 | 1.1             | 0.5       | 0.1    | 0.1       | 5.6       | 0.9       | 1.9       | 0.3       | 0.8       | 0.2       | 0.1       | 0.2       | 0.04      | 0.3       | 0.04      | 0.2       | 0.01      | 0.1       | 0.04      | 0.5       | 0.2       | 0.2      | 0.2   |       |       |           |      |      |  |  |  |
| RSD (%)                                       |       |                 | 20              | 9         | 12     | 53        | 51        | 3         | 4         | 4         | 3         | 3         | 5         | 3         | 4         | 5         | 3         | 4         | 3         | 4         | 3         | 2         | 7         | 8        | 16    |       |       |           |      |      |  |  |  |

**Table 3.5:** Major and trace element data for 17 deep-sea coral samples from the Drake Passage analysed by ICP-MS at the Open University. All results were obtained on digests of resampled pieces of original corals, including two modern specimen (*italic*) and 14 fossil ones. One fossil specimen was resampled twice at the top and lower section, denoted “up” (upper part) and “lp” (lower part), respectively. Ce, Gd, and Eu nomalies and HREE/LREE ratios were calculated from PAAS-normalised results (see caption Table 3.3). Results were obtained during two analytical sessions comprising two runs each. During the first session Al, Ca, Ti, Mn and Fe were analysed at 1000 ppm Ca level. The rare earth elements, thorium and uranium were analysed at 2000 ppm Ca level during the second analytical session. LOD denotes the limit of detection calculated for each particular run during the respective analytical session. The reproducibility of our in house coral standard, and USGS standards JLS-1 and BCR-2 are reported to assess reproducibility. JLS-1 was only analysed at 1000 ppm Ca level. Note that one outlier in the Ti results was omitted for RSD calculations on JLS-1. Coral species: All samples names starting with a ‘D’ and ‘Big Beauty’ are *D. dianthus*, ‘B’ stands for *Balanophyllia*, and ‘G’ is an abbreviation for *Gardeneria*.

Table 3.6: Nd concentration results from U-Th dating chemistry cuts. See Table caption for details.

| Cruise  | Event | Sample               | Species            | Location | Lat     | Long    | Depth (m) | Sample mass (g) | <sup>238</sup> U (ng/g) | <sup>232</sup> Th (pg/g) | ZSE <sup>a</sup> | $\delta^{234}\text{U}$ | ZSE  | Nd <sub>total</sub> (ng/g) | ZSE (ep) <sup>b</sup> |
|---------|-------|----------------------|--------------------|----------|---------|---------|-----------|-----------------|-------------------------|--------------------------|------------------|------------------------|------|----------------------------|-----------------------|
| NBP0805 | T804  | Dn-A-12              | <i>D. dianthus</i> | B. Bank  | -54.734 | -62.216 | 816       | 0.5804          | 3126                    | 10                       | 3237.4           | 149.6                  | 12.8 | ≥ 98.1                     | 0.0011                |
| NBP0805 | T804  | Dn-A-11              | <i>D. dianthus</i> | B. Bank  | -54.734 | -62.216 | 816       | 0.6110          | 3646                    | 12                       | 784.5            | 149.2                  | 2.9  | ≥ 87.9                     | 0.0013                |
| NBP0805 | T804  | Dn-A-13              | <i>D. dianthus</i> | B. Bank  | -54.734 | -62.216 | 816       | 0.6351          | 3921                    | 13                       | 175.4            | 149.4                  | 3.2  | ≥ 9.3                      | 0.0002                |
| NBP0805 | T804  | Dn-D-6               | <i>D. dianthus</i> | B. Bank  | -54.734 | -62.216 | 816       | 0.6664          | 3744                    | 12                       | 185.9            | 153.3                  | 1.1  | ≥ 24.3                     | 0.0002                |
| NBP0805 | T804  | Dn-B-4               | <i>D. dianthus</i> | B. Bank  | -54.734 | -62.216 | 816       | 0.6357          | 3920                    | 13                       | 629.2            | 153.1                  | 3.3  | ≥ 45.6                     | 0.0006                |
| NBP0805 | T804  | Dn-E-3               | <i>D. dianthus</i> | B. Bank  | -54.734 | -62.216 | 816       | 0.7319          | 4727                    | 16                       | 181.3            | 148.1                  | 5.5  | ≥ 10.1                     | 0.0001                |
| NBP0805 | T804  | Dn-A-10a             | <i>D. dianthus</i> | B. Bank  | -54.734 | -62.216 | 816       | 0.3377          | 3125                    | 10                       | 1217.6           | 155.5                  | 6.1  | ≥ 50.1                     | 0.0004                |
| NBP0805 | T804  | Dn-A-10b*            | <i>D. dianthus</i> | B. Bank  | -54.734 | -62.216 | 816       | 0.6317          | 3112                    | 10                       | 736.8            | 157.7                  | 2.5  | ≥ 39.2                     | 0.0002                |
| NBP0805 | DR40  | Dc-A-1               | <i>D. dianthus</i> | Sars     | -59.732 | -68.933 | 1323      | 0.7697          | 3680                    | 11                       | 251.8            | 145.1                  | 1.8  | ≥ 57.2                     | 0.0008                |
| NBP0805 | DR35  | Dc-A-1a              | <i>D. dianthus</i> | Sars     | -59.723 | -68.881 | 695       | 1.1426          | 3723                    | 14                       | 120.3            | 146.0                  | 1.5  | ≥ 10.9                     | 0.0001                |
| NBP0805 | DR35  | Dc-A-1b              | <i>D. dianthus</i> | Sars     | -59.723 | -68.881 | 695       | 1.1126          | 4163                    | 27                       | 159.1            | 145.8                  | 1.3  | ≥ 23.8                     | 0.0002                |
| NBP0805 | DR34  | Dc-A-2               | <i>D. dianthus</i> | Sars     | -59.733 | -68.743 | 869       | 1.0447          | 4089                    | 22                       | 232.6            | 149.4                  | 1.1  | ≥ 90.2                     | 0.0060                |
| NBP0805 | DR34  | Dc-A-1               | <i>D. dianthus</i> | Sars     | -59.733 | -68.881 | 869       | 0.6169          | 3875                    | 12                       | 313.4            | 150.9                  | 1.3  | ≥ 75.9                     | 0.0013                |
| NBP0805 | DR35  | Dc-C-2               | <i>D. dianthus</i> | Sars     | -59.723 | -68.881 | 695       | 1.1910          | 4191                    | 19                       | 183.6            | 153.3                  | 1.0  | ≥ 15.3                     | 0.0002                |
| NBP0805 | DR35  | Dc-D-4               | <i>D. dianthus</i> | Sars     | -59.723 | -68.881 | 695       | 0.5816          | 4062                    | 13                       | 224.0            | 150.5                  | 1.2  | ≥ 36.0                     | 0.0004                |
| NBP0805 | DR35  | Dc-D-5               | <i>D. dianthus</i> | Sars     | -59.723 | -68.881 | 695       | 0.6451          | 3918                    | 14                       | 323.1            | 150.6                  | 4.4  | ≥ 47.0                     | 0.0005                |
| NBP0805 | DR36  | Dc-A-1               | <i>D. dianthus</i> | Sars     | -59.707 | -69.008 | 1750      | 0.7086          | 4057                    | 13                       | 206.7            | 150.5                  | 2.3  | ≥ 38.9                     | 0.0004                |
| NBP0805 | DR35  | Dc-D-1               | <i>D. dianthus</i> | Sars     | -59.723 | -68.881 | 695       | 0.6187          | 4506                    | 16                       | 157.4            | 149.3                  | 8.4  | ≥ 27.3                     | 0.0003                |
| NBP0805 | DR35  | Dc-D-3               | <i>D. dianthus</i> | Sars     | -59.723 | -68.881 | 695       | 0.5463          | 4312                    | 14                       | 226.2            | 148.6                  | 7.9  | ≥ 39.7                     | 0.0003                |
| NBP0805 | DR35  | Dc-B-1a              | <i>D. dianthus</i> | Sars     | -59.723 | -68.881 | 695       | 0.9327          | 5852                    | 21                       | 334.8            | 147.8                  | 2.4  | ≥ 22.5                     | 0.0002                |
| NBP0805 | DR35  | Dc-B-1b              | <i>D. dianthus</i> | Sars     | -59.723 | -68.881 | 695       | 0.5730          | 4713                    | 16                       | 393.5            | 147.3                  | 4.7  | ≥ 44.6                     | 0.0004                |
| NBP0805 | DR35  | Dc-A-2c*             | <i>D. dianthus</i> | Sars     | -59.723 | -68.881 | 695       | 1.0374          | 3887                    | 14                       | 551.3            | 149.9                  | 1.8  | ≥ 91.4                     | 0.0023                |
| NBP0805 | DR35  | Dc-C-1a              | <i>D. dianthus</i> | Sars     | -59.723 | -68.881 | 695       | 0.6913          | 4259                    | 14                       | 302.3            | 148.3                  | 1.9  | ≥ 28.1                     | 0.0002                |
| NBP0805 | DR35  | Dc-C-1b*             | <i>D. dianthus</i> | Sars     | -59.723 | -68.881 | 695       | 0.8933          | 4427                    | 16                       | 303.5            | 147.2                  | 1.4  | ≥ 23.1                     | 0.0002                |
| NBP0805 | DR39  | Dc-A-1               | <i>D. dianthus</i> | Sars     | -59.729 | -68.901 | 798       | 0.8002          | 6545                    | 27                       | 1040.0           | 147.3                  | 3.6  | ≥ 53.1                     | 0.0005                |
| NBP0805 | DR38  | Dc-A-1               | <i>D. dianthus</i> | Sars     | -59.743 | -68.898 | 978       | 0.6612          | 6026                    | 22                       | 916.0            | 146.2                  | 3.4  | ≥ 51.1                     | 0.0007                |
| NBP0805 | DR35  | Dc-E-1a              | <i>D. dianthus</i> | Sars     | -59.723 | -68.881 | 695       | 0.5033          | 4234                    | 14                       | 788.1            | 150.4                  | 3.2  | ≥ 76.1                     | 0.0008                |
| NBP0805 | DR35  | Dc-E-1b*             | <i>D. dianthus</i> | Sars     | -59.723 | -68.881 | 695       | 0.6319          | 4949                    | 17                       | 649.7            | 147.3                  | 2.5  | ≥ 38.2                     | 0.0004                |
| NBP0805 | DR35  | Dc-E-1c <sup>#</sup> | <i>D. dianthus</i> | Sars     | -59.723 | -68.881 | 695       | 0.7371          | -                       | -                        | -                | -                      | -    | ≥ 42.4                     | 0.0003                |
| NBP0805 | DR36  | Dc-A-2a              | <i>D. dianthus</i> | Sars     | -59.707 | -69.008 | 1750      | 0.7749          | 3828                    | 13                       | 349.9            | 150.0                  | 1.6  | ≥ 73.5                     | 0.0015                |
| NBP0805 | DR36  | Dc-A-2b <sup>#</sup> | <i>D. dianthus</i> | Sars     | -59.707 | -69.008 | 1750      | 0.1311          | -                       | -                        | -                | -                      | -    | ≥ 80.4                     | 0.0010                |
| NBP1103 | DH120 | Dc-25                | <i>D. dianthus</i> | Sars     | -59.797 | -68.965 | 1701      | 0.3520          | 3756                    | 7                        | 508.5            | 148.3                  | 2.1  | ≥ 96.1                     | 0.0004                |
| NBP0805 | DR36  | Dc-A-3               | <i>D. dianthus</i> | Sars     | -59.707 | -69.008 | 1750      | 0.6101          | 4116                    | 13                       | 472.3            | 148.4                  | 2.1  | ≥ 138.6                    | 0.0042                |

Table 3.6 (continued)

| Cruise         | Event        | Sample                    | Species                   | Location    | Lat            | Long           | Depth (m)   | Sample mass (g) | <sup>238</sup> U (ng/g) | ZSE <sup>1</sup> | <sup>232</sup> Th (pg/g) | ZSE         | $\delta^{234}\text{U}_i$ | ZSE        | Nd <sub>coral</sub> (ng/g) | ZSE (ep) <sup>b</sup> |
|----------------|--------------|---------------------------|---------------------------|-------------|----------------|----------------|-------------|-----------------|-------------------------|------------------|--------------------------|-------------|--------------------------|------------|----------------------------|-----------------------|
| NBP1103        | DH120        | Dn-1a                     | <i>D. dianthus</i>        | Sars        | -59.797        | -68.965        | 1701        | 0.3040          | 5022                    | 9                | 709.7                    | 3.0         | 147.6                    | 0.4        | ≥ 145.5                    | 0.0006                |
| <b>NBP1103</b> | <b>DH120</b> | <b>Dn-1b</b>              | <b><i>D. dianthus</i></b> | <b>Sars</b> | <b>-59.797</b> | <b>-68.965</b> | <b>1701</b> | <b>0.2765</b>   | <b>5071</b>             | <b>9</b>         | <b>753.1</b>             | <b>3.1</b>  | <b>148.0</b>             | <b>0.4</b> | <b>≥ 147.6</b>             | <b>0.0006</b>         |
| NBP1103        | DH120        | Dc-33                     | <i>D. dianthus</i>        | Sars        | -59.797        | -68.965        | 1701        | 0.1843          | 4260                    | 12               | 429.9                    | 2.1         | 146.0                    | 4.7        | ≥ 133.2                    | 0.0006                |
| NBP1103        | DH120        | Dc-21a                    | <i>D. dianthus</i>        | Sars        | -59.797        | -68.965        | 1701        | 0.2007          | 4046                    | 7                | 455.9                    | 1.9         | 149.1                    | 0.4        | ≥ 129.9                    | 0.0007                |
| <b>NBP1103</b> | <b>DH120</b> | <b>Dc-21b</b>             | <b><i>D. dianthus</i></b> | <b>Sars</b> | <b>-59.797</b> | <b>-68.965</b> | <b>1701</b> | <b>0.2246</b>   | <b>4054</b>             | <b>7</b>         | <b>494.5</b>             | <b>2.1</b>  | <b>148.7</b>             | <b>0.4</b> | <b>≥ 129.8</b>             | <b>0.0006</b>         |
| NBP1103        | DH117        | Dn-7                      | <i>D. dianthus</i>        | Sars        | -59.764        | -68.936        | 981         | 0.2727          | 3659                    | 10               | 362.9                    | 1.7         | 152.0                    | 4.7        | ≥ 114.8                    | 0.0004                |
| NBP1103        | DH117        | Dc-20                     | <i>D. dianthus</i>        | Sars        | -59.764        | -68.936        | 981         | 0.3099          | 3473                    | 6                | 1041.4                   | 4.3         | 152.0                    | 0.5        | ≥ 263.1                    | 0.0019                |
| NBP1103        | DH117        | Dc-29a                    | <i>D. dianthus</i>        | Sars        | -59.764        | -68.936        | 981         | 0.4441          | 4196                    | 10               | 305.1                    | 1.4         | 151.2                    | 4.3        | ≥ 29.5                     | 0.0003                |
| <b>NBP1103</b> | <b>DH117</b> | <b>Dc-29b<sup>#</sup></b> | <b><i>D. dianthus</i></b> | <b>Sars</b> | <b>-59.764</b> | <b>-68.936</b> | <b>981</b>  | <b>0.7930</b>   | -                       | -                | -                        | -           | -                        | -          | <b>≥ 61.8</b>              | <b>0.0003</b>         |
| NBP0805        | DR35         | Dc-A-2a <sup>+</sup>      | <i>D. dianthus</i>        | Sars        | -59.723        | -68.881        | 695         | 0.4737          | 4761                    | 16               | 376.7                    | 6.8         | 148.1                    | 0.7        | ≥ 53.7                     | 0.0005                |
| NBP0805        | DR35         | Dc-D-2                    | <i>D. dianthus</i>        | Sars        | -59.723        | -68.881        | 695         | 0.1780          | 3743                    | 13               | 159.9                    | 6.7         | 227.6                    | 3.2        | ≥ 38.1                     | 0.0012                |
| NBP1103        | DH120        | Dc-32                     | <i>D. dianthus</i>        | Sars        | -59.797        | -68.965        | 1701        | 0.3711          | 3976                    | 7                | 537.9                    | 2.3         | 147.7                    | 0.4        | ≥ 164.5                    | 0.0011                |
| NBP1103        | DH117        | Dc-36                     | <i>D. dianthus</i>        | Sars        | -59.764        | -68.936        | 981         | 0.1498          | 3673                    | 11               | 259.7                    | 1.4         | 153.9                    | 4.6        | ≥ 43.7                     | 0.0007                |
| NBP1103        | DH117        | Dc-9a                     | <i>D. dianthus</i>        | Sars        | -59.764        | -68.936        | 981         | 0.1900          | 4729                    | 13               | 1773.4                   | 8.2         | 146.5                    | 4.5        | ≥ 118.5                    | 0.0007                |
| <b>NBP1103</b> | <b>DH117</b> | <b>Dc-9b</b>              | <b><i>D. dianthus</i></b> | <b>Sars</b> | <b>-59.764</b> | <b>-68.936</b> | <b>981</b>  | <b>0.2493</b>   | <b>4695</b>             | <b>8</b>         | <b>2027.5</b>            | <b>8.4</b>  | <b>147.4</b>             | <b>0.5</b> | <b>≥ 274.8</b>             | <b>0.0012</b>         |
| NBP1103        | DH74         | Dc-3                      | <i>D. dianthus</i>        | Interim     | -60.606        | -66.004        | 1064        | 0.1546          | 3820                    | 12               | 949.7                    | 4.5         | 151.4                    | 4.8        | ≥ 124.5                    | 0.0014                |
| NBP1103        | DH75         | Dc(f)-37                  | <i>D. dianthus</i>        | Interim     | -60.601        | -66.002        | 1195.5      | 0.1120          | 4354                    | 8                | 668.4                    | 2.9         | 148.3                    | 0.4        | ≥ 244.8                    | 0.0009                |
| NBP1103        | DH74         | Dc-4                      | <i>D. dianthus</i>        | Interim     | -60.606        | -66.004        | 1064        | 0.2133          | 4158                    | 7                | 1878.7                   | 7.8         | 155.5                    | 0.6        | ≥ 304.7                    | 0.0010                |
| NBP0805        | DR27         | Dc-A-1                    | <i>D. dianthus</i>        | Interim     | -60.547        | -65.949        | 1134        | 0.2010          | 5919                    | 19               | 1452.8                   | 11.4        | 144.3                    | 0.8        | ≥ 261.3                    | 0.0007                |
| NBP0805        | DR27         | Dc-A-2                    | <i>D. dianthus</i>        | Interim     | -60.547        | -65.949        | 1134        | 0.1737          | 5338                    | 17               | 1900.4                   | 6.4         | 148.1                    | 1.0        | ≥ 317.7                    | 0.0006                |
| NBP0805        | DR23         | Dc-A-6                    | <i>D. dianthus</i>        | SFZ         | -60.182        | -57.834        | 819         | 0.2241          | 4060                    | 13               | 349.6                    | 4.0         | 153.2                    | 0.7        | ≥ 48.3                     | 0.0007                |
| NBP0805        | DR23         | Dc-A-5                    | <i>D. dianthus</i>        | SFZ         | -60.182        | -57.834        | 819         | 0.2959          | 3388                    | 11               | 625.2                    | 2.5         | 146.4                    | 0.7        | ≥ 81.8                     | 0.0013                |
| NBP0805        | DR23         | Dc-A-7                    | <i>D. dianthus</i>        | SFZ         | -60.182        | -57.834        | 819         | 0.3702          | 4183                    | 14               | 602.9                    | 2.4         | 149.1                    | 0.7        | ≥ 128.3                    | 0.0055                |
| NBP1103        | DH40         | Dc-3a                     | <i>D. dianthus</i>        | SFZ         | -60.179        | -57.837        | 806         | 0.1034          | 3671                    | 12               | 1346.2                   | 6.6         | 150.0                    | 4.6        | ≥ 151.2                    | 0.0015                |
| <b>NBP1103</b> | <b>DH40</b>  | <b>Dc-3b</b>              | <b><i>D. dianthus</i></b> | <b>SFZ</b>  | <b>-60.179</b> | <b>-57.837</b> | <b>806</b>  | <b>0.0850</b>   | <b>3654</b>             | <b>7</b>         | <b>2871.3</b>            | <b>11.9</b> | <b>148.8</b>             | <b>0.6</b> | <b>≥ 430.9</b>             | <b>0.0016</b>         |
| NBP1103        | DH43         | Dc-6                      | <i>D. dianthus</i>        | SFZ         | -60.182        | -57.833        | 823         | 0.1130          | 3337                    | 11               | 1361.9                   | 6.7         | 143.5                    | 4.8        | ≥ 145.6                    | 0.0016                |
| NBP0805        | DR23         | Dc-A-4                    | <i>D. dianthus</i>        | SFZ         | -60.182        | -57.834        | 819         | 0.0798          | 3527                    | 12               | 1499.3                   | 9.2         | 143.9                    | 0.8        | ≥ 279.0                    | 0.0021                |
| NBP1103        | DH43         | Dc-1                      | <i>D. dianthus</i>        | SFZ         | -60.182        | -57.833        | 823         | 0.1409          | 5679                    | 11               | 162.2                    | 1.8         | 144.6                    | 0.4        | ≥ 65.3                     | 0.0009                |
| NBP1103        | DH40         | Dc-5                      | <i>D. dianthus</i>        | SFZ         | -60.179        | -57.837        | 806         | 0.2593          | 2990                    | 6                | 382.6                    | 1.6         | 144.9                    | 0.5        | ≥ 48.6                     | 0.0005                |
| NBP1103        | DH43         | Dc-8a                     | <i>D. dianthus</i>        | SFZ         | -60.182        | -57.833        | 823         | 0.2499          | 4069                    | 8                | 6416.5                   | 27.4        | 149.3                    | 0.9        | ≥ 393.6                    | 0.0025                |
| <b>NBP1103</b> | <b>DH43</b>  | <b>Dc-8b</b>              | <b><i>D. dianthus</i></b> | <b>SFZ</b>  | <b>-60.182</b> | <b>-57.833</b> | <b>823</b>  | <b>0.1292</b>   | <b>4122</b>             | <b>16</b>        | <b>705.6</b>             | <b>3.5</b>  | <b>150.7</b>             | <b>6.2</b> | <b>≥ 49.3</b>              | <b>0.0010</b>         |
| NBP0805        | DR23         | Dc-A-1a                   | <i>D. dianthus</i>        | SFZ         | -60.182        | -57.834        | 819         | 0.4995          | 4055                    | 13               | 1555.0                   | 5.4         | 144.5                    | 0.8        | ≥ 75.6                     | 0.0044                |
| <b>NBP0805</b> | <b>DR23</b>  | <b>Dc-A-1b</b>            | <b><i>D. dianthus</i></b> | <b>SFZ</b>  | <b>-60.182</b> | <b>-57.834</b> | <b>819</b>  | <b>0.8263</b>   | <b>4385</b>             | <b>16</b>        | <b>2917.0</b>            | <b>9.2</b>  | <b>141.5</b>             | <b>1.0</b> | <b>≥ 117.2</b>             | <b>0.0034</b>         |

Table 3.6 (continued)

| Cruise         | Event       | Sample       | Species                         | Location       | Lat            | Long           | Depth (m)    | Sample mass (g) | $^{238}\text{U}$ (ng/g) | $^{232}\text{Th}$ (pg/g) | 2SE         | $\delta^{234}\text{U}$ | 2SE        | $\text{Nd}_{\text{coral}}$ (ng/g) | 2SE (ep) <sup>b</sup> |
|----------------|-------------|--------------|---------------------------------|----------------|----------------|----------------|--------------|-----------------|-------------------------|--------------------------|-------------|------------------------|------------|-----------------------------------|-----------------------|
| NBP1103        | DH43        | Dc-3         | <i>D. dianthus</i>              | SFZ            | -60.182        | -57.833        | 823          | 0.3599          | 3208                    | 789.8                    | 3.3         | 146.7                  | 0.5        | $\geq 55.8$                       | 0.0004                |
| NBP0805        | DR23        | Dc-A-2       | <i>D. dianthus</i>              | SFZ            | -60.182        | -57.834        | 819          | 0.4319          | 4921                    | 1032.9                   | 3.6         | 148.8                  | 0.8        | $\geq 240.6$                      | 0.0060                |
| NBP0805        | DR23        | Dc-A-3       | <i>D. dianthus</i>              | SFZ            | -60.182        | -57.834        | 819          | 0.3797          | 3472                    | 11009.8                  | 3.5         | 149.5                  | 0.8        | $\geq 136.2$                      | 0.0100                |
| LMG06-05       | 9           | 3            | <i>F. curvatum</i>              | B. Bank        | -54.485        | -62.214        | 318          | 0.5807          | 3533                    | 21.8                     | 2.6         | 148.4                  | 0.8        | $\geq 7.3$                        | 0.0002                |
| NBP1103        | DH19        | Fc-1         | <i>F. curvatum</i>              | B. Bank        | -54.809        | -62.166        | 1515.5       | 0.4253          | 2799                    | 994.2                    | 4.3         | 148.6                  | 0.5        | $\geq 35.4$                       | 0.0003                |
| NBP1103        | DH14        | Fc-277       | <i>F. curvatum</i>              | B. Bank        | -54.713        | -62.250        | 726.5        | 0.3011          | 4070                    | 682.8                    | 3.0         | 146.7                  | 0.5        | $\geq 88.8$                       | 0.0005                |
| NBP1103        | DH16        | Bc-9         | <i>B. malouinensis</i>          | B. Bank        | -54.808        | -62.119        | 1418.5       | 0.3487          | 3748                    | 2149.2                   | 9.2         | 148.4                  | 0.6        | $\geq 292.6$                      | 0.0032                |
| NBP1103        | DH14        | Bn-278       | <i>B. malouinensis</i>          | B. Bank        | -54.713        | -62.250        | 726.5        | 0.3761          | 4050                    | 481.8                    | 2.0         | 149.3                  | 0.5        | $\geq 37.8$                       | 0.0004                |
| LMG06-05       | 9           | 1            | <i>B. malouinensis</i>          | B. Bank        | -54.485        | -62.214        | 318          | 0.0921          | 3683                    | 108.1                    | 19.4        | 151.2                  | 0.7        | $\geq 12.5$                       | 0.0014                |
| NBP1103        | DH07        | Bn-2         | <i>B. malouinensis</i>          | B. Bank        | -54.507        | -62.228        | 328.5        | 0.4108          | 4485                    | 287.0                    | 1.3         | 146.5                  | 0.4        | $\geq 13.9$                       | 0.0003                |
| NBP1103        | DH16        | Bc-2         | <i>B. malouinensis</i>          | B. Bank        | -54.808        | -62.119        | 1418.5       | 0.1493          | 4611                    | 552.2                    | 3.6         | 147.4                  | 4.9        | $\geq 36.5$                       | 0.0009                |
| NBP1103        | DH14        | Bc-1002      | <i>B. malouinensis</i>          | B. Bank        | -54.713        | -62.250        | 726.5        | 0.1191          | 4375                    | 1240.7                   | 5.4         | 148.1                  | 0.5        | $\geq 122.0$                      | 0.0011                |
| NBP1103        | DH07        | Bn-3         | <i>B. malouinensis</i>          | B. Bank        | -54.507        | -62.228        | 328.5        | 0.3236          | 4019                    | 422.3                    | 1.9         | 147.6                  | 0.5        | $\geq 24.7$                       | 0.0004                |
| NBP1103        | DH15        | Bc-1         | <i>B. malouinensis</i>          | B. Bank        | -54.772        | -62.236        | 894          | 0.0899          | 5988                    | 1187.9                   | 5.3         | 145.0                  | 0.5        | $\geq 104.4$                      | 0.0014                |
| NBP1103        | DH88        | Cc-1a        | <i>Caryophyllia spp.</i>        | Interim        | -60.560        | -65.957        | 982.5        | 0.2130          | 3330                    | 431.6                    | 1.9         | 148.5                  | 0.5        | $\geq 90.0$                       | 0.0005                |
| <b>NBP1103</b> | <b>DH88</b> | <b>Cc-1b</b> | <b><i>Caryophyllia spp.</i></b> | <b>Interim</b> | <b>-60.560</b> | <b>-65.957</b> | <b>982.5</b> | <b>0.1691</b>   | <b>3357</b>             | <b>603.3</b>             | <b>2.7</b>  | <b>151.4</b>           | <b>0.5</b> | <b><math>\geq 152.1</math></b>    | <b>0.0006</b>         |
| NBP1103        | DH88        | Cc-1c        | <i>Caryophyllia spp.</i>        | Interim        | -60.560        | -65.957        | 982.5        | 0.0703          | 3620                    | 440.3                    | 2.7         | 144.6                  | 4.4        | $\geq 28.5$                       | 0.0019                |
| NBP1103        | DH75        | Gc-4         | <i>Gardineria</i>               | Interim        | -60.601        | -66.002        | 1195.5       | 0.0940          | 6064                    | 562.7                    | 2.7         | 147.0                  | 0.4        | $\geq 118.3$                      | 0.0011                |
| NBP1103        | DH75        | Gc-3         | <i>Gardineria</i>               | Interim        | -60.601        | -66.002        | 1195.5       | 0.1664          | 5169                    | 1046.4                   | 4.5         | 145.6                  | 0.5        | $\geq 256.7$                      | 0.0007                |
| NBP1103        | DH74        | Gc-2a        | <i>Gardineria</i>               | Interim        | -60.606        | -66.004        | 1064         | 0.1234          | 4598                    | 3495.8                   | 14.7        | 150.3                  | 0.6        | $\geq 964.5$                      | 0.0054                |
| <b>NBP1103</b> | <b>DH74</b> | <b>Gc-2b</b> | <b><i>Gardineria</i></b>        | <b>Interim</b> | <b>-60.606</b> | <b>-66.004</b> | <b>1064</b>  | <b>0.1058</b>   | <b>4129</b>             | <b>12</b>                | <b>12.6</b> | <b>150.8</b>           | <b>4.3</b> | <b><math>\geq 716.7</math></b>    | <b>0.0249</b>         |

(a) 2SE is the analytical 2 $\sigma$  standard error.(b) 2SE (ep) is the propagated 2  $\sigma$  standard error of Nd concentrations determined by isotope dilution.

**Table 3.6:** Nd concentration results from U-Th dating chemistry cuts for 71 fossil deep-sea corals and 16 re-sampled replicates processed through combined U-Th-Nd chemistry collected from the Drake Passage during cruises NBP0805, NPB1103 and LMG06-05. Samples grouped by species and location. All U and Th results are taken from Burke and Robinson (2012), Chen et al. (2015) and Burke et al. (unpubl. data) and reported here for completeness. Closed U<sub>argonite</sub> system behaviour can be monitored with initial  $\delta^{234}\text{U}_{\text{coral}}$  reflecting the value of ambient seawater, i.e.  $147 \pm 7\%$  for corals younger than 17 kyr BP and  $141.7 \pm 7.8\%$  for corals older than 17 kyr BP (Edwards et al., 1987; Robinson et al., 2006; Reimer et al., 2009). Neodymium concentration results were obtained by spiking after U-Th column chemistry and represent minimum concentrations (see caption of Table 3.4). Replicate samples are highlighted in bold font:

(\*) replicates carried out on two aliquots from poorly homogenised source sample (see text), remaining replicates are re-sampled pieces of the same coral processed through combined U-Th-Nd chemistry.

(#) re-sampled samples analysed for Nd isotopes only, and hence yielded accurate Nd concentrations, but lack U-Th age.

(+) analyses of two corals, one grown on top of the other so that IDs are widely similar.

### 3.5. Discussion

#### 3.5.1. Calibration of modern deep-sea corals against ambient seawater

##### 3.5.1.1. Drake Passage seawater data

Our new seawater data from the Drake Passage confirm that the vertical water column seems well mixed in terms of its Nd isotopic composition, as was pointed out by Stichel et al. (2012) and Piepgras and Wasserburg (1982) (Fig. 3.5). Despite the proximity of CTD stations to the continental margin and topographic features such as seamounts and fracture zones (Fig. 3.2), no indication of boundary exchange processes (Lacan and Jeandel, 2005a) can be detected, even though concentration data would be necessary to evaluate potential influence from seafloor sediments on bottom water signatures. A detailed comparison with the data presented by Stichel et al. (2012) (Fig. 3.5) reveals that there are some discrepancies in waters below 3000 m east of the Shackleton Fracture Zone and at Sars Seamount. Our data show slightly more radiogenic average values of  $\epsilon_{\text{Nd}} = -7.7$  ( $n = 7$ ; Fig. 3.5), whereas Stichel et al. (2012) found less radiogenic Nd isotopic compositions of  $\sim -9.0$ . Stichel et al. (2012) ascribed such unradiogenic values to episodic presence of deep and bottom waters from the nearby Weddel Shelf (Stichel et al., 2012: WSBW/AABW  $\epsilon_{\text{Nd}} \approx -9.1$ ). During NBP0805 a sharp drop in temperature and salinity paired with an increase in oxygen between 3200 and 3500 m water depth was observed at SFZ (Dalziel, 2015) indicating a water mass boundary towards the bottom, a hydrographic feature which is less pronounced near Sars seamount (Dalziel, 2015). This boundary may be caused by the presence of AABW known to fill the deep troughs in the southern Drake Passage as indicated by an oxygen maximum at depth (Sievers and Nowlin, 1984; Sudre et al., 2011; Fig. 3.2). Hydrographic properties at SFZ below 3500 m ( $\theta \approx -0.24^\circ\text{C}$ , salinity of 34.66,  $[\text{O}_2] \approx 4.9$  ml/l; Dalziel, 2015) are however not fully coherent with Weddel Sea Bottom Water (e.g., Sudre et al., 2011). Such properties indicate supposedly strong admixture of deep and bottom water masses sourced from the South Pacific (Sievers and Nowlin, 1984; Sudre et al., 2011), consistent with our Drake Passage data and South Pacific Nd isotope data from literature (Carter et al., 2012; Rickli et al., 2014; Basak et al., 2015; Fig. 3.2). This confirms the idea of spatial variability in Southern Ocean seawater Nd isotopic compositions at depth levels that are influenced by underlying bottom waters, as has been proposed based on FeMn nodule data (van de Flierdt et al., 2006a).

In overlying CDW, our Nd isotope results averaging at  $\epsilon_{\text{Nd}} \approx -8.2 \pm 0.5$  ( $n = 15$ ) are identical to results from previous work in the Drake Passage (Stichel et al., 2012; Fig. 3.5) and in the Pacific sector of the Southern Ocean (Carter et al., 2012; Rickli et al., 2014; Basak et al., 2015). As such CDW shows no indication of inter-basin heterogeneity. However, as noted by Rickli et al. (2014), the full range of circum-Antarctic LCDW salinity and temperature range is not yet covered with Nd isotope data.

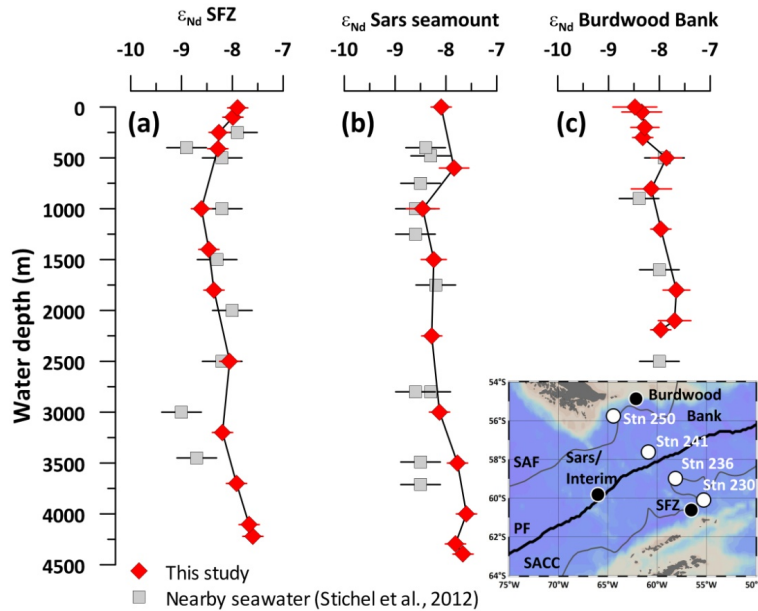


**Figure 3.5:** Seawater Nd isotope results from this study (red diamonds) compared to nearby seawater stations collected in the Drake Passage (grey squares; Stichel et al., 2012). Inset map illustrates sample locations from Stichel et al. (2012) (white circles) compared to new sampling locations (black circles). Note that stations 241 and 236 have been combined for comparison to the new Sars/Interim profile in panel (b). Abbreviations as in Figure 3.1.

A closer look at our new seawater Nd isotope data indicates that some sub-basin scale mixing processes are resolved in the Drake Passage seawater Nd isotopic composition. At Burdwood Bank two samples from 1800 and 2000 m water depth, i.e. at  $\gamma^n \approx 27.9 \text{ kg/m}^3$  (Dalziel, 2015), show  $\epsilon_{Nd}$  values of  $-7.7 \pm 0.3$  (Table 3.1, Figs. 3.2 and 3.5). Following the same isoneutral southward, it shoals to  $\sim 1000$  m water depth at Sars seamount, and  $\sim 400$  m water depth at SFZ, where  $\epsilon_{Nd}$  values of  $-8.5 \pm 0.3$  and  $-8.3 \pm 0.2$  are observed. This Nd isotope trend may be ascribed to increased influence of Pacific-derived water masses transported along the South American margin in a deep boundary current which disintegrates rapidly upon admixture into the zonal ACC flow in the Drake Passage (Well et al., 2003; Brearley et al., 2014). Any potential interpretation of the fine structure in our new data has however to remain tentative, as seawater samples were not filtered, offering an alternative explanation for some of the observed variations.

### 3.5.1.2. Calibrating modern deep-sea corals with seawater neodymium isotope data

A vital question for using deep-sea corals as a palaeoceanographic archive is whether different species of deep-sea corals are reliable recorders of ambient seawater. Towards this end our new data represent a valuable addition to existing calibrations (see Robinson et al. 2014 for a recent summary). With the exception of one specimen, all of the nine analysed modern deep-sea coral samples yielded Nd concentrations (5.4 to 27.0 ng/g; Table 3.4) that fall within the range of previously reported results ( $[\text{Nd}] \leq 38$  (51.3) ng/g, van de Flierdt et al., 2010;  $[\text{Nd}] \leq 110.1$  ng/g, Copard et al., 2011). This includes four specimens of *B. malouinensis*, a species previously not investigated for Nd concentrations. In terms of their Nd isotopic composition, however, only five out of the eight considered modern specimens from the Drake Passage and the North Atlantic (excluding one *B.*

*malouinensis* due to its very low  $\delta^{234}\text{U}_i$ ) show overlap with ambient seawater values within analytical uncertainty (Fig. 3.6, inset).

While *M. oculata* from the North Atlantic shows excellent agreement with ambient seawater, results from the Drake Passage indicate some strong species-dependence (Fig. 3.6, inset). The live collected *F. curvatum* specimen overlaps with seawater from 805 m water depth (AAIW depth range, Fig. 3.2) and is thus considered to reliably record seawater Nd isotopic composition even though the Nd concentration of this sample ( $[\text{Nd}_{\text{min}}] = 152.2 \text{ ng/g}$ ) falls outside the range for reported Nd concentrations in modern corals (this study; van de Flierdt et al., 2010; Copard et al., 2010, 2011, 2012). Of the three *D. dianthus* analysed, two individuals overlap with modern seawater. Sample TB04 Dp-A-2 however reveals a small offset of 0.15 epsilon units from ambient seawater (inset of Fig. 3.6), which seems at odds with the successful calibration of this species by van de Flierdt et al. (2010). This offset can be accounted for when considering the elevated  $^{232}\text{Th}$  concentration relative to Nd of this sample (344 pg/g and 11.0 ng/g, respectively). Assuming that all detected  $^{232}\text{Th}$  is of detrital origin and that the Nd concentration and isotopic composition of this contamination can be approximated using the Kasten corer sediment results from Burdwood Bank (Table 3.2), a theoretical offset (i.e. detrital contamination) of -0.41 epsilon units can be calculated for this coral thus accounting for the isotopic offset. FeMn oxyhydroxide contamination in modern coral skeletons is considered unlikely to affect the Nd isotopic composition as they would carry a modern seawater signal. We hence conclude that the aragonitic skeletons of both, *F. curvatum* and *D. dianthus*, are reliable recorders of seawater Nd isotopic compositions once potential contamination is rendered minor and/or accounted for through mass balance correction.

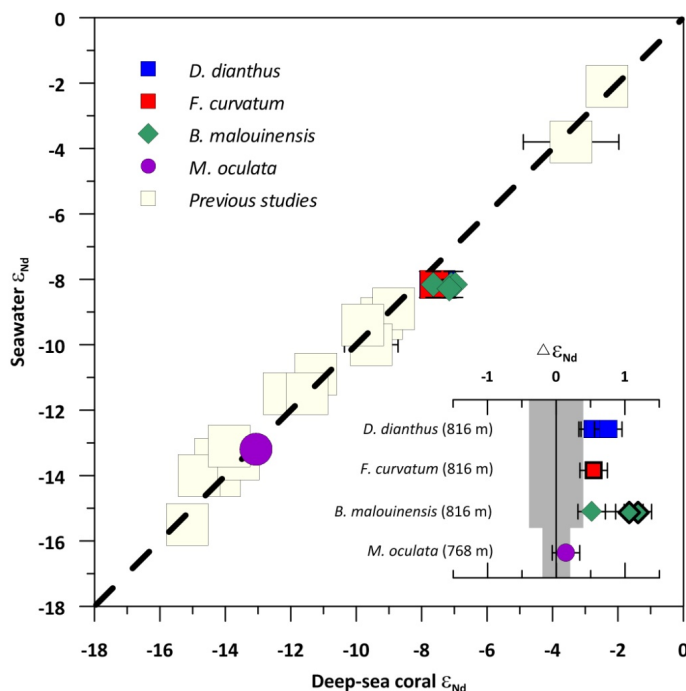


**Figure 3.6:** Global calibration of deep-sea coral Nd isotope data against modern seawater. Yellow squares indicate previously published modern calibration data (Copard et al., 2010; van de Flierdt et al., 2010). The inset shows the deviation of modern deep-sea coral  $\epsilon_{\text{Nd}}$  from ambient seawater, expressed as  $\Delta\epsilon_{\text{Nd}}$ . The grey bar represents the analytical uncertainty of the respective ambient seawater measurement. One *D. Dianthus* was replicated within analytical uncertainty (not shown here). Coral specimens collected alive are framed with thick black line.

*B. malouinensis* is a species that has not been calibrated before. Two specimens collected alive and one additional specimen dated to be recently dead (158 yr BP; Table 3.4) show a range of  $\sim 0.7$  epsilon units in their Nd isotopic composition. The least radiogenic value of  $-7.6 \pm 0.2$  was generated for specimen LMG0605/5-20 from 854 m water depth and thus reproduces modern seawater ( $\epsilon_{\text{Nd}} = -8.2 \pm 0.4$ ; Fig. 3.6, inset). The remaining *B. malouinensis* (Mod. Balano-1 and Mod. Balano-2, Table 3.4) however show  $\epsilon_{\text{Nd}}$  values of  $-7.1 \pm 0.2$  and  $-7.0 \pm 0.2$  respectively.

We here consider two possible mechanisms to explain these deviations of analysed coral skeletons from ambient seawater. Firstly, the offset may be related to contaminant sources of radiogenic Nd. Indeed, core-top sediment collected from Burdwood Bank is characterised by a Nd isotopic composition of  $-5.0 \pm 0.2$  (Table 3.2), and one of the two corals shows similarly high  $^{232}\text{Th}$  concentrations (377 pg/g) relative to Nd (14.2 ng/g), as discussed above for a *D. dianthus* specimen. Furthermore,  $^{232}\text{Th}$  and  $\text{Nd}_{\text{min}}$  concentrations in fossil *B. malouinensis* specimens show a strong positive correlation ( $R^2 = 0.96$ ,  $n = 11$ , Fig. 3.7), which may relate to the fissured structure of the skeletons and the porous top section (Fig. 3.3) making the cleaning of *B. malouinensis* skeletons challenging. In contrast to *D. dianthus*, which is known to live on hard substrates, *B. malouinensis* is either weakly attached to coarse substrate or sits in seafloor sediment as indicated by its cornutiform base (Squires, 1961; Cairns, 1982). This living habitat is reflected by geochemical results obtained from sub-sampling fossil *B. malouinensis* specimen NBP1103 DH16 Bc-2 at the upper and lower part of the solid skeleton (Fig. 3.3). Al and Ti concentrations are 6 to 7 times higher in the lower part (Table 3.5), indicating potential sedimentary contamination and/or interaction with porewaters. In order to test for sedimentary contamination we use mass balance calculations, assuming a  $^{232}\text{Th}$ -free modern coral and sediments as a sole source of contaminant Th. Detrital contamination can only account for a maximum Nd isotope shift of  $-0.29$  epsilon units, which is still insufficient to achieve overlap with modern seawater at the coral collection site. This supports speculations that porewaters may play an additional role. The impact of pore waters may be amplified by the porous skeletal structure, a hypothesis which is however impossible to test in the absence of porewater samples from the coral sampling locations. Some insight could be obtained from sediment and *B. malouinensis* data from locations with different geochemical properties.

Alternatively, the Nd isotope offset may be related to coral growth rate and thus the length of the time integrated in a particular sub-sample (i.e. the slower the coral growth rate, the longer the time interval recorded in sub-samples of a given size). Adkins et al. (2004) presented vertical extension rates of  $\sim 0.5$  to 2 mm/yr for *D. dianthus*, which hence integrates Nd isotope signals over a time interval of up to  $\sim 100$  or 200 years. In contrast, growth rates for the species *M. oculata* are up to about one order of magnitude higher (e.g., Orejas et al., 2008; Sabatier et al., 2012) than in *D. dianthus*, significantly reducing the time-integrated signal in a given sub-sample. Growth rates for *B. malouinensis* are yet unconstrained. Therefore, if *B. malouinensis* specimens would live for a long time, and would grow very slowly, they could integrate temporal water mass variability. In the case of

the Drake Passage, the specimens in question were recovered from a water depth bathed by AAIW, a water mass which is known for its temporal variability and the involvement of water bodies with a more radiogenic signature (Jeandel, 1993; Carter et al., 2012; Stichel et al., 2012 supplement). Such a scenario would resolve the apparent contradiction of seawater-like REE patterns displayed by *B. malouinensis* (e.g., enrichment in HREE, negative Ce anomaly, and positive Gd anomaly, Tables 3.4 and 3.5) and non-seawater-like Nd isotopic compositions.

Regardless, both hypotheses have to remain speculative and hence *B. malouinensis* should be excluded from palaeoclimatic applications for Nd isotopes until further studies can investigate this species in more detail.

### 3.5.2. In search for the Nd carrier phases in coralline aragonite

The Nd concentrations reported here for modern deep-sea corals fall mostly within the range of previously published Nd concentrations in deep-sea corals (see Robinson et al. (2014) for a recent summary). But what does this concentration range mean and how representative is it? Rare earth elements in seawater are predominantly present as carbonate complexes (e.g., Cantrell and Byrne, 1987). Early work assumed that this would favour direct incorporation into the aragonitic lattice of corals (e.g., Shaw and Wasserburg, 1985; Sholkovitz and Shen, 1995). Distribution constants ( $K_D$ ; cf. IUPAC, 2014) of 1.2 to 2.1 seemed to support this idea, but inorganic precipitation experiments have expanded this range ( $K_{DS} \approx 4$  to 4.5, Terakado and Masuda, 1988). Subsequent studies reported Nd concentrations in shallow water corals of up to 55.5 ng/g (Akagi et al., 2004; Wyndham et al., 2004). This concentration range is comparable to the one reported for deep-sea corals, and implies  $K_{DS} > 20$ , an observation which seems confirmed by high Nd concentrations found by Copard et al. (2011, 2012) and for one specimen of alive collected *F. curvatum* (152.2 ng/g; Table 3.4;  $K_D = 99$ ). One caveat in evaluating this concentration range is that even including our new results, the number of concentration analyses performed on modern and recently dead deep-sea coral specimens is relatively small ( $n = 96$ , of which  $n = 47$  are transect analyses on only three individual corals; Copard et al., 2010, 2011, 2012; van de Flierdt et al., 2010; Montero-Serrano et al., 2013; this study). We can, however, extend the database by including fossil deep-sea corals ( $n = 151$ , including transect analyses as individual samples, usually only 2-3 transect analyses per individual coral; Colin et al., 2010; Copard et al., 2010, 2011, 2012; van de Flierdt et al., 2010; Crocket et al., 2014; Wilson et al., 2014; this study). Neodymium concentrations in 102 sub-samples of 71 fully-cleaned fossil coral samples analysed for this study alone range from 5 to 964.5 ng/g (Tables 3.5 and 3.6). Crocket et al. (2014) listed a number of potential sources for intra-and inter-skeletal variability in fossil corals, including potential sampling bias. Our fossil corals indicate clear evidence for the latter. Different parts of individual coral specimens, resampled, cleaned and reanalysed, show Nd concentrations deviating by up to ~615 ng/g in *G. antarctica* and ~280 ng/g in *D. dianthus* (Tables 3.5 and 3.6; Fig. 3.9). A similar observation (e.g., intraskeletal Nd variability from a few ng/g up to ~50 ng/g in *D. dianthus*) was also noted by

Copard et al. (2010) (pers. comm. by P. Montagna). Interestingly, variable Nd concentrations seem not to translate to variable Nd isotopic compositions (i.e. excellent reproducibility between different pieces of the same coral specimen; not shown), indicating the carrier phase responsible for elevated Nd concentrations may be authigenic in origin. In the following, we will first evaluate the role of lithogenic and FeMn phases for the coralline Nd budget, to then focus on an assessment of organic matter and secondary authigenic precipitates (i.e. phosphates) as potential Nd carrier.

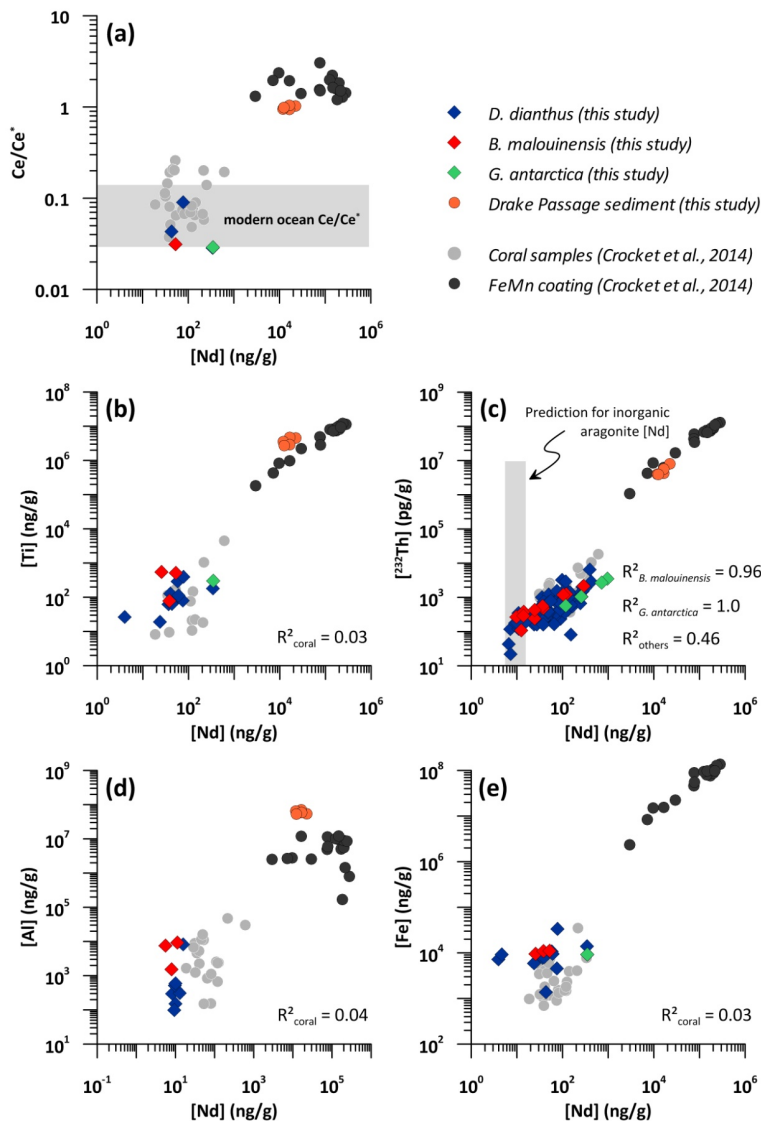


**Figure 3.7:** Drake Passage deep-sea coral trace metal data (in colour). All results but Nd concentrations in panel (c) are derived by ICP-MS analyses of resampled corals. (a)  $[\text{Nd}]$  vs.  $\text{Ce}/\text{Ce}^*$ ;  $\text{Ce}/\text{Ce}^* = 2 \times \text{Ce}/(\text{La} + \text{Pr})$ ; modern deep ocean  $\text{Ce}/\text{Ce}^*$  from Hathorne et al. (2015, and references therein). (b)  $[\text{Nd}]$  vs.  $[\text{Ti}]$ , (c) Isotope dilution results for  $^{232}\text{Th}$  (Burke and Robinson, 2012; Chen et al., 2015; Burke et al., unpubl. data; Tables 3.4 and 3.6). Neodymium concentrations are based on isotope dilution calculations as well, but as samples were only spiked after U-Th chemistry, all concentrations are minimum estimates (see text and Tables 3.4 and 3.6 for further information). Correlation coefficient for  $[\text{Nd}]$  vs.  $^{232}\text{Th}$  for all corals:  $R^2_{\text{linear}} = 0.48$  ( $n = 91$ ). Higher coefficients are found when only considering *B. malouinensis* ( $R^2_{\text{linear}} = 0.96$ ;  $n = 11$ ), and *G. antarctica* ( $R^2_{\text{linear}} = 1$ ;  $n = 4$ ). Grey bar indicates predicted  $[\text{Nd}]_{\text{coral}}$  calculated from inorganic precipitation  $K_D$  value 4.3 (Terakado and Masuda, 1988) assuming a  $[\text{Nd}]_{\text{seawater}}$  range of 10-19 pmol/kg, based on concentration data for Drake Passage seawater from Stichel et al. (2012). (d)  $[\text{Nd}]$  vs.  $[\text{Al}]$ . (e)  $[\text{Nd}]$  vs.  $[\text{Fe}]$ , no sediment Fe data available.

### 3.5.2.1. Lithogenic and FeMn oxyhydroxide phases as Nd carrier in coral skeletons

Ferromanganese oxyhydroxide coatings and lithogenic phases have strong potential as contaminants as their Nd concentrations are  $\sim 2 - 3$  orders of magnitude elevated in detrital phases (e.g., Taylor and McLennan, 1985; Table 3.3) and 3 - 4 orders of magnitude in FeMn coatings (e.g., Bau et al., 1996; Crocket et al., 2014; Figs. 3.7 and 3.8) compared to concentrations obtained in

aragonitic skeletons. Figure 3.7 illustrates that elements such as Th, Al, Fe, and Ti, which all have been used as indicators of contamination (e.g., Frank et al., 2004; Robinson et al., 2006; van de Flierdt et al., 2010; Copard et al., 2010; Crocket et al., 2014), are significantly less abundant in corals than in local sediments and FeMn coatings. Moreover, neither Al, nor Fe or Ti concentrations in cleaned coral aragonite do show any significant covariation with Nd concentrations (Fig. 3.7; Table 3.5;  $R^2 < 0.08$ ). Crocket et al. (2014) furthermore suggested the Ce anomaly ( $Ce/Ce^*$ ) as a sensitive tracer for contamination in cleaned coral aragonite (Fig. 3.8) as a negative Ce anomaly is unique to seawater due to oxidation of  $Ce^{3+}$  to the insoluble  $Ce^{4+}$  under oxic conditions (e.g., Elderfield and Greaves, 1982; de Baar et al., 1985). As Ce concentrations are low in cleaned coral skeletons (e.g., often below the limit of detection; Table 3.5),  $Ce/Ce^*$  could only be calculated for five coral samples (Fig. 3.7). These results are consistent with Ce anomalies observed in modern global deep waters, including results from nearby Drake Passage seawater (Hathorne et al., 2015, and references therein). In summary, lithogenic source tracers do not indicate significant contribution from contaminant sources in cleaned coral skeletons.

We can further test this statement by reverting to the extensive  $^{232}Th$  concentration dataset (Burke and Robinson, 2012; Chen et al., 2015; Burke et al., unpubl. data; Table 3.6), as  $^{232}Th$  seems to be the only lithogenic contaminant that shows some co-variation with Nd concentrations in corals (Fig. 3.7;  $R^2 = 0.48$ ,  $n = 91$ , including replicates and modern corals). We adopted the approach from Crocket et al. (2014) to calculate Th-based contribution of  $[Nd]_{detrital}$  to  $[Nd]_{min}^{coral}$ , assuming that pure coral aragonite contains no  $^{232}Th$  so that all  $^{232}Th$  can be attributed to contaminant sources (e.g., Robinson et al., 2006). In order to calculate the proportion of Th-based detrital Nd in a physically and chemically cleaned coral sub-sample we use the Nd/Th ratio of nearby sediment samples (Table 3.3) and apply the following equation:

$$\%Nd_{detrital\ contribution} = \left( \frac{[Th]_{final} \times \left( \frac{[Nd]}{[Th]} \right)_{sediment}}{[Nd]_{final}} \right) \times 100 \quad (1)$$

The subscript *final* refers to the concentration of the respective element measured in the aragonitic skeletons of a deep-sea coral. The obtained average contribution to the coral Nd pool is ~3% ( $n = 91$ ), of which 13 samples show values between 5 and 10%. Results are corroborated when computing equation 1 for other terrigenous elements such as Ti ( $n = 16$ ).

In order to evaluate the effect of such levels of detrital contamination on the Nd isotopic composition of fossil corals, we assume Nd isotopic compositions in the range of  $\epsilon_{Nd} = -5.1$  to  $\epsilon_{Nd} = -8.4$  (Chapters 4, 5 and 6) and sediment results reported in Table 3.3:

$$IC_{coral\ calculated} = \frac{IC_{final} \times ([Nd]_{final} \times f_{final} + [Nd]_{sediment} \times f_{sediment}) - (IC_{sediment} \times [Nd]_{sediment} \times f_{sediment})}{([Nd]_{final} \times f_{final})} \quad (2)$$

IC in above equation refers to the Nd isotopic composition. The resulting average change in  $\epsilon_{Nd}$  is 0.05 units, with seven samples exceeding our typical  $2\sigma$  external reproducibility of 20 ppm on  $^{143}Nd/^{144}Nd$  measurements. These seven samples deviate by 0.21 to 0.41 epsilon units and could thus be affected by significant lithogenic contamination. The largest shift of 0.41  $\epsilon_{Nd}$  is calculated for modern *D. dianthus* NBP0805 TB04 Dp-A-02, which may thus account for the observed offset from seawater (Fig. 3.6, Table 3.4; see previous section).

The same equations can be used to calculate the potential contamination by FeMn oxyhydroxide phases. Using a Nd/Th ratio of 2.02 for FeMn coatings (average of 19 coatings reported by Crocket et al., 2014) and a Nd isotopic composition of  $\epsilon_{Nd} = -7.01 \pm 0.36$  as reported for a 17.1 kyr BP *D. dianthus* coating collected in 1125 m water depth at Sars seamount; Robinson and van de Flierdt (2009)), the average contribution of FeMn-bound Nd to the coralline Nd budget is 2.1%. This equates to an average shift in Nd isotopic compositions of 0.04 epsilon units ( $n = 91$ ). Maximum contributions are up to 7.5%, which would result in a correction of 0.32  $\epsilon_{Nd}$ . However, only three samples, one of which is modern NBP0805 TB04 Dp-A-02, would experience a shift in excess of the external reproducibility of 20 ppm on  $^{143}Nd/^{144}Nd$  measurements.

In summary, the only way to create an isotopic effect from detrital or FeMn contaminants in our fossil coral data set from the Drake Passage is to assume no  $^{232}Th$  in pure authigenic aragonite, linear coupling of Nd and  $^{232}Th$ , and 100% sourcing of  $^{232}Th$  from the respective contaminant phase. But even under these extreme assumptions, only a small number of corals show potential calculated shifts of up to 0.4 epsilon units. We hence conclude that interpretations of shifts in excess of this signal are robust for the Nd and  $^{232}Th$  concentration ranges observed. We further propose to apply conservative mass balance scenarios to rule out significant contribution of contaminant phases. Alternatively, a correction can be applied, based on lithogenic source tracers such as  $^{232}Th$  or Ti concentrations and characterisation of contaminant phases as done in the case for the Drake Passage. A  $^{232}Th$ -based correction may however imply overcorrection as  $^{232}Th$  could also be concentrated from seawater in precipitating phases and may require alternative lithogenic source tracers such as Ti. However, the above mass balance exercise renders detrital or FeMn coatings an implausible source of the majority of the elevated Nd concentrations. This calls for an authigenic (seawater-derived) Nd carrier phase causing the enrichment of Nd within the coralline aragonite. In other words, the elevated Nd concentrations are derived from ambient seawater to be incorporated in the skeleton while the coral was still alive.

### 3.5.2.2. Rare earth element case for a seawater origin

Further support for an insignificant role of Nd contamination by detritus and FeMn coatings on fully cleaned fossil and modern deep-sea coral aragonite comes from shale-normalised REE patterns (Table 3.5, Fig. 3.8). Local sediments show relatively flat REE patterns, with no notable Ce anomaly, and a slight enrichment in HREE over LREE. FeMn coatings reported by Crocket et al.

(2014) show relatively flat patterns with a positive Ce anomaly and a slight buldge in mid-REE (Fig. 3.8). In contrast, all results obtained from modern and fossil deep-sea corals ( $n = 17$ ) show pronounced negative Ce anomalies. Given the low concentrations of Ce in coralline aragonite, contamination from FeMn coatings and/or lithogenic sources should be readily detectable by a less pronounced Ce anomaly, which is however not the case (Figs. 3.7 and 3.8; Table 3.5). Moreover, stabilities of aqueous REE carbonate complexes in seawater increase with increasing atomic numbers resulting in characteristic HREE enrichment (e.g., de Baar et al., 1985; Cantrell and Byrne, 1987; Byrne and Li, 1995), and hence in modern CDW (Hathorne et al., 2015; Fig. 3.8). The same features can be observed in deep-sea coral aragonite, even for the species *B. malouinensis* and *G. antarctica*, which showed suspicious co-variations of Nd and  $^{232}\text{Th}$ . We conclude that the excess Nd over predicted  $[\text{Nd}]_{\text{coral}}$  from inorganic aragonite precipitation experiments seems authigenic in nature.

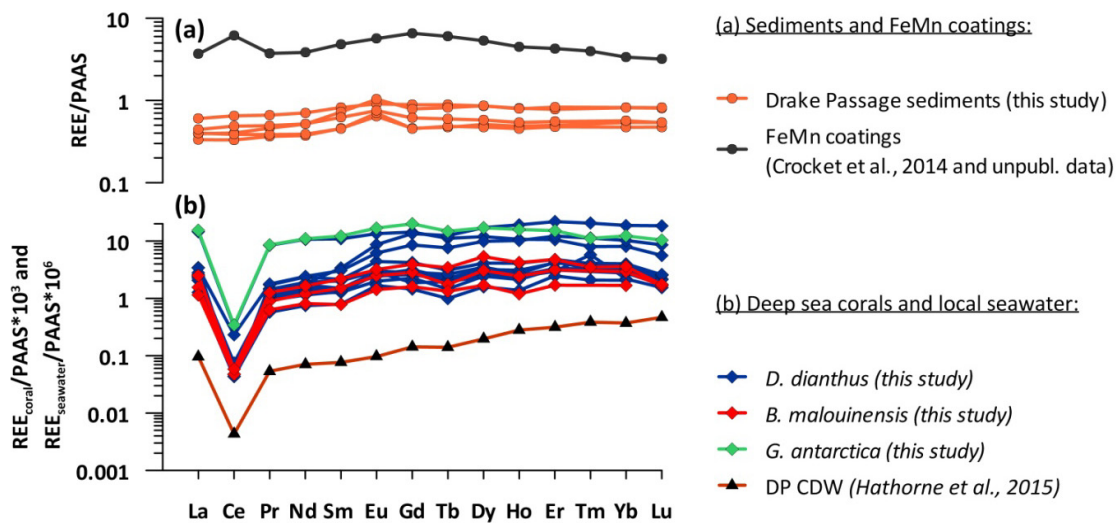


**Figure 3.8:** (a) Sedimentary REE pattern from locations across the Drake Passage (see Fig. 3.2) and average values for FeMn coating data from North Atlantic deep-sea corals ( $n = 18$ ; Crocket et al., 2014, unpubl. data). (b) Deep-sea coral REE results for a selected group of modern and fossil samples (see Table 3.5). Due to the low concentrations of REE in clean coral aragonite low abundance elements like Ce, Tm and Lu were at times below the detection limit (Table 3.5). For visualisation purposes we used the REE concentration of the detection limit to calculate shale-normalised values (Taylor and McLennan, 1985). Samples NBP0805 TB04 ‘Big Beauty’ and NBP0805 DR35 ‘Dc-A1’ yielded very low REE concentrations overall (Table 3.5), and were hence not included in the Figure. Seawater data from Drake Passage CDW is from 1250 m water depth at Stn 241 in Hathorne et al. (2015).

### 3.5.2.3. Organic phases as potential Nd carrier in coral skeletons

Skeletons of deep-sea corals are characterised by microstructures that feature an area where biologically mediated precipitation happens, which is called the centre of calcification (COC), and a chemically and morphologically distinct area of surrounding fibrous aragonite (e.g., Cuif and Dauphin, 1998; Adkins et al., 2003). COCs are characterised by high abundances of organic molecules, i.e. sugars and amino acids mediating the precipitation of amorphous aragonite precursor phases,

associated with strong chemical heterogeneity (Cuif and Dauphin, 1998, 2005; Dauphin et al., 2006; Przeniosło et al., 2008; Robinson et al., 2014). The presence of organic compounds in deep-sea corals is however not exclusively limited to COCs, but also involved in mediating cyclic inter- and intra-crystal growth and orientation of aragonitic fibres on micron to nano-scale (e.g., Cuif et al., 1999, 2003; Przeniosło et al., 2008; Webb et al., 2009). Anagnostou et al. (2011) ascribed regions of elevated Fe/Ca and Mn/Ca in covariation with P/Ca along a septum of *D. dianthus* to FeMn oxyhydroxide contaminations. Alternatively, such covariation with P/Ca may be interpreted in the light of organic compounds being present and causing enhanced surface sorption of elements from ambient seawater, which could be incorporated into the coral skeleton during ongoing growth. Heterogeneous distribution of inner-skeletal organics thus appears a potential candidate to cause intraskeletal Nd variability. A prediction arising from such a scenario would be enrichment in coral LREE relative to seawater, due to  $[\text{CO}_3^{2-}]$ -dependent preferential adsorption of LREE over HREE onto organic surfaces and particles (Byrne and Kim, 1990; Sholkovitz et al., 1994). The average  $\text{HREE/LREE}_{\text{coral}}$  (i.e.  $(\text{Yb} + \text{Er})/(\text{La} + \text{Nd})$ ) is 2.4 ( $n = 17$ , Table 3.5) and thus characterised by a slight LREE enrichment in comparison to local seawater from the Drake Passage ( $\text{HREE/LREE} = 4.1$ ; Hathorne et al., 2015; Fig. 3.8). According to (Byrne and Li, 1995) the degree of LREE enrichment caused by surface complexation depends on the type of ligands associated with the surfaces of organic matter, and could thus explain the relatively wide range of HREE/LREE ratios, from 0.7 to 10.0 observed in coral aragonite (Table 3.5). Byrne and Kim (1990) conducted exposure experiments on the algae *Ulva lactuca* to test partitioning of REE from aqueous onto organic phases. After exposure time of 12 hours they found  $K_{\text{DS}}$  ( $[\text{REE}]_{\text{organics}}/[\text{REE}]_{\text{seawater}}$ ) of  $\sim 750$  for Ce and Eu. Combining such high  $K_{\text{DS}}$  with observed seawater Nd concentrations in the Drake Passage of up to 30.09 pmol/kg (Stichel et al., 2012), a theoretical Nd concentration in organic phases of 3.3 ng/g can be calculated. Following furthermore the estimate from Cuif et al. (2004) that the overall proportion of organics in coral skeletons is  $\sim 2.5$  wt%, the maximum contribution of organic-bound Nd to the coral Nd budget would be less than 0.1 ng/g. The life cycle of a coral is however orders of magnitude longer than 12 hours (*D. dianthus*:  $\sim 100$  years; Adkins et al., 2004) and organic compounds exposed to seawater may thus accumulate Nd over the life cycle of a coral in analogy to processes observed in foraminifera (Vance et al., 2004; Martinez-Boti et al., 2009). On the basis of Gd anomalies ( $\text{Gd/Gd}^* = 2 \times \text{Gd}/(\text{Eu} + \text{Tb})$ ) we however rule out a dominant role of organics on the coral REE budget. If the REE budget was controlled by organic scavenging from seawater the Gd anomaly should then be negative (Lee and Byrne, 1993). The average  $\text{Gd/Gd}^*_{\text{coral}}$  is however  $1.2 \pm 0.1$  ( $n = 15$ ; Table 3.5), i.e. slightly positive, and rather resembles Drake Passage UCDW Gd anomalies, which are also slightly positive ( $\text{Gd/Gd}^* \approx 1.3$ ; Hathorne et al., 2015).

### 3.5.2.4. Phosphate phases as Nd carrier in coral skeletons

Another authigenic phase previously identified in coral aragonite and capable to concentrate seawater REE are phosphates like apatite (Montagna et al., 2006; Mason et al., 2011). Mason et al. (2011) investigated septae and thecae of modern and fossil *D. dianthus*, *Flabellum sp.* and *Lophelia pertusa* specimens from various marine environments. A combination of laser-ablation ICP-MS, solid-state NMR (nuclear magnetic resonance) spectroscopy and solution ICP-MS was used to identify hydroxyapatite as a significant phosphate-hosting mineral in coral skeletons (Mason et al., 2011). Concentrations of hydroxyapatite were found to be highly variable between individual samples, independent of environmental factors such as dissolved inorganic phosphate or depth, and were not related to bulk coral phosphate content or preservation state (Mason et al., 2011).

While surficial apatite would be removed during the cleaning procedure, such inorganic hydroxyapatite inclusions may be enriched in seawater-derived REE (i.e. in analogy to biogenic apatite; Elderfield and Pagett, 1986; Martin et al., 2010) and thus cause the large range of Nd concentrations observed in fossil and modern deep-sea coral skeletons as well as within individual coral specimens. The maximum solid-bound P in the coralline skeleton was found to be  $319 \pm 79 \mu\text{g/g}$  of which up to  $41 \pm 7\%$  are estimated to be apatite-bound (Mason et al., 2011). Hydroxyapatite has the formula  $\text{Ca}_5(\text{PO}_4)_3(\text{OH})$ , in which P accounts for 92.9 of the 502.3 amu, yielding a P/apatite ratio of 0.185 leading to a P-based maximum estimate of  $\sim 707 \mu\text{g/g}$  of apatite in coralline aragonite. Fish teeth are known to contain seawater-like REE patterns (e.g., Elderfield and Pagett, 1986; Martin and Scher, 2010) even though they contain Nd concentrations of up to  $1460 \mu\text{g/g}$ . We use this estimate as upper limit for  $[\text{Nd}]_{\text{apatite}}$ , which calculates to  $\sim 1 \mu\text{g}$  apatite-bound Nd per g of coral skeleton. This value is in excellent agreement with the highest Nd concentration observed in our entire set of fossil and modern corals (i.e.  $\text{Nd}_{\text{min}} = 964.5 \text{ ng/g}$ ; Tables 3.4 and 3.6), and reflected in similar P/Nd of  $\sim 130$  in coral skeletons and fish teeth, respectively.

Importantly, apatite inclusions (surficial apatite would be removed during cleaning) in coral skeletons may have a major impact on the Nd budget, without affecting other elemental concentrations such as U. For example, U concentrations in fish teeth are  $0.7 - 11 \mu\text{g/g}$  (Baturin, 2001) and Nd/U ratios (using  $1460 \mu\text{g/g}$  Nd, from Elderfield and Pagett, 1986) vary between  $\sim 133$  and 2086. Since such Nd/U ratios in apatite are about one order of magnitude higher than in coral skeletons (e.g., Baturin, 2001; Robinson et al., 2006; Crocket et al., 2014; this study) the effect of heterogeneously distributed apatite inclusions on  $[\text{}^{238}\text{U}]_{\text{coral}}$  would be expected to be limited. This observation is consistent with the data shown in Figure 3.9 revealing relatively good reproducibility of U concentrations from different sub-samples of the same coral specimen ( $R^2 = 0.76$ ), while  $\text{Nd}_{\text{min}}$  is very poorly reproduced (i.e., more heterogeneous;  $R^2 = 0.35$ ). A similar concentration range in fish teeth was found for Th (e.g.,  $4.4$  to  $9.5 \mu\text{g/g}$ ; Baturin, 2001) which would yield Nd/Th ratios of  $\sim 154 - 332$  in apatite (based on  $1460 \mu\text{g/g}$  Nd; Elderfield and Pagett, 1986), similar to those observed in coral aragonite ( $\text{Nd/Th} \leq 403$  omitting one sample; Table 3.6). This may indicate that the Th budget of the

coral skeleton may be controlled to a significant degree by apatite inclusions, which would however necessarily imply strong Th heterogeneity in the coral skeleton, similar to Nd. Moreover, Baturin (2001) ascribed the Th in fish teeth to contaminant phases so that the Th budget of cleaned coral skeletons may be determined by impurities in both, apatite and aragonite. However, the reproducibility of  $[^{232}\text{Th}]_{\text{coral}}$  is significantly better than that of  $\text{Nd}_{\text{min}}$  (Fig. 3.9), suggesting that the coral Th budget is not dominated by apatite inclusions, but rather by detrital and/or FeMn contamination of the aragonite itself. It may be further speculated that the exposure of coral-bound apatite in coral skeletons to contaminant phases such as sediments and FeMn coatings is reduced in comparison to sediment-bound fish teeth. Nevertheless, a significant proportion of the coral-bound  $^{232}\text{Th}$  may be concentrated from seawater thus explaining the overall correlation between Nd and Th in coral skeletons (Fig. 3.7). The relatively good reproducibility of  $[^{232}\text{Th}]$  from re-sampled coral pieces provides, however, evidence that most of the  $^{232}\text{Th}$  in deep-sea coral skeletons is likely associated with contaminant phases in the coral skeleton. The overall contribution of such contaminant phases to the clean coral skeleton Nd budget is however minor as shown by the above worst case mass balance.

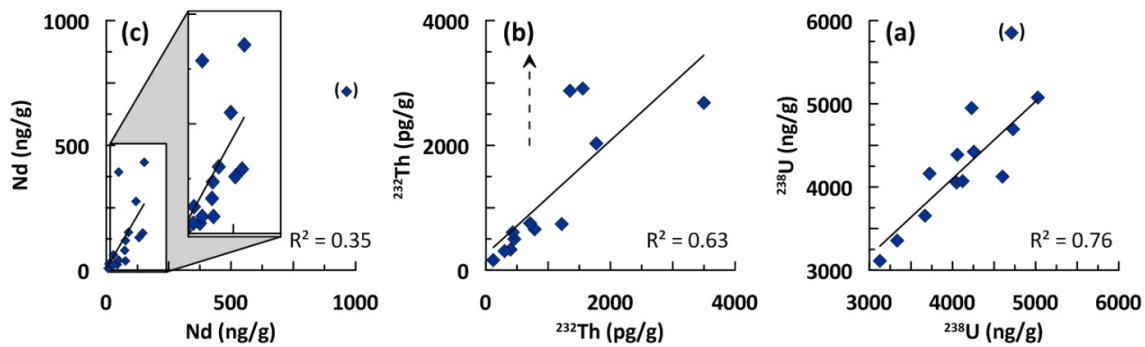


**Figure 3.9:** Trace metal results of different sub-samples of the same coral. Plotted are  $^{238}\text{U}$ ,  $^{232}\text{Th}$ , and  $\text{Nd}_{\text{min}}$  concentrations (<12% Nd loss) obtained from isotope dilution (Tables 3.4 and 3.6; see text for details). The correlation coefficients were generated by excluding one outlier per plot which is indicated by brackets. The dashed arrow in (b) indicates outlier result of  $[^{232}\text{Th}] = 6417$  pg/g.

It is therefore proposed that apatite inclusions dominate the coral aragonite Nd budget, consistent with the  $\text{REE}_{\text{coral}}$  data presented. Experimental studies showed that a slight depletion in HREE in coral aragonite, compared to seawater, is controlled by the combined effect of sorption onto hydroxyapatite surfaces (i.e.  $K_{\text{DS}}$  decrease towards HREE: Koepfenkastro and De Carlo, 1992) and quantitative assimilation of the REE from ambient seawater (Reynard et al., 1999). Overall, the large variability of major and trace element concentrations in apatite is consistent with the observed difficulty to reproduce coral Nd concentrations (Fig. 3.9) as well as the fact that different individual locations, such as the Northwest Atlantic (Crocket et al., 2014), the Northeast Atlantic (Colin et al., 2010; Copard et al., 2011, 2012; Montero-Serrano et al., 2013), and the Drake Passage (this study), all show large ranges of coral Nd concentrations, even though contaminant non-authigenic phases indicated only very limited effect on the budgets of rigorously cleaned coral aragonite.

### 3.6. Conclusions

We here presented new data that expand on the existing modern calibration of deep-sea coral aragonite as an archive for seawater Nd isotopes. By comparing alive-collected and recently deceased corals of the species *F. curvatum* and *D. dianthus* from the Drake Passage with results for ambient seawater, we show that these species are robust seawater archives. A similar conclusion can be reached for the species *M. oculata* based on new results from the North Atlantic. Less straightforward is, however, the use of the species *B. malouinensis* as seawater archive. Two of the three specimens investigated, which show closed system U-series ages, do not match modern seawater Nd isotopic composition. This species should hence be treated with caution until further modern studies (e.g., on growth rate or in combination with pore waters) become available.

Despite the overall good overlap of modern coral-bound Nd isotopes with modern seawater Nd isotope signatures, this study confirms earlier findings that Nd concentrations in coralline aragonite can be significantly elevated over that expected from inorganic precipitation experiments. Modern and fossil coral skeletons furthermore reveal variability in Nd concentrations of up to two orders of magnitude. Mass balance considerations using new results from local sediments as well as previously published results on ferromanganese oxyhydroxide phases can rule out major contributions from these phases. Seawater-like REE patterns in corals provide strong evidence for a predominantly authigenic nature of Nd in corals. Mass balance considerations render organic phases as carrier phase unlikely and suggest that elevated and variable Nd concentrations in modern and fossil corals can most readily be explained by heterogeneously distributed apatite. Such apatite inclusions concentrate ambient seawater REE, and thus do not compromise the use of fossil deep-sea coral skeletons as robust recorders of seawater Nd isotopic composition.

**Declaration:** This work was completed as part of a collaborative effort. I conducted the Nd isotope and concentration analyses at Imperial College London and, in collaboration with Sam Hammond the trace metal analyses at Open University. Kais M. Falcon masterminded Drake Passage sediment collection. Andrea Burke, Laura F. Robinson, Louisa I. Bradtmiller and Maureen E. Auro conducted the U-series work and made samples available. The Nd fraction was collected following the procedures outlined in Chapter 2.

## **Chapter 4**

**The deglacial Southern Ocean:  
centennial-scale circulation changes  
recorded in deep-sea coral skeletons?**

## Abstract

The Southern Ocean has been identified to play a pivotal role during rapid climate change across the past deglaciation, characterised by changes in the global distribution of heat, freshwater and carbon. Past investigations on deep oceanic re-organisation focused, however, on North Atlantic variability. In order to evaluate glacial to interglacial ocean dynamics from a Southern Ocean perspective, we here use neodymium (Nd) isotopes extracted from mid-depth Drake Passage and Tasmanian deep-sea corals.

The Drake Passage Nd isotope time series shows a long-term trend towards less radiogenic signatures with characteristic short-term fluctuations superimposed, ranging in total from  $\epsilon_{\text{Nd}} = -5.9 \pm 0.2$  to  $\epsilon_{\text{Nd}} = -8.3 \pm 0.2$  between 26 and 11 kyr BP (i.e. thousand years before present). In contrast, the most prominent feature of the Tasmanian time series is a single pronounced Nd isotope shift from  $\epsilon_{\text{Nd}} = -4.9 \pm 0.2$  to  $\epsilon_{\text{Nd}} = -7.3 \pm 0.2$  during Heinrich Stadial 1 (HS1). As such, the different characteristics suggest that the two sampling locations captured different features of mid-depth ocean circulation between 26 and 11 kyr BP. We consider the Drake Passage corals as recorders of glacial Upper Circumpolar Deep Water (UCDW). The relatively unradiogenic nature of glacial UCDW Nd isotope signatures suggests a strong contribution of Atlantic-sourced water masses mixing dynamically with underlying deep Pacific-imprinted water masses, likely in response to wind-driven millennial to (sub) centennial variability of interoceanic exchange and vertical mixing. Similar to the deep Southern Ocean, the Tasmanian margin was dominated by more radiogenic, Pacific-derived water masses during the peak glacial. The mid-depth Tasmanian corals recorded, however, significantly better ventilation than underlying deep waters. In combination with the Drake Passage data this implies (i) a deeply stratified glacial Southern Ocean, (ii) ventilation of mid-depth waters from the (North) Pacific and (iii) reduced exchange between Pacific and Southern Ocean water masses at mid-depth.

This glacial scenario was likely induced by the Southern Hemisphere westerly winds (SWW) dictating the position of oceanic fronts. Specifically, the equatorward migration of the SWW is considered to reach a critical position during the glacial such that the Subantarctic Front (SAF) off Chile is partly deflected northward thus reducing the lateral and vertical mixing of water masses. At a critical SWW position, bipolar (atmospheric) feedbacks could drive abrupt changes in water mass mixing. Such abrupt events are particularly evident during the period from 16.7 to 14.8 kyr BP when the isotopic difference between the two coral sampling locations, and to underlying deep waters, was eroded. Alongside, the glacial circulation scenario ended, associated with a mid-HS1 change of Southern Ocean ventilation state between 15.8 and 15.2 kyr BP. This change in ventilation state was also a turning point in the nature of Southern Ocean  $\text{CO}_2$  degassing. Whereas Pacific-derived water masses dominated the Southern Ocean during early deglacial oceanic degassing, Atlantic-derived water masses were associated with oceanic  $\text{CO}_2$  release during the later part.

#### 4.1. Introduction

The Southern Ocean is key for the global exchange and re-distribution of ocean properties such as heat, freshwater and carbon (e.g., Ganachaud and Wunsch, 2000; Marshall and Speer, 2012; Talley 2013). The modern Southern Ocean circulation system is dominated by the zonal flow of the Antarctic Circumpolar Current (ACC) mixing major water masses from the Atlantic, Pacific and Indian Oceans. The zonal flow is concentrated in jets of which the Polar Front (PF) and Subantarctic Front (SAF) transport ~80% of the total ACC flow (e.g., Orsi et al., 1995; Cunningham et al., 2003). The (meridional) water mass exchange with the major ocean basins occurs pre-dominantly along, but also across, upward sloping isoneutrals influencing the vertical structure of the ACC (Reid and Lynn, 1971; Callahan, 1972; Naveira Garabato et al., 2003; Fig. 4.1). At mid-depth, the ACC is dominated by Circumpolar Deep Water (CDW), subdivided into upper and lower CDW, the latter being colder, more saline and higher in oxygen due to stronger influence of North Atlantic Deep Water (NADW) on LCDW. Upper Circumpolar Deep Water (UCDW) is characterised by the imprint of Pacific Deep Water (PDW) and Indian Deep Water (IDW) (Reid and Lynn, 1971; Callahan, 1972; Mantyla and Reid, 1995; Figs. 4.1, 4.2 and 4.3).

The deep wind-induced upwelling along the ACC brings deep waters to the surface mixed layer where they exchange with the atmosphere and participate in the formation of Subantarctic Mode Water (SAMW) and its denser companion Antarctic Intermediate Water (AAIW), both of which are subducted into the ocean interior north of the Polar Front (PF) (Piola and Georgi, 1982; Bostock et al., 2013). South of the PF, upwelling CDW mixes with water masses on the Antarctic shelves which, through brine rejection in polynyas, heat loss and/or supercooling in contact with ice shelves, feed into the formation of shelf bottom water masses (e.g., Orsi et al., 1999; Ohshima et al., 2013). Such shelf bottom waters overflow the shelf edge whereby they incorporate CDW to eventually form Antarctic Bottom Water (AABW) which penetrates north and ventilates the abyss of all ocean basins (Orsi et al., 1999; Figs. 4.1 and 4.2).

The northward export of Antarctic intermediate and bottom waters is balanced by the mid-depth return flow of NADW, PDW and IDW (e.g., Lumpkin and Speer, 2007). Today, the majority of the global deep ocean is ventilated by water masses sourced from the marginal seas of the North Atlantic where heat loss of formerly (sub) tropical saline surface waters drives the formation of North Atlantic Deep Water (NADW) (Talley and McCartney, 1982; Broecker, 1991; Lilly et al., 1999; Ronski and Budéus, 2005; Kuhlbrodt et al., 2007; Fig. 4.1). In contrast to the North Atlantic, no deep water formation takes place in the modern North Pacific (Warren, 1983; Emile-Geay et al., 2003). The deep water masses associated with the return flow in the Indian and Pacific basins are pre-dominantly generated from slow mixing and diffusion so that North PDW is the oldest deep water in the modern ocean, characterised by low oxygen and high nutrient contents (Mantyla and Reid, 1995; Reid, 1997; Lumpkin and Speer, 2007; Kawabe and Fujio, 2010). This meridional flow pattern has been described as two global-scale meridional circulation cells, the upper one of which is pre-dominantly driven by

wind-induced upwelling in the Southern Ocean and the lower one by diffusion in the ocean interior (e.g., Lumpkin and Speer, 2007; Marshall and Speer, 2012; Talley, 2013). As such, the modern deep Indian and Pacific Oceans are dominated by diffusion-driven lower cell circulation rendering the Atlantic basin unique as both cells share a surface ocean water source through NADW formation in the North Atlantic as an integral part of the Atlantic Meridional Overturning Circulation (AMOC) (e.g., Lumpkin and Speer, 2007).

It has been recognised early on that the AMOC may have more than one stable state (e.g., Stommel, 1961), which in turn has been identified to play an important role in the interhemispheric distribution of heat in a millennial-scale bipolar seesaw pattern, i.e. cooling in one hemisphere is accompanied by warming in the other (e.g., Broecker, 1998; Blunier and Brook, 2001; Stocker and Johnson, 2003; Barker et al., 2009; Shakun et al., 2012). Thereby, the interhemispheric lead and lag relationship is subject to discussion (e.g., Steig and Alley, 2002; Schmittner et al., 2003; Huybers and Denton, 2008; Huybers, 2009; Barker et al., 2011, WAIS Divide project members, 2015). Stocker and Johnson (2003) postulated a bipolar seesaw model recognising the Southern Ocean's thermal inertia dampening the response to abrupt temperature changes. The interhemispheric distribution of heat is however expressed in shifts of oceanic fronts and sea ice extension in the Southern Ocean (Gersonde et al., 2005; Barker et al., 2009). The position of Southern Ocean fronts controls, in turn, the interbasin exchange of water masses, including the surface return flow of warm and saline waters to the North Atlantic Ocean thus acting as a potential AMOC feedback mechanism (Bjastoch et al., 2009; Beal et al., 2011; De Deckker et al., 2012; Dyez et al., 2014; Lamy et al., 2015).

In addition, the position of oceanic fronts is tied to outcropping isoneutrals in the Southern Ocean which implies significant control of meridional frontal movements and associated sea ice extent on the vertical distribution of water masses (e.g., Ferrari et al., 2014). During glacial periods, the interface between NADW and AABW shoaled (e.g., Sarnthein et al., 1994; Curry and Oppo, 2005) leading to deep stratification, in particular in the Southern Ocean (e.g., Anderson et al., 2009; Skinner et al., 2010; Burke and Robinson, 2012). Such deep stratification has been considered to contribute significantly to sequestration of carbon in the glacial deep ocean (Knox and McElroy, 1984; Sarmiento and Toggweiler, 1984; Siegenthaler and Wenk, 1984), acting as a positive feedback mechanism towards Earth's peak glacial state (e.g., Toggweiler, 1999; Blunier and Brook, 2001). Across the deglacial, such deeply stored carbon is then released back into the atmosphere through intensification of deep upwelling in the Southern Ocean caused by the southwards migration of the Southern Hemisphere westerly wind belt (SWW; e.g., Toggweiler, 1999; Toggweiler et al., 2006; Anderson et al., 2009; Burke and Robinson, 2012). The Southern Ocean dynamics during these glacial-interglacial re-organisations seem critically associated with the global overturning circulation system (cf. Anderson et al., 2009; Burke and Robinson, 2012; Marshall and Speer, 2012; Talley, 2013). Investigations of past deep Southern Ocean circulation have, however, been hampered by the lack of suitable high-resolution archives. Past efforts have shown that deep-sea corals are a suitable

archive for multiple proxy reconstructions (see Robinson et al., 2014 for a recent review). Deep-sea corals are highly abundant in critical Southern Ocean locations (Burke et al., 2010; Thiagarajan et al., 2013; Margolin et al., 2014), and it has been demonstrated that they reliably incorporate the Nd isotope signature of ambient seawater (Copard et al., 2010; van de Flierdt et al., 2010; Chapter 3).

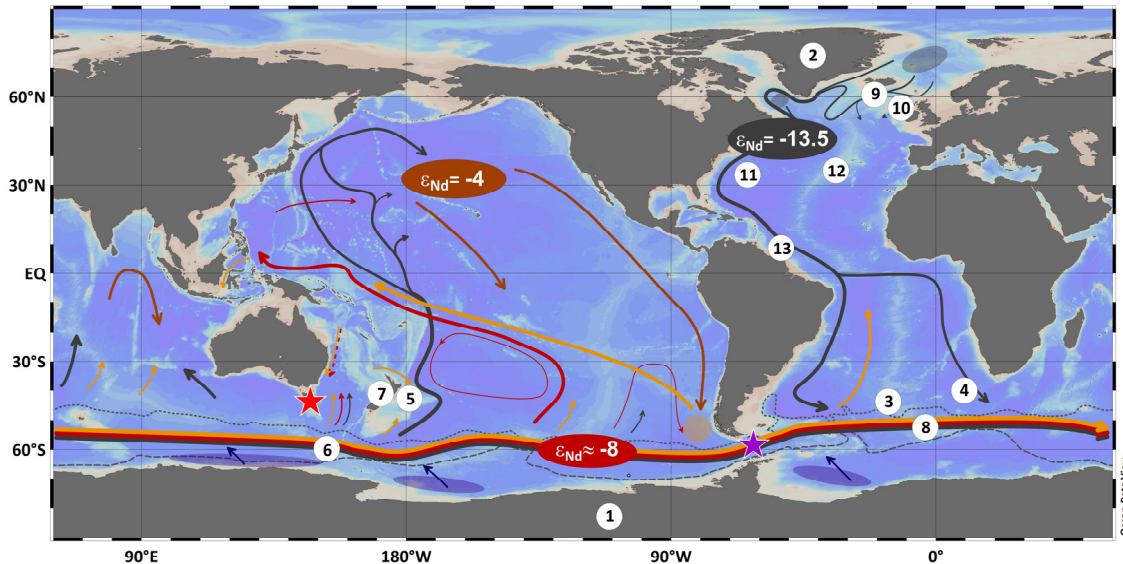


**Figure 4.1:** Global map with simplified sub-surface ocean circulation superimposed (after Piola and Georgi, 1982; Talley and McCartney, 1982; Reid, 1989, 1994, 1997; McCartney, 1992; Mantyla and Reid, 1995; Sokolov and Rintoul, 2000; Macdonald et al., 2009; Kawabe and Fujio, 2010; Bostock et al., 2013; base map generated with ODV: Schlitzer, 2012). Dark grey: North Atlantic Deep Water (NADW) and Lower Circumpolar Deep Water (LCDW); red: Upper Circumpolar Deep Water (UCDW) and Indian Deep Water (IDW) as a result of interior mixing; yellow: Antarctic Intermediate Water (AAIW). Hatched areas indicate main formation regions for NADW (grey), AAIW (yellow) and AABW (Antarctic Bottom Water; deep blue). Note that AABW fills the abyss of all major ocean basins (not shown here; see Orsi et al., 1999 and references therein) and that AAIW is also formed along the Antarctic Circumpolar Current (ACC) in all ocean basins (e.g., Piola and Georgi, 1982; Bostock et al., 2013). Stippled and dashed grey lines in the Southern Ocean indicate the Subantarctic Front (SAF) and the southern ACC front (SACC), respectively (Orsi et al., 1995). Global seawater Nd isotope systematics represented by NADW ( $\epsilon_{Nd} = -13.5$ ; Piepgras and Wasserburg, 1987), PDW ( $\epsilon_{Nd} = -4$ ; Amakawa et al., 2009) and UCDW ( $\epsilon_{Nd} = -8$ ; Stichel et al., 2012; Chapter 3). Red star: deep-sea coral sampling location south of Tasmania (Hines et al., 2015; this study). Purple star: deep-sea coral sampling locations in the Drake Passage (Robinson and van de Flierdt, 2009; Burke and Robinson, 2012; Chen et al., 2015; Burke et al., unpubl. data; this study). White dots denote locations presented in Figures 4.5 and 4.7. (1) WAIS Divide oxygen isotope (WAIS Divide project members, 2013) and CO<sub>2</sub> record (Marcott et al., 2014). (2) NGRIP oxygen isotope record (Andersen et al., 2006; Svensson et al., 2006). (3) Nd isotope record from MD07-3076 in the deep western South Atlantic basin (3770 m; Skinner et al., 2013). (4) Cape Basin Nd isotope record from TNO57-21 in the deep eastern Atlantic (4981 m; Piotrowski et al., 2005, 2012). (5) Nd isotope records extracted from CHAT5K (4240 m) and CHAT10k (3003 m) at Chatham Rise (Noble et al., 2013). (6) Opal flux record of upwelling intensity from E27-23 in the Southwest Pacific sector of the Southern Ocean (Anderson et al., 2009). (7) Stable isotope record of westerly wind intensity from New Zealand Hollyhock cave in the Northwest of the South Island (Whittaker et al., 2011). (8) Opal flux record of upwelling intensity from TNO57-13 in the Atlantic sector of the Southern Ocean (Anderson et al., 2009). (9) Subsurface oxygen isotope data (Thornalley et al., 2010) and mid-depth (1237 - 2303 m) ventilation ages from South of Iceland (Thornalley et al., 2011). (10) Nd isotope record from Rockall Trough core ODP980 (2168 m) in the Northeast Atlantic (Crocket et al., 2011). (11) Mid-depth deep-sea coral Nd isotope and radiocarbon data from the New England seamounts (Wilson et al., 2014) and deep Bermuda Rise where two <sup>231</sup>Pa/<sup>230</sup>Th records have been extracted from OCE326-GGC5 (4550 m; McManus et al., 2004) and ODP1063 (4584 m; Böhm et al., 2015). (12) Mid-depth (2150 m) <sup>231</sup>Pa/<sup>230</sup>Th from core MD95-2037 in the central North Atlantic (Gherardi et al., 2009). (13) Intermediate depth (946 m) Nd isotope record from Demerara Rise core KNR197-46CDH (Huang et al., 2014).

Neodymium (Nd) isotopes can serve as a powerful chemical water mass tracer due to their quasi-conservative behaviour in the open ocean (e.g., von Blanckenburg, 1999). Water masses acquire their Nd isotope signature mainly in their source region in vicinity to the continental margins (Frank, 2002; Goldstein and Hemming, 2003). The Nd isotopic composition is usually expressed as  $\epsilon_{\text{Nd}} = ((^{143}\text{Nd}/^{144}\text{Nd}_{\text{sample}})/(^{143}\text{Nd}/^{144}\text{Nd}_{\text{CHUR}}) - 1) \times 10,000$  where CHUR is the chondritic uniform reservoir (Jacobsen and Wasserburg, 1980). The oceanic residence time of Nd is  $\sim 400 - 2000$  years (Tachikawa et al., 1999, 2003), with more recent studies pointing towards the lower end of this range (Siddall et al., 2008; Arsouze et al., 2009). The global distribution of dissolved Nd isotopes in the ocean is dominated by two source regions of distinct isotopic composition, i.e. the North Atlantic, where NADW forms with  $\epsilon_{\text{Nd}} \approx -13.5$  (Piepgras and Wasserburg, 1987), and the North Pacific, where a volcanogenic signature of  $\epsilon_{\text{Nd}} \approx -4$  (Amakawa et al., 2009) is imprinted on PDW. As the Southern Ocean circumpolar flow is mainly the result of conservative mixing between PDW and NADW, the major water masses in the Drake Passage, i.e. AAIW, UCDW and LCDW, are characterised by intermediate values of  $\epsilon_{\text{Nd}} = -7.6 \pm 0.2$  to  $\epsilon_{\text{Nd}} = -8.6 \pm 0.2$  (Stichel et al., 2012; Chapter 3). Due to strong isoneutral and dianeutral mixing in the lee of topography (St. Laurent et al., 2012; Thompson and Sallée, 2012; Watson et al., 2013) observed zonal Nd isotope variability is generally small in the Southern Ocean (cf. Carter et al., 2012; Stichel et al., 2012; Garcia-Solsona et al., 2014; Rickli et al., 2014; Basak et al., 2015). Variability is most pronounced in locally formed SAMW/AAIW and AABW as a result from non-conservative behaviour of source waters on the Antarctic shelves (Carter et al., 2012; Stichel et al., 2012; Rickli et al., 2014; Basak et al., 2015). Although recent findings question past isotopic stability of global endmembers (Wilson et al., 2014; Böhm et al., 2015; Roberts and Piotrowski, 2015), and thus limit quantitative conclusions, Nd isotopes still serve as a powerful qualitative tool to trace water mass origin and admixture.

This work presents the first mid-depth Nd isotope records from two locations in the Southern Ocean covering the time interval from 26 to 11 thousand years before present (BP). The time series reveal high-frequency Nd isotope variability of  $\sim 2$  epsilon units in the Drake Passage and a pronounced Nd isotope shift of  $\sim 3$  epsilon units near Tasmania. The different nature of both records raises the question about the dynamics associated with the observed variability.

## 4.2. Material and Methods

For this study, Nd isotope data was extracted from Southern Ocean deep-sea corals which serve as a high-resolution, multi-proxy archive with precise age control by uranium-series dating (see Robinson et al., 2014 for a recent review). Deep-sea corals are prime archives in areas of high current speeds providing a unique opportunity to reconstruct Southern Ocean water mass properties across the last deglaciation.

#### 4.2.1. Drake Passage coral samples

In order to reconstruct the past Nd isotopic composition in the Drake Passage, we used 43 fossil specimens collected by dredging and trawling during three different cruises in the Drake Passage (NBP0805, NBP1103 and LMG0605) between 2006 and 2011.

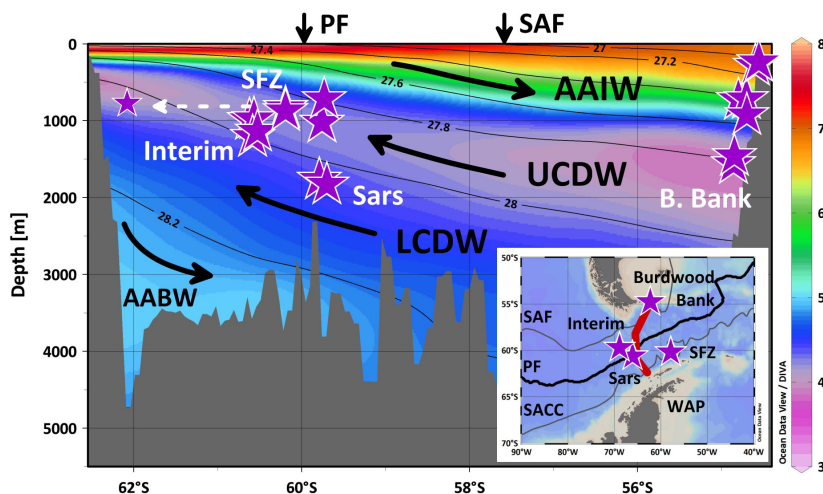


**Figure 4.2:** Latitudinal section of oxygen concentration (red line in inset) across the Drake Passage (in ml/l; WOA13; Garcia et al., 2013; generated with ODV software: Schlitzer, 2012). Purple stars indicate coral sample locations at Shackleton Fracture Zone (SFZ), Interim and Sars seamounts, and Burdwood Bank. Thin black lines represent surfaces of neutral density anomaly  $\gamma^n$  (Jackett and McDougall, 1997; in  $\text{kg/m}^3$ ). Sample locations superimposed on the oxygen section are strictly latitudinal so that SFZ is plotted in between Interim and Sars seamounts. Based on hydrography and the bathymetric orientation of the Drake Passage channel the actual SFZ location would translate into the position indicated by the dashed white arrow and the small purple star. Black arrows schematise orientation of net meridional flow. Note that the pre-dominant (mean) flow in the Drake Passage is zonal (see text). AAIW: Antarctic Intermediate Water; UCDW: Upper Circumpolar Deep Water; LCDW: Lower Circumpolar Deep Water; AABW: Antarctic Bottom Water. Note the oxygen minimum in the UCDW depth range resulting from PDW admixture. Inset shows map with sampling locations across the Drake Passage and their position in relation to ACC fronts (Orsi et al., 1995). SAF: Subantarctic Front; PF: Polar Front; SACC: Southern ACC front; WAP: West Antarctic Peninsula.

The sample set includes the species *Desmophyllum dianthus* ( $n = 27$ ), *Balanophyllia malouinensis* ( $n = 8$ ), *Flabellum curvatum* ( $n = 3$ ), *Gardinieria antarctica* ( $n = 3$ ) and *Caryophyllia spp.* ( $n = 2$ ). All samples have been precisely dated by uranium-series isotopes and analysed for their radiocarbon content (Burke et al., 2010; Chen et al., 2015; Burke et al., unpubl. data). They cover a time period from 26.0 to 12.2 kyr BP. Sampling locations were at Burdwood Bank (318 to 1515.5 m), Sars Seamount (695 to 1750 m), Interim Seamount (982.5 to 1195.5 m), and the Shackleton Fracture Zone (SFZ) (Figs. 4.1 and 4.2; Burke et al., 2010; Margolin et al., 2014). As illustrated in Figure 4.2, the samples are pre-dominantly bathed in UCDW, AAIW/SAMW or mixed layer water masses. In the Drake Passage, the boundary between AAIW and UCDW has been defined at  $\gamma^n = 27.6 \text{ kg/m}^3$ , whereas the lower limit of UCDW is marked by a smooth transition to underlying LCDW centred near  $\gamma^n = 28.0 \text{ kg/m}^3$  (Sudre et al., 2011). Hence, some samples are bathed by a mixture of UCDW and LCDW (Fig. 4.2).

#### 4.2.2. Deep-sea corals from south of Tasmania

A second set of 29 deep-sea corals has been selected from south of Tasmania (Thiagarajan et al., 2013). The coral samples were collected in 2008-2009 during cruise TN-228 on the R/V Thompson (43°S - 47°S and 144°E - 152°E) using the remotely operated deep submergence vehicle JASON. All deep-sea corals are of the species *Desmophyllum dianthus*, and were collected from a narrow band between 1480 and 1689 m water depth at the southern margin of Tasmania (~44°S and ~147°E) (Figs. 4.1 and 4.3). Samples have been analysed for U-series ages and radiocarbon content and cover the time interval from 26.2 to 12.7 kyr BP (Hines et al., 2015). These corals are currently bathed in UCDW and influenced by admixed PDW as illustrated in Figure 4.3 (Reid and Lynn, 1971; Callahan, 1972; Sokolov and Rintoul, 2000; Macdonald et al., 2009). The lower boundary of AAIW in the area has been demonstrated to be at ~1200 m water depth (i.e.  $\sigma_0 = 27.3 \text{ kg/m}^3$ , roughly equivalent to  $\gamma^n = 27.55 \text{ kg/m}^3$ ; Bostock et al., 2013 and references therein; Fig. 4.3).

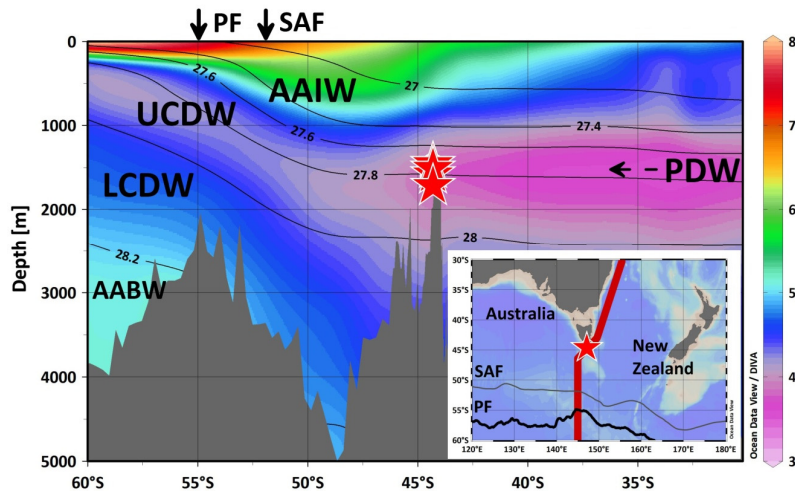


**Figure 4.3:** Latitudinal section (red line in inset) of oxygen concentration from the Tasman Sea toward Antarctica (in ml/l; WOA13: Garcia et al., 2013; generated with ODV software: Schlitzer, 2012). Thin black lines indicate surfaces of neutral density anomaly  $\gamma^n$  (Jackett and McDougall, 1997; in  $\text{kg/m}^3$ ). Red stars represent coral sample locations. Note the oxygen minimum associated with the admixture of PDW (Pacific Deep Water) from the north (Reid and Lynn, 1971; Callahan, 1972). Abbreviations as in Fig. 4.2.

#### 4.2.3. Sample preparation and analytical procedures

The analytical procedures for Nd isotope analyses followed the approach outlined in Chapter 2. In brief, physically and chemically cleaned deep-sea coral samples were processed through anion exchange chromatography for U-series dating (Burke and Robinson, 2012; Chen et al., 2015; Hines et al., 2015; Burke et al., unpubl. data). The Nd fraction was subsequently purified during a two-step column chemistry, optimised for TIMS Nd isotope analyses as  $\text{NdO}^+$ . Full procedural blanks of combined U, Th and Nd separation from the aragonitic sample matrix ranged from 2 to 35 pg Nd, averaging at 12 pg ( $n = 30$ ). Full procedural blanks of Nd separation from aragonitic sample matrix alone yielded 1 to 17 pg Nd, averaging at 4 pg ( $n = 10$ ).

Over a period of 26 months 5 and 15 ng loads of pure JNdi-1 were analysed ( $^{143}\text{Nd}/^{144}\text{Nd} = 0.512105 \pm 0.000009$ , 2SD,  $n = 110$ ) to monitor instrumental offset and normalise mass bias corrected  $^{143}\text{Nd}/^{144}\text{Nd}$  ratios of samples to the reference ratio of  $^{143}\text{Nd}/^{144}\text{Nd} = 0.512115 \pm 0.000007$  (Tanaka et al., 2000). Repeated analyses of 10 and 30 ng Nd loads of BCR-2 rock reference material define our  $2\sigma$  external reproducibility yielding  $^{143}\text{Nd}/^{144}\text{Nd} = 0.512637 \pm 0.000011$  ( $n = 32$ ). A similar precision was obtained from replicate analyses of 10 and 30 ng loads of our in-house coral standard ( $^{143}\text{Nd}/^{144}\text{Nd} = 0.512336 \pm 0.000009$ ;  $n = 23$ ).

### 4.3. Results

#### 4.3.1. Drake Passage deep-sea coral data

Results on the Nd isotopic composition of the aragonitic skeletons of deep-sea corals are reported in Table 4.1 and illustrated in Figure 4.4 according to the water mass they were collected from (i.e. AAIW and UCDW).

The aragonitic skeletons of *D. dianthus*, *F. curvatum* and *Caryophyllia* have been shown to reliably record ambient seawater Nd isotope signatures and are hence considered in detail. Three deep-sea corals from the sample set are currently bathed in AAIW or mixed layer waters and show relatively invariable Nd isotope signatures of  $\epsilon_{\text{Nd}} = -6.0 \pm 0.2$  to  $\epsilon_{\text{Nd}} = -6.4 \pm 0.2$ . Corals recovered from UCDW depths range in their Nd isotopic composition from  $\epsilon_{\text{Nd}} = -6.3 \pm 0.2$  to  $\epsilon_{\text{Nd}} = -8.4 \pm 0.2$  and show a trend towards less radiogenic values from 26 to 12.2 kyr BP (Table 4.1; Fig. 4.4). The Antarctic Cold Reversal (ACR) values (and most of the early Holocene values; Chapter 6) overlap with the range of modern seawater reported from the Drake Passage (Piepgras and Wasserburg, 1987; Stichel et al., 2012; Fig. 4.4). Superimposed on this long-term trend, we observe significant short-term variability (Fig. 4.4). In particular, during times of high temporal resolution in the mid to late deglacial from ~17 to 12 kyr BP we find centennial-scale fluctuations of ~2  $\epsilon_{\text{Nd}}$  in the UCDW record, the amplitude of which is, however, reduced to ~1 epsilon unit after about 14.7 kyr BP.

It is noted that eight specimens of *B. malouinensis* are excluded from further interpretation as they have been shown to not reliably record ambient seawater Nd isotopic compositions. This may be due to their porous skeletal structure and/or contamination in their preferred sedimentary habitat (Chapter 3). Nevertheless, we report the results here (and illustrate them in Figure 4.4) as future work may resolve this issue. The same reasoning applies to three specimens of *G. antarctica*, a species which has not yet been calibrated for Nd isotopes. However, it should be noted that *G. antarctica* may incorporate a seawater-derived rare earth element signal, as this species, recovered from 1064 to 1196 m water depth at Interim seamount, was not associated with sedimented areas, which may cause the problems observed with *B. malouinensis* (Chapter 3).

Table 4.1: Drake Passage deep-sea coral results (see caption for details).

| Sample                       | Location       | Lat            | Long           | Species                    | Depth (m)    | Age (kyr BP) | 2SE <sup>a</sup> | <sup>143</sup> Nd/ <sup>144</sup> Nd <sup>b</sup> | 2SE             | ε <sub>Nd</sub> <sup>c</sup> | 2SE         | 2SD <sup>d</sup> | Smp Nd (ng/g) | 2SE (ep)       |
|------------------------------|----------------|----------------|----------------|----------------------------|--------------|--------------|------------------|---|-----------------|------------------------------|-------------|------------------|---------------|----------------|
| UCDW depth range:            |                |                |                |                            |              |              |                  |   |                 |                              |             |                  |               |                |
| NBP0805-DR36-Dc-A-2a         | Sars           | -59.707        | -69.008        | <i>D. dianthus</i>         | 1750         | 12.23        | 0.09             | 0.512229  | 0.000004        | -7.97                        | 0.07        | 0.21             | 73.5          | 0.00153        |
| <b>NBP0805-DR36-Dc-A-2b</b>  | <b>Sars</b>    | <b>-59.707</b> | <b>-69.008</b> | <b><i>D. dianthus</i></b>  | <b>1750</b>  | -            | -                | <b>0.512236</b>                                   | <b>0.000005</b> | <b>-7.84</b>                 | <b>0.11</b> | <b>0.21</b>      | <b>80.4</b>   | <b>0.00101</b> |
| NBP1103-DH120-Dc-25          | Sars           | -59.797        | -68.965        | <i>D. dianthus</i>         | 1701         | 12.56        | 0.12             | 0.512232  | 0.000004        | -7.93                        | 0.08        | 0.21             | 96.1          | 0.00043        |
| NBP0805-DR36-Dc-A-3          | Sars           | -59.707        | -69.008        | <i>D. dianthus</i>         | 1750         | 12.74        | 0.10             | 0.512228  | 0.000003        | -8.00                        | 0.07        | 0.21             | 138.6         | 0.00423        |
| NBP1103-DH120-Dn-1a          | Sars           | -59.797        | -68.965        | <i>D. dianthus</i>         | 1701         | 13.11        | 0.13             | 0.512255  | 0.000006        | -7.48                        | 0.10        | 0.21             | 145.5         | 0.00058        |
| <b>NBP1103-DH120-Dn-1b</b>   | <b>Sars</b>    | <b>-59.797</b> | <b>-68.965</b> | <b><i>D. dianthus</i></b>  | <b>1701</b>  | <b>13.16</b> | <b>0.13</b>      | <b>0.512250</b>                                   | <b>0.000005</b> | <b>-7.57</b>                 | <b>0.10</b> | <b>0.21</b>      | <b>147.6</b>  | <b>0.00055</b> |
| NBP0805-DR23-Dc-A-5          | SFZ            | -60.182        | -57.834        | <i>D. dianthus</i>         | 819          | 13.13        | 0.15             | 0.512215  | 0.000004        | -8.25                        | 0.08        | 0.21             | 81.8          | 0.00128        |
| NBP1103-DH120-Dc-33          | Sars           | -59.797        | -68.965        | <i>D. dianthus</i>         | 1701         | 14.05        | 0.16             | 0.512265  | 0.000006        | -7.27                        | 0.12        | 0.21             | 133.2         | 0.00062        |
| NBP1103-DH120-Dc-21a         | Sars           | -59.797        | -68.965        | <i>D. dianthus</i>         | 1701         | 14.10        | 0.11             | 0.512266  | 0.000006        | -7.26                        | 0.12        | 0.21             | 129.9         | 0.00068        |
| <b>NBP1103-DH120-Dc-21b</b>  | <b>Sars</b>    | <b>-59.797</b> | <b>-68.965</b> | <b><i>D. dianthus</i></b>  | <b>1701</b>  | <b>14.06</b> | <b>0.12</b>      | <b>0.512266</b>                                   | <b>0.000005</b> | <b>-7.26</b>                 | <b>0.09</b> | <b>0.21</b>      | <b>129.8</b>  | <b>0.00061</b> |
| NBP1103-DH117-Dn-7           | Sars           | -59.764        | -68.936        | <i>D. dianthus</i>         | 981          | 14.14        | 0.16             | 0.512258  | 0.000005        | -7.41                        | 0.09        | 0.21             | 114.8         | 0.00043        |
| NBP1103-DH117-Dc-20          | Sars           | -59.764        | -68.936        | <i>D. dianthus</i>         | 981          | 14.18        | 0.24             | 0.512244  | 0.000005        | -7.68                        | 0.10        | 0.21             | 263.1         | 0.00193        |
| NBP1103-DH117-Dc-29a         | Sars           | -59.764        | -68.936        | <i>D. dianthus</i>         | 981          | 14.61        | 0.15             | 0.512269  | 0.000006        | -7.20                        | 0.12        | 0.21             | 29.5          | 0.00028        |
| <b>NBP1103-DH117-Dc-29b</b>  | <b>Sars</b>    | <b>-59.764</b> | <b>-68.936</b> | <b><i>D. dianthus</i></b>  | <b>981</b>   | -            | -                | <b>0.512268</b>                                   | <b>0.000008</b> | <b>-7.21</b>                 | <b>0.15</b> | <b>0.21</b>      | <b>61.8</b>   | <b>0.00034</b> |
| NBP0805-DR35-Dc-A-2a         | Sars           | -59.723        | -68.881        | <i>D. dianthus</i>         | 695          | 14.65        | 0.09             | 0.512255  | 0.000006        | -7.46                        | 0.11        | 0.21             | 53.7          | 0.00049        |
| NBP1103-DH74-Dc-3            | Interim        | -60.61         | -66.004        | <i>D. dianthus</i>         | 1064         | 14.71        | 0.24             | 0.512214  | 0.000006        | -8.27                        | 0.13        | 0.21             | 124.5         | 0.00141        |
| NBP1103-DH120-Dc-32          | Sars           | -59.797        | -68.965        | <i>D. dianthus</i>         | 1701         | 14.78        | 0.13             | 0.512242  | 0.000005        | -7.72                        | 0.10        | 0.21             | 164.5         | 0.00105        |
| NBP1103-DH117-Dc-36          | Sars           | -59.764        | -68.936        | <i>D. dianthus</i>         | 981          | 14.89        | 0.16             | 0.512315  | 0.000007        | -6.31                        | 0.14        | 0.21             | 43.7          | 0.00067        |
| NBP1103-DH88-Cc-1c           | Interim        | -60.560        | -65.957        | <i>Caryophyllia</i>        | 982.5        | 15.17        | 0.18             | 0.512282  | 0.000018        | -6.94                        | 0.35        | 0.35             | 28.5          | 0.00185        |
| NBP1103-DH75-Dc(f)-37        | Interim        | -60.601        | -66.002        | <i>D. dianthus</i>         | 1195.5       | 15.22        | 0.14             | 0.512228  | 0.000007        | -7.99                        | 0.13        | 0.21             | 244.8         | 0.00093        |
| NBP1103-DH74-Dc-4            | Interim        | -60.606        | -66.004        | <i>D. dianthus</i>         | 1064         | 15.25        | 0.36             | 0.512231  | 0.000004        | -7.94                        | 0.09        | 0.21             | 304.7         | 0.00105        |
| NBP1103-DH88-Cc-1a           | Interim        | -60.560        | -65.957        | <i>Caryophyllia</i>        | 982.5        | 15.41        | 0.13             | 0.512234  | 0.000005        | -7.89                        | 0.10        | 0.21             | 90.0          | 0.00048        |
| <b>NBP1103-DH88-Cc-1b</b>    | <b>Interim</b> | <b>-60.560</b> | <b>-65.957</b> | <b><i>Caryophyllia</i></b> | <b>982.5</b> | -            | -                | <b>0.512238</b>                                   | <b>0.000005</b> | <b>-7.81</b>                 | <b>0.10</b> | <b>0.21</b>      | <b>152.1</b>  | <b>0.00061</b> |
| NBP0805-DR23-Dc-A-6          | SFZ            | -60.182        | -57.834        | <i>D. dianthus</i>         | 819          | 15.63        | 0.10             | 0.512252  | 0.000006        | -7.52                        | 0.12        | 0.21             | 48.3          | 0.00067        |
| NBP1103-DH19-Fc-1            | B. Bank        | -54.809        | -62.166        | <i>F. curvatum</i>         | 1515.5       | 15.76        | 0.29             | 0.512299  | 0.000006        | -6.61                        | 0.11        | 0.21             | 35.4          | 0.00032        |
| NBP1103-DH117-Dc-9a          | Sars           | -59.764        | -68.936        | <i>D. dianthus</i>         | 981          | 16.85        | 0.34             | 0.512291  | 0.000006        | -6.76                        | 0.11        | 0.21             | 118.5         | 0.00073        |
| <b>NBP1103-DH117-Dc-9b</b>   | <b>Sars</b>    | <b>-59.764</b> | <b>-68.936</b> | <b><i>D. dianthus</i></b>  | <b>981</b>   | <b>17.21</b> | <b>0.35</b>      | <b>0.512262</b>                                   | <b>0.000005</b> | <b>-7.33</b>                 | <b>0.09</b> | <b>0.21</b>      | <b>274.8</b>  | <b>0.00123</b> |
| NBP1103-DH40-Dc-3a           | SFZ            | -60.179        | -57.837        | <i>D. dianthus</i>         | 806          | 18.05        | 0.34             | 0.512247  | 0.000008        | -7.63                        | 0.15        | 0.21             | 151.2         | 0.00155        |
| <b>NBP1103-DH40-Dc-3b</b>    | <b>SFZ</b>     | <b>-60.179</b> | <b>-57.837</b> | <b><i>D. dianthus</i></b>  | <b>806</b>   | <b>18.63</b> | <b>0.62</b>      | <b>0.512235</b>                                   | <b>0.000005</b> | <b>-7.87</b>                 | <b>0.09</b> | <b>0.21</b>      | <b>430.9</b>  | <b>0.00157</b> |
| NBP1103-DH43-Dc-6            | SFZ            | -60.182        | -57.833        | <i>D. dianthus</i>         | 823          | 19.63        | 0.38             | 0.512292  | 0.000010        | -6.74                        | 0.19        | 0.21             | 145.6         | 0.00163        |
| NBP0805-DR23-Dc-A-4          | SFZ            | -60.182        | -57.834        | <i>D. dianthus</i>         | 819          | 20.27        | 0.34             | 0.512256  | 0.000006        | -7.45                        | 0.11        | 0.21             | 279.0         | 0.00210        |
| NBP1103-DH43-Dc-1            | SFZ            | -60.182        | -57.833        | <i>D. dianthus</i>         | 823          | 20.37        | 0.12             | 0.512335  | 0.000006        | -5.91                        | 0.12        | 0.21             | 65.3          | 0.00092        |
| NBP0805-DR27-Dc-A-1          | Interim        | -60.547        | -65.949        | <i>D. dianthus</i>         | 1134         | 21.47        | 0.22             | 0.512253  | 0.000006        | -7.51                        | 0.11        | 0.21             | 261.3         | 0.00065        |
| NBP1103-DH40-Dc-5            | SFZ            | -60.179        | -57.837        | <i>D. dianthus</i>         | 806          | 22.58        | 0.16             | 0.512267  | 0.000006        | -7.24                        | 0.11        | 0.21             | 48.6          | 0.00051        |
| NBP1103-DH43-Dc-8b           | SFZ            | -60.182        | -57.833        | <i>D. dianthus</i>         | 823          | 22.70        | 0.31             | 0.512314  | 0.000009        | -6.32                        | 0.18        | 0.21             | 49.3          | 0.00103        |
| <b>NBP1103-DH43-Dc-8a</b>    | <b>SFZ</b>     | <b>-60.179</b> | <b>-57.003</b> | <b><i>D. dianthus</i></b>  | <b>823</b>   | <b>24.96</b> | <b>1.23</b>      | <b>0.512304</b>                                   | <b>0.000005</b> | <b>-6.52</b>                 | <b>0.09</b> | <b>0.21</b>      | <b>393.6</b>  | <b>0.00248</b> |
| NBP0805-DR23-Dc-A-1a         | SFZ            | -60.182        | -57.834        | <i>D. dianthus</i>         | 819          | 25.59        | 0.32             | 0.512308  | 0.000005        | -6.43                        | 0.10        | 0.21             | 75.6          | 0.00438        |
| <b>NBP0805-DR23-Dc-A-1b*</b> | <b>SFZ</b>     | <b>-60.182</b> | <b>-57.834</b> | <b><i>D. dianthus</i></b>  | <b>819</b>   | <b>26.00</b> | <b>0.54</b>      | <b>0.512306</b>                                   | <b>0.000006</b> | <b>-6.48</b>                 | <b>0.12</b> | <b>0.21</b>      | <b>117.2</b>  | <b>0.00336</b> |

Table 4.1 (continued)

| Sample                   | Location | Lat     | Long    | Species                | Depth (m) | Age (kyr BP) | $2\sigma^a$ | $^{143}\text{Nd}/^{144}\text{Nd}^b$ | $2\sigma^c$ | $\epsilon_{\text{Nd}}^c$ | $2\sigma^d$ | Smp Nd (ng/g) | $2\sigma^e$ (ep) |         |
|--------------------------|----------|---------|---------|------------------------|-----------|--------------|-------------|-------------------------------------|-------------|--------------------------|-------------|---------------|------------------|---------|
| AAIW depth range:        |          |         |         |                        |           |              |             |                                     |             |                          |             |               |                  |         |
| LMG06-05-9-3             | B. Bank  | -54.485 | -62.214 | <i>F. curvatum</i>     | 318       | 13.65        | 0.07        | 0.512311                            | 0.000008    | -6.38                    | 0.16        | 0.21          | 7.3              | 0.00023 |
| NBP0805-TB04-Dn-A-10a    | B. Bank  | -54.734 | -62.216 | <i>D. dianthus</i>     | 816       | 16.34        | 0.31        | 0.512311                            | 0.000007    | -6.37                    | 0.13        | 0.21          | 50.1             | 0.00036 |
| NBP0805-TB04-Dn-A-10b*   | B. Bank  | -54.734 | -62.216 | <i>D. dianthus</i>     | 816       | 16.52        | 0.19        | 0.512315                            | 0.000006    | -6.30                    | 0.11        | 0.21          | 39.2             | 0.00024 |
| NBP1103-DH14-Fc-277      | B. Bank  | -54.713 | -62.250 | <i>F. curvatum</i>     | 726.5     | 16.41        | 0.16        | 0.512331                            | 0.000005    | -5.99                    | 0.09        | 0.21          | 88.8             | 0.00047 |
| <i>B. malouinensis</i> : |          |         |         |                        |           |              |             |                                     |             |                          |             |               |                  |         |
| NBP1103-DH14-Bn-278      | B. Bank  | -54.713 | -62.250 | <i>B. malouinensis</i> | 726.5     | 13.05        | 0.12        | 0.512335                            | 0.000006    | -5.90                    | 0.12        | 0.21          | 37.8             | 0.00036 |
| LMG06-05-9-1             | B. Bank  | -54.485 | -62.214 | <i>B. malouinensis</i> | 318       | 13.34        | 0.07        | 0.512376                            | 0.000016    | -5.12                    | 0.31        | 0.31          | 12.5             | 0.00141 |
| NBP1103-DH07-Bn-2        | B. Bank  | -54.507 | -62.228 | <i>B. malouinensis</i> | 328.5     | 13.76        | 0.09        | 0.512310                            | 0.000006    | -6.39                    | 0.11        | 0.21          | 13.9             | 0.00032 |
| NBP1103-DH16-Bc-2        | B. Bank  | -54.808 | -62.119 | <i>B. malouinensis</i> | 1418.5    | 14.01        | 0.21        | 0.512293                            | 0.000013    | -6.73                    | 0.25        | 0.25          | 36.5             | 0.00091 |
| NBP1103-DH07-Bn-3        | B. Bank  | -54.507 | -62.228 | <i>B. malouinensis</i> | 328.5     | 14.38        | 0.12        | 0.512355                            | 0.000005    | -5.51                    | 0.10        | 0.21          | 24.7             | 0.00040 |
| NBP1103-DH14-Bn-1002     | B. Bank  | -54.713 | -62.250 | <i>B. malouinensis</i> | 726.5     | 15.42        | 0.24        | 0.512305                            | 0.000006    | -6.49                    | 0.12        | 0.21          | 122.0            | 0.00110 |
| NBP1103-DH15-Bc-1        | B. Bank  | -54.772 | -62.236 | <i>B. malouinensis</i> | 894       | 16.86        | 0.18        | 0.512351                            | 0.000006    | -5.60                    | 0.12        | 0.21          | 104.4            | 0.00145 |
| <i>G. antarctica</i> :   |          |         |         |                        |           |              |             |                                     |             |                          |             |               |                  |         |
| NBP1103-DH75-Gc-4        | Interim  | -60.601 | -66.002 | <i>G. antarctica</i>   | 1195.5    | 16.18        | 0.11        | 0.512232                            | 0.000005    | -7.93                    | 0.09        | 0.21          | 118.3            | 0.00107 |
| NBP1103-DH75-Gc-3        | Interim  | -60.601 | -66.002 | <i>G. antarctica</i>   | 1195.5    | 25.90        | 0.22        | 0.512263                            | 0.000006    | -7.32                    | 0.11        | 0.21          | 256.7            | 0.00074 |
| NBP1103-DH74-Gc-2b       | Interim  | -60.633 | -66.004 | <i>G. antarctica</i>   | 1064      | 25.77        | 0.56        | 0.512253                            | 0.000004    | -7.52                    | 0.07        | 0.21          | 716.7            | 0.02491 |
| NBP1103-DH74-Gc-2a       | Interim  | -60.606 | -66.004 | <i>G. antarctica</i>   | 1064      | 26.55        | 0.61        | 0.512252                            | 0.000005    | -7.54                    | 0.11        | 0.21          | 964.5            | 0.00543 |

(a)  $2\sigma$  is the analytical  $2\sigma$  standard error.(b)  $^{143}\text{Nd}/^{144}\text{Nd}$  ratios were corrected for the offset of the measured JNdI-1 ratio of 0.512105  $\pm$  0.000009 ( $n = 110$ ) from the published value of 0.512115  $\pm$  0.000007 (Tanaka et al., 2000).(c)  $\epsilon_{\text{Nd}}$  was calculated using the present day CHUR value of  $^{143}\text{Nd}/^{144}\text{Nd} = 0.512638$  (Jacobson and Wasserburg, 1980).(d)  $2\sigma$  refers to the  $2\sigma$  standard deviation derived from the longterm reproducibility of BCR-2 standards (see text) which is the reported error.(e)  $2\sigma$  (ep) is the propagated  $2\sigma$  standard error of Nd concentrations determined by isotope dilution.

**Table 4.1:** Neodymium isotope and concentration results for deep-sea corals collected from the Shackleton Fracture Zone (SFZ), Sars and Interim seamounts, and Burdwood Bank. Samples are grouped by the modern water mass they were recovered from and sorted by age. *B. malouinensis* and *G. antarctica* are listed separately as there are concerns that these species may not reliably reproduce ambient seawater Nd isotope signatures, or have not yet been calibrated for Nd isotopes, respectively (Chapter 3). Full U-Th-Nd replicate analyses of re-sampled coral pieces are in bold; asterisks denote replicates produced from splits of a poorly homogenised crushed coral. Depth is the average water depth of the respective dredge track (see Margolin et al., 2014). Age (kyr) BP is reported in thousand years before present, i.e. 1950. All U-series data from Burke and Robinson (2012), Chen et al. (2015) and Burke (unpubl. data). ‘Smp Nd’ refers to the Nd concentration in the sample after co-precipitation and anion exchange chromatography for U-Series dating. This concentration is hence a minimum concentration, which may be too low by  $\sim 10\%$  (Chapter 2).

**Table 4.2:** Tasmanian deep-sea coral results.

| Sample                             | Latitude | Longitude | Species            | Water depth (m) | Age (kyr BP) | 2SE <sup>a</sup> | <sup>143</sup> Nd/ <sup>144</sup> Nd <sup>b</sup> | 2SE      | ε <sub>Nd</sub> <sup>c</sup> | 2SE  | Smp Nd (ng/g) | 2SE (ep) <sup>e</sup> |        |
|------------------------------------|----------|-----------|--------------------|-----------------|--------------|------------------|---|----------|------------------------------|------|---------------|-----------------------|--------|
| TN228-J2-382-1216-1350-03-1523-008 | -44.34   | 146.89    | <i>D. dianthus</i> | 1523            | 12.68        | 0.03             | 0.512276  | 0.000008 | -7.06                        | 0.16 | 0.21          | 18.2                  | 0.0005 |
| TN228-J2-382-1216-1350-03-1523-002 | -44.34   | 146.89    | <i>D. dianthus</i> | 1523            | 13.31        | 0.13             | 0.512302  | 0.000005 | -6.55                        | 0.10 | 0.21          | 101.7                 | 0.0007 |
| TN228-J2-387-1226-1635-23-1599-014 | -44.39   | 147.27    | <i>D. dianthus</i> | 1599            | 13.35        | 0.03             | 0.512282  | 0.000009 | -6.95                        | 0.17 | 0.21          | 9.0                   | 0.0005 |
| TN228-J2-387-1226-1148-20-1680-005 | -44.39   | 147.27    | <i>D. dianthus</i> | 1680            | 13.35        | 0.09             | 0.512285  | 0.000005 | -6.89                        | 0.09 | 0.21          | 302.8                 | 0.0019 |
| TN228-J2-387-1226-1148-20-1680-009 | -44.39   | 147.27    | <i>D. dianthus</i> | 1680            | 13.59        | 0.08             | 0.512240  | 0.000009 | -7.76                        | 0.17 | 0.21          | 35.7                  | 0.0006 |
| TN228-J2-387-1226-1148-20-1680-004 | -44.39   | 147.27    | <i>D. dianthus</i> | 1680            | 13.64        | 0.32             | 0.512267  | 0.000006 | -7.24                        | 0.12 | 0.21          | 62.3                  | 0.0006 |
| TN228-J2-387-1226-1635-23-1599-020 | -44.39   | 147.27    | <i>D. dianthus</i> | 1599            | 14.13        | 0.24             | 0.512265  | 0.000005 | -7.27                        | 0.10 | 0.21          | 216.9                 | 0.0009 |
| TN228-J2-387-1226-1148-20-1680-008 | -44.39   | 147.27    | <i>D. dianthus</i> | 1680            | 14.16        | 0.08             | 0.512257  | 0.000005 | -7.43                        | 0.09 | 0.21          | 122.4                 | 0.0006 |
| TN228-J2-387-1226-1148-20-1680-013 | -44.39   | 147.27    | <i>D. dianthus</i> | 1680            | 14.35        | 0.07             | 0.512243  | 0.000007 | -7.70                        | 0.13 | 0.21          | 36.7                  | 0.0005 |
| TN228-J2-387-1226-1635-23-1599-016 | -44.39   | 147.27    | <i>D. dianthus</i> | 1599            | 14.39        | 0.08             | 0.512296  | 0.000005 | -6.68                        | 0.10 | 0.21          | 122.3                 | 0.0006 |
| TN228-J2-387-1226-1148-20-1680-017 | -44.39   | 147.27    | <i>D. dianthus</i> | 1680            | 14.58        | 0.08             | 0.512251  | 0.000008 | -7.55                        | 0.16 | 0.21          | 24.1                  | 0.0005 |
| TN228-J2-387-1226-1507-22-1616-004 | -44.39   | 147.27    | <i>D. dianthus</i> | 1616            | 14.83        | 0.03             | 0.512266  | 0.000005 | -7.26                        | 0.10 | 0.21          | 55.3                  | 0.0004 |
| TN228-J2-382-1216-1010-01-1689-002 | -44.34   | 146.89    | <i>D. dianthus</i> | 1689            | 16.72        | 0.06             | 0.512386  | 0.000007 | -4.92                        | 0.13 | 0.21          | 15.8                  | 0.0006 |
| TN228-J2-382-1216-1010-01-1689-004 | -44.34   | 146.89    | <i>D. dianthus</i> | 1689            | 17.28        | 0.11             | 0.512389  | 0.000006 | -4.86                        | 0.11 | 0.21          | 113.1                 | 0.0006 |
| TN228-J2-382-1216-1010-01-1689-009 | -44.34   | 146.89    | <i>D. dianthus</i> | 1689            | 17.61        | 0.16             | 0.512370  | 0.000007 | -5.22                        | 0.14 | 0.21          | 113.9                 | 0.0006 |
| TN228-J2-383-1217-0725-01-1575-006 | -44.32   | 147.26    | <i>D. dianthus</i> | 1575            | 18.10        | 0.07             | 0.512403  | 0.000006 | -4.59                        | 0.12 | 0.21          | 23.2                  | 0.0007 |
| TN228-J2-382-1216-1350-03-1523-007 | -44.34   | 146.89    | <i>D. dianthus</i> | 1523            | 18.33        | 0.04             | 0.512387  | 0.000005 | -4.90                        | 0.10 | 0.21          | 47.4                  | 0.0005 |
| TN228-J2-383-1217-1320-05-1460-008 | -44.32   | 147.26    | <i>D. dianthus</i> | 1460            | 19.27        | 0.06             | 0.512366  | 0.000007 | -5.30                        | 0.13 | 0.21          | 31.8                  | 0.0007 |
| TN228-J2-383-1217-1320-05-1460-009 | -44.32   | 147.26    | <i>D. dianthus</i> | 1460            | 19.48        | 0.06             | 0.512374  | 0.000006 | -5.16                        | 0.12 | 0.21          | 57.1                  | 0.0007 |
| TN228-J2-382-1217-0725-01-1575-023 | -44.34   | 146.89    | <i>D. dianthus</i> | 1575            | 19.79        | 0.19             | 0.512374  | 0.000004 | -5.14                        | 0.09 | 0.21          | 604.4                 | 0.0007 |
| TN228-J2-382-1216-1350-03-1523-006 | -44.34   | 146.89    | <i>D. dianthus</i> | 1523            | 20.37        | 0.11             | 0.512348  | 0.000004 | -5.66                        | 0.08 | 0.21          | 70.4                  | 0.0006 |
| TN228-J2-382-1216-1350-03-1523-005 | -44.34   | 146.89    | <i>D. dianthus</i> | 1523            | 21.40        | 0.18             | 0.512368  | 0.000005 | -5.27                        | 0.09 | 0.21          | 313.7                 | 0.0009 |
| TN228-J2-383-1217-1320-05-1460-007 | -44.32   | 147.26    | <i>D. dianthus</i> | 1460            | 21.41        | 0.06             | 0.512338  | 0.000006 | -5.86                        | 0.12 | 0.21          | 22.3                  | 0.0006 |
| TN228-J2-382-1216-1350-03-1523-003 | -44.34   | 146.89    | <i>D. dianthus</i> | 1523            | 21.70        | 0.16             | 0.512364  | 0.000005 | -5.35                        | 0.10 | 0.21          | 420.7                 | 0.0044 |
| TN228-J2-395-0114-0057-09-1500-002 | -44.30   | 147.45    | <i>D. dianthus</i> | 1500            | 23.34        | 0.07             | 0.512382  | 0.000004 | -5.00                        | 0.09 | 0.21          | 108.5                 | 0.0006 |
| TN228-J2-395-0114-0057-09-1500-010 | -44.30   | 147.45    | <i>D. dianthus</i> | 1500            | 25.20        | 0.14             | 0.512379  | 0.000006 | -5.06                        | 0.12 | 0.21          | 108.0                 | 0.0006 |
| TN228-J2-395-0114-0057-09-1500-008 | -44.30   | 147.45    | <i>D. dianthus</i> | 1500            | 25.53        | 0.21             | 0.512340  | 0.000005 | -5.82                        | 0.10 | 0.21          | 76.0                  | 0.0007 |
| TN228-J2-382-1216-1350-03-1523-010 | -44.34   | 146.89    | <i>D. dianthus</i> | 1523            | 25.77        | 0.38             | 0.512359  | 0.000005 | -5.44                        | 0.10 | 0.21          | 495.7                 | 0.0058 |
| TN228-J2-383-1217-0725-01-1575-017 | -44.32   | 147.26    | <i>D. dianthus</i> | 1575            | 26.19        | 0.06             | 0.512348  | 0.000005 | -5.65                        | 0.11 | 0.21          | 25.4                  | 0.0006 |

(a) 2SE is the analytical 2σ standard error.

(b) <sup>143</sup>Nd/<sup>144</sup>Nd ratios were corrected for the offset of the measured JNdi-1 ratio of 0.512105 ± 0.000009 (n = 110) from the published value of 0.512115 ± 0.000007 (Tanaka et al., 2000)(c) ε<sub>Nd</sub> was calculated using the present day CHUR value of <sup>143</sup>Nd/<sup>144</sup>Nd = 0.512638 (Jacobsen and Wasserburg, 1980).

(d) 2SD refers to the 2σ standard deviation derived from the long-term reproducibility of BCR-2 standards (see text). If the internal 2σ SE was larger than the external one, the internal error is reported.

(e) 2SE (ep) is the propagated 2σ standard error of Nd concentrations determined by isotope dilution.

**Table 4.2:** Neodymium isotope and concentration results of deep-sea corals collected south of Tasmania listed by their U-series age (kyr BP), which is expressed in thousand years before present (i.e. 1950) (Hines et al., 2015). Depth is the water depth where samples have been collected using ROV Jason. ‘Smp Nd’ refers to the Nd concentration in the sample after co-precipitation and anion exchange chromatography for U-series dating. This concentration is hence a minimum concentration, which may be too low by ~10% (Chapter 2).

### 4.3.2. Deep-sea coral data from south of Tasmania

The readily cleaned *D. dianthus* skeletons from south of Tasmania show more radiogenic Nd isotopic compositions than observed in the Drake Passage from 26 to 16.7 kyr BP ( $\epsilon_{\text{Nd}} = -4.6 \pm 0.2$  to  $\epsilon_{\text{Nd}} = -5.9 \pm 0.2$ ), followed by unradiogenic values around and throughout the ACR ( $\epsilon_{\text{Nd}} = -6.6 \pm 0.2$  to  $\epsilon_{\text{Nd}} = -7.8 \pm 0.2$ ) (Table 4.2; Fig. 4.4). The pronounced Nd isotope shift from a radiogenic  $\epsilon_{\text{Nd}}$  value of  $-4.6 \pm 0.2$  at 16.7 kyr BP to less radiogenic values (i.e.  $\epsilon_{\text{Nd}} = -7.3/-7.7 \pm 0.2$   $\epsilon_{\text{Nd}}$ ) at 14.8/14.6 kyr BP (Fig. 4.4, Table 4.1) is the most prominent feature of the Tasmanian record. The unradiogenic values after  $\sim 14.8$  kyr BP are similar to those observed in the Drake Passage during the ACR and overlap with modern-day values in UCDW in the Pacific sector of the ACC (Carter et al., 2012; Rickli et al., 2014; Basak et al., 2015). In contrast to the record from the Drake Passage, short-term variability is less pronounced, for instance millennial-scale fluctuations of up to 1.2 epsilon units during the glacial to early deglacial interval (26 to  $\sim 16.7$  kyr BP) are relatively smooth (Fig. 4.3).

### 4.3.3. Significance of the Nd isotope signal recorded in Southern Ocean deep-sea corals

We also carried out a suite of replicate analyses ( $n = 11$ ) on Drake Passage corals which are not included in the palaeoclimatic time series illustrated in Figure 4.4. Replicate analyses were performed either on re-sampled coral pieces or on aliquots of poorly homogenised coral pieces (Table 4.1). The Nd isotopic composition reproduces mostly within analytical uncertainty, except one replicate from early HS1 showing a small Nd isotope offset of 0.17 epsilon units (Table 4.1). Such offset can, however, be ascribed to different age intervals covered by the respective subsamples, i.e. changes in contemporaneous seawater chemistry (e.g., Eltgroth et al., 2006; Wilson et al., 2014). Alternatively, the offset might be a statistical artefact as the applied 2SD uncertainty implies that one out of  $\sim 20$  analyses may not reproduce within the calculated 2SD range (see section 4.2.3.).

### 4.3.4. Generating a time series from individual corals

The Drake Passage samples were collected from a depth range between 695 to 1750 m which requires assessment whether or not different sampling depths (and locations) show individual trends. Therefore, we grouped our data into categories according to sampling depth and/or density of water masses currently bathing the sampling locations (Fig. 4.4). In the Drake Passage, the relative position to the PF is hereby crucial, as upwelling LCDW comes close to the surface ocean poleward to the PF (Fig. 4.2). Sars and Interim seamounts are both close to the PF so that their depth ranges can be categorised into three groups (Fig. 4.4). Shackleton Fracture Zone is, however, further east so that samples collected at SFZ in 806 - 823 m water depth correspond hydrographically with the deepest Sars seamount samples from  $\sim 1700$  - 1750 m water depth (along  $\gamma^{\text{n}}$  of  $\sim 28.05$  kg/m<sup>3</sup>; Fig. 2) and are therefore summarised in one group (Fig. 4.4). Neodymium isotope (in)variability occurs coherently across the sampled depth range from 695 to 1750 m during particular intervals (Fig. 4.4). Therefore, we are confident to interpret our deep-sea coral data set as a single high resolution time series.

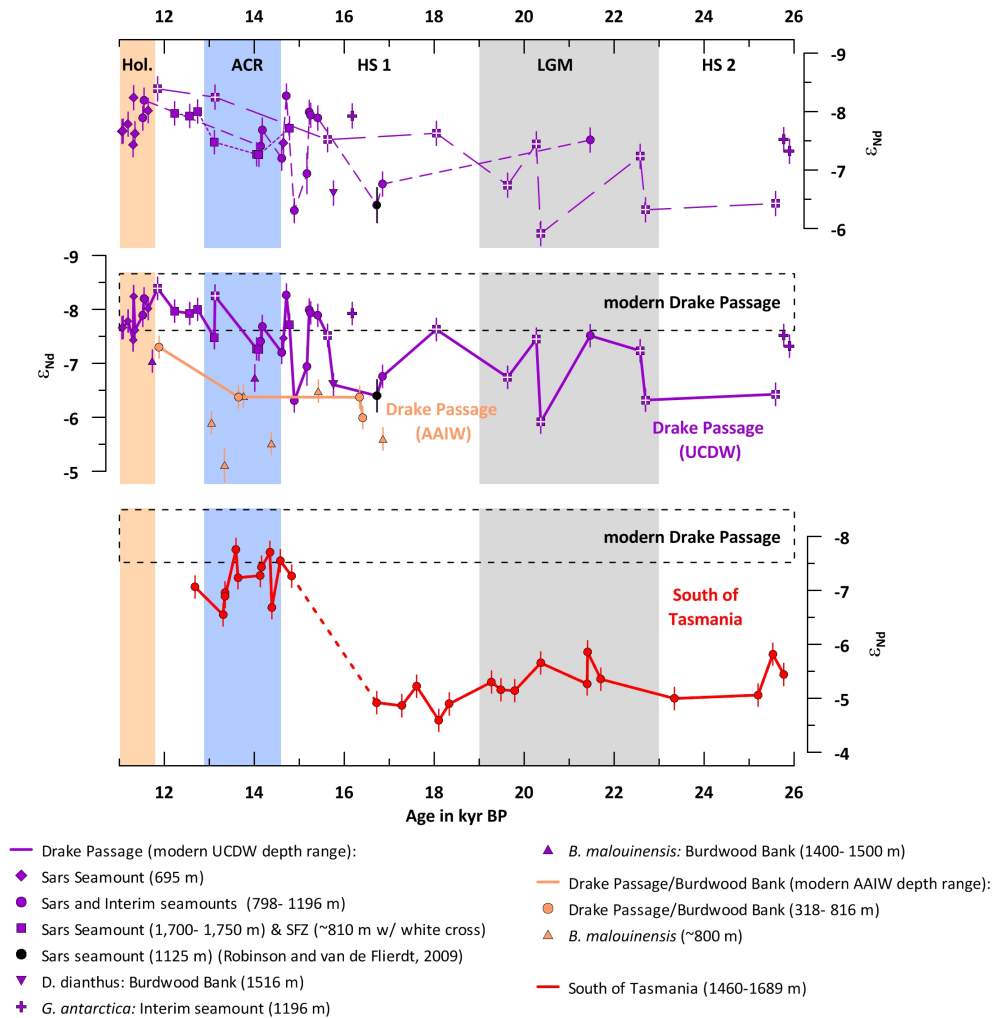


**Figure 4.4:** Results of Drake Passage (top, middle) and Tasmanian (bottom) deep-sea coral Nd isotope analyses. Drake Passage UCDW group (purple) is sub-divided according to depth ranges and hydrography (top) in order to evaluate depth-dependence of observed variability (see text for details), including HS1 coral from Robinson and van de Fliedrt (2009) and Holocene corals from Chapter 6. Successfully calibrated coral species (Chapter 3 and references therein) are connected to generate Drake Passage UCDW and AAIW time series (middle). Of the replicates we chose to include the samples with lower  $^{232}\text{Th}$  and lower age uncertainty (Table 4.1). One exception was made for sample NBP1103-DH88-Cc-1c. Based on its  $\sim 1$   $\epsilon_{\text{Nd}}$  and age offset compared to sub-samples NBP1103-DH88-Cc-1a and NBP1103-DH88-Cc-1b DH88-Cc-1c was not treated as a replicate (Table 4.1), but included in the Nd isotope time series. Similarly, the Tasmanian corals are sub-divided into two groups. Dash-lined boxes represent modern Drake Passage UCDW Nd isotope signature (Chapter 3). Highlighted time intervals are Holocene, Antarctic Cold Reversal (ACR), Heinrich Stadials 1 and 2 (HS1 and HS2) and the Last Glacial Maximum (LGM).

Similarly, we grouped the limited amount of samples currently bathed in AAIW/mixed layer waters, i.e. samples collected at Burdwood Bank above  $\sim 900$  m water depth (Table 4.1, Fig. 4.2). In contrast to the Drake Passage samples, the Tasmanian corals have been collected in a narrow band between 1480 and 1689 m water depth from locations being very close to one another (Table 4.2, Fig. 4.3). For the purpose of simplification, we will refer to the Drake Passage records as UCDW and AAIW records, even though the chemical (and physical) properties of both water masses most certainly changed over the past 26,000 years.

## 4.4. Discussion

### 4.4.1. Processes influencing the recorded seawater Nd isotope signal

The Nd isotopic composition of seawater seems to act as a conservative water mass tracer in the ocean interior on global scale (von Blanckenburg, 1999; Goldstein and Hemming, 2003) and locally in the Southern Ocean (Carter et al., 2012; Stichel et al., 2012; Garcia-Solsona et al., 2014). The local Nd isotopic composition of seawater can, however, change through time due to a multitude of factors, including (i) boundary exchange and changes in input sources, (ii) vertical movement of water mass boundaries and local water mass formation and (iii) lateral admixture of different water masses.

Boundary exchange processes describe the interaction of a water mass with marine deposits, typically along continental margins (e.g., Lacan and Jeandel, 2005; Wilson et al., 2012; Pearce et al., 2013), and as such, may influence the recorded Nd isotope signal. The seawater data presented in Chapter 3 have yielded no indication for boundary exchange processes in the modern Drake Passage although all sampling sites are located near volcanogenic features (Chapter 3). This is due to the fact that the substantial zonal ACC flow of  $\sim 140$  Sv ( $\text{Sv} = 10^6 \text{m}^3/\text{s}$ ) is mostly tied to the Subantarctic and Polar Front (Cunningham et al., 2003) and hence not in contact with nearby continental margins (Orsi et al., 1995; Figs. 4.1 and 4.2). Therefore, no deep currents transport significant volumes of water from the margin towards the open ocean sampling sites.

However, variable current speed through time could potentially change the efficiency of boundary exchange (Wilson et al., 2012). McCave et al. (2014) showed that the current speed south of the SAF was fairly constant over the time interval discussed here. Hence, we conclude that boundary exchange was unlikely to alter the Nd isotope signal recorded by the open Drake Passage deep-sea corals over the past 26,000 years (Fig. 4.2). Regardless, more erosion from the volcanogenic margins could similarly change the seawater Nd isotope signature locally (cf. Robert and Piotrowski, 2015). The high volumes of water transported by the ACC would require substantial input to stain the underlying water masses locally, a condition generally fulfilled as the overall terrestrial flux from the margins to the ocean was higher during the glacial (e.g., Caniupán et al., 2011; Weber et al., 2012; Lamy et al., 2014). The radiogenic Nd isotope signatures of nearby land masses and margins (e.g., Hegner et al., 2007; Noble et al., 2012; Chapter 3) would then drive the seawater Nd isotope signature towards more radiogenic values, in contrast to the relatively unradiogenic Nd isotope signatures recorded in the glacial Drake Passage. Likewise, the Tasmanian data is unlikely to be significantly influenced by a change in input sources as the Tasmanian and Australian source regions are predominantly less radiogenic ( $\epsilon_{\text{Nd}} < -10$ ; Jeandel et al., 2007) than the glacial seawater Nd isotope signal recorded in our coral data (Table 4.2). The radiogenic nature of the Nd isotope signature in glacial deep-sea corals is therefore inconsistent with significant influence from increasing glacial erosion of Tasmanian and Australian sources (Petherik et al., 2013; Reeves et al., 2013). New Zealand is, however, a radiogenic source acting to influence the Nd isotopic composition of passing boundary

currents (Noble et al., 2013), and it has been shown that New Zealand experienced increased glacial ice cover and erosion (e.g., Putnam et al., 2010; Upton et al., 2013; Rother et al., 2014). Deglacial New Zealand glaciers were subject to significant decay and re-advance (Putnam et al., 2010; Rother et al., 2014), processes expected to enhance terrestrial (radiogenic) input from New Zealand. This is in contrast to the pronounced deglacial shift of  $>2$  epsilon units to less radiogenic Nd isotope values recorded at Tasmania. Furthermore, northward penetrating unradiogenic UCDW recorded at the sampling sites after 14.8 kyr BP (Fig. 4.4) was unlikely to be driven by changes in New Zealand sediment input as New Zealand is located downstream. Moreover, it has been demonstrated that CDW Nd behaves conservatively in the ACC (Carter et al., 2012), a condition unlikely to have changed in the remote upstream Indian sector of the glacial Southern Ocean. Regardless, alteration of the seawater Nd isotope signal could play a role, in particular north of the Tasman Sea where boundary exchange processes were shown to influence the modern seawater Nd isotope signature (Amakawa et al., 2013; Grenier et al., 2013). Consequently, at times when the recorded signal was more radiogenic, i.e. until 16.7 kyr BP (Fig. 4.4), water masses coming from the north of the Tasman Sea may have been subjected to boundary exchange. Here we focus on the qualitative extension of particular water masses so that the conclusions drawn from the discussion below are not compromised by boundary exchange processes and/or potential changes in input from New Zealand sources.

Secondly, the potential of vertical movement of water mass boundaries needs to be addressed. In the modern ocean, AAIW is subducted into the ocean interior below the SAF along the ACC flow path with major formation areas in the Southeast Pacific and Indian Oceans (e.g., Piola and Georgi, 1982; Bostock et al., 2013). Such AAIW is the only downwelling water mass in the open Southern Ocean capable to transfer a relevant surface water signal to greater depths. It is well known that the meridional water mass geometry was different in the glacial ocean including a characteristic reduction of NADW volume (Curry and Oppo, 2005).

While we consider an upward shift of the AABW boundary to the depths of coral sampling locations in the Drake Passage and south of Tasmania unlikely, it has been suggested that AAIW formation was enhanced and potentially deepened during the LGM in response to reduced North Atlantic water mass formation (e.g., Pahnke et al., 2008; Wainer et al., 2012). Pahnke and Zahn (2005) presented evidence that AAIW in the Pacific sector shoaled, confirmed by Ronge et al. (2015) who suggested that the northward displacement of oceanic fronts caused increased glacial freshwater fluxes at the sea ice edge ultimately reducing the depth of AAIW subduction. There exists no direct evidence for a northward displacement and/or shoaling of AAIW in the Drake Passage. In general, intermittent deepening of more radiogenic AAIW source waters (AAIW  $\epsilon_{Nd} \approx -6$  in the Drake Passage and in the Southwest Atlantic Ocean; Pahnke et al., 2008; this study) would be consistent with ‘UCDW values’ as radiogenic as  $\epsilon_{Nd} \approx -5.9$  at Shackleton Fracture Zone in 823 m water depth (Fig. 4.4). As described above, the UCDW record presented in Figure 4.4 is assembled from corals spanning a water depth from 695 to 1750 m so that any enhanced Nd isotope variability induced by

deepening of a more radiogenic AAIW should be reflected in samples from the shallowest locations in 695 m water depth (Fig. 4.2), which is, however, not the case (Fig. 4.4). Moreover, AAIW deepening would be associated with a poleward shift of outcropping isoneutrals, and thus oceanic fronts. Currently, i.e. under peak interglacial conditions, corals bathed by UCDW would require warming conditions in excess of modern temperatures in order to allow for a significant poleward shift of oceanic fronts in the Drake Passage to cause deepening of AAIW and/or the surface mixed layer waters feeding into AAIW. This scenario appears highly unlikely during the last deglaciation.

In conclusion, the Nd isotope signals recorded in the depth ranges of the deep-sea corals used for this study are unlikely to be significantly affected by vertical shifts of water mass boundaries and/or local water mass formation. It hence follows, that the recorded Nd isotope signals in the Southern Ocean are pre-dominantly driven by water mass mixing.

#### 4.4.2. Millennial-scale evolution of glacial and deglacial Southern Ocean water mass mixing

Our new Nd isotope data add seawater provenance information to existing radiocarbon work done on Drake Passage (Burke and Robinson, 2012; Chen et al., 2015; Burke et al., unpubl. data) and Tasmanian deep-sea corals (Hines et al., 2015). Over the investigated interval between 26 and 11 kyr BP, the overall Nd isotope evolution in the Drake Passage shows a multi-millennial trend towards less radiogenic values with short-term fluctuations superimposed. In comparison to existing deep ocean Nd isotope data, the Drake Passage time series shows Nd isotope signatures similar to the deep Southeast Atlantic Ocean (4981 m water depth) during the glacial and deglacial (Piotrowski et al., 2004, 2012; Fig. 4.5). The deep western Atlantic water masses (3770 m water depth) seem, however, to have carried a more radiogenic Nd isotope signature throughout (Skinner et al., 2013; Fig. 4.5).

In contrast, the Tasmanian deep-sea corals recorded glacial Nd isotope signatures similar to values extracted from deep Southwest Pacific sediments at Chatham Rise (Noble et al., 2013; Fig. 4.5) and deep Southwest Atlantic Nd isotope data (Skinner et al., 2013; Fig. 4.5), which, in turn, are similar to modern Pacific seawater (e.g., Amakawa et al., 2009, 2013), but isotopically different to the Drake Passage. A characteristic deglacial shift of more than 2 epsilon units from  $\epsilon_{\text{Nd}} = -4.9 \pm 0.2$  at 16.7 kyr BP to  $\epsilon_{\text{Nd}} = -7.3 \pm 0.2$  at 14.8 kyr BP results in Nd isotope signatures similar to contemporaneous Drake Passage values (Fig. 4.5). The difference of the characteristic features of the two time series leads us to hypothesise that both sample locations capture complimentary features of Southern Ocean circulation. In detail, Drake Passage corals are likely to record an ACC UCDW signal, whereas the Tasmanian corals are likely to record mixing between UCDW and Pacific-derived water masses. Understanding the processes defining the different characteristics of both records is therefore crucial to understand glacial-deglacial mid-depth dynamics in the Southern Ocean.

#### 4.4.2.1. Water mass mixing south of Tasmania: evidence for ventilation from the North Pacific

The pattern of the Tasman time series is similar to the deep South Atlantic and Indian Ocean Nd isotope records (Piotrowski et al., 2004, 2009, 2012; Skinner et al., 2013), paced by an “Antarctic” timing, i.e. a characteristic stepwise evolution during the deglacial. This is expressed in the covariation with Antarctic temperatures (e.g., Petit et al., 1999; WAIS Divide project members, 2013; Fig. 4.5), a poleward shift in frontal positions and associated upwelling intensity (Anderson et al., 2009; Fig. 4.5), but also with the onset of re-invasion of NADW production recorded by  $^{231}\text{Pa}/^{230}\text{Th}$  in the North Atlantic (e.g., McManus et al., 2004; Gherardi et al., 2009; Fig. 4.5). Regardless the similarity with deep ocean Nd isotope trends, the relatively good ventilation between 26 and 16.7 kyr BP ( $\Delta\Delta^{14}\text{C} \approx -110$  to  $-240\text{‰}$ ; Hines et al., 2015; Figs. 4.5 and 4.6) renders underlying radiogenic ( $\epsilon_{\text{Nd}} \approx -5$  to  $-6$ , Noble et al., 2013; Skinner et al., 2013; Fig. 4.5), but poorly-ventilated water masses ( $\Delta\Delta^{14}\text{C} \leq \sim -400\text{‰}$ ; Skinner et al., 2010, 2015; Fig. 4.6) an unlikely source of  $\epsilon_{\text{Nd}}$  values between  $-4.6 \pm 0.2$  and  $-5.9 \pm 0.2$  (Fig. 4.6). The most radiogenic Nd isotope signatures of  $\epsilon_{\text{Nd}} = -4.6 \pm 0.2$  to  $\epsilon_{\text{Nd}} = -5.2 \pm 0.2$  are associated with  $\Delta\Delta^{14}\text{C}$  of about  $-110$  to  $-200\text{‰}$  during Heinrich Stadials 1 and 2 (HS1 and HS2) (Hines et al., 2015; Fig. 4.5). Such radiocarbon values indicate better ventilation of radiogenic water masses recorded south of Tasmania than contemporaneous Drake Passage UCDW (Figs. 4.5 and 4.6). This implies ventilation of mid-depth waters (above  $\sim 2$  km water depth due to bathymetry) from north of Tasmania, consistent with deepened water mass formation in the North Pacific during Heinrich Stadials (e.g., Okazaki et al., 2010; Menviel et al., 2011; Max et al., 2014; Rae et al., 2014) and during the LGM so that this water mass is consequently referred to as Glacial North Pacific Intermediate Water, i.e. GNPIW (e.g., Keigwin, 1998; Matsumoto et al., 2002). This is evident from our data during both, HS1 and HS2, although the later part of HS1 is not covered by our coral data (Table 4.2; Fig. 4.5). Between 22 and 19 kyr BP slightly less radiogenic Nd isotope signatures from  $\epsilon_{\text{Nd}} = -5.1 \pm 0.2$  to  $\epsilon_{\text{Nd}} = -5.9 \pm 0.2$  are associated with  $\Delta\Delta^{14}\text{C}$  between  $-140$  to  $-250\text{‰}$  indicating increased admixture of UCDW which is characterised by average  $\Delta\Delta^{14}\text{C}$  of  $-290\text{‰}$  (Burke and Robinson, 2012; Chen et al., 2015) and  $\epsilon_{\text{Nd}} \approx -7$  in the glacial Drake Passage (Figs. 4.5 and 4.6). Thereafter, a pronounced shift towards Nd isotopic compositions similar to contemporaneous and modern UCDW indicates the end of this glacial circulation mode in the SW Pacific (Figs. 4.5 and 4.6). Hence, the Tasmanian margin witnessed the glacial expansion of well-ventilated GNPIW at mid-depths between  $\sim 26$  and 16.7 kyr BP. This could be associated with strengthened Pacific overturning at the expense of Atlantic overturning as found in models in direct response to the position of the SWW (Sijp and England, 2009), but also through ocean-atmosphere feedbacks as for instance during North Atlantic meltwater events (e.g., Okazaki et al., 2010; Menviel et al., 2011; Rae et al., 2014) including SWW feedbacks (Menviel et al., 2012).

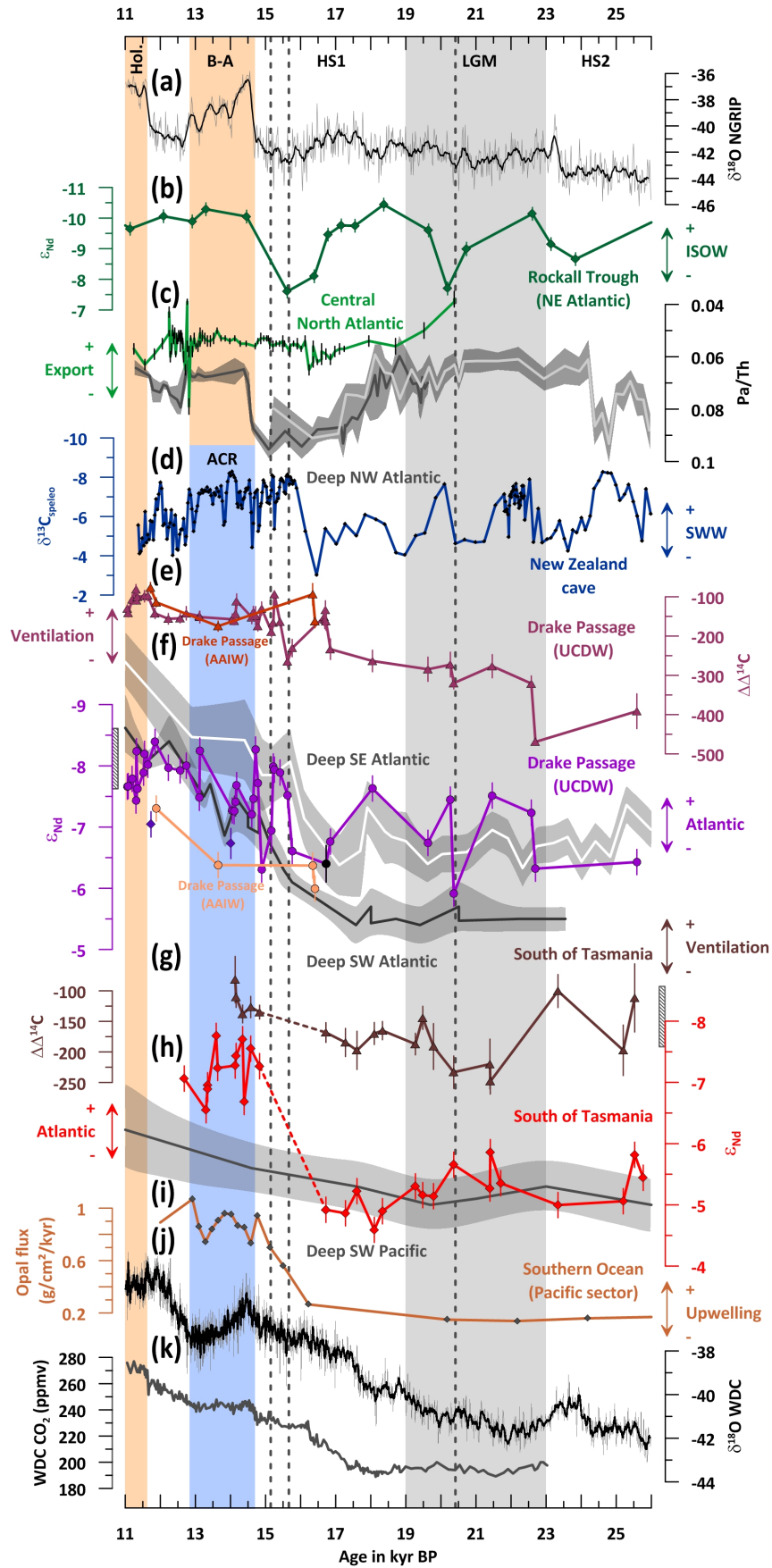


**Figure 4.5:** The Southern Ocean deep-sea coral time series in the context of relevant proxy records during the interval from 26 to 11 kyr BP. (a) NGRIP oxygen isotope record (Rasmussen et al., 2006; Svensson et al., 2006). (b) Nd isotope record from the Rockall Trough core ODP 980 indicating Iceland-Scotland Overflow Water (ISOW) strength (Crocket et al., 2011). (c) North Atlantic  $^{231}\text{Pa}/^{230}\text{Th}$  records indicative of water mass export. Deep Northwest Atlantic cores (~4600 m) are summarised by grey shading (dark grey line: McManus et al., 2004; light grey line: Böhm et al., 2015), mid-depth core (2150 m) from the central North Atlantic plotted in grass green (Gherardi et al., 2009). (d) Hollywood cave  $\delta^{13}\text{C}$  record of SWW influence over South Island, New Zealand (Whittaker et al., 2011). (e) Drake Passage radiocarbon deep-sea coral time series of UCDW and AAIW depth ranges, expressed as  $\Delta\Delta^{14}\text{C}$ , i.e. the offset of  $\Delta^{14}\text{C}_{\text{coral}}$  from  $\Delta^{14}\text{C}_{\text{atmosphere}}$ , the latter is calculated from the IntCal13  $\Delta^{14}\text{C}_{\text{atmosphere}}$  (Reimer et al., 2013) averaged across  $2\sigma$  age uncertainty per individual coral with propagated error reported (Burke and Robinson, 2012; Chen et al., 2015; Burke et al., unpubl. data). (f) Drake Passage deep-sea coral Nd isotope time series of UCDW (purple) and AAIW (peach) depth ranges (this study and Chapter 6; HS1 coral from Robinson and van de Flierdt, 2009 in black). Nd isotope records from deep (3770 m) Southwest Atlantic core MD07-3076 (grey shading, dark line; Skinner et al., 2013) and from deep (4981 m) Southeast Atlantic core TNO57-21 (grey shading, white line; Piotrowski et al., 2005, 2012) on updated time scale of Barker and Diz (2014). (g) Tasmanian deep-sea coral  $\Delta\Delta^{14}\text{C}$  calculated from IntCal13  $\Delta^{14}\text{C}_{\text{atmosphere}}$  as in (e), errors calculated from maximum  $^{14}\text{C}$  and U-Th age uncertainty (cf. Hines et al., 2015). (h) Tasmanian deep-sea coral Nd isotope time series of UCDW depth range (this study), and Nd isotope record from CHAT5K in the LCDW depth range at Chatham Rise in the Southwest Pacific (Noble et al., 2013). (i) Opal flux record of upwelling intensity from E27-23 in the Indo-Pacific sector of the Southern Ocean (Anderson et al., 2009). (j) WAIS Divide oxygen isotope record (WAIS Divide project members, 2013). (k) WAIS Divide ice core  $\text{CO}_2$  record (Marcott et al., 2014). Grey stippled lines indicate abrupt Nd isotope changes in Drake Passage Nd isotope data at 15.2, 15.7 and 20.4 kyr BP, respectively. Grey bars at the y axes of (f) and (h) indicate the modern range of UCDW at the Drake Passage coral sampling locations (Chapter 3). B-A refers to Bølling-Allerød interstadial in the Northern Hemisphere, other abbreviations as in Fig. 4.4.

#### 4.4.2.2. Glacial water mass mixing in the Drake Passage and implications for the overturning circulation

The Drake Passage time series is characterised by the frequent re-occurrence of relatively unradiogenic Nd isotope signatures of  $\epsilon_{\text{Nd}} \approx -7$  to  $-8$  throughout the entire investigated interval and is consistently less radiogenic than the Tasmanian Nd record (Figs. 4.5 and 4.6). Whereas PDW and IDW are sources of rather radiogenic Nd isotope signatures (Piotrowski et al., 2009; Noble et al., 2013; Figs. 4.5 and 4.6), such unradiogenic mid-depth Nd isotopic compositions are most likely sourced from the (North) Atlantic (e.g., Roberts et al., 2010; Wilson et al., 2014; Böhm et al., 2015). This is illustrated in radiocarbon-Nd isotope space (Fig. 4.6) where most glacial Drake Passage UCDW data plot between (relatively well-ventilated and unradiogenic) NADW/GNAIW and a poorly-ventilated radiogenic source. Before and during the earliest LGM at 25.6 and 22.7 kyr BP, mixing occurred pre-dominantly with underlying radiocarbon-depleted ( $\Delta\Delta^{14}\text{C} \approx -550\%$ ) and radiogenic ( $\epsilon_{\text{Nd}} \approx -5.5$ ) deep waters as found in the South Atlantic (Skinner et al., 2010, 2013; Figs. 4.5 and 4.6). During most of the LGM, mixing of UCDW was dominated by GNAIW influence and deep Pacific-derived waters (Noble et al., 2013; Skinner et al., 2015), the latter of which may have been derived from mixing with an even more radiocarbon-depleted deep Pacific source (Tiedemann et al., 2015). The resulting Drake Passage UCDW chemistry was similar to the contemporaneous deep Cape Basin (Piotrowski et al., 2005, 2012; Barker et al., 2010) indicating a similar mixture of water masses in the deep Southeast Atlantic (Fig. 4.6).

The prominent role of Atlantic-sourced water masses in glacial UCDW is consistent with the meridional LGM water mass geometry (Curry and Oppo, 2005), South Atlantic stable isotope data (Lund et al., 2015), active overflows in the Northeast Atlantic (Crocket et al., 2011; Fig. 4.5), relatively unradiogenic Nd isotope signatures in the deep North Atlantic (Roberts et al., 2010; Böhm et al., 2015) and active (pre-dominantly mid-depth/GNAIW) export of water masses from the North Atlantic (McManus et al., 2004; Gherardi et al., 2009; Böhm et al., 2015). At the same time, the admixture of well-ventilated GNPIW, recorded south of Tasmania, into UCDW was limited (Fig. 4.6). The modern Southern Ocean density structure reveals that the Tasmanian corals were sampled from depths bathed by water masses of slightly lower density compared to water masses bathing most Drake Passage sampling sites (Figs. 4.2 and 4.3). This could have reduced the influence of GNPIW on deep waters recorded at Drake Passage sampling sites.

However, there is significant overlap in the modern water mass density range covered by corals at both sampling locations, i.e. at the Tasmanian margin and in the Drake Passage (Figs. 4.2 and 4.3). Therefore, the pronounced isotopic gradients between both locations translate into significant chemical differences between ACC-bound UCDW, represented by Drake Passage UCDW, and relatively well-ventilated GNPIW evident south of Tasmania. This is particularly remarkable because the ACC fronts (and alongside the ACC-bound UCDW) are believed to have migrated north during the LGM (Gersonde et al., 2005; Anderson et al., 2009; De Deckker et al., 2012; Ferrari et al., 2014). From this follows that the LGM mid-depth water mass exchange between the South Pacific and Southern Ocean was limited, despite vigorous advection of GNPIW from the North Pacific. Thus, GNPIW was likely to recirculate within the Pacific basin and feed significantly into AAIW formation, thereby contributing to increased glacial AAIW ventilation, in particular in the Pacific sector of the Southern Ocean (e.g., Muratli et al., 2010). The combined radiocarbon-Nd isotope data provide supporting evidence that the mid-depth glacial ocean was ventilated from both, the North Pacific and the North Atlantic, consistent with oxygen isotope data (e.g., Duplessy et al., 2002; Matsumoto et al., 2002; Adkins, 2013). In the Pacific Ocean, the well-ventilated GNPIW recorded at the Tasmanian margin was consequently associated with a mid-depth Pacific overturning cell (reaching down to ~1.5 to 2 km water depth; e.g., Matsumoto et al., 2002) which mixed, however, only marginally into the ACC core. Vertical Nd isotope ( $\sim 2 \epsilon_{\text{Nd}}$ ; Skinner et al., 2013; this study) and/or radiocarbon offsets ( $\Delta\Delta^{14}\text{C}$  of  $\sim 250\%$ ; Skinner et al., 2010, Burke and Robinson, 2012; Figs. 4.5 and 4.6) indicate a deeply stratified water column. Nevertheless, glacial mixing with underlying deep water masses did not cease in the Southern Ocean (Fig. 4.6) implying (reduced) interaction between upper and lower overturning circulation cells (cf. Ferrari et al., 2014). This glacial circulation pattern existed until at least ~17 kyr BP.

Considering that the modern vertical Nd isotope distribution in the ACC is rather homogeneous (Stichel et al., 2012) and that UCDW dominates the modern mid-depth Tasman Sea (e.g., Sokolov and Rintoul, 2000), the implied lateral and vertical gradients are mechanistically

challenging, in particular in the light of a more northerly LGM position of ACC-bound UCDW flow (e.g., Barrows and Juggins, 2005; Gersonde et al., 2005; Anderson et al., 2009; Ferrari et al., 2014).

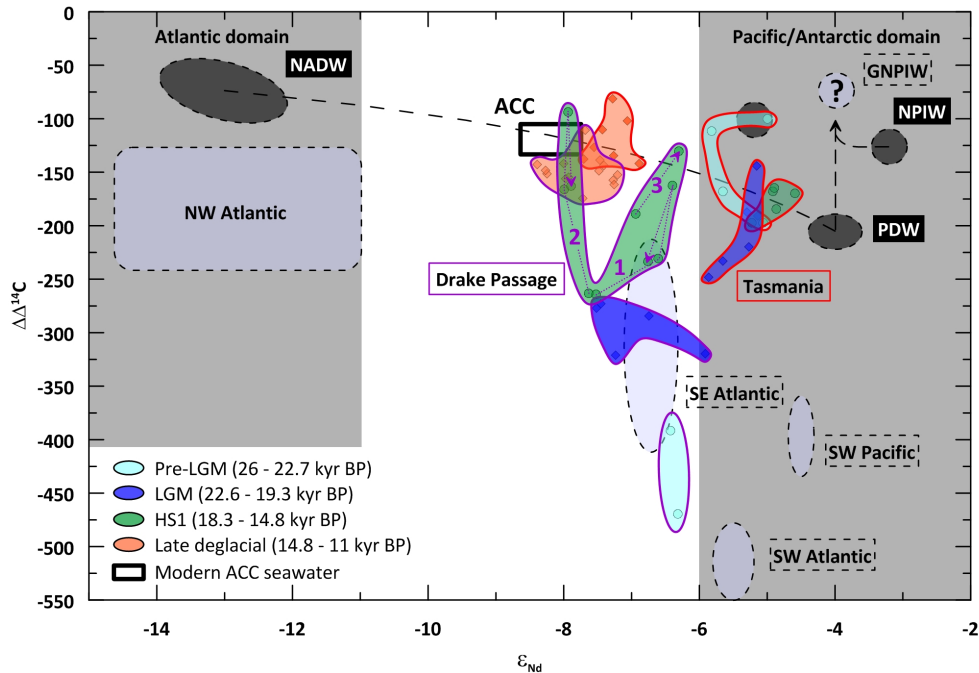


**Figure 4.6:** Drake Passage (purple line) and Tasmanian (red line) deep-sea coral data in radiocarbon-Nd isotope space (Burke and Robinson, 2012; Chen et al., 2015; Hines et al., 2015; Burke et al., unpubl. data). The coral data is grouped by time intervals and location. Results from early (1), mid (2) and late (3) HS1 periods in the Drake Passage are connected with stippled purple arrows. The arrow direction indicates the evolution with time. Radiocarbon data for modern water masses from GLODAP data base natural seawater  $\Delta^{14}\text{C}$  reconstruction (Key et al., 2004). Modern (i.e. 1950)  $\Delta^{14}\text{C}_{\text{atmosphere}}$  (Reimer et al., 2013) used to generate seawater  $\Delta\Delta^{14}\text{C}$  ( $\Delta\Delta^{14}\text{C} = \Delta^{14}\text{C}_{\text{coral}} - \Delta^{14}\text{C}_{\text{atmosphere}}$ ). Coral  $\Delta\Delta^{14}\text{C}$  calculated with IntCal13 (Reimer et al., 2013; see also caption Fig. 4.5). Modern Nd isotope endmember data for western (Northwest Atl. AII 109-1 Stn30; Piepgras and Wasserburg, 1987) and eastern NADW (Ovide St. 15; Copard et al., 2011), central North Pacific PDW (BO-3; Amakawa et al., 2009), North Pacific Intermediate Water (NPIW) (Station 4; Zimmermann et al., 2009), Antarctic shelf waters (Carter et al., 2012), and modern UCDW and AAIW bathing the coral sampling sites (Chapter 3). The arrows from modern PDW and NPIW point to well-ventilated Glacial North Pacific Intermediate Water (GNPIW; cf. e.g., Matsumoto et al., 2002). The dashed black line represents conservative mixing between modern NADW and PDW. Powder blue polygons indicate potential glacial endmember values from the literature. Southwest Atlantic data from MD07-3076, 3777 m water depth (Skinner et al., 2010, 2013). Southwest Pacific cores CHAT5k (4240 m), CHAT10k (3003 m) and MD97-2121 (2314 m) (Noble et al., 2013; Skinner et al., 2015). Southeast Atlantic core TNO57-21 (4981 m) (Piotrowski et al., 2005; 2012; Barker et al., 2010). Northwest Atlantic deep-sea corals collected between 1713 and 2546 m water depth (Wilson et al., 2014 and references therein). Note the two directions of mixing during LGM (Last Glacial Maximum) and HS1 (Heinrich Stadial 1) in the Drake Passage and lacking overlap with Tasmanian coral data until 14.8 kyr BP (late deglacial).

It has been suggested that deep ocean stratification is mainly the result of extended perennial sea ice cover in the Southern Ocean causing changes in water mass geometry, ultimately reducing (dianeutral) mixing between the upper and lower overturning cells in the global ocean (Ferrari et al., 2014). Such reduced mixing would be expressed in a deeply stratified Southern Ocean, a feature particularly evident from combined radiocarbon-Nd isotope data (Skinner et al., 2010, 2013; Burke and Robinson, 2012; this study). However, McCave et al. (2014) showed that the bottom flow of the

ACC through the Drake Passage was nearly constant from the Last Glacial Maximum (LGM) to the Holocene. This constant flow was questioned by Lamy et al. (2015) who argued for a partial northward deflection of water masses bound to the northern ACC flank in response to northerly displaced SWW. Despite, the vigorous ACC flow postulated by McCave et al. (2014) would have limited the northwards extension of perennial sea ice cover. As the Drake Passage is a crucial location with respect to isoneutral and dianeutral mixing (St. Laurent et al., 2012; Thompson and Sallée, 2012; Watson et al., 2013), it may be expected that mixing in a widely ice-free LGM Drake Passage was similar to modern. This would reduce the influence of northwards expanding sea-ice on reducing (dianeutral) mixing between upper and lower overturning cells (cf. Watson et al., 2013; Ferrari et al., 2014). Past work showed that both, wind-induced zonal and meridional ACC mean circulation imply counteracting (“compensating”) eddy circulation, but their sensitivity to atmospheric forcing is distinct (e.g., Marshall and Radko, 2003, Morrison and Hogg, 2013; Munday et al., 2013).

The meridional overturning as the residual circulation along interior density surfaces (Marshall and Radko, 2003) shows significant sensitivity to combined wind and buoyancy forcing scaling with eddy circulation (e.g., Abernathey et al., 2011, Meredith et al., 2012; Munday et al., 2013). Moreover, isoneutral and dianeutral eddy mixing is enhanced near  $\gamma^n \approx 28.0$ , i.e. the interface of UCDW and LCDW (cf. Smith and Marshall, 2009; Abernathey et al., 2010; Ledwell et al., 2011; Watson et al., 2013; Tulloch et al., 2014). This implies sensitivity of mixing and water mass ventilation at this critical depth to (changing) westerly wind forcing (cf. Tulloch et al., 2014), consequently affecting water column stratification without the need of sea-ice expansion into the Drake Passage. As hypothesised by Toggweiler et al. (2006), both mechanisms may be linked through thermal feedbacks ultimately controlling deep stratification. Due to the distinct response of zonal ACC transport and Southern Ocean overturning circulation to atmospheric forcing (e.g., Morrison and Hogg, 2013; Munday et al., 2013) aforementioned sensitivity of the overturning circulation can be consistent with constant zonal flow through large parts of the Drake Passage. This is due to the relationships found in eddy-resolving models (e.g., Marshall et al., 2006a; Meredith et al., 2012; Munday et al., 2013) so that constant mean flow paired with decreased wind forcing over the Drake Passage channel requires a reduction in the counteracting eddy field. The glacial deflection of SAF-bound water masses (Lamy et al., 2015) might then have contributed to this eddy mixing effect on the overturning circulation such that SAF-related turbulence in the northern Drake Passage was reduced. The resulting reduction of mixing is evident for instance from radiocarbon and Nd isotopes (Figs. 4.5 and 4.6).

Similar processes may have been crucial in generating the strong lateral Nd isotope gradient between UCDW and GNPIW during the LGM, represented by the Drake Passage and Tasmanian corals, respectively (Figs. 4.5 and 4.6). Mixing in the Southern Ocean occurs pre-dominantly in the lee of bathymetrical obstacles and along the equatorward ACC flank, whereas mixing within the ACC is reduced (Sallée et al., 2011; Thompson and Sallée, 2012). The strongest cross-frontal mixing is

observed in the Drake Passage area and reduced in the Pacific sector of the Southern Ocean (Thompson and Sallée, 2012) where mean flow can act to suppress eddy mixing (Naveira Garabato et al., 2011). Assuming overall northward displacement of LGM fronts (Gersonde et al., 2005), GNPIW bathing the Tasmanian corals may have mixed isoneutrally into the eastward flow along the northern ACC flank (cf. Abernathy et al., 2010; Sallée et al., 2011; Thompson and Sallée, 2012). As cross-frontal mixing is, however, limited upon flow through the Pacific sector of the Southern Ocean (Naveira Garabato et al., 2011; Thompson and Sallée, 2012), GNPIW is considered to have been (partly) re-injected into the Pacific basin before the core of the ACC would pass the Drake Passage. One potential location is in the central Pacific where GNPIW could be carried northward similar to UCDW in the modern Pacific (Fig. 4.1). This could also have contributed to the radiogenic Nd isotope signatures extracted from mid-depth Chatham Rise sediments (partly ascribed to boundary exchange; cf. Noble et al., 2013). Alternatively, the LGM northward frontal zone displacement (Gersonde et al., 2005; Kohfeld et al., 2013) could have induced enhanced northward deflection of ACC waters off Chile (Lamy et al., 2015). The latter location implies the potential for abrupt changes of Drake Passage UCDW properties in response to latitudinal shifts of wind fields once a critical SWW position was reached. Thereby, mid-depth water chemistry would be altered efficiently by both, vertical mixing with underlying water masses due to increased turbulence and lateral admixture of GNPIW into the ACC core (cf. Anderson et al., 2009; Lamy et al., 2015). Beside Lamy et al.'s work, direct evidence for stronger deflection of ACC waters during the glacial is sparse. Nevertheless, thermal isolation of Campbell Plateau water masses highlights the possibility of small-scale latitudinal gradients along the northern ACC flank (Neil et al., 2004). In addition, reduced productivity as a result of suppressed coastal upwelling (e.g., Hebbeln et al., 2002; Mohtadi et al., 2008), enhanced LGM AAIW oxygenation (Muratli et al., 2010) and colder SSTs (Feldberg and Mix, 2002) are consistent with partial northward deflection of ACC water masses off Chile in response to equatorward shifted westerlies (Kohfeld et al., 2013; Lamy et al., 2015) and oceanic fronts (Gersonde et al., 2005).

In order to evaluate the millennial-scale variations, we here focus on the transition from the LGM to HS1 as it provides the best data coverage. Similar to previous work, our Nd isotope data seem to indicate an early HS1 breakdown of deep stratification in the Drake Passage, i.e. during an interval of southward migrating fronts (vertical Nd isotope homogenisation at  $\sim 16.7$  kyr BP, including AAIW,  $\epsilon_{\text{Nd}} \approx -6.0$  to  $-6.5$ ; Fig. 4.5). Alongside, reduced Atlantic overturning was partly compensated for by enhanced Pacific overturning facilitated by ocean-atmosphere propagation under glacial boundary conditions (e.g., Saenko et al., 2004; Okazaki et al., 2010; Menviel et al., 2011; Hu et al., 2012; Rae et al., 2014), consistent with reconstructions from AAIW depth range (Huang et al., 2014; Freeman et al., 2015). Enhanced Pacific overturning is expressed in strong influence of relatively well-ventilated GNPIW recorded south of Tasmania ( $\epsilon_{\text{Nd}} = -4.9 \pm 0.2$  and  $\Delta\Delta^{14}\text{C} \approx -170\%$ ) at  $\sim 16.7$  kyr BP (Figs. 4.5 and 4.6). The radiocarbon-Nd isotope space shows that early HS1 Drake Passage

UCDW was dominated GNPIW-imprinted waters from south of Tasmania mixing with a North Atlantic component (Figs. 4.5 and 4.6). Hence, lateral admixture controlled early HS1 Drake Passage UCDW properties rather than vertical mixing with deep radiocarbon-depleted sources. This lateral GNPIW admixture peaked at ~16.7 kyr BP ( $\epsilon_{\text{Nd}} = -6.4 \pm 0.3$ ,  $\Delta\Delta^{14}\text{C} \approx -130$  to  $-160\%$ ; Robinson and van de Flierdt, 2009; Fig. 4.6). Following the scenario hypothesised for the LGM Southern Ocean, poleward migration of the SWW and an accompanied shift of Southern Ocean fronts (e.g., Mohtadi et al., 2008; Anderson et al., 2009; Barker et al., 2009) might have deflected SAF-bound waters carrying a strong GNPIW component into the circumpolar flow. Supporting evidence for this mechanism is provided by New Zealand speleothem  $\delta^{13}\text{C}$  data considered to be pre-dominantly driven by SWW-induced rainfall (Whittaker et al., 2011). The  $\delta^{13}\text{C}_{\text{speleo}}$  shows close covariation with glacial and early deglacial Drake Passage Nd isotope variability (Fig. 4.5). Between ~26 and 13 kyr BP, radiogenic Nd isotopic compositions in the Drake Passage were associated with reduced SWW influence in New Zealand and vice versa. Hence, reduced northerly SWW influence can be linked with (i) increased lateral admixture of Pacific-derived waters into the circumpolar flow, but also with (ii) enhanced intrusion of deep waters at times (cf. Anderson et al., 2009; Lamy et al., 2015; Fig. 4.6).

Alternatively, reduced North Atlantic water mass export in response to meltwater input may be invoked (e.g., Seidov and Maslin, 2001; Rahmstorf, 2002; Robinson and van de Flierdt, 2009) as North Atlantic buoyancy forcing has a strong control on Atlantic overturning strength (e.g., Yeager and Danabasoglu, 2014). Indeed, millennial-scale variability of North Atlantic overflow activity linked to meltwater events (Crocket et al., 2011; Fig. 4.5) reveals intriguing covariation with Drake Passage Nd isotope signals during early HS1, HS2 and at 20.4 kyr BP (Fig. 4.5). Meltwater-induced reduction of ventilation from the North Atlantic and, alongside, reduced AMOC activity during HS1 have been inferred from a number of records throughout the Atlantic basin (e.g., Sarthein et al., 1994; McManus et al., 2004; Pahnke et al., 2008; Gherardi et al., 2009; Roberts et al., 2010; Crocket et al., 2011; Huang et al., 2014; Skinner et al., 2014; Böhm et al., 2015; Freeman et al., 2015; Fig 4.5). In this scenario, reduced export of Atlantic-sourced water masses would increase the proportion of Pacific-derived water masses in the Southern Ocean.

The resulting net effect on the Drake Passage Nd isotope signature is similar from both mechanisms as both would, under glacial boundary conditions, reduce the proportion of Pacific-sourced waters in the ACC during Southern Ocean cold phases and vice versa. Moreover, both mechanisms are linked through the involved bipolar seesaw effect describing an antiphasing in the interhemispheric distribution of heat (Seidov and Maslin, 2001; Stocker and Wright, 2003; Barker et al., 2009). Strong bipolar seesaw effects have been shown to be associated with North Atlantic meltwater events (e.g., Seidov and Maslin, 2001; Anderson et al., 2009; Barker et al., 2009) and considered to propagate North Atlantic signals through the ocean into the Southern Hemisphere (e.g., Seidov and Maslin, 2001; WAIS Divide project members, 2015). The Drake Passage UCDW data show radiogenic Nd isotope signatures around 16.7, 20.4, 22.7 and 25.6 kyr BP (Fig. 4.5). The first

three events coincided with a reduction in overflow activity and/or export of deep water masses from the North Atlantic, ascribed to meltwater-induced cold phases (McManus et al., 2004; Gherardi et al., 2009; Crocket et al., 2011; Böhm et al., 2015; Fig 4.5). In the Southern Ocean, such intervals were expressed as warming phases paired with poleward intensification of the SWW (e.g., Anderson et al., 2009; Barker et al., 2009; WAIS Divide project members, 2015) and a breakdown of deep Southern Ocean stratification (Toggweiler et al., 2006; Anderson et al., 2009; Burke and Robinson, 2012; Fig. 4.5). Bipolar seesawing in the atmosphere is, however, significantly faster (cf. Stocker and Johnson, 2003; Barker et al., 2009; Wang et al., 2015) and has been shown to operate between  $\sim 74$  and 11 kyr BP (Whittaker et al., 2011). The consistent and abrupt nature of change in our Drake Passage Nd isotope record favours the idea that SWW forcing (Whittaker et al., 2011; Fig. 4.5) was the predominant control on Southern Ocean water mass properties during the last glacial through efficient modulation of lateral and vertical mixing.

#### 4.4.3. Transition into the interglacial Southern Ocean between 18 and 14 kyr BP

The structure of the Southern Ocean water column during HS1 was more differentiated than the early HS1 scenario between 16.9 and 15.8 kyr BP. In the Drake Passage, centennial fluctuations of  $\sim 2$  epsilon units are evident, paired with a major transition in ventilation state at  $\sim 15.3$  kyr BP (Burke et al., unpubl. data; Figs. 4.6 and 4.7). At the same time, the Tasman time series shows a gap between 16.7 and 14.8 kyr BP, i.e. during the interval of maximum increase of Southern Ocean opal flux (Anderson et al., 2009) and intensification of the SWW in the Indo-Pacific sector of the Southern Ocean (Whittaker et al., 2011; Figs. 4.5 and 4.7).

Variability on millennial to (sub) centennial time scales during late HS1 and the ACR was reconstructed from high resolution surface ocean proxies in Southern Ocean (Martínez-Botí et al., 2015), Cape Basin (Barker et al., 2009) and North Atlantic sediments (Bard et al., 2000; Carlson et al., 2008; Thornalley et al., 2011; Fig. 4.5), and identified in North Atlantic deep-sea corals (Robinson et al., 2005; Eltgroth et al., 2006; Thiagarajan et al., 2014; Wilson et al., 2014; Fig. 4.7). Similar to shifts in the Drake Passage time series (Fig. 4.7), Piotrowski et al. (2004, 2005) found significant pre-Bølling Nd isotope fluctuations of  $\sim 2 - 3$  epsilon units in the deep Cape Basin. The original record was re-visited by Piotrowski et al. (2012) with a refined approach which missed, however, sampling the full variability. The resulting deglacial evolution was significantly smoother, similar to other deep ocean  $\epsilon_{Nd}$  records (Piotrowski et al., 2009; Skinner et al., 2013; Fig. 4.7) rendering the Drake Passage high frequency Nd isotope variability unique in the deeper water column of the Southern Ocean.

##### 4.4.3.1. Overturning circulation and ocean ventilation: the 15.8 to 14.7 kyr BP interval

During mid-HS1 between 15.8 and 15.2 kyr BP, and hence before the ACR transition, our data show a shift from  $\epsilon_{Nd} = -6.6 \pm 0.2$  to  $\epsilon_{Nd} = -7.9 \pm 0.2$  leading a ventilation peak ( $\Delta\Delta^{14}C \approx -90\%$ ) at  $\sim 15.3$  kyr BP during an interval of intense wind-induced upwelling (Anderson et al., 2009) and

enhanced SWW activity over New Zealand (Whittaker et al., 2011; Fig. 4.7). The abruptness of the initial shift at  $\sim 15.8$  kyr BP could partly result from the fact that the coral recording  $\epsilon_{\text{Nd}} = -6.6 \pm 0.2$  at Burdwood Bank was under stronger influence from Pacific-derived water masses bound to the SAF and the boundary current joining the ACC at the depth of the sampling location (Well et al., 2003; Brearley et al., 2014; Fig. 4.2). In the modern ocean, the effect of this boundary current on the Nd isotope distribution at Burdwood Bank is, however, barely significant (Chapter 3). Nevertheless, the initial transition towards Drake Passage UCDW  $\epsilon_{\text{Nd}} = -7.5 \pm 0.2$  paired with low  $\Delta\Delta^{14}\text{C}$  of  $\sim -260\%$  points to significant admixture of radiocarbon-depleted glacial water masses from the North Atlantic (Wilson et al., 2014; Figs. 4.6 and 4.7) and was led by stronger influence of SWW over New Zealand (Whittaker et al., 2011). Based on deep-sea coral data from the New England Seamounts (NES) in the western North Atlantic it has been speculated that the build-up of a warm, saline, radiocarbon-depleted and radiogenic sub-surface water mass from 15.8 kyr BP was fed from the Southern Ocean (Thiagarajan et al., 2014, Wilson et al., 2014). Given the well-ventilated and unradiogenic signal recorded in the Drake Passage at the same time, this seems an unlikely scenario (Fig. 4.7).

In the tropical and central North Atlantic, enhanced mid-depth circulation was recorded from  $\sim 16.3$  kyr BP (Gherardi et al., 2009; Huang et al., 2014; Fig. 4.7) and Nd isotope data from the abyssal Cape basin indicate stronger influence of Atlantic water masses from around 16 kyr BP (Piotrowski et al., 2012). At the same time, the western basin remained relatively invariant (Skinner et al., 2013; Fig. 4.7), consistent with stable isotope data indicating reduced admixture of northern-sourced waters to the deep Southwest Atlantic Ocean until  $\sim 15$  kyr BP (Lund et al., 2015). Such deep processes coincided with a rapid rise in sub-surface dwelling *G. inflata*  $\delta^{18}\text{O}_{\text{ivc}}$  in the Northeast Atlantic (i.e. ice-volume corrected  $\delta^{18}\text{O}$ , representing subsurface density; Thornalley et al., 2010), ventilation of extremely radiocarbon-depleted Arctic Mediterranean water masses (Thornalley et al., 2015), as well as mid-depth ventilation, and hence overturning activity in the Northeast Atlantic (cf. Thornalley et al., 2011; Fig. 4.7). The close relationship between North Atlantic surface ocean conditions and water mass formation has been diagnosed by Manabe and Stouffer (1995).

The mid-HS1 ventilation of extremely radiocarbon-depleted and radiogenic deep waters in the Northeast Atlantic and Nordic Seas (Crocket et al., 2011; Thornalley et al., 2011; 2015) could have mixed with a less radiocarbon-depleted and unradiogenic source in the Northwest Atlantic to cause mid-depth fluctuations between  $\epsilon_{\text{Nd}}$  of  $-11.5$  to  $-12.5/\Delta\Delta^{14}\text{C} \approx -120$  to  $-130\%$  and  $\epsilon_{\text{Nd}}$  of  $-13$  to  $-14.5/\Delta\Delta^{14}\text{C} \approx -160$  to  $-180\%$  recorded in the Northwest Atlantic (Wilson et al., 2014). From Figure 4.6 follows that Drake Passage UCDW of  $\Delta\Delta^{14}\text{C} \approx -260\%$  and  $\epsilon_{\text{Nd}} \approx -7.5 \pm 0.2$  at  $\sim 15.6$  kyr BP could then result from mixing between mid-depth Northwest Atlantic water masses with  $\epsilon_{\text{Nd}}$  of  $-13$  to  $-14.5$  and  $\Delta\Delta^{14}\text{C} \approx -160$  to  $-180\%$  at 15.8 kyr BP (Wilson et al., 2014) with underlying radiogenic and radiocarbon-depleted water masses in the Southwest Atlantic and/or Pacific (Skinner et al., 2010, 2013, 2015; Noble et al., 2013; Fig. 4.6), consistent with Atlantic transfer times (Huhn et al., 2008).

The transfer of this water mass could thus relate to an early spin-up of mid-depth Atlantic circulation around 16 kyr BP (Gherardi et al., 2009; Huang et al., 2011).

The following short-lived ventilation pulse at 15.3 kyr BP ( $\Delta\Delta^{14}\text{C} \approx -90\text{‰}$ ) paired with a strong North Atlantic contribution to Drake Passage UCDW ( $\epsilon_{\text{Nd}} = -7.9 \pm 0.2$ ; Fig. 4.6) is inconsistent with mid-HS1  $\Delta\Delta^{14}\text{C}$  values of -120 to -230‰ in the Northwest Atlantic over the entire period (Wilson et al., 2014; Fig. 4.7). Unless the formation of unknown deep water masses did occur in the Southern Ocean, the strong ventilation signal bypassed the NES or, alternatively, was not sampled. The latter is supported by the fact that the NES data set has a gap between  $\sim 15.4$  and 15.1 kyr BP (Wilson et al., 2014). Regardless, the western basin was dominated by old radiocarbon-depleted water masses (Wilson et al., 2014) whereas Northeast Atlantic was well-ventilated (Thornalley et al., 2011) pointing to different water masses dominating the respective basins during mid-HS1 (Fig. 4.7). Such inter-basin gradients have, moreover, been recognised in stable isotope data (e.g., Matsumoto and Lynch-Stieglitz, 1999) and Nd isotopes (Roberts et al., 2010, 2015; Piotrowski et al., 2012), likely resulting from stronger influence of relatively radiogenic Nordic Seas overflow waters in the eastern basin (Crocket et al., 2011) and/or local effects (Roberts et al., 2015). A Nd isotope gradient is also evident in the deep South Atlantic Ocean throughout the entire 18 to 14 kyr BP interval with, however, different signs to the North Atlantic (Piotrowski et al., 2012; Skinner et al., 2013; Fig. 4.7). During mid-HS1 the inter-basin Nd isotope contrast in the South Atlantic was most pronounced when  $\epsilon_{\text{Nd}} \approx -8$  was recorded in the abyssal Cape Basin (4981 m water depth; Piotrowski et al., 2012) whereas the western South Atlantic basin showed  $\epsilon_{\text{Nd}} \approx -6.4$  in 3770 m water depth (Skinner et al., 2013; Fig. 4.5). The Cape Basin record has been interpreted in the light of admixed NADW controlling the Nd isotope signal in response to overturning strength (Piotrowski et al., 2004, 2005 and 2012) thus indicating enhanced admixture of Atlantic-sourced waters during mid-HS1 (Fig. 4.7). It can therefore be speculated that the pre-dominant export route of deep Atlantic water masses into the Southern Ocean was through the eastern (South) Atlantic, consistent with stable isotope data (Lund et al., 2015). Assuming that the core of GNAIW was significantly shallower (e.g., Curry and Oppo, 2005) than the deep Cape basin core location in 4981 m water depth (Piotrowski et al., 2012) implies substantial deepening and/or intensification of GNAIW/NADW export through the eastern Atlantic basin during mid-HS1. This signal would propagate into the ACC where a strong Atlantic contribution to the circumpolar flow was recorded in the Drake Passage towards 15.3 kyr BP when  $\epsilon_{\text{Nd}}$  was  $-7.9 \pm 0.2$ . Intriguingly, the Nd isotope shift at  $\sim 15.8$  kyr BP, potentially induced by North Atlantic buoyancy forcing, was led by a pronounced SWW intensification over New Zealand (Whittaker et al., 2011; Fig. 4.7). These processes were presumably linked through bipolar atmospheric coupling (e.g., Wang et al., 2015; Whittaker et al., 2011), thus both influencing Southern Ocean water mass mixing on, however, different time scales (Fig. 4.7; section 4.4.2.).



**Figure 4.7:** The Southern Ocean deep-sea coral time series during the transition to interglacial circulation between 18 and 14 kyr BP. (a) NGRIP oxygen isotope record (Rasmussen et al., 2006; Svensson et al., 2006). (b) Intermediate-depth Nd isotope record from Demerara Rise indicating flow vigour of upper AMOC circulation cell (Huang et al., 2014). (c) Mid-depth  $^{231}\text{Pa}/^{230}\text{Th}$  record from central North Atlantic indicating water mass export from the North Atlantic (Gherardi et al., 2009). (d) Deep-sea coral Nd isotope data from the New England seamounts (Wilson et al., 2014). (e) Northeast Atlantic  $\delta^{18}\text{O}_{\text{ivc}}$  of subsurface dwelling foraminifer *G. inflata* as a seawater density indicator (Thornalley et al., 2010). (f) Offset between benthic and planktic radiocarbon signature as a measure of ventilation state downstream of ISOW in the Northeast Atlantic (Thornalley et al., 2011). (g) opal flux record of upwelling intensity from the South Atlantic sector of the Southern Ocean (Anderson et al., 2009) and Hollywood cave  $\delta^{13}\text{C}$  record of SWW influence over South Island, New Zealand (Whittaker et al., 2011). (h) Drake Passage radiocarbon deep-sea coral time series of UCDW depth range indicating ventilation (Burke and Robinson, 2012; Chen et al., 2015; Burke et al., unpubl. data; see Fig. 4.5 caption for details). (i) Drake Passage deep-sea coral Nd isotope time series of UCDW depth range from this study (purple) with U-series age uncertainties from Burke and Robinson (2012), Chen et al. (2015) and Burke et al., (unpubl. data); HS1 coral (black) from Robinson and van de Flierdt (2009); Nd isotope record from MD07-3076 in the deep western basin of the South Atlantic (grey shading, dark line; Skinner et al., 2013) and Nd isotope record from the deep Cape Basin in the Southeast Atlantic (grey shading, white line; Piotrowski et al., 2005, 2012). (j) Tasman deep-sea coral radiocarbon data representing ventilation in the Southwest Pacific sector of the Southern Ocean (Hines et al., 2015; see Fig. 4.5 caption for details). (k) Tasman deep-sea coral Nd isotope time series, stippled line indicates data gap (this study), and deep Nd isotope record from CHAT5K at Chatham Rise in the deep Southwest Pacific (Noble et al., 2013). (l) WAIS Divide oxygen isotope record (WAIS Divide project members, 2013). (m) WAIS Divide ice core  $\text{CO}_2$  record (Marcott et al., 2014). Grey stippled lines indicate events at 15.2, 15.7, 16.2 and 20.4 kyr BP, respectively. Grey bars at the y axes of I and K indicate the modern Nd isotope range of UCDW at the Drake Passage coral sampling locations (Chapter 3). B-A refers to Bølling-Allerød interstadial in the Northern Hemisphere, others as in Fig. 4.4.

Regardless, the Drake Passage Nd isotope signal of  $\epsilon_{\text{Nd}} = -7.9 \pm 0.2$  was not a pure North Atlantic signal (Roberts et al., 2010; Crocket et al., 2011; Piotrowski et al., 2012; Wilson et al., 2014; Roberts and Piotrowski, 2015) and required admixture of water masses with a more radiogenic Nd isotope signature, similar to the modern setting (e.g., Stichel et al., 2012). At the same time, the Drake Passage  $\Delta\Delta^{14}\text{C}$  was  $-90\text{‰}$  in 1064 m water depth, and as such better ventilated than modern UCDW ( $\Delta\Delta^{14}\text{C} \approx -115\text{‰}$ ; Key et al., 2004). Despite the high variability of northern water mass radiocarbon signatures during HS1 (e.g., Robinson et al., 2005; Wilson et al., 2014), significantly better-than-modern NADW ventilation is unlikely (i.e.  $\Delta\Delta^{14}\text{C} \approx -70\text{‰}$ ; Key et al., 2004). Therefore, we suggest that two similarly strong overturning cells operated in both, the Atlantic and Pacific Ocean during the mid-HS1 interval efficiently ventilating large parts of the global mid-depth ocean.

At 15.2 kyr BP,  $\Delta\Delta^{14}\text{C}$  drops abruptly to  $\sim -160\text{‰}$  while the  $\epsilon_{\text{Nd}}$  remains unradiogenic at  $-8.0 \pm 0.2$  (in the same coral) showing that the strong ventilation pulse from the North Atlantic was a very short-lived event and/or a deep old Atlantic carbon reservoir was eroded (Fig. 4.7). The fact that one coral recorded changes in radiocarbon while Nd isotopes remained invariable underpins that such abrupt changes were unlikely to be dominated from simple vertical movements of water mass boundaries (isoneutrals). This is because both geochemical parameters would be expected to respond simultaneously without delay among one another. After  $\sim 15.2$  kyr BP a drop in Nd isotopic composition to a more Pacific-like signal of  $\epsilon_{\text{Nd}} = -6.3 \pm 0.2$  at 14.9 kyr BP was associated with  $\Delta\Delta^{14}\text{C}$  of  $-140\text{‰}$  (Figs. 4.6 and 4.7). At the same time, the North Atlantic was characterised by freshwater-induced (sub-) surface density reductions during this 300-year-long interval (Bard et al., 2000;

Thornalley et al., 2010). The surface ocean perturbations were paired with reduced deep convection in the Nordic Seas (Thornalley et al., 2015), expressed in poor GNAIW/NADW ventilation (Thornalley et al., 2011). A decrease of GNAIW/NADW export to the Southern Ocean could then partly be compensated by enhanced Pacific export to the Southern Ocean leading to Drake Passage  $\epsilon_{Nd} = -6.3 \pm 0.2$  (Fig. 4.7). On the other hand, a more direct way would be SWW-controlled admixture of Pacific water masses into the Southern Ocean (e.g., Lamy et al., 2015). The lack of covariation with influence in New Zealand around  $\sim 15$  kyr BP (Fig. 4.7) may result from dating and age model uncertainties during such abrupt and short-lived events, but also from the asymmetric response of different Southern Ocean sectors to climatic forcing (e.g., Sallée et al., 2008). The following ACR/B-A transition is characterised by a shift of about 2  $\epsilon_{Nd}$  towards stronger contribution of Atlantic-sourced waters, consistent with high subsurface ocean density in the Northeast Atlantic, overflow activity, overall deepening of well-ventilated North Atlantic water masses, their penetration into the global deep ocean (e.g., McManus et al., 2004; Gherardi et al., 2009; Piotrowski et al., 2004, 2012; Barker et al., 2010; Crocket et al., 2011; Thornalley et al., 2011; Noble et al., 2013; Skinner et al., 2010, 2013, 2014) and the extension of UCDW into the SW Pacific (Figs. 4.6 and 4.7). The overlying well-ventilated Drake Passage AAIW appears to have followed the UCDW Nd isotope trend with an offset of about one epsilon unit (Fig. 4.5). The sparse Nd isotope values were remarkably similar to contemporaneous AAIW Nd isotope signatures extracted from Brazilian margin sediments (Pahnke et al., 2008). The radiogenic nature of AAIW Nd isotope signatures could have resulted from incorporation of surface water masses, either from the Antarctic or from the Chilean shelves, both of which characterised by relatively radiogenic Nd isotopic compositions (Walter et al., 2000; Carter et al., 2012; Noble et al., 2012 and references therein; Chapter 3).

It has been shown for the last deglaciation that the global temperature signal was led by the Northern Hemisphere (Shakun et al., 2012). A bipolar seesaw behaviour propagated North Atlantic signals to the South Atlantic Ocean on millennial time scales (Barker et al., 2009), and through atmospheric teleconnections to the Pacific sector of the Southern Ocean (Whittaker et al., 2011). As noted above, our data can be interpreted to reflect a mechanistic link between North Atlantic salt content, deep water formation and export to the Southern Ocean, a link that has been diagnosed to respond to freshwater perturbations on appropriate time scales (Manabe and Stouffer, 1995; Stouffer et al., 2007). Moreover, the results of Manabe and Stouffer (1995) show multi-decadal response to freshwater perturbations superimposed on a centennial-scale recovery after initialisation indicating that some of the high frequency oscillations may be immanent to the system.

However, the close covariation with SWW intensity leads us to suggest that these Northern Hemisphere processes were strongly moderated by Southern Hemisphere atmospheric dynamics as pointed out by Williams et al. (2005) and shown by Whittaker et al. (2011). A direct link between the SWW and North Atlantic Ocean dynamics is established through the Agulhas salt leakage providing an important dynamic feedback during AMOC recovery (Biaostoch et al., 2009; Beal et al., 2011;

Durgadoo et al., 2013), but also by interoceanic exchange of water masses through the Drake Passage (Lamy et al., 2015) and south of Australia (De Deckker et al., 2012). North Atlantic freshwater events cause salt and heat accumulation in the tropical and subtropical Atlantic which may then contribute to the re-invigoration of Atlantic overturning (e.g., Broecker et al., 1990; Schmidt et al., 2004; Carlson et al., 2008). Thus, salt feedbacks and atmospheric teleconnections linking interoceanic and bipolar seesawing were likely involved in the changes recorded in Drake Passage UCDW deep-sea corals. If the partial deflection of SAF-bound waters in response to SWW dynamics (Lamy et al., 2015) changed Drake Passage water mass mixing, atmospheric propagation of interhemispheric feedbacks played presumably a critical role (Williams et al., 2005; Whittaker et al., 2011; Wang et al., 2015) as the oceanic build-up of heat acts on the order of hundreds of years (Stocker and Johnson, 2003) and is thus too slow.

Therefore, it seems likely that the SWW controlled a significant portion of the abrupt Nd isotope variability in the ACC, likely superimposed on centennial to millennial scale changes of global overturning circulation (cf. WAIS Divide project members, 2015). Such abrupt changes would require the SWW to steer the ACC bifurcation toward a threshold position thus inducing northward deflection of SAF-bound water masses. Through atmospheric feedbacks, potentially linked with Northern Hemisphere perturbations, this mechanism could drive abrupt changes in Drake Passage water mass mixing.

#### **4.4.3.2. The role of Southern Ocean mid-depth circulation in atmospheric CO<sub>2</sub> rise**

The sampling resolution of our deep-sea coral time series across a crucial interval during the last deglaciation allows speculation on pathways and origin of CO<sub>2</sub> released from the deep ocean into the atmosphere via the Southern Ocean (Anderson et al., 2009; Burke and Robinson, 2012).

Our data set shows that the early deglacial rise in atmospheric CO<sub>2</sub> was associated with deep Pacific-derived water masses dominating the Southern Ocean, following an overall Antarctic timing (e.g., Marcott et al., 2014). However, Marcott et al. (2014) speculated that phases of pronounced rapid atmospheric CO<sub>2</sub> rise at ~16.2, 14.8 and 11.7 kyr BP (Figs. 4.4 and 4.5) might result from re-organisation of the AMOC. The Nd isotope data presented here does not show a simple deglacial link between circulation and atmospheric CO<sub>2</sub> rise. After the mid-HS1 event, enhanced atmospheric CO<sub>2</sub> rise occurred during an interval of relatively strong advection of well-ventilated Atlantic-derived water masses into the Southern Ocean at 14.7 and 11.7 kyr BP (Burke and Robinson, 2012; Chen et al., 2015; Marcott et al., 2014; Fig. 4.5). Expansion of Pacific-derived water masses into the Southern Ocean was vice versa associated with phases of reduced CO<sub>2</sub> rise such as recorded at ~15 kyr BP in the Drake Passage and south of Tasmania during the late ACR (Fig. 4.5). Before ~15.3 kyr BP, this relationship seems to have been reverse such that stronger influence of Pacific-derived waters in the Southern Ocean was associated with enhanced atmospheric CO<sub>2</sub> rise during early HS1.

Recent work of Martínez-Botí et al. (2015) shows intriguing abrupt (sub) millennial variability of Southern Ocean CO<sub>2</sub> degassing. Their boron isotope data indicate that the Southern Ocean turned into a net source during mid-HS1 and the ACR (Martínez-Botí et al., 2015). These intervals are characterised by a strong contribution of relatively well-ventilated Atlantic-sourced waters in the Southern Ocean reflected in average Nd isotope signatures of  $\epsilon_{\text{Nd}} = -7.7 \pm 0.3$  ( $n = 22$ ) during and after the ACR and  $\epsilon_{\text{Nd}} = -7.8 \pm 0.2$  ( $n = 4$ ) during the mid-HS1 between 15.8 and 15.2 kyr BP (Fig. 4.5). The deglacial Eastern Equatorial Pacific turned into a significant CO<sub>2</sub> source at 15 kyr BP (Martínez-Botí et al., 2015), paralleled by northward penetration of UCDW in the Southwest Pacific as recorded south of Tasmania at 14.8 kyr BP (Fig. 4.5) indicating that replacement of deep Pacific-sourced waters enhanced oceanic CO<sub>2</sub> degassing. Age model uncertainties and different temporal resolution do, however, limit a more detailed analysis of the relationship between circulation changes and Southern Ocean degassing. Moreover, changing ocean-atmosphere equilibration time and re-injection of poorly equilibrated/high pCO<sub>2</sub> water masses into the ocean interior, a process referred to as “ocean tunnelling” (e.g., Martínez-Botí et al., 2015), could have delayed a direct response of atmospheric CO<sub>2</sub> content to Southern Ocean radiocarbon content.

In summary, these findings support the idea that the deglacial atmospheric CO<sub>2</sub> rise was associated with changes in the global overturning circulation, underpinning the crucial role of the Southern Ocean during the deglacial climate re-organisation (Anderson et al., 2009; Skinner et al., 2010, 2013; Schmitt et al., 2012). Notably, it is important to consider age model uncertainties and signal smoothing limiting applicability of comparison between palaeoceanographic archives; a problem that may be overcome with high-resolution archives and resolute age control, such as deep-sea corals, allowing multi-proxy approaches on the same samples.

#### 4.5. Summary and conclusions

We presented combined Nd isotope and radiocarbon data extracted from deep-sea corals collected south of Tasmania and in the Drake Passage in order to constrain glacial to deglacial Southern Ocean dynamics. We generated two mid-depth high resolution time series from individual corals covering the interval between 26 and 12 kyr BP.

The Tasman Nd isotope time series suggests a pronounced southward extension of relatively well-ventilated GNPIW from 26 to 16.7 kyr BP (HS2 to HS1). This Pacific influence was lost just before the Antarctic Cold Reversal, with a timing that paralleled Antarctic temperature and CO<sub>2</sub> changes, as well as increased upwelling associated with southward frontal movement and a reduction of deep stratification in the Southern Ocean. During the ACR, a pronounced change in water mass mixing was linked with the expansion of UCDW and enhanced ventilation recorded by deep-sea coral radiocarbon content.

The mid-depth Drake Passage Nd isotope and radiocarbon signatures do not follow such Antarctic timing. In particular, the Nd isotope signal is characterised by a modern-like baseline,

punctuated by (sub) millennial to centennial phases of intensified Pacific influence. During the LGM, the Drake Passage UCDW was dominated by mixing of mid-depth North Atlantic and underlying deep waters. The LGM scenario substantiates previous reconstructions of a deeply stratified Southern Ocean water column, but provides also evidence for occasional admixture of significant volumes of deep waters to mid-depths.

The Nd isotope difference between water masses bathing the Tasmanian margin and the Drake Passage imply a pronounced Nd isotope gradient between circumpolar flow, which can be monitored in the Drake Passage, and water masses originating from the North Pacific, recorded south of Tasmania, until 16.7 kyr BP. The lateral admixture of such GNPIW into the circumpolar flow as well as deepening of Southern Ocean mixing seem to be related to SWW forcing and the position of oceanic fronts. This glacial mode of operation with two mid-depth cells ventilating a deeply stratified glacial ocean was replaced by a modern type of circulation between 16.7 and 14.8 kyr BP. Significant deepening of Southern Ocean mixing during early HS1 was followed by a change in Southern Ocean ventilation state, and presumably of large parts of the global ocean during mid-HS1, i.e. the interval from ~15.8 to 15.2 kyr BP. This occurred likely in dynamic interaction of North Atlantic processes coupled interhemispherically with the SWW.

The mid-HS1 interval was also a turning point for the relation of Southern Ocean water mass mixing and the outgassing of old carbon from the glacial deep ocean into the deglacial atmosphere. After mid-HS1, enhanced CO<sub>2</sub> degassing from the ocean was associated with the extension of Atlantic water masses into the Southern Ocean. This indicates that stronger Atlantic overturning promoted a reduction of global ocean stratification. During the early deglacial, this relationship was reverse when atmospheric CO<sub>2</sub> rise was associated with (deep) Pacific-derived water masses dominating the Southern Ocean.

**Declaration:** This work was completed as part of a collaborative multi-proxy investigation. I contributed the Nd isotope and concentration analyses. Andrea Burke and Sophie K. Hines provided the uranium-series and radiocarbon data and collected the neodymium fraction as outlined in Chapter 2. The data was generated from sample material provided by Laura F. Robinson and Jess F. Adkins.

## **Chapter 5**

# **Mid-depth ocean circulation during MIS 2 and MIS 3: neodymium isotope evidence for interhemispheric coupling**

## Abstract

The insolation-driven transition into the Last Glacial Maximum (LGM) was punctuated by abrupt millennial-scale oscillations, termed Dansgaard-Oeschger (D/O) cycles, comprising cold (stadial) and warm (interstadial) conditions in the Northern Hemisphere. We here aim to evaluate the interhemispheric oceanic response during the long-term transition into peak glacial conditions and intermittent short-term oscillations. Therefore, we use the neodymium (Nd) isotopic composition extracted from absolutely dated deep-sea coral skeletons recording mid-depth (695 - 1986 m) seawater signatures from the North Atlantic and the Southern Ocean.

In the North Atlantic, peak glacial conditions featured reduced influence from the Northwest Atlantic source region (i.e. Labrador Sea) on mid-depth waters. This is reflected in a Nd isotope trend from  $\epsilon_{\text{Nd}} \approx -12.6 \pm 0.2$  to  $\epsilon_{\text{Nd}} = -10.6 \pm 0.3/-11.3 \pm 0.4$  between  $\sim 47$  and  $\sim 25$  kyr BP at the New England Seamounts (NES). Southern Ocean source waters can be ruled out as a significant influence, consistent with available Nd isotope and  $^{231}\text{Pa}/^{230}\text{Th}$  data. Instead, Northeast Atlantic deep-sea coral data suggest that a reduction of Labrador Sea Water (LSW) may have been compensated for by expansion of water masses sourced from the Nordic Seas and/or from the Mediterranean Sea. This implies significant isotopic variability of deep water masses exported from the North Atlantic.

At the same time, Upper Circumpolar Deep Water (UCDW) recorded in the Drake Passage appears remarkably invariable at  $\epsilon_{\text{Nd}} \approx -7.5$  between 39.2 and 27.2 kyr BP, a baseline value which is also evident during MIS 2 and close to modern UCDW values. In contrast, mid-depth Nd isotope data from south of Tasmania, spanning the same time interval from 44.1 to 27.0 kyr BP, display seawater Nd isotope compositions between  $\epsilon_{\text{Nd}} = -4.9 \pm 0.2$  and  $\epsilon_{\text{Nd}} = -6.9 \pm 0.2$ . The most radiogenic values are observed towards the end of MIS 3 and during the LGM ( $\epsilon_{\text{Nd}} \approx -5.5$ ). Local inputs and vertical shifts of water mass boundaries can be excluded to cause these values. Instead, the recorded signal was dominated by dynamic mixing of unradiogenic ACC-derived UCDW and radiogenic Glacial North Pacific Intermediate Water (GNPIW). Under glacial conditions, a southward expansion of GNPIW was paired with the northward migration of ACC fronts, likely along with the ACC-bound UCDW core. We consider the implied gradient to result from reduced cross-frontal mixing of GNPIW into the ACC core. Presumably, equatorward intensification of glacial Southern Hemisphere westerly winds (SWW) enhanced northward deflection of water masses bound to the northern flank of the ACC.

The immediate effect of SWW forcing on the Tasmanian Nd isotope signal is demonstrated for an interval of high resolution data coverage across Heinrich Stadial 3 (HS3). In contrast to long-term trends, northwards shifts seem to have induced abrupt ‘flushing’ of the Tasman Sea with UCDW. The Tasmanian margin data can be integrated into a sequence of events involving North Atlantic subsurface ocean warming promoting ice-sheet melting towards the Heinrich IRD event and followed by intrinsic oscillations. This sequence is interhemispherically linked through atmospheric teleconnections thus dictating abrupt Tasmanian margin Nd isotope changes.

## 5.1. Introduction

The pen-ultimate interglacial (Marine Isotope Stage 5e; 130 - 123 kyr BP) was followed by Marine Isotope Stages (MIS) 4 (71 - 57 kyr BP) and 3 (57 - 29 kyr BP) comprising the transition into peak glacial conditions of the Last Glacial Maximum (LGM; 23 - 19 kyr BP). While glacial-interglacial climate conditions are ultimately driven by Northern Hemisphere insolation, detailed records are influenced by nonlinearities and feedbacks in the climate system (e.g., Milankovitch, 1941; Hays et al., 1976; Broecker and Denton, 1989; Imbrie et al., 1992, 1993; Clark et al., 2009). Superimposed on the long-term trends, millennial-scale stadial-interstadial oscillations (cold and warm phases, respectively), the Dansgaard-Oeschger (D/O) cycles (Dansgaard et al., 1993), follow a characteristic saw tooth pattern of rapid warming and gradual cooling as revealed by Greenland ice core data (Barker et al., 2011). At times, D/O cycles are preceded by large ice rafting events in the Northern Hemisphere, referred to as Heinrich events (Bond and Lotti, 1995), which stand out in the marine record (Hemming, 2004).

The abruptness of interstadial D/O inceptions is not recorded in Antarctic ice core records. Instead, rather smooth millennial-scale variability is observed (Blunier et al., 1998; Blunier and Brook, 2001). On orbital time scales, the Southern Hemisphere appears to lead the Northern (Imbrie et al., 1992), whereas more recent work suggests a northern lead (e.g., Huybers, 2009; Shakun et al., 2012; WAIS Divide project members, 2015). Similarly, lead and lag relationships on millennial time scales are under debate (e.g., Steig and Alley, 2002; Schmittner et al., 2003). Stocker and Johnson (2003) put forward a conceptual model of the thermal bipolar seesaw considering the Southern Ocean's thermal inertia dampening and integrating abrupt changes initiated in the North Atlantic, consequently implying "near zero-phase anticorrelation" (Barker et al., 2011).

In the surface ocean such seesaw behavior is expressed in shifts of sea surface temperatures and the position of oceanic fronts in response to the cross-equatorial re-distribution of salt and heat (Broecker et al., 1990; Broecker, 1998; Bard and Rickaby, 2000; Schmidt et al., 2004; Barker et al., 2009; Sikes et al., 2009). As the surface ocean is the ultimate source to form deep water masses (Stocker and Wright, 1991), it has been proposed that such bipolar seesaw behaviour is translated into deep water formation and export rates, water mass geometry and overturning strength (e.g., Broecker, 1998; Seidov and Maslin, 2001; Seidov et al., 2001; Piotrowski et al., 2005; Barker et al., 2009; Skinner et al., 2013). All such processes are integral parts of the global meridional overturning circulation (MOC; e.g., Lumpkin and Speer, 2007; Talley, 2013).

The modern mode of MOC operation is dominated by Atlantic overturning (AMOC) and characterised by strong southward export of NADW (e.g., Marshall and Speer, 2012) which is fed by dense waters formed in the Labrador (e.g., Lilly et al., 1999; Jenkins et al., 2015), Mediterranean (Gascard, 1978; Schlitzer et al., 1991) and Nordic Seas (e.g., Ronski and Budéus, 2005; Jenkins et al., 2015) from cooling of northward flowing warm and saline surface water masses. In the Atlantic Ocean interior, the southward NADW flow is balanced by intermediate and bottom water masses sourced

from the Southern Ocean, i.e. Antarctic Intermediate Water (AAIW) and Antarctic Bottom Water (AABW), respectively (e.g., Lumpkin and Speer, 2007). Their formation is connected to the dynamics of the Antarctic Circumpolar Current (ACC) where NADW mixes with old, nutrient-rich and oxygen-poor water masses from the Indian and Pacific Ocean, i.e. Pacific Deep Water (PDW) and Indian Deep Water (IDW) to form Circumpolar Deep Water (CDW) (Reid and Lynn, 1971; Callahan, 1972; Talley, 2013; Fig. 5.1). The admixture of PDW and IDW into the ACC occurs pre-dominantly in the upper deep level causing a distinct minimum in oxygen and salinity paired with local maxima in nutrient content and consequently referred to as Upper Circumpolar Deep Water (UCDW) (Reid and Lynn, 1971; Callahan, 1972). Lower Circumpolar Deep Water (LCDW), in contrast, is characterised by a salinity maximum, oxygen and nutrient minima due to the dominant influence of NADW (Reid and Lynn, 1971; Callahan, 1972; Fig. 5.2). Strong westerly winds induce intense mixing, steepening of isoneutrals and upwelling of deep water masses into the surface mixed layer (Marshall and Speer, 2012; Fig. 5.2). Here, in particular UCDW participates in the formation of AAIW which is then subducted into the ocean interior north of the Polar Front (PF) (Piola and Georgi, 1982; Bostock et al., 2013; Talley, 2013). South of the PF, upwelling CDW mixes with local water masses on the Antarctic shelves to form shelf bottom waters upon brine rejection (Orsi et al., 1999). Such dense shelf bottom waters overflow the shelf edge whereby they incorporate CDW to ultimately form Antarctic Bottom Water (AABW) ventilating the abyss of all ocean basins (Orsi et al., 1999; Fig. 5.1). Northward flowing AABW mixes diapycnally into overlying water masses thereby closing the global overturning circulation system (Lumpkin and Speer, 2007; Talley, 2013). In the Pacific Ocean, such slow diapycnal mixing is the dominant driver of deep overturning (MacDonald et al., 2009; Talley, 2013) as a low salinity layer prohibits deep water formation in the North Pacific (Warren, 1983; Emile-Geay et al., 2003).

It has been proposed that variability in overturning circulation and associated interhemispheric seesaw patterns played a critical role for glacial-interglacial changes of atmospheric CO<sub>2</sub>, i.e. for the CO<sub>2</sub> decrease towards peak glacial conditions (Blunier and Brook, 2001) as well as for the deglacial rise (Anderson et al., 2009; Marcott et al., 2014). Similarly, interhemispheric temperature changes identified in ice cores were associated with oceanic re-organisation during D/O cycles (Blunier and Brook, 2001). Changes in atmospheric CO<sub>2</sub> concentrations are likely to be related to the nature of deep ocean circulation. This is due to the linkage between wind-driven Southern Ocean upwelling, deep carbon sequestration, the position of the NADW-AABW boundary and resulting mixing efficiency between the upper and lower meridional circulation cells (e.g., Anderson et al., 2009; Sigman et al., 2010; Ferrari et al., 2014).

In order to decipher ocean-atmosphere interaction and associated implications for the climate system, it is crucial to constrain past circulation patterns. A suitable proxy to trace water mass provenance, and hence ocean circulation, is the neodymium (Nd) isotopic composition of seawater (e.g., von Blanckenburg, 1999). The Nd isotopic composition is usually expressed as  $\epsilon_{Nd} =$

$((^{143}\text{Nd}/^{144}\text{Nd}_{\text{sample}})/(^{143}\text{Nd}/^{144}\text{Nd}_{\text{CHUR}}) - 1) \times 10,000$  where CHUR is the chondritic uniform reservoir (Jacobsen and Wasserburg, 1980).

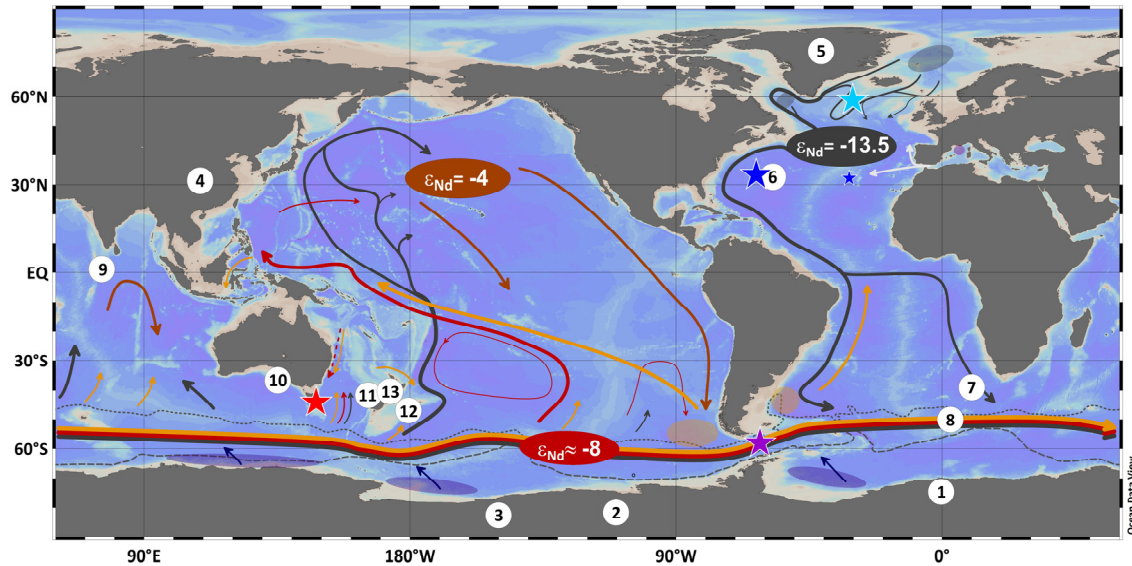


**Figure 5.1:** Global map with simplified sub-surface ocean circulation pattern superimposed (after Piola and Georgi, 1982; Talley and McCartney, 1982; Reid, 1989, 1994, 1997; McCartney, 1992; Mantyla and Reid, 1995; Talley, 1996; Sokolov and Rintoul, 2000; Macdonald et al., 2009; Kawabe and Fujio, 2010; Bostock et al., 2013; base map generated in ODV: Schlitzer, 2012). Dark grey: North Atlantic Deep Water (NADW) and Lower Circumpolar Deep Water (LCDW); red: Upper Circumpolar Deep Water (UCDW); red-brown: Pacific Deep Water (PDW) and Indian Deep Water (IDW); yellow: Antarctic Intermediate Water (AAIW). Hatched areas indicate main formation regions for NADW (grey), Mediterranean Outflow Water (MOW; purple), AAIW (yellow) and AABW (Antarctic Bottom Water; dark blue). Note that AABW fills the abyss of all major ocean basins (not shown here; see Orsi et al., 1999 and references therein) and that AAIW is also formed along the Antarctic Circumpolar Current (ACC) in all ocean basins (e.g., Piola and Georgi, 1982; Bostock et al., 2013). Stippled and dashed grey lines in the Southern Ocean indicate Subantarctic Front (SAF) and the southern ACC front (SACC), respectively (Orsi et al., 1995). Global seawater Nd isotope systematics represented by NADW ( $\epsilon_{\text{Nd}} \approx -13.5$ ; Piepgras and Wasserburg, 1987), PDW ( $\epsilon_{\text{Nd}} \approx -4$ ; Amakawa et al., 2009) and UCDW ( $\epsilon_{\text{Nd}} \approx -8$ ; Stichel et al., 2012; Chapter 3). Red star: deep-sea coral sampling location south of Tasmania (Fig. 5.2). Purple star: deep-sea coral sampling locations in the Drake Passage (Fig. 5.2). Sky blue star: deep-sea coral sampling location at Reykjanes Ridge. Note that Iceland Scotland Overflow Water (ISOW; grey line in the Northwest Atlantic Ocean) flows around the Reykjanes Ridge. Pink stars: the large star in the Northwest Atlantic indicates New England Seamounts coral sampling location as well as the location for a sedimentary deep North Atlantic Nd isotope and  $^{231}\text{Pa}/^{230}\text{Th}$  record from Bermuda Rise (Böhm et al., 2015); the small star in the central North Atlantic marks a coral sampling location off the Mid-Atlantic Ridge (Fig. 5.2). White stars denote locations of data used in Figures 5.5 and 5.7. (1) EDML oxygen isotope ice core record (EPICA community members, 2006, 2010). (2) Byrd icecore  $\text{CO}_2$  record (Ahn and Brook, 2008), WAIS Divide methane record (Rhodes et al., 2015). (3) Siple Dome C carbon dioxide record (Ahn and Brook, 2014). (4) Hulu cave speleothem oxygen isotope record (Wang et al., 2001). (5) NGRIP oxygen isotope ice core record (NGRIP, 2004). (6) Deep Nd isotope and  $^{231}\text{Pa}/^{230}\text{Th}$  record from ODP 1063 (4584 m; Böhm et al., 2015) (7) Deep Southeast Atlantic (4981 m water depth) Nd isotope record from Cape Basin core TNO57-21 (4981 m; Piotrowski et al., 2005). (8) Southern Ocean opal record from core TNO21-14PC (Anderson et al., 2009). (9) Deep Indian Ocean (3800 m) Nd isotope record from Chagos Trench core SK129-CR2 (Piotrowski et al., 2009). (10) Planktonic foraminifera abundance from MD03-2611 off Southern Australia (De Deckker et al., 2012). (11) Mid-depth Tasman Sea carbon isotope records from cores MD06-2986 (1477 m water depth) and MD06-2990/SO136\_003GC (944 m water depth) (Ronge et al., 2015). (12) Mid-depth Chatham Rise cores SO213/2\_82-1 (2066 m water depth), SO213/2\_84-1 (972 m water depth) (Ronge et al., 2015), and MD97-2120 (1210 m water depth) (Pahnke and Zahn, 2005). (13) Hollywood Cave speleothem record from Northwest South Island, New Zealand (Whittaker et al., 2011).

Water masses acquire their Nd isotope signature mainly in their source region in vicinity to the continental margins (Frank, 2002; Goldstein and Hemming, 2003). Distal changes of the seawater Nd isotopic composition are usually ascribed to atmospheric inputs (e.g., Greaves et al., 1999) and exchange processes with bathymetric features (Lacan and Jeandel, 2005a). The global distribution of dissolved Nd isotopes in the ocean is dominated by two source regions of distinct isotopic composition, i.e. the North Atlantic where NADW forms with  $\epsilon_{Nd} \approx -13.5$  (Piepgras and Wasserburg, 1987), and the North Pacific where a more volcanogenic signature of  $\epsilon_{Nd} \approx -4$  (Amakawa et al., 2009) is imprinted on PDW (Fig. 5.1). Such water mass-specific isotopic fingerprints result from the low oceanic Nd residence time of  $\sim 400$  to 2000 years (Tachikawa et al., 1999, 2003). Therefore, the intermediate Nd isotopic composition of ACC water masses ( $\epsilon_{Nd} \approx -8$ ) is dominated by efficient mixing between PDW and NADW (Carter et al., 2012; Stichel et al., 2012; Garcia-Solsona et al., 2014; Rickli et al., 2014; Basak et al., 2015; Fig. 5.1). Nevertheless, some water mass Nd isotope heterogeneity can be resolved in the Southern Ocean, in particular of locally formed bottom waters (Carter et al., 2012; Stichel et al., 2012; Garcia-Solsona et al., 2014; Rickli et al., 2014; Basak et al., 2015). Deciphering past Southern Ocean water mass signatures requires information about potential Nd isotope variability of source waters, e.g., NADW and PDW. Along those lines, recent work from the North Atlantic indicates that the Nd isotopic composition of NADW was variable (Wilson et al., 2014; Böhm et al., 2015; Roberts and Piotrowski, 2015).

Here, we present new Nd isotope data for the mid-depth (695 - 1986 m) ocean from precisely-dated deep-sea coral skeletons. The new records will be evaluated with respect to past variability in the North Atlantic source region and Southern Ocean water mass mixing during the latter parts of the last glacial cycle including phases of abrupt change, namely Heinrich events and D/O cycles.

## 5.2. Material and Methods

### 5.2.1. Deep-sea coral samples

#### 5.2.1.1. North Atlantic

Deep-sea coral specimens *Desmophyllum dianthus* from the North Atlantic have been collected at three locations, the New England Seamounts (n = 9), Reykjanes Ridge (n = 7) and in the central North Atlantic (n = 1). Samples from the New England Seamounts (NES) were collected with the deep submergence vehicle ALVIN from 1222 to 1986 m water depth and were Uranium-series dated to ages within MIS 3 and 2 (47.1 to 25.1 kyr BP; updated ages after Robinson et al., 2007) (Table 5.1; Fig. 5.2). All samples are currently bathed by upper NADW (uNADW; Fig. 5.2) carrying a strong LSW component (Talley and McCartney, 1982; Jenkins et al., 2015; Lambelet et al., accepted). One single *D. dianthus* has been collected from 1420 m water depth at the eastern flank of the Mid-Atlantic Ridge in the central North Atlantic and yielded an age of  $24.9 \pm 0.2$  (Adkins, unpubl. data). This sample was retrieved from uNADW range located just outside the modern Mediterranean Outflow Water (MOW) core depth of  $\sim 1000$  m (Reid, 1994; Fusco et al., 2008). MOW spreads from

the Strait of Gibraltar into the Eastern North Atlantic and its influence can be traced down to ~2500 m water depth in the Western North Atlantic (Reid, 1994; Figs. 5.1 and 5.2).

At the Reykjanes Ridge, *D. dianthus* specimens were raised by dredging from water depths between 997 and 1680 m during cruise CE0806 (Fig. 5.2). Nine U-series dates on seven individual corals covered MIS 5 to MIS 3 in the range from 109.8 to 35.9 kyr BP (Burke et al., 2012; Table 5.1). The mid-depth samples were collected along the northwestern flank of the Reykjanes Ridge and are pre-dominantly bathed by LSW with some admixture of modified ISOW (McCartney, 1992; Xu et al., 2010; Fig. 5.2). One intermediate-depth sample was dredged from 997 m water depth, i.e. between LSW and overlying SPMW (Fig. 5.2) (McCartney and Talley, 1982; Talley and McCartney, 1982; Fig. 5.2).

#### 5.2.1.2. Drake Passage

Five fossil specimens of *Desmophyllum dianthus* from the Drake Passage were processed, three of which have been U-series dated to be within MIS 3 and 2 ( $39.2 \pm 0.3$ ,  $35.4 \pm 0.2$  and  $27.2 \pm 0.2$  kyr BP), and the other two individuals are  $103.5 \pm 0.7$  and  $226.0 \pm 3.4$  kyr BP old (Table 5.1). The samples have been collected by dredging or trawling during cruises NBP0805 and NBP1103 from 695, ~820 and 1134 m water depth at Sars seamount, Shackleton Fracture Zone (SFZ) and Interim seamount, respectively (Table 5.1; Figs. 5.1 and 5.2; Burke et al., 2010; Margolin et al., 2014; see Chapter 3 for detailed description of sampling locations). The Drake Passage coral samples used here were raised from water depths currently dominated by UCDW (Sievers and Nowlin, 1984; Sudre et al., 2011; Fig. 5.2).

#### 5.2.1.3. South of Tasmania

At the southern margin of Tasmania (~44°S and ~147°E), a set of 31 deep-sea corals has been selected. The *Desmophyllum dianthus* specimens were collected during cruise TN-228 in 2008-2009 from water depths between 1480 and 1689 m using the remotely operated deep submergence vehicle JASON (Thiagarajan et al., 2013). They yielded U-series ages of 67.5 to 27.0 kyr BP (Hines et al., 2015) (Table 5.1; Figs. 5.1 and 5.2) and are currently bathed in UCDW with admixed PDW as indicated by the mid-depth oxygen minimum in Figure 5.2 (Reid, 1997; Rintoul and Bullister, 1999; Sokolov and Rintoul, 2000; Macdonald et al., 2009). The sampling sites are located below the lower boundary of AAIW which is at ~1200 m water depth (i.e.  $\sigma_0 = 27.3$ ,  $\gamma^n \approx 27.55$  kg/m<sup>3</sup>; Bostock et al., 2013 and references therein; Fig. 5.2). The southward penetration of PDW into the modern Tasman Sea is limited to water depths above ~2000 m due to the bathymetric restrictions along the northern Tasman Sea margin (Sokolov and Rintoul, 2000; Fig. 5.1).

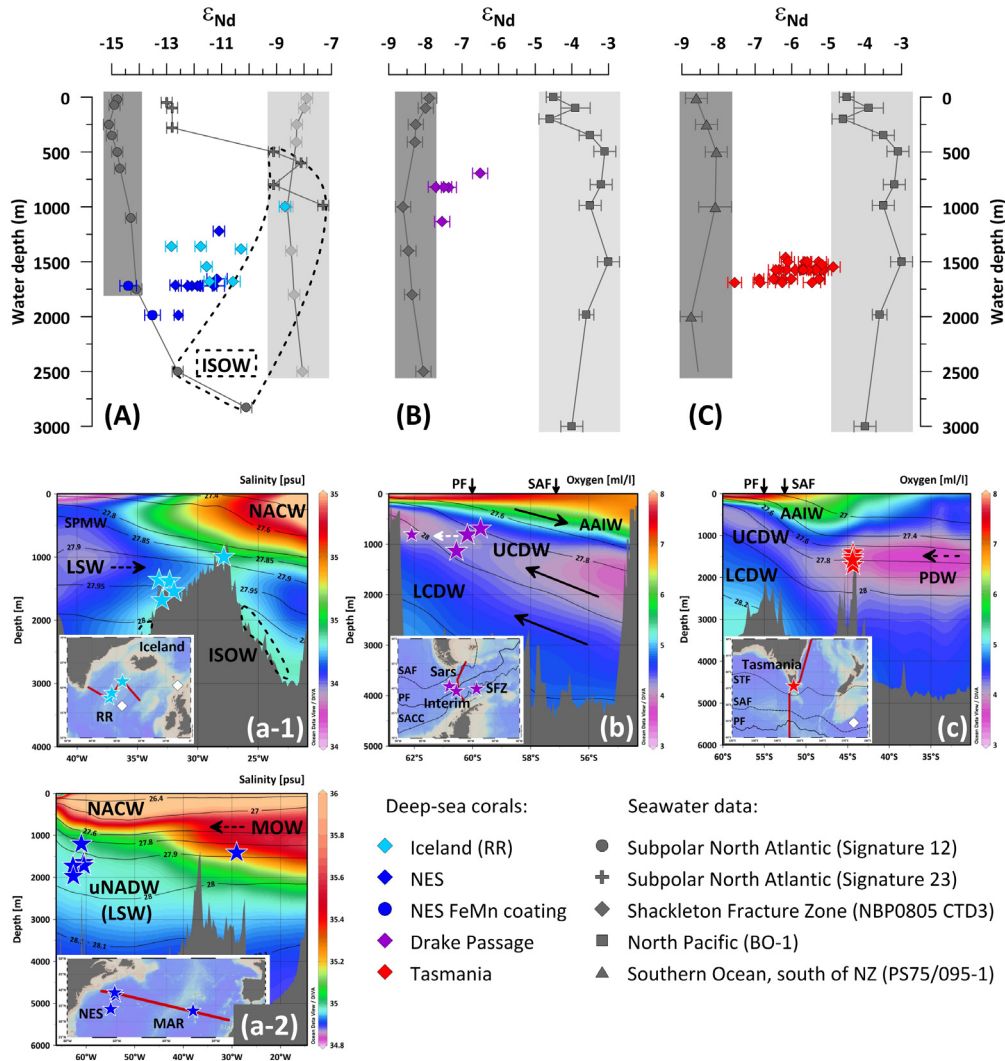


**Figure 5.2:** Deep-sea coral Nd isotope results from late MIS 5 to MIS 2 from various global locations in context with ambient modern seawater profiles (Table 5.1). Unradiogenic source waters (lower  $\epsilon_{Nd}$ ) are highlighted with dark bars, and more radiogenic source waters (higher  $\epsilon_{Nd}$ ) with grey bars. (A) Deep-sea coral Nd isotope results from Reykjanes Ridge (RR) south of Iceland and from the New England Seamounts (NES) in the Northwest Atlantic. NES FeMn coatings were scraped off the aragonitic coral skeletons. Note that two radiogenic water mass endmembers are considered (i.e. a southern source represented by a seawater profile from the Shackleton Fracture Zone, Drake Passage (Chapter 3; grey diamonds) and subpolar gyre water masses from Signature 12 (Lacan and Jeandel, 2004a, 2005b) and Signature 23 (Lacan and Jeandel, 2004b), both sampling ISOW Nd isotope signatures at depth (indicated by dashed polygon). (a-1) Northeast Atlantic sampling locations (sky blue stars) superimposed on salinity section across Reykjanes Ridge south of Iceland. LSW: Labrador Sea Water, SPMW: Subpolar Mode Water, NACW: North Atlantic Central Water, ISOW: Iceland Scotland Overflow Water (highlighted by dashed polygons at both sides of Reykjanes Ridge). (a-2) New England Seamount (NES) and central Atlantic (off the MAR, i.e. the Mid-Atlantic Ridge) sampling locations (blue stars) superimposed on salinity section across the subtropical North Atlantic. NACW: North Atlantic Central Water, MOW: Mediterranean Outflow Water, uNADW: upper North Atlantic Deep Water carrying a strong Labrador Sea Water (LSW) component (e.g., Jenkins et al., 2015). (B) Drake Passage coral Nd isotope results compared to local seawater Nd isotope data (dark grey bar; Chapter 3) and central North Pacific data (light grey bar; Amakawa et al., 2009). (b) Oxygen section across the Drake Passage. Purple stars denote position of samples in the water column. The dashed white arrow and small deep purple star indicate the position of the SFZ in density space, i.e. relative to the more westerly locations of Sars and Interim seamounts (see inset). Black arrows: net direction of upwelling deep waters and downwelling intermediate waters, roughly separated by  $\gamma^{\rho} \approx 27.6 \text{ kg/m}^3$  (cf. Sudre et al., 2011; Marshall and Speer, 2012). LCDW: Lower Circumpolar Deep Water, UCDW: Upper Circumpolar Deep Water, AAIW Antarctic Intermediate Water. Oceanic fronts from Orsi et al. (1995); SAF: Subantarctic Front, PF: Polar Front, SACC: southern ACC front.

(C) Nd isotope data from Tasmanian deep-sea corals. Seawater Nd isotope data from north of the polar fronts, sampled Southeast off New Zealand (dark grey bar; Basak et al., 2015) and from the central North Pacific (light grey bar; Amakawa et al., 2009). (c) Latitudinal oxygen section from the Tasman Sea to Antarctica crossing sample location at the Tasmanian margin (black dots). PDW: Pacific Deep Water, indicated to mix isoneutrally with UCDW, other water mass abbreviations as in (b). STF: Subtropical Front, other fronts as in (b). Salinity and oxygen sections with superimposed density anomaly surfaces (in  $\text{kg/m}^3$ , thin black lines) generated from WOA13 (Jackett and McDougall, 1997; Garcia et al., 2013; Zweng et al., 2013) with ODV software (Schlitzer, 2012). Inset maps: coral locations are indicated by stars in respective colours, white diamonds indicate nearby seawater locations used for plots (A), (B) and (C). Drake Passage seawater profile from Shackleton Fracture Zone overlaps with coral sample location (indicated by blue star in inset map of (b)).

### 5.2.2. Sample preparation and analytical procedures

The analytical procedures for Nd isotope analyses carried out in the MAGIC laboratories at Imperial College London followed the approach outlined in Chapter 2. In brief, physically and chemically cleaned deep-sea coral samples were subjected to Fe coprecipitation to concentrate trace metals to then separate uranium (U) and thorium (Th) for U-series dating (Burke and Robinson, 2012; Chen et al., 2015; Hines et al., 2015). The Nd fraction is collected during U-Th separation, passed for purification through a two-step column chemistry, and analysed by TIMS as  $\text{NdO}^+$ . A  $^{150}\text{Nd}$  spike was added after Fe coprecipitation and U-Th separation (inducing about 10-12 % Nd loss) so that reported Nd concentrations are minimum values (Chapters 2 and 3). Samples from the NES processed for Nd analyses only yield accurate Nd concentrations (Table 5.1; cf. Crocket et al., 2014).

Over a period of 26 months 5 and 15 ng loads of pure JNdi-1 were analysed ( $^{143}\text{Nd}/^{144}\text{Nd} = 0.512105 \pm 0.000009$ , 2SD,  $n = 110$ ) to monitor instrumental offset and normalise mass bias corrected  $^{143}\text{Nd}/^{144}\text{Nd}$  ratios of samples to the reference ratio of  $^{143}\text{Nd}/^{144}\text{Nd} = 0.512115 \pm 0.000007$  (Tanaka et al., 2000). BCR-2 rock reference material yielded  $^{143}\text{Nd}/^{144}\text{Nd}$  ratios of  $0.512637 \pm 0.000011$  ( $2 \sigma$  SD;  $n = 32$ ), and a similar precision was obtained from replicate analyses of our in-house coral reference material ( $^{143}\text{Nd}/^{144}\text{Nd} = 0.512336 \pm 0.000009$ ;  $n = 23$ ). Full procedural blanks of combined U, Th and Nd separation from aragonitic matrix ranged from 2 to 27 pg Nd, averaging at 6 pg ( $n = 20$ ). Full procedural blanks of Nd separation from the aragonitic sample matrix were 1 to 17 pg, averaging at 4 pg Nd ( $n = 10$ ).

Some NES corals were analysed in 2006 by T. van de Flierdt at Lamont-Doherty Earth Observatory (Table 5.1). These samples were subjected to similar physical and chemical cleaning procedures as outlined by van de Flierdt et al. (2006b, 2010) and subsequently processed through anion exchange chemistry for U-series dating (Robinson et al., 2005, 2007; van de Flierdt et al., 2006b). After Fe coprecipitation, the rare earth elements were separated on TRU spec<sup>®</sup> resin and neodymium was subsequently isolated by  $\alpha$ -HIBA and cation exchange resin. Samples were loaded with Si gel for  $\text{NdO}^+$  analyses on a VG Sector 54-30 thermal ionisation mass spectrometer by dynamic multicollection. Mass bias was corrected for by using  $^{146}\text{Nd}/^{144}\text{Nd} = 0.7219$  and instrumental offset was accounted for by normalising to a nominal La Jolla value of  $^{143}\text{Nd}/^{144}\text{Nd} = 0.511858 \pm 0.000007$ . Repeated analyses of 5 and 35 ng La Jolla Nd standards resulted in average  $^{143}\text{Nd}/^{144}\text{Nd} = 0.511858 \pm 0.000016$  ( $n = 5$ ) and  $^{143}\text{Nd}/^{144}\text{Nd} = 0.511856 \pm 0.000020$  ( $n = 8$ ) for two analytical sessions.

### 5.3. Results

#### 5.3.1. North Atlantic

Northwest Atlantic deep-sea corals from the New England Seamounts (NES) represent predominantly stadial phases (Robinson et al., 2007; Fig. 5.3), characterised by a trend towards more radiogenic values from  $\epsilon_{\text{Nd}} \approx -12.6 \pm 0.2$  around 47.1 kyr BP to  $\epsilon_{\text{Nd}} \approx -10.6 \pm 0.3/-11.3 \pm 0.4$  at 25.1 kyr BP (Table 5.1; Fig. 5.3). The range of Nd isotopic compositions falls in between the values of modern subpolar water masses influenced from the Labrador Sea ( $\epsilon_{\text{Nd}} \approx -14$ ; Lacan and Jeandel, 2004a, 2005b; Lambelet et al., accepted), the overflow waters from the Nordic Seas and/or Southern Ocean waters ( $\epsilon_{\text{Nd}} \approx -8$  to  $-9$ ; Lacan and Jeandel, 2004b, 2005a,b; Stichel et al., 2012; Garcia-Solsona et al., 2014; Fig. 5.2). For one sample, top and bottom sections were analysed, yet the bottom section had to be excluded from palaeoceanographic interpretation due to elevated  $^{232}\text{Th}$  concentrations of  $\sim 9$  ng/g. High  $^{232}\text{Th}$  concentrations cause high uncertainty in the calculated age, but more importantly, could indicate significant detrital contamination (Table 5.1). Two ferromanganese crusts scraped off the skeletons of 47.1 and 31.4 kyr BP old corals yielded  $\epsilon_{\text{Nd}} = -13.5 \pm 0.3$  and  $\epsilon_{\text{Nd}} = -14.4 \pm 0.3$ , respectively. Such signatures are less radiogenic than Nd isotopes extracted from the corresponding aragonitic skeletons themselves (Table 5.1) and show close similarity to current North Atlantic subpolar gyre seawater Nd isotopic compositions (Lacan and Jeandel, 2004a, 2005b; Fig. 5.2).

In the Northeast Atlantic, the few available deep-sea coral Nd isotope results from mid-depths fall within a similar range as the western Atlantic specimens, i.e. from  $\epsilon_{\text{Nd}} = -11.8 \pm 0.3$  to  $\epsilon_{\text{Nd}} = -10.6 \pm 0.2$  (Table 5.1; Fig. 5.3). One additional sample of MIS 5 age from 1385 m water depth was dated to 109.8 kyr BP and its Nd isotope signature is  $\epsilon_{\text{Nd}} = -10.3 \pm 0.2$  (Table 5.1). The most radiogenic Nd isotope signal of  $\epsilon_{\text{Nd}} = -8.7 \pm 0.2$  was recorded at 42.3 kyr BP in 997 m water depth (Table 5.1; Fig. 5.3). Samples CE0806-Dr16-5b and CE0806-Dr15-3 show signs of contamination and are therefore omitted from the data set (see caption Table 5.1).

The single *D. dianthus* specimen from the central North Atlantic shows a Nd isotopic composition of  $\epsilon_{\text{Nd}} = -13.1 \pm 0.2$  at  $24.9 \pm 0.2$  kyr BP (Table 5.1; Figs. 5.1, 5.2 and 5.3).

#### 5.3.2. Drake Passage

Out of the five additional corals analysed from the Drake Passage (see also Chapter 4), two cover MIS 3 and one was dated of MIS 2 age aligning along a potential glacial Nd isotope baseline of  $\epsilon_{\text{Nd}} \approx -7.5$  between 39.2 kyr BP and 27.2 kyr BP. Due to the large age difference to the remaining data set, the two older samples from  $\sim 103.5$  and 226.0 kyr BP (Table 5.1) are not discussed in detail here. All deep-sea coral Nd isotope signatures plot in between modern CDW from the Drake Passage ( $\epsilon_{\text{Nd}} \approx -8$ ; Chapter 3) and PDW ( $\epsilon_{\text{Nd}} \approx -4$ ; Amakawa et al., 2009; Fig. 5.2).

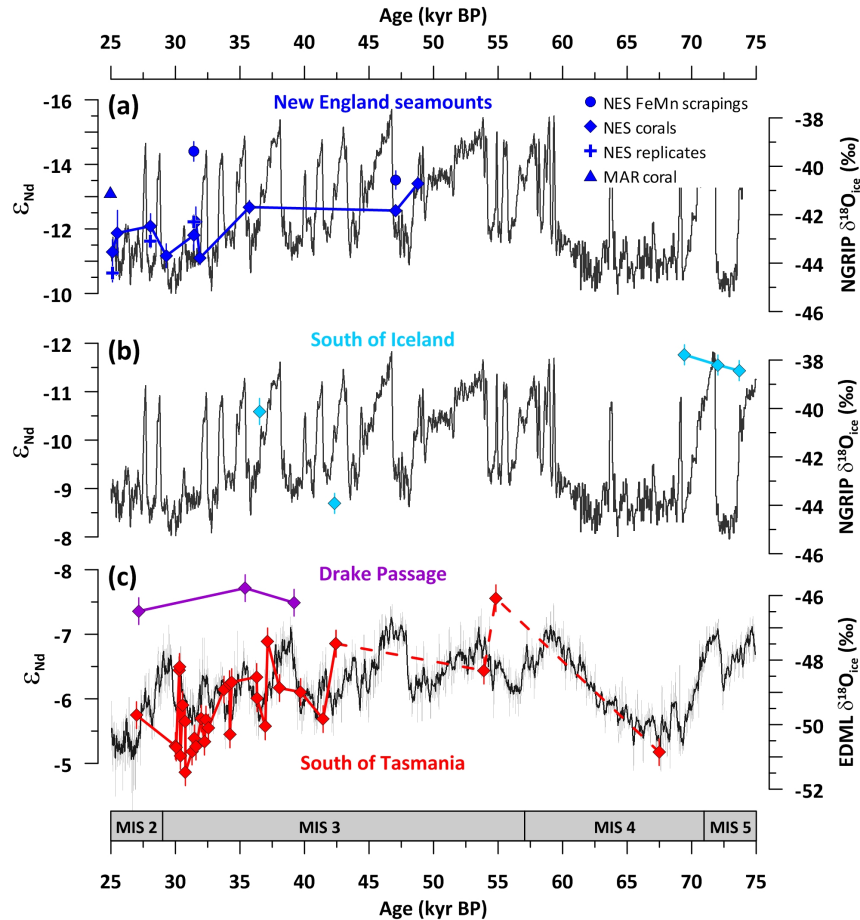


**Figure 5.3:** Deep-sea coral Nd isotope data analysed for latest MIS 5 to MIS 2 (MIS boundaries after Lisiecki and Raymo, 2005), superimposed on ice core oxygen isotope records of respective hemisphere. (a) and (b) NGRIP oxygen isotope record (NGRIP, 2004) on GICC05/NALPS time scale (Andersen et al., 2006; Svensson et al., 2008; Barker and Diz, 2014) for climatological reference. Oldest coral in (a) is taken from van de Flierdt et al. (2006b) with an updated age of 48.8 kyr BP. Pink triangle in (a) represents central North Atlantic coral from MAR, other sample material from the New England Seamounts (NES), including full procedural replicate results (see Fig. 5.2 and text for details). (c) EDML oxygen isotope record from EPICA community members (2006, 2010).

### 5.3.3. South of Tasmania

The new MIS 4 and 3 deep-sea coral Nd isotope data from the southern Tasmanian margin cover the time interval from ~68 to 27 kyr BP (Hines et al., 2015) and show variability between  $\epsilon_{\text{Nd}} = -4.9 \pm 0.2$  and  $\epsilon_{\text{Nd}} = -7.6 \pm 0.2$  (Table 5.1). The highest data coverage is between 42 and 27 kyr BP, when 28 specimens document a radiogenic trend towards peak glacial values around  $\epsilon_{\text{Nd}} \approx -5.5$  (Fig. 5.3; Chapter 4). Superimposed on the long-term trend, short-lived fluctuations occur with pronounced unradiogenic punctuations in seawater Nd isotopic composition at 42.4, 37.1 and 30.3 kyr BP ( $\epsilon_{\text{Nd}} = -6.5 \pm 0.2$  to  $-6.9 \pm 0.2$ ), each of which deviating by up to ~1.5 epsilon units from the background trend (Table 5.1; Fig. 5.3). The Tasmanian Nd isotope signatures during MIS 3 and 2 are more radiogenic than the Drake Passage at similar density surfaces. Values plot in between modern Pacific sector ACC waters ( $\epsilon_{\text{Nd}} \approx -8$ ; Basak et al., 2015) and North Pacific Deep Water ( $\epsilon_{\text{Nd}} \approx -4$ ; Amakawa et al., 2009; Table 5.1, Fig. 5.2).

Table 5.1: North Atlantic and Southern Ocean deep-sea coral data.

| Coral ID                        | Water depth (m) | Latitude | Longitude | Location   | Species            | $^{238}\text{U}$ | $^{232}\text{Th}$ | $\delta^{234}\text{U}$ | ZSE | Age (kyr BP) | ZSE | $^{142}\text{Nd}/^{146}\text{Nd}$ | ZSE | $\epsilon_{\text{Nd}}$ | ZSE      | Nd (ng/g) | 2SE (ep) | MB corr. |       |         |
|---------------------------------|-----------------|----------|-----------|------------|--------------------|------------------|-------------------|------------------------|-----|--------------|-----|-----------------------------------|-----|------------------------|----------|-----------|----------|----------|-------|---------|
| <b>Northwest Atlantic</b>       |                 |          |           |            |                    |                  |                   |                        |     |              |     |                                   |     |                        |          |           |          |          |       |         |
| ALV-3889-1311-001-008 top*      | 1719            | 33.859   | -62.672   | Muir       | <i>D. dianthus</i> | 3852             | 1                 | 1363                   | 7   | 149.6        | 1.1 | 25.1                              | 0.3 | 0.512060               | 0.000014 | -11.28    | 0.28     | 0.39     |       |         |
| (ALV-3889-1311-001-008 bottom*) | 1719            | 33.859   | -62.672   | Muir       | <i>D. dianthus</i> | 3712             | 1                 | 9047                   | 39  | 146.2        | 1.2 | 27.7                              | 1.3 | 0.512063               | 0.000025 | -11.22    | 0.48     | 0.48     |       |         |
| ALV-3889-1311-001-008 Nd repl.  |                 |          |           |            |                    |                  |                   |                        |     |              |     |                                   |     |                        |          |           |          |          |       |         |
| ALV-3889-1311-001-002*          | 1719            | 33.859   | -62.672   | Muir       | <i>D. dianthus</i> | 4253             | 2                 | 2624                   | 19  | 147.2        | 1.1 | 25.5                              | 0.4 | 0.512029               | 0.000014 | -10.63    | 0.27     | 0.27     | 21.6  | 0.0001  |
| ALV-3889-1311-001-006*          | 1719            | 33.859   | -62.672   | Muir       | <i>D. dianthus</i> | 3316             | 1                 | 1011                   | 9   | 146.2        | 1.2 | 28.1                              | 0.3 | 0.512018               | 0.000015 | -12.08    | 0.30     | 0.39     |       |         |
| ALV-3889-1311-001-006 Nd repl.  |                 |          |           |            |                    |                  |                   |                        |     |              |     |                                   |     |                        |          |           |          |          |       |         |
| ALV-3892-1421-002-001-07        | 1655            | 38.703   | -60.536   | Manning    | <i>D. dianthus</i> | 4070             | 1                 | 496                    | 8   | 141.6        | 4.0 | 29.3                              | 0.2 | 0.512066               | 0.000019 | -11.17    | 0.37     | 0.37     | 49.0  | 0.0001  |
| ALV-3889-1311-001-005*          | 1719            | 33.859   | -62.672   | Muir       | <i>D. dianthus</i> | 3257             | 1                 | 4458                   | 20  | 147.2        | 1.2 | 31.4                              | 0.8 | 0.512033               | 0.000024 | -11.80    | 0.46     | 0.46     |       |         |
| ALV-3889-1311-001-005 Nd repl.  |                 |          |           |            |                    |                  |                   |                        |     |              |     |                                   |     |                        |          |           |          |          |       |         |
| ALV-3889-1311-001-005 crust*    |                 |          |           |            |                    |                  |                   |                        |     |              |     |                                   |     |                        |          |           |          |          |       |         |
| ALV-3889-1311-001-001*          | 1719            | 33.859   | -62.672   | Muir       | <i>D. dianthus</i> | 3977             | 1                 | 2613                   | 13  | 144.5        | 1.1 | 31.6                              | 0.5 | 0.512011               | 0.000024 | -12.22    | 0.46     | 0.46     |       |         |
| ALV-3891-1725-005-007           | 1222            | 38.948   | -61.028   | Gregg      | <i>D. dianthus</i> | 3852             | 2                 | 2342                   | 15  | 147.7        | 1.1 | 31.9                              | 0.5 | 0.512069               | 0.000005 | -11.10    | 0.10     | 0.21     | 220.5 | 0.0012  |
| ALV-3892-1315-001-002           | 1713            | 38.203   | -60.535   | Manning    | <i>D. dianthus</i> | 3143             | 1                 | 376                    | 8   | 149.0        | 4.0 | 35.7                              | 0.3 | 0.511988               | 0.000005 | -12.68    | 0.11     | 0.21     | 89.9  | 0.0002  |
| ALV-3885-1325-002-039*          | 1986            | 33.774   | -62.570   | Muir       | <i>D. dianthus</i> | 3695             | 1                 | 1147                   | 14  | 143.6        | 1.2 | 47.1                              | 0.4 | 0.511994               | 0.000003 | -12.57    | 0.07     | 0.16     | 165.8 | 0.0004  |
| ALV-3885-1325-002-039 crust*    |                 |          |           |            |                    |                  |                   |                        |     |              |     |                                   |     |                        |          |           |          |          |       |         |
| <b>Northeast Atlantic</b>       |                 |          |           |            |                    |                  |                   |                        |     |              |     |                                   |     |                        |          |           |          |          |       |         |
| (CE0806-Dr16-5b)                | 1680            | 57.937   | 32.947    | Rev. Ridge | <i>D. dianthus</i> | 3358             | 11                | 1262                   | 4   | 142.7        | 0.8 | 35.9                              | 0.3 | 0.512138               | 0.000005 | -9.75     | 0.11     | 0.21     | 17.5  | 0.0004  |
| (CE0806-Dr16-5b chem. repl.)    | 1680            | 57.937   | 32.947    | Rev. Ridge | <i>D. dianthus</i> | 3158             | 11                | 1232                   | 4   | 140.3        | 0.8 | 36.0                              | 0.4 | 0.512146               | 0.000005 | -9.59     | 0.09     | 0.21     | 16.3  | 0.0004  |
| CE0806-Dr16-5 full repl.        | 1680            | 57.937   | 32.947    | Rev. Ridge | <i>D. dianthus</i> | 4021             | 15                | 696                    | 2   | 141.2        | 0.8 | 36.5                              | 0.2 | 0.512095               | 0.000014 | -10.59    | 0.27     | 0.27     | 32.5  | 0.1657  |
| CE0806-Dr29A-2                  | 997             | 61.407   | 27.855    | Rev. Ridge | <i>D. dianthus</i> | 4686             | 15                | 3864                   | 13  | 143.0        | 0.9 | 42.3                              | 0.7 | 0.512192               | 0.000005 | -8.69     | 0.09     | 0.21     | 162.1 | 0.0010  |
| CE0806-Dr15-1                   | 1361            | 57.738   | 33.197    | Rev. Ridge | <i>D. dianthus</i> | 3408             | 11                | 686                    | 11  | 146.1        | 0.9 | 69.4                              | 0.4 | 0.512035               | 0.000007 | -11.76    | 0.14     | 0.21     | 27.2  | 0.0009  |
| (CE0806-Dr15-3)                 | 1361            | 57.738   | 33.197    | Rev. Ridge | <i>D. dianthus</i> | 3058             | 10                | 851                    | 3   | 158.0        | 0.9 | 69.3                              | 0.5 | 0.511980               | 0.000006 | -12.83    | 0.11     | 0.21     | 105.2 | 0.0012  |
| CE0806-Dr19A-3                  | 1545            | 58.837   | 31.976    | Rev. Ridge | <i>D. dianthus</i> | 3170             | 10                | 1683                   | 6   | 151.4        | 0.9 | 72.0                              | 0.6 | 0.512046               | 0.000006 | -11.55    | 0.12     | 0.21     | 83.9  | 0.0004  |
| CE0806-Dr16-1                   | 1680            | 57.937   | 32.947    | Rev. Ridge | <i>D. dianthus</i> | 4636             | 15                | 593                    | 2   | 141.8        | 0.8 | 73.7                              | 0.4 | 0.512052               | 0.000006 | -11.44    | 0.11     | 0.21     | 22.7  | 0.0003  |
| CE0806-Dr18-1                   | 1385            | 58.511   | 32.321    | Rev. Ridge | <i>D. dianthus</i> | 5031             | 17                | 808                    | 3   | 146.4        | 1.0 | 109.8                             | 0.8 | 0.512110               | 0.000006 | -10.29    | 0.11     | 0.21     | 31.1  | 0.0004  |
| CE0806-Dr18-1                   | 1420            | 33.22    | -29.13    | Off MAR    | <i>D. dianthus</i> |                  |                   |                        |     |              |     | 24.9                              | 0.2 | 0.511965               | 0.000004 | -13.13    | 0.08     | 0.16     | 121.2 | 0.0003  |
| JFA 62.3*                       |                 |          |           |            |                    |                  |                   |                        |     |              |     |                                   |     |                        |          |           |          |          |       |         |
| <b>Drake Passage</b>            |                 |          |           |            |                    |                  |                   |                        |     |              |     |                                   |     |                        |          |           |          |          |       |         |
| NBP103-DR43-Dc-3                | 823             | -60.182  | -57.833   | SFZ        | <i>D. dianthus</i> | 3208             | 6                 | 790                    | 3   | 146.7        | 0.5 | 27.2                              | 0.2 | 0.512261               | 0.000006 | -7.36     | 0.11     | 0.21     | 55.8  | 0.0038  |
| NBP0805-DR23-Dc-A-2             | 819             | -60.182  | -57.834   | SFZ        | <i>D. dianthus</i> | 4921             | 16                | 1033                   | 4   | 148.8        | 0.8 | 35.4                              | 0.2 | 0.512243               | 0.000003 | -7.71     | 0.06     | 0.21     | 240.6 | 0.00602 |
| NBP0805-DR23-Dc-A-3             | 819             | -60.182  | -57.834   | SFZ        | <i>D. dianthus</i> | 3472             | 11                | 1010                   | 3   | 149.5        | 0.8 | 39.2                              | 0.3 | 0.512254               | 0.000005 | -7.49     | 0.10     | 0.21     | 136.2 | 0.01005 |
| NBP0805-DR27-Dc-A-2             | 1134            | -60.547  | -65.949   | Interim    | <i>D. dianthus</i> | 5338             | 17                | 1900                   | 6   | 148.1        | 1.0 | 103.5                             | 0.7 | 0.512251               | 0.000006 | -7.54     | 0.13     | 0.21     | 317.7 | 0.00065 |
| NBP0805-DR35-Dc-D-2             | 695             | -59.723  | -68.881   | Sats       | <i>D. dianthus</i> | 3743             | 13                | 160                    | 7   | 227.6        | 3.2 | 226.0                             | 3.4 | 0.512305               | 0.000005 | -6.50     | 0.09     | 0.21     | 38.1  | 0.00117 |

Table 5.1 (continued)

| Coral ID                           | Water depth (m) | Latitude | Longitude | Location | Species            | $^{238}\text{U}$ | $^{232}\text{Th}$ ( $\mu\text{g/g}$ ) | $\delta^{234}\text{U}$ | Age (kyr BP) | ZSE   | $^{143}\text{Nd}/^{144}\text{Nd}$ | ZSE  | $\epsilon_{\text{Nd}}$ <sup>c</sup> | ZSE      | $^{235}\text{U}$ | ZSE   | $^{143}\text{Nd}/^{144}\text{Nd}$ | $\epsilon_{\text{Nd}}$ <sup>c</sup> | ZSE   | $^{235}\text{U}$ | ZSE | Nd (ng/g) | ZSE (ep) <sup>e</sup> |  |  |
|------------------------------------|-----------------|----------|-----------|----------|--------------------|------------------|---------------------------------------|------------------------|--------------|-------|-----------------------------------|------|-------------------------------------|----------|------------------|-------|-----------------------------------|-------------------------------------|-------|------------------|-----|-----------|-----------------------|--|--|
| <b>Southwest Pacific</b>           |                 |          |           |          |                    |                  |                                       |                        |              |       |                                   |      |                                     |          |                  |       |                                   |                                     |       |                  |     |           |                       |  |  |
| TN228-J2-383-1217-0725-01-1575-010 | 1575            | -44.323  | 147.264   | Tasmania | <i>D. dianthus</i> | 4539             | 3                                     | 906                    | 17           | 144.7 | 0.6                               | 27.0 | 0.1                                 | 0.512343 | 0.000004         | -5.75 | 0.08                              | 0.21                                | 102.2 | 0.0008           |     |           |                       |  |  |
| TN228-J2-395-0114-0057-09-1500-006 | 1500            | -44.300  | 147.447   | Tasmania | <i>D. dianthus</i> | 5460             | 5                                     | 1712                   | 10           | 141.1 | 1.4                               | 30.0 | 0.2                                 | 0.512368 | 0.000004         | -5.27 | 0.08                              | 0.21                                | 92.9  | 0.0005           |     |           |                       |  |  |
| TN228-J2-393-0112-0124-06-1657-013 | 1657            | -45.137  | 146.978   | Tasmania | <i>D. dianthus</i> | 5689             | 4                                     | 1407                   | 13           | 137.8 | 0.5                               | 30.1 | 0.1                                 | 0.512369 | 0.000004         | -5.25 | 0.08                              | 0.21                                | 785.6 | 0.0116           |     |           |                       |  |  |
| TN228-J2-393-0112-0124-06-1657-007 | 1657            | -45.137  | 146.978   | Tasmania | <i>D. dianthus</i> | 4723             | 3                                     | 671                    | 13           | 144.2 | 0.6                               | 30.3 | 0.1                                 | 0.512308 | 0.000005         | -6.44 | 0.10                              | 0.21                                | 224.9 | 0.0009           |     |           |                       |  |  |
| TN228-J2-393-0112-0124-06-1657-003 | 1657            | -45.137  | 146.978   | Tasmania | <i>D. dianthus</i> | 4798             | 3                                     | 1391                   | 14           | 144.5 | 0.5                               | 30.3 | 0.1                                 | 0.512305 | 0.000005         | -6.49 | 0.10                              | 0.21                                | 338.4 | 0.0016           |     |           |                       |  |  |
| TN228-J2-383-1217-0725-01-1575-016 | 1575            | -44.323  | 147.264   | Tasmania | <i>D. dianthus</i> | 3898             | 2                                     | 896                    | 12           | 145.8 | 0.7                               | 30.4 | 0.1                                 | 0.512376 | 0.000004         | -5.11 | 0.07                              | 0.21                                | 189.2 | 0.0005           |     |           |                       |  |  |
| TN228-J2-383-1217-0725-01-1575-020 | 1575            | -44.323  | 147.264   | Tasmania | <i>D. dianthus</i> | 4340             | 3                                     | 2307                   | 16           | 144.0 | 0.7                               | 30.6 | 0.2                                 | 0.512335 | 0.000004         | -5.90 | 0.08                              | 0.21                                | 161.6 | 0.0007           |     |           |                       |  |  |
| TN228-J2-395-0114-0057-09-1500-003 | 1500            | -44.300  | 147.447   | Tasmania | <i>D. dianthus</i> | 4238             | 3                                     | 1725                   | 13           | 144.5 | 0.9                               | 30.8 | 0.2                                 | 0.512348 | 0.000004         | -5.65 | 0.07                              | 0.21                                | 158.5 | 0.0006           |     |           |                       |  |  |
| TN228-J2-383-1217-0852-03-1548-005 | 1548            | -44.323  | 147.264   | Tasmania | <i>D. dianthus</i> | 4656             | 3                                     | 484                    | 9            | 142.4 | 0.5                               | 30.8 | 0.1                                 | 0.512389 | 0.000004         | -4.86 | 0.08                              | 0.21                                | 168.4 | 0.0006           |     |           |                       |  |  |
| TN228-J2-383-1217-0725-01-1575-007 | 1575            | -44.323  | 147.264   | Tasmania | <i>D. dianthus</i> | 4578             | 3                                     | 1602                   | 13           | 143.5 | 0.7                               | 31.3 | 0.2                                 | 0.512372 | 0.000004         | -5.18 | 0.08                              | 0.21                                | 92.0  | 0.0006           |     |           |                       |  |  |
| TN228-J2-383-1217-0725-01-1575-013 | 1575            | -44.323  | 147.264   | Tasmania | <i>D. dianthus</i> | 3767             | 3                                     | 747                    | 15           | 144.1 | 0.7                               | 31.5 | 0.1                                 | 0.512362 | 0.000004         | -5.39 | 0.08                              | 0.21                                | 69.7  | 0.0006           |     |           |                       |  |  |
| TN228-J2-393-0112-0124-06-1657-001 | 1657            | -45.137  | 146.978   | Tasmania | <i>D. dianthus</i> | 4120             | 3                                     | 655                    | 14           | 147.3 | 0.5                               | 31.6 | 0.1                                 | 0.512368 | 0.000005         | -5.26 | 0.09                              | 0.21                                | 204.9 | 0.0008           |     |           |                       |  |  |
| TN228-J2-383-1217-0725-01-1575-012 | 1575            | -44.323  | 147.264   | Tasmania | <i>D. dianthus</i> | 4911             | 3                                     | 873                    | 11           | 140.9 | 0.7                               | 32.0 | 0.1                                 | 0.512346 | 0.000003         | -5.69 | 0.06                              | 0.21                                | 123.0 | 0.0006           |     |           |                       |  |  |
| TN228-J2-383-1217-0725-01-1575-009 | 1575            | -44.323  | 147.264   | Tasmania | <i>D. dianthus</i> | 5486             | 3                                     | 1379                   | 13           | 144.4 | 0.7                               | 32.2 | 0.1                                 | 0.512364 | 0.000004         | -5.34 | 0.08                              | 0.21                                | 156.7 | 0.0005           |     |           |                       |  |  |
| TN228-J2-383-1217-0725-01-1575-018 | 1575            | -44.323  | 147.264   | Tasmania | <i>D. dianthus</i> | 4067             | 2                                     | 662                    | 12           | 144.7 | 0.7                               | 32.4 | 0.1                                 | 0.512347 | 0.000005         | -5.68 | 0.10                              | 0.21                                | 57.4  | 0.0006           |     |           |                       |  |  |
| TN228-J2-383-1217-0725-01-1575-014 | 1575            | -44.323  | 147.264   | Tasmania | <i>D. dianthus</i> | 5638             | 3                                     | 2073                   | 10           | 142.9 | 0.7                               | 32.6 | 0.2                                 | 0.512353 | 0.000004         | -5.55 | 0.09                              | 0.21                                | 144.0 | 0.0004           |     |           |                       |  |  |
| TN228-J2-383-1217-0725-01-1575-003 | 1575            | -44.323  | 147.264   | Tasmania | <i>D. dianthus</i> | 4983             | 3                                     | 1353                   | 8            | 142.0 | 0.5                               | 33.8 | 0.1                                 | 0.512323 | 0.000004         | -6.14 | 0.09                              | 0.21                                | 201.8 | 0.0006           |     |           |                       |  |  |
| TN228-J2-393-0112-0124-06-1657-010 | 1657            | -45.137  | 146.978   | Tasmania | <i>D. dianthus</i> | 4772             | 2                                     | 2138                   | 11           | 143.6 | 0.5                               | 34.2 | 0.2                                 | 0.512319 | 0.000005         | -6.23 | 0.09                              | 0.21                                | 249.4 | 0.0013           |     |           |                       |  |  |
| TN228-J2-382-1216-1010-01-1689-010 | 1689            | -44.337  | 146.886   | Tasmania | <i>D. dianthus</i> | 4495             | 2                                     | 1280                   | 25           | 144.3 | 0.6                               | 34.2 | 0.1                                 | 0.512359 | 0.000004         | -5.45 | 0.08                              | 0.21                                | 291.8 | 0.0030           |     |           |                       |  |  |
| TN228-J2-382-1216-1010-01-1689-007 | 1689            | -44.337  | 146.886   | Tasmania | <i>D. dianthus</i> | 5019             | 3                                     | 1596                   | 31           | 138.1 | 0.7                               | 34.4 | 0.2                                 | 0.512317 | 0.000006         | -6.26 | 0.11                              | 0.21                                | 297.9 | 0.0023           |     |           |                       |  |  |
| TN228-J2-393-0114-0057-09-1500-004 | 1500            | -44.300  | 147.447   | Tasmania | <i>D. dianthus</i> | 4122             | 3                                     | 1608                   | 10           | 145.8 | 0.5                               | 36.3 | 0.2                                 | 0.512313 | 0.000005         | -6.34 | 0.09                              | 0.21                                | 119.6 | 0.0006           |     |           |                       |  |  |
| TN228-J2-393-0112-0124-06-1657-004 | 1657            | -45.137  | 146.978   | Tasmania | <i>D. dianthus</i> | 5344             | 3                                     | 1270                   | 13           | 140.0 | 0.5                               | 36.3 | 0.1                                 | 0.512330 | 0.000004         | -6.01 | 0.09                              | 0.21                                | 117.3 | 0.0006           |     |           |                       |  |  |
| TN228-J2-395-0114-0057-09-1500-005 | 1500            | -44.300  | 147.447   | Tasmania | <i>D. dianthus</i> | 3698             | 4                                     | 469                    | 17           | 144.7 | 1.0                               | 37.0 | 0.1                                 | 0.512352 | 0.000006         | -5.57 | 0.12                              | 0.21                                | 38.5  | 0.0008           |     |           |                       |  |  |
| TN228-J2-393-0112-0124-06-1657-011 | 1657            | -45.137  | 146.978   | Tasmania | <i>D. dianthus</i> | 4295             | 4                                     | 1260                   | 17           | 139.6 | 0.7                               | 37.1 | 0.1                                 | 0.512285 | 0.000005         | -6.89 | 0.10                              | 0.21                                | 279.9 | 0.0011           |     |           |                       |  |  |
| TN228-J2-383-1217-1320-05-1460-005 | 1460            | -44.323  | 147.264   | Tasmania | <i>D. dianthus</i> | 4559             | 4                                     | 761                    | 13           | 145.2 | 1.0                               | 38.1 | 0.1                                 | 0.512322 | 0.000007         | -6.17 | 0.13                              | 0.21                                | 34.3  | 0.0006           |     |           |                       |  |  |
| TN228-J2-395-0114-0057-09-1500-009 | 1500            | -44.300  | 147.447   | Tasmania | <i>D. dianthus</i> | 4113             | 3                                     | 1355                   | 12           | 147.1 | 1.1                               | 39.7 | 0.2                                 | 0.512325 | 0.000004         | -6.10 | 0.08                              | 0.21                                | 229.2 | 0.0007           |     |           |                       |  |  |
| TN228-J2-383-1217-0725-01-1575-005 | 1575            | -44.323  | 147.264   | Tasmania | <i>D. dianthus</i> | 5137             | 3                                     | 1123                   | 8            | 141.0 | 0.5                               | 41.4 | 0.1                                 | 0.512347 | 0.000005         | -5.69 | 0.09                              | 0.21                                | 51.3  | 0.0005           |     |           |                       |  |  |
| TN228-J2-382-1216-1010-01-1689-008 | 1689            | -44.337  | 146.886   | Tasmania | <i>D. dianthus</i> | 4998             | 3                                     | 1560                   | 28           | 141.6 | 0.7                               | 42.4 | 0.2                                 | 0.512287 | 0.000006         | -6.85 | 0.12                              | 0.21                                | 305.4 | 0.0027           |     |           |                       |  |  |
| TN228-J2-383-1217-0725-01-1575-022 | 1575            | -44.323  | 147.264   | Tasmania | <i>D. dianthus</i> | 4599             | 3                                     | 1329                   | 12           | 148.6 | 0.7                               | 53.9 | 0.1                                 | 0.512308 | 0.000005         | -6.44 | 0.10                              | 0.21                                | 117.0 | 0.0005           |     |           |                       |  |  |
| TN228-J2-382-1216-1010-01-1689-001 | 1689            | -44.337  | 146.886   | Tasmania | <i>D. dianthus</i> | 4891             | 3                                     | 941                    | 30           | 139.1 | 0.7                               | 54.8 | 0.1                                 | 0.512251 | 0.000007         | -7.56 | 0.14                              | 0.21                                | 232.4 | 0.0014           |     |           |                       |  |  |
| TN228-J2-382-1216-1350-03-1523-004 | 1523            | -44.337  | 146.886   | Tasmania | <i>D. dianthus</i> | 4548             | 3                                     | 1053                   | 10           | 145.9 | 0.7                               | 67.5 | 0.1                                 | 0.512373 | 0.000005         | -5.17 | 0.11                              | 0.21                                | 302.7 | 0.0009           |     |           |                       |  |  |

(a) ZSE is the analytical  $2\sigma$  standard error.(b)  $^{143}\text{Nd}/^{144}\text{Nd}$  ratios were corrected for the instrumental offset from the published value of  $0.512115 \pm 0.000007$  (Tanaka et al., 2000) (see section 5.2.2).(c)  $\epsilon_{\text{Nd}}$  was calculated using the present day CHUR value of  $^{143}\text{Nd}/^{144}\text{Nd} = 0.512638$  (Jacobson and Wasserburg, 1980).(d) ZSD refers to the  $2\sigma$  standard deviation derived from the long-term reproducibility of respective reference materials (see section 5.2.2). If the internal  $2\sigma$  SE was larger than the external one, the internal error is reported.(e) ZSE (ep) is the propagated  $2\sigma$  standard error of Nd concentrations, determined by isotope dilution.

\* Samples analysed at LDEO and processed through combined U-Th-Nd chemistry (cf. Chapter 2).

# Samples processed by K. C. Crockett at Imperial College London following Crockett et al. (2014).

+ Sample analysed by T. van de Fliedert at Imperial College London on a Nu Plasma II MC-ICP-MS.

---

**Table 5.1:** Neodymium isotope and concentration results of deep-sea corals used for this study grouped by location and listed by their U-series age (kyr BP), which is expressed in thousand years before present (i.e. 1950). Uranium-series data from the Northwest Atlantic updated from Robinson et al. (2007), Northeast Atlantic from Burke (2012), Central North Atlantic (off the Mid-Atlantic Ridge) from Adkins (unpubl. data), Drake Passage from Burke and Robinson (2012) and Chen et al. (2015), Tasmania from Hines et al. (2015). Water depth is the depth of sample collection. Some of the Northwest Atlantic corals have been processed through different analytical procedures (see methods section). All remaining Nd isotope results were generated at Imperial College London (see methods section) of which the Northwest Atlantic Nd concentrations are accurate whereas all others are minimum estimates for Nd concentrations (i.e. assuming no Nd loss during U-Th chemistry, which may be an underestimation by at least 10%; see Chapters 2 and 3). ‘chem. repl.’ indicates replicate analyses from sample splits processed through combined U-Th-Nd chemistry, ‘full repl.’ denotes re-sampled corals processed through combined U-Th-Nd chemistry, ‘Nd repl.’ demarks individual sub-samples processed for Nd isotope analyses only. ‘Top’ and ‘bottom’ indicate top and bottom part of respective coral. Crust marked by hashtag has been analysed on a Nu Plasma II MC-ICP-MS at Imperial College London, while all other data were measured by TIMS. Mass balance corrected (‘MB corr.’) results based on worst case scenario using Nd/Th = 4.5 of BCR-2 (Wilson, 1997) and  $\epsilon_{Nd} = 8.98$  (Kempton et al., 2000), applied to Northeast Atlantic corals (cf. Chapter 3). Samples which show signs of contamination (in grey and bracketed) are omitted from palaeoceanographic interpretation, i.e. CE0806-Dr16-5b (mass balance results), CE0806-Dr15-3 (high  $\delta^{234}U_i$ ) and ALV-3889-1311-001-008 bottom (high  $^{232}Th$ ).

---

## 5.4. Discussion

While it has been demonstrated that deep-sea corals are reliable recorders of seawater Nd isotopes (e.g., Copard et al., 2010; van de Flierdt et al., 2010), changing source water compositions through time can challenge the (too) simplified notion of using Nd isotopes as a quantitative tracer of water mass mixing and overturning. Temporal variations in seawater Nd isotopes can furthermore be caused by local changes of continental inputs (eolian and riverine) and/or boundary exchange processes (e.g., Frank, 2002; Goldstein and Hemming, 2003; Lacan and Jeandel, 2005a). In the following, both of these points are discussed before turning to an interpretation of our new records in the context of vertical and/or lateral water mass movement.

### 5.4.1. The significance of local inputs for the Nd isotope signature of ambient water masses

Dust is generally considered an important source of oceanic Nd (e.g., Tachikawa et al., 1999), even though its impact on the Nd isotopic composition of the deeper water column seems to be limited in the modern ocean (e.g., Jones et al., 1994; Greaves et al., 1999; Stichel et al., 2015). Towards peak glacial conditions dust deposition increased, however, significantly in both hemispheres (Mayewski et al., 1994; Fischer et al., 2007). Figure 5.4 shows the new deep-sea coral Nd isotope records compared to ice-rafted detritus (IRD) and magnetic susceptibility (MS) from proximal sediment core locations. The latter represents an integrated signal of ferromagnetic mineral input from terrestrial sources including dust, IRD as well as submarine downslope and along-slope mass transports (e.g., Mienert and Chi, 1995; Weber et al., 2012). Therefore, MS can serve as a proxy for the significance of local Nd input at our various sample locations.

The NES are located close to the North American continent which is dominated by old rocks with unradiogenic Nd isotope signatures ( $\epsilon_{Nd} < -20$ ; Jeandel et al., 2007). Thus, it is expected that enhanced terrestrial input from nearby glacial and peri-glacial environments in North America as

recorded by higher MS (except during carbonate IRD events; Hemming, 2004) would be associated with less radiogenic coral Nd isotope signatures. The Labrador Sea MS baseline remains rather constant from MIS 3 towards peak glacial conditions of MIS 2 with high multi-millennial fluctuations superimposed (Weber et al., 2001). This pattern is hence unsuitable to explain the trend in the NES deep-sea coral Nd isotope data (Fig 5.4).

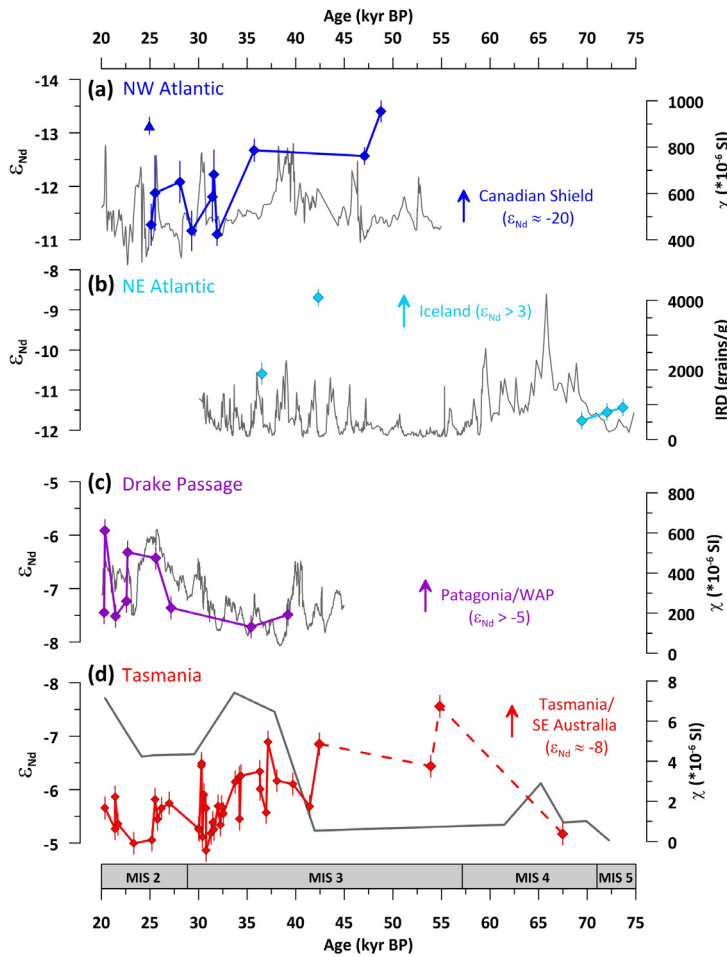


**Figure 5.4:** Time series of deep-sea coral Nd isotope data compared to tracers for local input. Nd isotope data in (c) and (d) younger than 27 kyr BP from Chapter 4. (a) Magnetic susceptibility data from Orphan Knoll core MD95-2024 in the southern Labrador Sea (Weber et al., 2001). Oldest coral sample from van de Flierdt et al. (2006b). Symbols as in Fig. 5.3. (b) Ice-rafted detritus record from Denmark Strait core PS2644-5 (Voelker et al., 2015). (c) Magnetic susceptibility data from Scotia Sea core MD07-3134 (Weber et al., 2012). (d) Low resolution magnetic susceptibility data from ODP 1170 drilled on nearby Tasman Rise (Nürnberg et al., 2004). The arrows point in the direction into which local input would drive the seawater Nd isotope signature, i.e. unradiogenic (low  $\epsilon_{Nd}$ ) from the Canadian shield and Tasmania/SE Australia and radiogenic (high  $\epsilon_{Nd}$ ) from Iceland and Patagonia/West Antarctic Peninsula (WAP). Bulk terrestrial source Nd isotope estimates based on Gingele and De Deckker (2005) Jeandel et al. (2007), Noble et al. (2012) and Chapter 3. MIS boundaries from Lisiecki and Raymo, (2005)

In the Northeast Atlantic, enhanced local input from Iceland ( $\epsilon_{Nd} > 0$ ; Jeandel et al., 2007) should be reflected in more radiogenic coral Nd isotopic compositions. A nearby IRD record from the Iceland Sea (Voelker et al., 2015) was chosen to indicate detrital release from glaciated Iceland and from more distal sources. Although the coral data from this region is limited, the increase in IRD abundance paired with constant (or even slightly declining) Nd isotope signatures between  $\sim 73.7$  and  $69.4$  kyr BP is diagnostic that increased erosion in Iceland is not driving the observed Nd isotope variations (Fig. 5.4). Moreover, the two coral data points from MIS 3 in the Northeast Atlantic deviate by  $\sim 2$  epsilon units from each other, and are both more radiogenic than the older samples, but not accompanied by a significant trend in the IRD record (Voelker et al., 2015; Fig. 5.4). Our conclusion of insignificant local Nd influence on the seawater signature at the Reykjanes Ridge is further

corroborated by a 109.8 kyr BP old coral showing a relatively radiogenic Nd isotope signature ( $\epsilon_{\text{Nd}} = -10.3 \pm 0.2$ , Table 5.1), despite very low fluxes from terrestrial sources (e.g., IRD of ODP 983; Barker et al., 2015 and OPD 980; Oppo et al., 2006).

In the Drake Passage, local terrestrial sources, i.e. Patagonia and the Westantarctic Peninsula, show Nd isotopic compositions of  $\epsilon_{\text{Nd}} > \sim -5$  (Noble et al., 2012 and references therein; Chapter 3). It has been demonstrated that both regions experienced intensified erosion during glacial times associated with significant environmental change, in particular in Patagonia (e.g., Sugden et al., 2009; Kaiser and Lamy, 2010; Caniupán et al., 2011). A nearby MS record from the Scotia Sea serves as an indicator for local terrestrial inputs to the open Drake Passage dominated by dust fluxes (Weber et al., 2012). The 3-4-fold increase in MS during late MIS 3 is not accompanied by a contemporaneous trend in coral Nd isotope signatures as the MIS 3-2 baseline remains stable at around  $\epsilon_{\text{Nd}} \approx -7.5$  (Fig. 5.4). This indicates that local terrestrial fluxes were unlikely to affect the Drake Passage seawater Nd isotopic composition significantly. Nevertheless, the Nd isotope variability after  $\sim 27$  kyr BP appears to potentially covary with MS. However, given the high throughput of water resulting from high current speeds in the Drake Passage on glacial-interglacial time scales (McCave et al., 2014), it is unlikely that short-lived events would have a strong effect whereas substantial long-term increases do not induce Nd isotope changes. Therefore, the potential covariation after  $\sim 27$  kyr BP is more likely related to a common underlying climatic mechanism.

South of Tasmania, the Nd isotope data is compared to a nearby low resolution MS record (Nürnberg et al., 2004). The MS data indicate stronger terrestrial input from MIS 4 towards MIS 2, likely reflecting the integrated result of glacier build-up, snow accumulation and reduced vegetation facilitating efficient physical erosion towards the ocean (Petherik et al., 2013; Reeves et al., 2013). Jeandel et al. (2007) presented estimates of relatively unradiogenic Tasmanian and Southeast Australian hinterland Nd isotope signatures which are also reflected in Southeastern Australia clay mineral isotopic compositions of  $\epsilon_{\text{Nd}} < \sim -8$  (Gingele and De Deckker, 2005). Significant influence of increased local input would drive the seawater Nd isotopic composition towards less radiogenic values, opposite to the trend in our deep-sea coral data (Fig. 5.4). Such anti-correlative trends indicate that local inputs are unlikely to drive the multi-millennial Nd isotope signal recorded in the coral skeletons. Due to the low resolution of the MS record, we cannot exclude short-lived inputs to influence the seawater Nd isotopic composition. However, given that substantial long-term changes in input have only an insignificant effect on the recorded Nd isotope signal, it appears unlikely that short-lived events would alter the recorded Nd isotopic composition efficiently (Fig. 5.4). Moreover, *D. dianthus* specimens live in exposed strong-current environments and skeletal sub-samples integrate a decadal-scale signal (Chapter 3). This renders efficient alteration of seawater Nd isotopic composition by short-lived erosional events even less likely in this area. The role of New Zealand has been discussed in Chapter 4 for the deglacial interval when enhanced erosion of radiogenic terrestrial material (e.g., Frost and Coombs, 1989) is accompanied by a pronounced 2 epsilon unit shift towards

less radiogenic values. The fact that New Zealand is downstream of Tasmania and following the reasoning in Chapter 4, potential New Zealand influence on the seawater Nd isotope signal would not compromise the conclusions drawn from the discussion below.

In summary, the lack of covariation, in particular on (multi-) millennial time scales between Nd isotope changes and local terrestrial fluxes (monitored by records of MS and IRD) throughout MIS 4, 3 and 2, leads us to conclude that oceanographic changes are most likely the dominant driver of the Nd isotope variability archived in our fossil deep-sea corals.

#### **5.4.2. The North Atlantic: composition of exported northern sourced water during MIS 3 and 2**

The Northwest Atlantic deep-sea coral Nd isotope record (~1200 to 2000 m water depth) evolved to more radiogenic values from 47.1 to 25.1 kyr BP, in concert with the deep ocean Nd isotopic composition at Bermuda Rise (4584 m water depth; Böhm et al., 2015; Fig. 5.5). The overall amplitude of Nd isotope variability over this time period was, however, lower in the mid-depth coral record (~2 epsilon units) than in the sedimentary deep water record (~5 epsilon units). This could be an artefact of the lower temporal resolution of the coral record and the fact that stadial phases were sampled preferentially (Table 5.1). Having ruled out any significant local inputs, changes in intermediate (and deep) water mass compositions at the New England Seamounts could be attributed to (i) admixture of southern-sourced water masses, i.e. AAIW and AABW, (ii) deepening of North Atlantic Central Water (NACW), (iii) expansion of MOW, or (iv) changes in the upstream source areas of predominant water masses.

The majority of deep-sea corals from the NES were collected from water depths between 1719 and 1986 m, a depth range where AAIW has neither been traced in the glacial nor in the interglacial North Atlantic (Pahnke et al., 2008; Xie et al., 2012, 2014; Huang et al., 2014; Jenkins et al., 2015). For AABW, such depths are probably too shallow rendering southern-sourced waters unlikely to control the NES Nd isotope pattern. Alternatively, enhanced admixture of MOW (~1000 m water depth,  $\epsilon_{Nd} = -9.4 \pm 0.2$ ; Tachikawa et al., 2004; Jenkins et al., 2015) or deepening of West North Atlantic Central Water (WNACW; ~200 to 800 m water depth,  $\epsilon_{Nd} = -9.7 \pm 0.2$ ; Jenkins et al., 2015; Lambelet et al., accepted) could create more radiogenic NES Nd isotope signatures. Despite that, both scenarios seem to be precluded by the unradiogenic Nd isotopic composition of  $\epsilon_{Nd} = 13.1 \pm 0.2$  recorded at 24.9 kyr BP by the central North Atlantic coral in 1420 m water depth. It is noted that either water mass could have influenced the one shallow sample (1222 m) from Gregg seamount at 31.9 kyr BP (where  $\epsilon_{Nd} = -11.1 \pm 0.2$ ; Table 1, Figs. 5.2 and 5.3).

As none of the scenarios discussed above seem to be fully adequate to explain our new NES data, we consider changes in NADW (or its shoaled glacial analogue GNAIW, i.e. Glacial North Atlantic Intermediate Water) source waters. One striking observation is the similarity of mid-depth coral data with the authigenic  $\epsilon_{Nd}$  values extracted from deep Bermuda Rise sediments (4584 m; Böhm et al., 2015; Fig. 5.5). The deep Bermuda Rise Nd isotope baseline values are near  $\epsilon_{Nd} \approx -13$  during

most of MIS 3 and 4 with superimposed peaks as unradiogenic as  $\epsilon_{\text{Nd}} \approx -16$ . Towards peak glacial conditions, the Nd isotope baseline decreased to about  $\epsilon_{\text{Nd}} \approx -11$ . This could be interpreted to result from increasing admixture of radiogenic AABW. However, a relatively constant  $^{231}\text{Pa}/^{230}\text{Th}$  baseline of  $\sim 0.6$  persisted from MIS 4 to MIS 2 indicating a net Pa export from the North Atlantic throughout this interval, despite the trend towards more radiogenic Nd isotope signatures (Böhm et al., 2015; Fig. 5.5). Is it possible that these values reflect a change in the mixture of exported northern-sourced waters during the glacial? Modern NADW is a delicate mixture of various water masses (e.g., Jenkins et al., 2015), so that past changes in formation rates and/or depth seem possible (e.g., Wilson et al., 2014). The new deep-sea coral data from the Northeast Atlantic provide a window to test this idea (at least in part). The corals from the Reykjanes Ridge are currently bathed by LSW with some ISOW admixed (e.g., McCartney, 1992; Xu et al., 2010; Fig. 5.2). The deep-sea corals from 73.7 to 69.4 kyr BP and at 36.5 kyr BP fall pre-dominantly in stadial intervals (Fig. 5.3). Hence, the stadial coral Nd isotope signatures of  $\epsilon_{\text{Nd}} = -11.6 \pm 0.2$  (73.7 to 69.4 kyr BP),  $\epsilon_{\text{Nd}} = -10.6 \pm 0.3$  (36.5 kyr BP) and  $\epsilon_{\text{Nd}} = -8.7 \pm 0.2$  (42.3 kyr BP) are significantly more radiogenic than modern seawater in the LSW-dominated mid-depth Northeast Atlantic ( $\epsilon_{\text{Nd}} \approx -14$ ; Lacan and Jeandel, 2004a, 2005b; Lambelet et al., accepted; Chapter 3; Figs. 5.2 and 5.3). Furthermore, these values are more radiogenic than the contemporaneous Northwest Atlantic (Böhm et al., 2015) indicating reduced influence of LSW in the North Atlantic during stadials (Fig. 5.5).

It has been hypothesised that the absence of Atlantic water masses reduced the salt supply to the Labrador Sea thus enhancing stratification and suppressing deep water formation during stadials (Rasmussen et al., 2003; Schmidt et al., 2004; Gibb et al., 2014). Such processes could then render source waters from the Northeast Atlantic to be more prominent in exported northern water masses (Rasmussen et al., 2003; Thornalley et al., 2013). Convectional seesawing between the two dominant North Atlantic deep convection centres is evident from modern observations (e.g., Dickson et al., 1996), models (e.g., Bentsen et al., 2004; Renssen et al., 2005; Oka et al., 2006) and palaeoceanographic reconstructions (Solignac et al., 2004; Hillaire-Marcel et al., 2011). In other words, formation rates and extension of LSW were progressively reduced, and replaced by water masses with more radiogenic Nd isotope signatures sourced from the overflows (Figs. 5.3 and 5.5). The relatively radiogenic Nd isotope signal recorded in the mid-depth Northeast Atlantic may then have been corroborated by strengthened MOW ( $\epsilon_{\text{Nd}} = -9.4 \pm 0.2$ ; Tachikawa et al., 2004) acting as a salt supplier to the (glacial) North Atlantic (Voelker et al., 2006). It can be speculated if enhanced stadial/glacial MOW flow (Cacho et al., 2000; Voelker et al., 2006) partly replaced LSW in the Northeast Atlantic to be incorporated into the cascading overflows, thus influencing both, the mid-depth and deep water column in the Northwest Atlantic (Fig. 5.5).

Such a scenario could explain differences in Nd isotopic composition observed between the western and eastern North Atlantic basin on glacial-interglacial time scales (see also Roberts et al., 2010; Piotrowski et al., 2012; Böhm et al., 2015). Moreover, this would be consistent with the constant

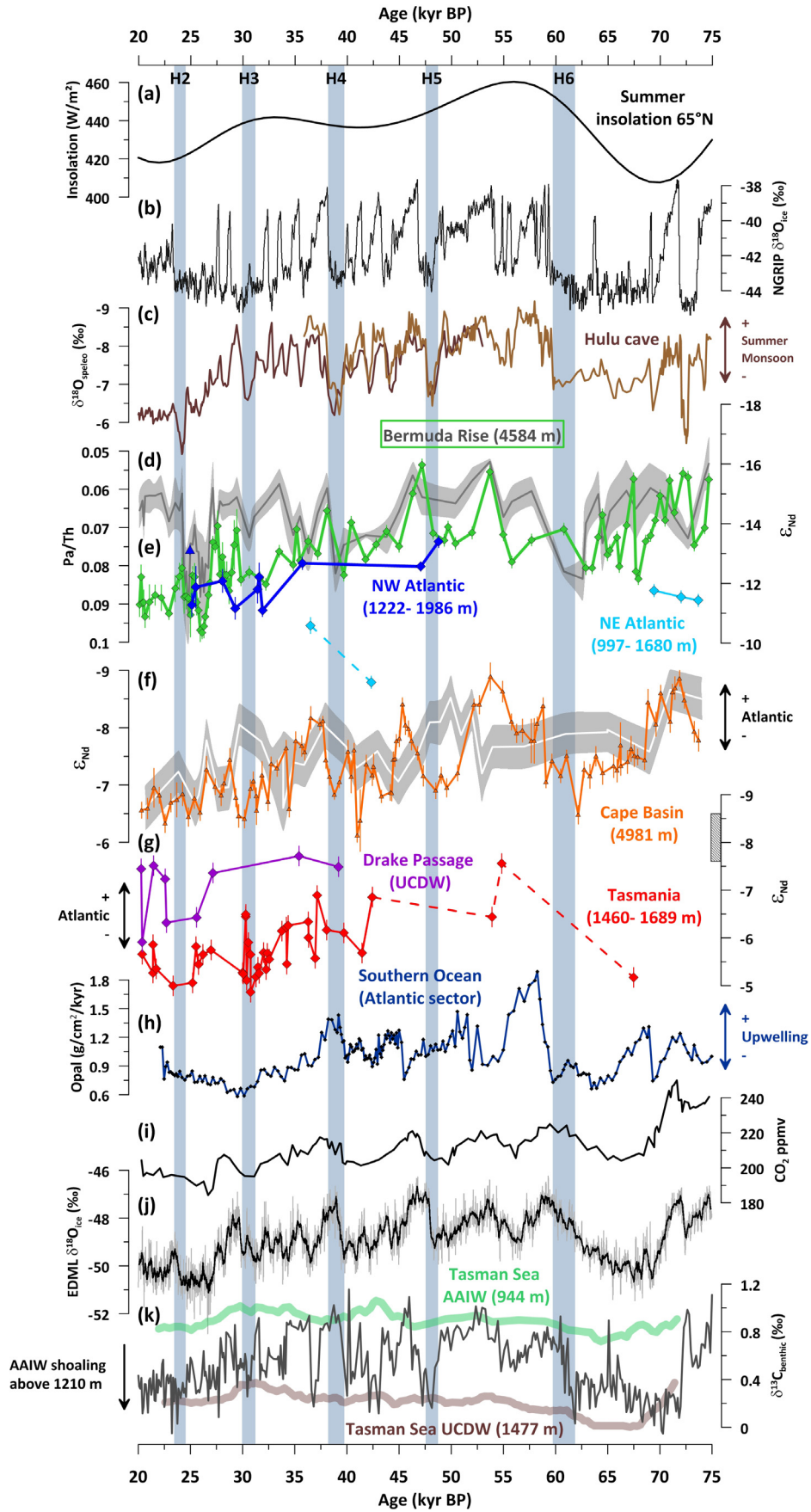
baseline in  $^{231}\text{Pa}/^{230}\text{Th}$  indicating pre-dominant strong southwards water mass export throughout MIS 3 and 2 (Böhm et al., 2015; Fig. 5.5). The suggestion that mid-depth North Atlantic water masses were subject to particularly dynamic Nd isotope changes during times of rapid climate transition has already been formulated by Wilson et al. (2014). Here, we suggest that the interplay of LSW, overflow waters, and MOW in the Northeast Atlantic (see also Hanebuth et al., 2015) changed during the transition towards peak glacial conditions consequently altering the Nd isotope signature of mid-depth water masses exported from the North Atlantic.

Interestingly, the FeMn coatings scraped off the aragonitic skeletons are offset towards less radiogenic values (Table 5.1; Fig. 5.3). On a first order, this seems consistent with an integrated signal recorded by exposed FeMn coatings versus a snapshot archived in the coralline aragonite itself. But more importantly, such unradiogenic signal of FeMn coatings is clearly not representative of the seawater-derived Nd isotope signal characteristic of cold intervals (Figs. 5.3 and 5.5). Or more precisely, the unradiogenic nature of the Nd isotopic composition of FeMn oxyhydroxides coated onto North Atlantic corals is similar to Nd isotope signatures of seawater-derived phases precipitated during warm intervals (Böhm et al., 2015; Figs. 5.3 and 5.5). This suggests that FeMn oxyhydroxides in the North Atlantic were precipitated preferentially during phases of unradiogenic seawater Nd isotopic composition, i.e. during warm intervals. This could explain the relatively stable and unradiogenic Nd isotope signal in North Atlantic glacial-interglacial FeMn crust data (Foster and Vance, 2006).

---

**Figure 5.5:** Comparison of deep-sea coral Nd isotope data with literature data for MIS 4, 3 and 2. (a) Summer insolation at 65°N (Berger and Loutre, 1992). (b) NGRIP oxygen isotope ice core record (NGRIP, 2004) on GICC05/NALPS time scale (Andersen et al., 2006; Svensson et al., 2008; Barker and Diz, 2014). (c) Hulu cave speleothem oxygen isotope record representing monsoon patterns in central China (Wang et al., 2001). (d)  $^{231}\text{Pa}/^{230}\text{Th}$  record from Bermuda Rise ODP site 1063 (4584 m water depth; in grey) (Böhm et al., 2015). (e) Authigenic North Atlantic Nd isotope record from ODP site 1063 (spring green; Böhm et al., 2015). Coral Nd isotope data from the New England Seamounts (blue; this study and van de Flierdt et al., 2006b), the central North Atlantic (blue triangle, this study) and the Reykjanes Ridge (sky blue diamonds, this study). Note the offset between Northeast and Northwest Atlantic coral data and the close similarity of Nd isotopic composition recorded at in the Northwest Atlantic at mid-depth and in the abyss. (f) Deep Southeast Atlantic (4981 m water depth) Nd isotope record from Cape Basin core TNO57-21 (Piotrowski et al., 2005) and deep Indian Ocean Nd record from core SK129-CR2 (3800 m water depth; grey polygon) from the Chagos Trench (Piotrowski et al., 2009). (g) Drake Passage and Tasmanian deep-sea coral Nd isotope data (data younger than 27 kyr BP from Chapter 3). Note that Drake Passage data are consistently less radiogenic than the Tasmanian record with absolute Nd isotope signatures similar to deep records in (e). (h) Southern Ocean (Atlantic sector) opal flux record from TN057-14PC4 indicative of upwelling intensity. (i) Byrd icecore CO<sub>2</sub> record (Ahn and Brook, 2008) on GICC05/NALPS time scale (Barker and Diz, 2014). (j) EDML stable oxygen isotope record (EPICA community members, 2006, 2010). (k) Light green and brown bands are running averages of mid-depth Tasman Sea carbon isotope records from cores MD06-2990/SO136\_003GC (944 m water depth) and MD06-2986 (1477 m water depth) (Ronge et al., 2015). Chatham Rise  $\delta^{13}\text{C}_{\text{benthic}}$  record from core MD97-2120 (1210 m water depth; black; Pahnke and Zahn, 2005). Note that AAIW shoaled when MD97-2120  $\delta^{13}\text{C}_{\text{benthic}}$  approached values of deeper Tasman Sea MD06-2986 which are in turn similar to Chatham Rise core SO213/2\_82-1 from 2066 m water depth (Ronge et al., 2015).

---



### 5.4.3. Unmixing the Nd isotope signal south of Tasmania: identifying dominant source water masses

Currently, the Tasmanian coral sampling locations are bathed by UCDW (Fig. 5.2), but overlying AAIW has been identified to shoal and deepen on glacial to interglacial time scales, respectively (Ronge et al., 2015). This led to fluctuations of the AAIW-UCDW boundary across 1210 m water depth as recorded in core MD97-2120 at Chatham Rise (Pahnke and Zahn, 2005; Ronge et al., 2015; Fig. 5.5). AAIW is formed from Antarctic surface waters which, in turn, are strongly influenced by upwelling deep waters (Piola and Georgi, 1982; Bostock et al., 2013; Cerovečki et al., 2013), but may also include a local component derived from the Antarctic shelves (Carter et al., 2012). However, the formation regions of AAIW from south of Tasmania are remote from Antarctic shelf water masses (Bostock et al., 2013). This is reflected in the Nd isotope signature of modern Southwest Pacific AAIW resembling the signature of underlying source waters ( $\epsilon_{Nd} \approx -8.2$ ; Basak et al., 2015). Therefore, changes in AAIW formation and/or circulation are unlikely candidates to explain the observed variation. Compelling evidence for this hypothesis is provided by Ronge et al. (2015) using the  $\delta^{13}C_{benthic}$  signal from a set of regional cores to conclude that AAIW remained above 1477 m water depth near 44°S in the Tasman Sea during the last 350 kyrs.

Therefore, we consider the observed Nd isotope variability recorded at the southern margin of Tasmania to be pre-dominantly set by the dynamic mixing of UCDW, as a relatively unradiogenic source, the composition of which can be approximated by the data from the Drake Passage, with a source of radiogenic Nd. Two potential candidates for the latter source are underlying deep waters and North Pacific water masses (Fig. 5.2). Southern Ocean deep and bottom waters have been shown to carry very radiogenic Nd isotope signatures of  $\epsilon_{Nd} \approx -5$  during glacial intervals (Piotrowski et al., 2005; Elderfield et al., 2012; Noble et al., 2013; Skinner et al., 2013). Direct upward intrusion of such waters appears unlikely given the rapid fluctuations in the Tasmanian time series and low average vertical eddy diffusivity ( $\kappa \approx 1.3 \text{ cm}^2/\text{sec}$ ) and upwelling rates ( $\omega \approx 1.2 \text{ cm/day}$ ) (Munk, 1966). Based on simple geometry of steepened isoneutrals a 10-15° northward shift of ACC fronts would be required to bath the Tasmanian margin in LCDW (Fig. 5.2). Reconstructions do not provide supporting evidence for such tremendous migration in this region (cf. Neil et al., 2004; Barrows and Juggins, 2005; Nürnberg and Groeneveld, 2006; De Deckker et al., 2012; Kohfeld et al., 2013; Figs. 5.2 and 5.6). As the Southern Ocean is a region of deep wind-driven mixing (e.g., Marshall and Speer, 2012), underlying radiogenic deep water masses may have been mixed into the overlying water masses at times, similar to processes reconstructed for the deglacial period (Anderson et al., 2009; Skinner et al., 2010; Burke and Robinson, 2012). However, work from the glacial mid-depth Southwest Pacific suggests a deeply stratified water column near 2000 m water depth (Sikes et al., 2000; Skinner et al., 2015; Hines et al., 2015) and that deeper mixing is rather associated with a southward shift of the frontal system during Southern Hemisphere warm periods (e.g., Toggweiler et al., 2006; Anderson et al., 2009). In other words, an increase of upward mixing of LCDW is associated with southward frontal shifts. Thus, LCDW can be ruled out to have caused progressively increasing

admixture of radiogenic Nd into mid-depth Southwest Pacific water masses towards peak glacial conditions.

It follows that the most likely source for radiogenic Nd near Tasmania is derived from the (North) Pacific, i.e. PDW and/or Glacial North Pacific Intermediate Water (GNPIW; e.g., Matsumoto et al., 2002; Chapter 4), consistent with modern hydrography of the Tasman Sea indicating mixing of upper PDW into UCDW above ~2000 m water depth (Fig. 5.2). Modern PDW has a Nd isotope signature of  $\epsilon_{Nd} \approx -4$  in the North Pacific (Amakawa et al., 2009; Figs. 5.1 and 5.2) and appears to have been stable across the past glacial cycle (Abouchami et al., 1997).

#### **5.4.4. Southern Ocean water mass mixing and implications for ocean circulation during MIS 3 and MIS 2**

The least radiogenic Nd isotope value of the entire record is displayed with  $\epsilon_{Nd} = -7.6 \pm 0.2$  during early MIS 3 at 54.8 kyr BP reflecting increased influence of UCDW at the sampling location during warmer periods. In contrast, towards peak glacial conditions the Pacific influence increased progressively (Fig. 5.5) paralleling reduced North Atlantic derived waters in the deep Atlantic and Indian Oceans (Piotrowski et al., 2005, 2009; Böhm et al., 2015; Jonkers et al., 2015; Fig. 5.5). Such progressive reduction of Atlantic overturning towards peak glacial conditions was associated with changes in the cross-equatorial heat transport in the Atlantic dictating a southward migration of the Atlantic Intertropical Convergence Zone (ITCZ; Zariess et al., 2011) and alteration of East Asian Monsoon patterns (e.g., Wang et al., 2001; Deplazes et al., 2014). This was paired with reduced upwelling in the Southern Ocean (Anderson et al., 2009; Fig. 5.5) driven by northward migration of the SWW (Kaiser et al., 2005; Anderson et al., 2009; Whittaker et al., 2011). So how can this be reconciled? Neodymium isotope records from the deep South Atlantic (Piotrowski et al., 2005) and Indian Ocean (Piotrowski et al., 2009) are located upstream of the NADW flow direction with respect to Tasmania and are thus likely to more readily indicate reduced NADW influence on the global deep ocean. Despite the similar trends on glacial-interglacial time scale, the deep Nd isotope signatures show less radiogenic values than the Tasman time series throughout (Fig. 5.5). This would be consistent with an expansion of PDW/GNPIW paired with reduced Atlantic overturning and progressive shoaling of Southwest Pacific AAIW towards peak glacial conditions (Ronge et al., 2015; Fig. 5.5). Indeed, combined Nd and radiocarbon analyses support a similar or better ventilation state of LGM mid-depth waters sourced from the North Pacific compared to UCDW in the glacial Drake Passage (Burke and Robinson, 2012; Chen et al., 2015; Hines et al., 2015; Burke et al., unpubl. data; Chapter 4). In combination with more vigorous deep Pacific inflow during glacial times (Hall et al., 2001), this indicates progressively intensifying Pacific overturning related to GNPIW expansion (e.g., Matsumoto et al., 2002) at the expense of UCDW resulting in radiogenic peak glacial Nd isotope signatures at the Tasmanian margin (Figs. 5.5 and 5.6).

At the same time, the ACC UCDW Nd isotope baseline archived in Drake Passage corals remains relatively invariable with less radiogenic values ( $\epsilon_{\text{Nd}} \approx -7.5$ ; Fig. 5.5) requiring admixture from an unradiogenic source, i.e. the North Atlantic. In context with other Nd isotope data, our mid-depth Southern Ocean records suggest that the multi-millennial trend from MIS 3 towards MIS 2 was likely controlled by the progressive evolution of two mid-depth overturning circulation cells. The evolution of the Pacific cell was related the southwards expansion of GNPIW, reflected in Tasmanian coral Nd isotope signatures of  $\epsilon_{\text{Nd}} \approx -5.5$ . The active overturning in the Atlantic can be inferred from relatively unradiogenic Nd isotope signatures of  $\epsilon_{\text{Nd}} \approx -7.5$  in the Drake Passage (Fig. 5.5). Nevertheless, such Drake Passage signatures were not a pure Atlantic signal where exported water masses carried  $\epsilon_{\text{Nd}} \approx -11$  to  $-12$  during late MIS 3 and MIS 2 (Fig. 5.5). This invokes interactive admixture to the Southern Ocean from both, the Atlantic and Pacific Ocean. It can be speculated if the Nd concentration of GNPIW participating in this mixing could have been lowered due to the Pacific overturning, similar to newly formed Atlantic water masses. This would imply that the actual proportion of Atlantic water masses could be small despite similar-to-modern Nd isotope signatures recorded in Drake Passage corals.

However, the vertical extent of overturning cells in both basins was likely restricted to above  $\sim 2$ - $2.5$  km water depth (Matsumoto et al., 2002; Hodell et al., 2003; Curry and Oppo, 2005; Skinner et al., 2015). The interaction with the lower cell was limited due to restricted diapycnal mixing (e.g., Sarnthein et al., 1994; Curry and Oppo, 2005; Ferrari et al., 2014) paired with reduced Southern Ocean upwelling induced by poorly aligned SWW (Toggweiler et al., 2006; Anderson et al., 2009; Chapter 4; Fig. 5.5). Limited mixing between upper and lower cells would facilitate sequestration of atmospheric  $\text{CO}_2$  and can therefore act as a positive feedback mechanism of insolation-driven global cooling (e.g., Toggweiler et al., 2006; Ferrari et al., 2014, Fig. 5.5) accompanied by NADW shoaling (e.g., Curry and Oppo, 2005). Shoaling of NADW hampers the southward geostrophic flow of NADW below the Drake Passage sill depth (Toggweiler and Samuels, 1995). As the transformation of upwelling NADW-imprinted LCDW to AABW on the Antarctic shelves implies heat loss, this process has a net warming effect on Antarctic temperatures (e.g., Talley, 2013). Consequently, NADW shoaling implies decreasing heat flux to the Antarctic continent thus amplifying the cooling trend.

The transition into peak glacial conditions comprised, besides NADW shoaling, the northwards migration of oceanic fronts, the sea-ice margin and the SWW (Gersonde et al., 2005; Kaiser et al., 2005; Anderson et al., 2009; Kohfeld et al., 2013). South of Tasmania, a northward frontal shift would be expected to feature a stronger influence of unradiogenic ACC-bound UCDW. On multi-millennial time scales, this is not the case. Instead, the southward expansion of GNPIW paired with northward migration of ACC-bound UCDW implies a pronounced lateral Nd isotope gradient in the Southwest Pacific (Fig. 5.6). Such gradient could be sustained only if the southward expansion of GNPIW, inferred from the Tasmanian corals, did not translate into volumetrically significant net export of GNPIW into the ACC flow. From a mechanistic point of view, the more

northerly position of oceanic fronts, and in particular the SAF during glacial times (Barrows and Juggins, 2005; Gersonde et al., 2005; Kohfeld et al., 2013) paired with bathymetrical constraints in the Southwest Pacific (Heath, 1981; Rintoul et al., 1997; Fig. 5.6) could act to restrict the export flow from the Tasman Sea, in analogy to modern observations (Rintoul and Bullister, 1999; Sokolov and Rintoul, 2000), and to thermal isolation on the Campbell Plateau (Neil et al., 2004). Deep waters entering the Tasman Sea from the north could then re-circulate within the restricted basin until they joined the eastward flow at the northern ACC flank. After circumventing the Campbell Plateau, such water masses might readily have been re-injected into the South Pacific Basin (Fig. 5.6). This could have contributed to the radiogenic CDW Nd isotope values extracted from glacial sediments at Chatham Rise ( $\epsilon_{Nd} \approx -4$ , partly ascribed to boundary exchange, see Noble et al., 2013) and the similarity of mid-depth  $\delta^{13}C$  east and west of New Zealand during MIS 3 (Ronge et al., 2015). Or alternatively, GNPIW was picked up by the eastward ACC flow, but limited cross-frontal mixing in the Pacific sector of the Southern Ocean led to reduced net admixture into the ACC core (monitored in the Drake Passage). Partial deflection of water masses associated with the northern flank of the ACC would then feed into the South Pacific Gyre (Lamy et al., 2015; Chapter 4) thus reducing the net admixture of GNPIW into the circumpolar flow, i.e. into the Drake Passage. It is noted that both re-circulation mechanisms still allow admixture of GNPIW into the ACC; a more northerly position of the SWW and associated oceanic fronts just reduces the net export into the circumpolar flow.

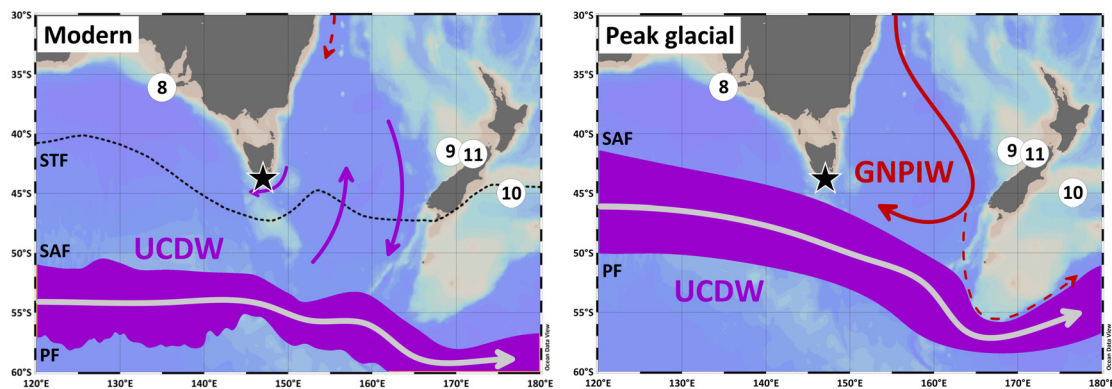


**Figure 5.6:** Schematic of Tasman Sea circulation. (left) Simplified modern circulation dominated by UCDW (purple arrows; after Rintoul and Bullister, 1999; Sokolov and Rintoul, 2000). Frontal positions after Orsi et al. (1995). STF: Subtropical Front, SAF: Subantarctic Front, PF: Polar Front. Black star indicates coral sampling location at the southern margin of Tasmania. (right) Proposed peak glacial circulation pattern with northward displaced fronts and associated circumpolar flow (after Barrows and Juggins, 2005; Gersonde et al., 2005; Kohfeld et al., 2013), southward expansion of GNPIW in the Tasman Sea and potential route around Campbell Plateau (red stippled line). Note that northward movement of the deep reaching SAF and PF is bathymetrically restricted by the Campbell Plateau south of New Zealand and probably also the Tasman plateau south of Tasmania. White dots denote locations of literature data (see caption Fig. 5.1).

#### 5.4.5. A Southern Hemisphere driver of North Atlantic Heinrich events?

The close similarity of the Tasmanian Nd isotope time series to Antarctic ice core records has already been pointed out. The high resolution interval between 32 and 30 kyr BP in our Tasmanian deep-sea coral Nd isotope data (Fig. 5.7) covers Heinrich Stadial 3 (HS3) starting at ~31.2 kyr BP

according to the absolutely dated speleothem chronology from Hulu cave (Wang et al., 2001). During this early phase, the Southern Hemisphere experienced gradual warming (EPICA community members, 2006, 2010; Fig. 5.7) and weak/southerly SWW (Whittaker et al., 2011), paralleled by changes in the terrestrial biosphere represented by high resolution WAIS Divide methane ( $\text{CH}_4$ ) data (Rhodes et al., 2015; Fig. 5.7), whereas Greenland temperatures remained rather stable (NGRIP members, 2004; Andersen et al., 2006; Fig. 5.7). Superimposed on the relatively smooth transition into HS3, a methane excursion, abrupt northward shifts of the SWW and the SAF paralleled by AAIW deepening preceded the actual Heinrich inception. This is not seen in other proxy data which may indicate the short-lived nature of this event (Fig. 5.7). The Heinrich inception was recorded by a change in Asian monsoon circulation at 31.2 kyr BP (Wang et al., 2001) and as instantaneous warming of Antarctic temperatures indicated by EDML ice core  $\delta^{18}\text{O}$ . In the Southwest Pacific, AAIW shoaling (Pahnke and Zahn, 2005; Ronge et al., 2015) coincided roughly with a northward migration of the Subantarctic Front (SAF) as reflected in the abundance of subpolar species in core MD03-2611 south of Australia (De Deckker et al., 2012; Figure 5.7). The most radiogenic Nd isotope signature of  $\epsilon_{\text{Nd}} = -4.9 \pm 0.2$  was recorded at  $\sim 30.8$  kyr BP, although the  $\sim 400$ -year data gap between 31.2 and 30.8 kyr BP may hold further variability. Nevertheless, the radiogenic signal at 30.8 kyr BP indicates strong influence of southward penetrating GNPIW at the sampling site accompanied by a more southerly position of oceanic fronts (De Deckker et al., 2012; Table 5.1; Fig. 5.7). The NES coral data between 32 and 31 kyr BP shows a tendency towards slightly less radiogenic values from  $\epsilon_{\text{Nd}} = -11.1 \pm 0.2$  to  $\epsilon_{\text{Nd}} \approx -12$  (high uncertainties on U-series dates; see Table 5.1 and Fig. 5.3) providing evidence that the Southwest Pacific trend was not simply driven by Nd isotope changes of North Atlantic source waters.

At 30.8 kyr BP, the Nd isotopic composition shifted abruptly ( $\sim$ one epsilon unit) towards less radiogenic values, in concert with northward shifting SAF and SWW, AAIW shoaling, changes in East Asian monsoon circulation and peaking  $\text{CH}_4$ . Atmospheric methane concentrations are predominantly controlled by changes of the terrestrial biosphere which, in turn, are driven by large scale atmospheric re-organisation (Chappellaz et al., 1993; Brook et al., 2000). Given this and the close covariation with SWW and ocean frontal positions suggests that changes in Southwest Pacific ocean circulation, expressed in Tasmanian Nd isotope variability, were coupled to atmospheric forcing. Most importantly, such atmospheric mechanism is consistent with the abrupt nature of change characterised by “flushing” of the GNPIW-dominated Tasman Sea with GNAIW-admixed UCDW from the south during abrupt stadial frontal shifts. In contrast to the multi-millennial evolution (Figs. 5.5 and 5.7) discussed above, the Nd isotope response across HS3 was in opposite direction, i.e. the peak glacial Pacific might have been closer to steady state (Fig. 5.6). Interestingly, Antarctic and Greenland ice core  $\delta^{18}\text{O}$  data show limited sensitivity during this interval providing evidence that the high latitude temperature response was decoupled from and/or insensitive to high-frequency mid-latitude variations (Fig. 5.7). The atmospheric  $\text{CO}_2$  content might, however, have been related to such abrupt northward expansion of UCDW (Ahn and Brook, 2014; Fig. 5.7).

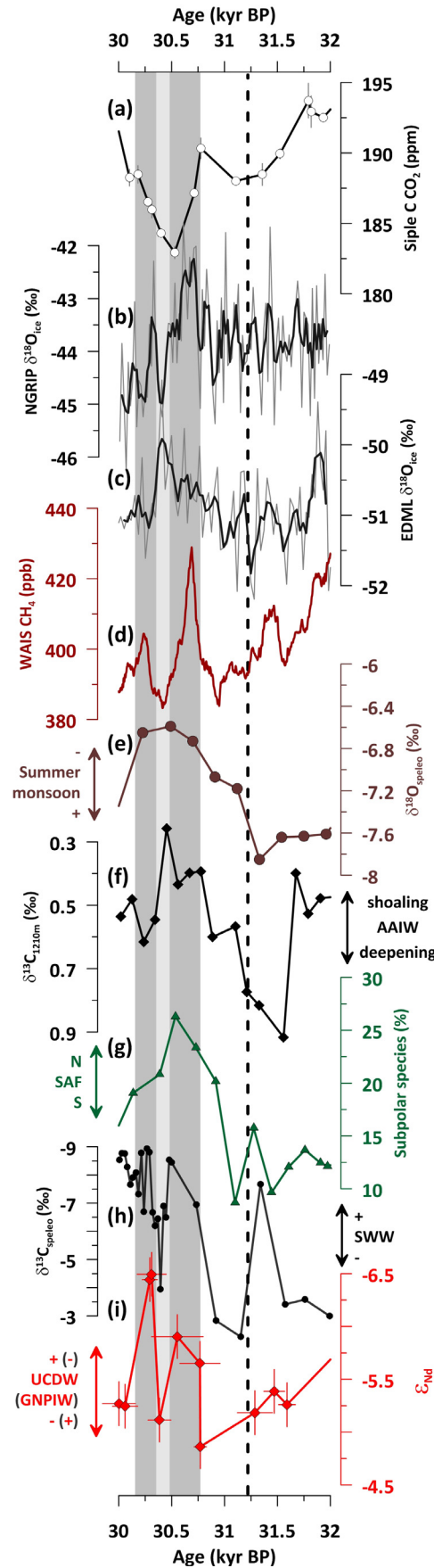


**Figure 5.7:** Time interval from 32 to 30 kyr BP covering Heinrich Stadial 3. (a) Siple Dome C carbon dioxide record on GICC05 time scale (Andersen et al., 2006; Ahn and Brook, 2014). (b) NGRIP oxygen isotope ice core record (NGRIP, 2004) on GICC05 time scale (Andersen et al., 2006). (c) EDML oxygen isotope ice core record (EPICA community members, 2006, 2010). (d) WAIS Divide methane record recording changes in pre-dominantly terrestrial sources (Rhodes et al., 2015). (e) Hulu cave speleothem oxygen isotope record (Wang et al., 2001). Note inverted y scale compared to Figure 5.5. (f)  $\delta^{13}\text{C}_{\text{benthic}}$  of MD97-2120 from 1210 m water depth (Pahnke and Zahn, 2005). (g) Planktonic foraminifera abundance from MD03-2611 off Southern Australia (De Deckker et al., 2012); SAF = Subantarctic Front. (h) Hollywood Cave  $\delta^{13}\text{C}_{\text{speleo}}$  record. Note inverted y-scale compared to Figure 5.5. (i) Tasmanian deep-sea coral Nd isotope record showing the interplay of less radiogenic UCDW and more radiogenic upper GNPIW/ PDW. Uncertainties of U-series ages from Hines et al. (2015) (see also Table 5.1). Grey shading indicates intervals of change recorded in Nd isotope data south of Tasmania. Stippled line shows onset of HS3 as recorded in Hulu cave speleothem data (Wang et al., 2001). Note that a northward frontal shift is associated with more prominent UCDW at the coral site, in contrast to the multi-millennial time scales where UCDW influence is reduced during glacial intervals (Fig. 5.5).

Remarkably, the Hulu Cave  $\delta^{18}\text{O}_{\text{speleo}}$  shifts towards heavier values considered to represent reduced summer monsoon, and thus a southward ITCZ migration, dominated by Northern Hemisphere dynamics (Wang et al., 2001). At the same time, the northward movement of oceanic fronts in the Southwest Pacific (De Deckker et al., 2012) could be expected to have induced a northward displacement of the tropical rain belt, and thus intensified summer monsoon. As the East Asian monsoon depends, among other factors, on Indian and Pacific Ocean sea surface temperatures (Yihui and Chan, 2005), it can be speculated if these opposing trends were partly caused by the re-distribution of heat associated with potential Pacific overturning during Heinrich events drawing a substantial amount of heat from low to high latitudes in the North Pacific (Hu et al., 2012; Menviel et al., 2014). This could change dominant sources and pathways of precipitation, but moreover simply alter the ratio of winter over summer precipitation (cf. Wang et al., 2001). Such scenario can involve asynchrony between Atlantic and Pacific atmospheric circulation (Liu and Hu, 2015) during which the Southern Hemisphere can act to influence the Hulu Cave  $\delta^{18}\text{O}$ , as considered in particular for cold intervals (Rohling et al., 2009). This way, atmospheric processes driving Tasmanian coral Nd isotope trends could be aligned directly with Hulu Cave  $\delta^{18}\text{O}$  (Fig. 5.7). Alternatively, a northward shift of Southern Ocean fronts could simply have been paired with southward displacement of the Indo-Pacific ITCZ, consequently enhancing Southern Hemisphere pressure gradients (Fig. 5.7). Such a scenario has previously been reconstructed for Heinrich intervals and demonstrated to strengthen SWW circulation over New Zealand (Whittaker et al., 2011).

After the initial shift, our Tasmanian deep-sea coral data indicate abrupt oscillations paralleled by shifts of the SWW and peaks in atmospheric methane concentrations (Fig. 5.7). Therefore, we suggest that atmospheric forcing induced changes in GNPIW-UCDW mixing resulting in shifts to  $\epsilon_{\text{Nd}} = -5.1 \pm 0.2$  at 30.4 kyr BP and back to unradiogenic values of  $\epsilon_{\text{Nd}} = -6.5 \pm 0.2$  at 30.3 kyr BP. Similar fluctuations have been reported for the intermediate-depth North Atlantic during Heinrich Stadials HS1, HS2 and HS4. They were ascribed to oscillations of the thermohaline circulation (Zahn et al., 1997), or more precisely, the AMOC (Wunsch, 2002). Moreover, Zahn et al. (1997) identified smooth multi-centennial to millennial transitions prior to the actual HS1, HS2 and HS4 IRD events in high resolution data from the Iberian Margin. Unfortunately, our data coverage across HS2 and HS4 is limited, but our HS3 data captured comparable high frequency oscillations occurring after a rather gradual transition into HS3. The similarity of the oceanic transition in the North Atlantic and Southwest Pacific supports the global reach of Heinrich-D/O cyclicity (e.g., Hemming, 2004; WAIS Divide project members, 2015). The lack of response in the Nd isotope data to the early SWW shift, superimposed on the gradual transition into HS3, then indicates that centennial-scale oceanic processes (cf. Stocker and Johnsen, 2003; Barker et al., 2011; WAIS Divide project members, 2015) could have played a pivotal role in driving the system towards a Heinrich event, decoupled from short-term atmospheric forcing. However, the (sub) decadal-scale Nd isotope shifts thereafter call for a faster mechanism, i.e. atmospheric forcing (Whittaker et al., 2011; Wang et al., 2015). In the

atmosphere, associated perturbations have been linked with changes in tropical rainfall driving atmospheric methane concentrations during HS1, HS2, HS4 and HS5 (Rhodes et al., 2015). It has been shown that Southern Hemisphere atmospheric circulation is sensitive to climate change and, alongside, influences ACC properties (Böning et al., 2008; Gille, 2008; Anderson et al., 2009; Whittaker et al., 2011) and CDW upwelling intensity on the shelves (e.g., Thoma et al., 2008; Shevenell et al., 2011; Chapter 6).

We therefore propose a sequence of events to fit our Southern Ocean Nd isotope data into a global framework. Freshwater runoff from glacial melting into the North Atlantic induced a gradual(?) transition of the AMOC (Zahn et al., 1997) leading to an increase of subsurface salinity and heat content (Marcott et al., 2011) paired with reduced and/or shoaled NADW/GNAIW formation (Rasmussen et al., 2003; Thornalley et al., 2013) and export prior to the Heinrich IRD event (e.g., Rasmussen et al., 2003; Piotrowski et al., 2005; Robinson and van de Flierdt, 2009; Böhm et al., 2015; Figs. 5.5 and 5.7). As the southward geostrophic flow of Atlantic-sourced waters feeding into the upwelling water masses on the Antarctic shelves can only be maintained below the Drake Passage sill depth (Toggweiler and Samuels, 1995), NADW shoaling reduces the deep southward flow. Notably, the wind-driven upwelling of NADW-spiked LCDW is a heat source to the circum-Antarctic shelves (Thoma et al., 2008; Holland et al., 2010; Shevenell et al., 2011; Talley, 2013). Therefore, reduced southward NADW flux induces Antarctic cooling, as recorded in the EDML ice core located near the coast in the Atlantic sector of Antarctica (EPICA community members, 2006, 2010; Figs. 5.1 and 5.7), in concert with decreasing atmospheric CH<sub>4</sub> levels (Rhodes et al., 2015) and expansion of GNPIW (Fig. 5.7). In the North Atlantic, the subsurface warming would not be recorded in Greenland ice core data, but induce melting of buttressing ice shelves (Shaffer et al., 2004; Marcott et al., 2011; Joughin et al., 2012; Rignot et al., 2015) accelerating thinning and ice loss of grounded Northern Hemisphere ice sheets (Shaffer et al., 2004; Rignot et al., 2004; Joughin et al., 2012), amplified by (regional) sea-level rise in direct response to AMOC reduction (Flückiger et al., 2006; Goddard et al., 2015). At a tipping point of subsurface warming, the (gradual) transition culminates in the actual Heinrich event (Marcott et al., 2011; Alvarez-Solas et al., 2013) which is then expressed in the wide-spread distribution of IRD and surface ocean freshening across the North Atlantic (Hemming, 2004). The interoceanic response during closed Bering Strait state would be expected to enhance Pacific overturning, and hence extension of GNPIW at the expense of GNAIW/UCDW through ocean-atmosphere feedbacks (Kiefer et al., 2001; Saenko et al., 2004; Okazaki et al., 2010; Rae et al., 2014), consistent with radiogenic Nd isotope signatures of  $\epsilon_{Nd} = -4.9 \pm 0.2$  south of Tasmania at 30.8 kyr BP (Fig. 5.7). This scenario involves a positive feedback loop in the North Atlantic which can be disrupted by a breakdown of stratification in the North Atlantic, i.e. by water column instability upon release of subsurface heat and salinity re-launching vigorous North Atlantic deep water formation (cf. Thiagarajan et al., 2014). Short-term resumption and reduction of the AMOC and associated atmospheric re-organisation, reflected in atmospheric CH<sub>4</sub> content (Rhodes et al., 2015), would be

progressed into the Southern Hemisphere through atmospheric teleconnections. The implied SWW response, expressed in Hollywood cave precipitation patterns, controlled UCDW-GNPIW mixing as represented by Tasmanian coral Nd isotope signatures (Whittaker et al., 2011; Fig. 5.7). Alternatively, re-stabilisation of the North Atlantic ice sheets at a new grounding line might cause the observed oscillations, but is surely a good candidate to ultimately give rise to AMOC intensification during the following D/O interstadial once the ice sheets returned to equilibrium. However, both mechanisms interrupting the positive feedback loop of subsurface heat buildup, glacial melt and freshwater capping in the North Atlantic could be subject to intrinsic oscillations resulting in abrupt interhemispheric variability exemplified by HS3. A similarly differentiated climatic sequence has recently been identified during deglacial HS1 (Thiagarajan et al., 2014; Wilson et al., 2014; Strikis et al., 2015; Chapter 4). The strong northward heat transport associated with a sustained AMOC resumption would lead into a subsequent warm D/O interstadial, but would also deliver moisture for increased continental snow and ice accumulation in the North Atlantic realm. The implied ice advance could then (slowly) drive the system into the next Heinrich-D/O cycle.

We here established an interhemispheric relationship for the HS3 interval which is different to other Heinrich intervals, in particular with regard to sources and timing of ice rafting in the North Atlantic (Hemming, 2004). Nevertheless, analogies in our data and pre-Heinrich Antarctic temperature evolution suggest that similar processes operated during other Heinrich Stadials (Fig. 5.5). During HS2, a trend towards more radiogenic values by ~one epsilon unit was paralleled by Antarctic temperature cooling recorded in EDML ice core  $\delta^{18}\text{O}$  and progressive AMOC reduction inferred from North Atlantic mid-depth stable isotope data (Zahn et al., 1997). Similar pre-Heinrich EDML cooling trends are observed prior to HS4 and HS5 (EPICA community members 2006, 2010; Figs. 5.5 and 5.7) so that our proposed sequence of events may apply to other Heinrich/IRD events.

Although our suggested scenario requires freshwater flux to the North Atlantic, the ultimate trigger might be found in the Southern Hemisphere as the centennial-scale prelude to the actual Heinrich IRD event is reflected in a characteristic gradual Nd isotope trend covarying with atmospheric  $\text{CH}_4$  content and EDML ice core  $\delta^{18}\text{O}$  (Fig. 5.7). It can be speculated if Southern Hemisphere atmospheric dynamics conditioned the North Atlantic towards Heinrich events. More specifically, cooling Antarctic temperatures could induce sea ice advance, shoaling of the NADW/AABW interface, which increased the distance of the Antarctic continent to the major ACC upwelling zone (cf. Ferrari et al., 2014) and eventually Antarctic heat supply. In the North Atlantic, excess northward oceanic heat transport would feed into subsurface ocean heat accumulation inducing ice melting (Marcott et al., 2011; Alvarez-Solas et al., 2013). The reduced water mass formation implied by North Atlantic stratification could have been compensated for by salinity-driven deepening and intensification of water mass formation in the North Pacific (Kiefer et al., 2001; Okazaki et al., 2010; Menviel et al., 2014; Rae et al., 2014). It needs to be tested if the (sub) centennial-scale interhemispheric response was a consistent feature of Heinrich events, in particular

the timing of inter- and intrahemispheric teleconnections, and if different boundary conditions such as the position of the margins of Northern Hemisphere ice sheets change the above ice-ocean-atmosphere feedback scenario.

### 5.5. Conclusions

We presented new deep-sea coral Nd isotope results from the North Atlantic and Southern Ocean covering the time period from MIS 4 to 2. In combination with available  $^{231}\text{Pa}/^{230}\text{Th}$  and Nd isotope data, our North Atlantic results suggest a progressive  $\sim 2$  epsilon unit Nd isotope “endmember” change of North Atlantic deep waters across MIS 3 resulting in peak glacial  $\epsilon_{\text{Nd}} \approx -11$  to  $-12$ . This change was probably caused by reduced spreading of upper deep water masses from the Labrador Sea, compensated for by more vigorous overflow circulation and northward expansion of MOW.

At the same time, UCDW Nd isotope signatures (monitored in the Drake Passage) show remarkably invariable  $\epsilon_{\text{Nd}} \approx -7.5$  between 39.2 and 27.2 kyr BP implying a strong contribution from Atlantic-sourced water masses. At the Tasmanian margin, consistently more radiogenic Nd isotope signatures indicate enhanced admixture of GNPIW. Such GNPIW expansion replaced reduced Atlantic-sourced Nd in the peak glacial ocean, similar to deep South Atlantic and Indian Ocean trends. The nature of our new Southern Ocean Nd isotope data in the context of previous work suggests the progressive evolution of mid-depth overturning cells in both, the Atlantic and Pacific Ocean reflected in the recordings of GNAIW and GNPIW in the Southern Ocean.

Remarkably, the transition into peak glacial conditions featured northward migrating ACC fronts paired with progressively reduced influence of UCDW near Tasmania. This is counterintuitive as a northward migration of ACC fronts was expected to result in a more dominant role of unradiogenic UCDW near Tasmania. The resulting Nd isotope gradient implies reduced mixing between ACC-bound and South Pacific water masses. If volumetrically relevant, the GNPIW export through the Tasman Sea occurred likely along the Campbell Plateau margin and may have been (partly) re-injected into the South Pacific via the DWBC east off New Zealand. On a larger scale, limited cross frontal mixing of water masses associated with the northern flank of the Pacific ACC paired with effective equatorward deflection off Chile could reduce the net admixture of radiogenic GNPIW into ACC-bound UCDW.

An interval of high resolution Nd isotope data coverage across Heinrich Stadial 3 between 32 and 30 kyr BP revealed that abrupt Nd isotope shifts occurred on decadal time scale. We integrated such abrupt events, characterised by “flushing” of the Tasman Sea with UCDW, in a global framework. A (southern) oceanic prelude to the actual North Atlantic Heinrich IRD event is indicated by the gradual expansion of GNPIW at the expense of GNAIW-spiked UCDW. Shoaling and/or reduction of NADW/GNAIW induced a chain of positive feedbacks leading to the North Atlantic IRD event. The positive feedback loop includes intrinsic oscillations of AMOC strength and/or ice sheet stability affecting the North Atlantic surface ocean, and alongside the atmosphere. Interhemispheric

signal propagation occurred likely through atmospheric teleconnections, expressed in SWW position/intensity and associated oceanic fronts dictating abrupt changes in UCDW-GNPIW mixing at the Tasmanian margin. The intrinsic feedback loop terminates through re-stabilisation of retreated Laurentide outlet glaciers allowing effective AMOC resumption (interstadial D/O state) which then supplies heat and moisture to slowly drive the system into the next D/O cycle.

**Declaration:** The work presented here was part of a collaborative multi-proxy investigation to which I contributed the Nd isotope and concentration data as discussed above. Some North Atlantic deep-sea coral and the coral crust Nd isotope data was kindly provided by Tina van de Flierdt and Kirsty C. Crocket. Laura F. Robinson and Jess F. Adkins provided sample material. Sophie K. Hines, Andrea Burke and Jess F. Adkins conducted the uranium-series work as indicated.

## **Chapter 6**

# **Holocene changes in Southern Ocean circulation in response to atmospheric forcing inferred from deep-sea corals**

## Abstract

The modern Southern Ocean is dominated by the dynamics associated with the circumpolar flow of the Antarctic Circumpolar Current (ACC). Southern Ocean water mass transformation and ACC dynamics are closely coupled to the Southern Hemisphere westerly winds (SWW) implying substantial turnover of key elements of the global climate system such as heat, freshwater and carbon. The current interglacial, namely the Holocene, can serve as a test ground to investigate the impact of small climatic changes on ocean circulation. We here use Nd isotopes from absolutely dated Drake Passage deep-sea corals from water depths currently bathed by Antarctic Intermediate Water (AAIW) and Upper Circumpolar Deep Water (UCDW).

Neodymium isotope results vary in total between  $\epsilon_{Nd} = -5.8 \pm 0.2$  and  $-8.4 \pm 0.2$ , far in excess of expected variation. Grouped into AAIW and UCDW density classes, our Nd isotope results reveal the different nature of these water masses during the Holocene. The AAIW record is characterised by a marked Nd isotope shift from  $\epsilon_{Nd} = -7.3 \pm 0.2$  to  $-5.9 \pm 0.2$  at 11.7 kyr BP and a gradual trend towards modern values thereafter. Our AAIW results show strong covariation with regional proxy data for temperature, SWW intensity/position and upwelling intensity. This leads us to conclude that our Nd isotope signal is intrinsically connected to SWW dynamics, inducing substantial early Holocene mixed layer deepening down to levels currently bathed by UCDW. Such deepening likely contributed to the early Holocene acceleration of atmospheric  $CO_2$  rise through enhanced air-sea gas exchange. The most pronounced feature of the Holocene mid-depth Nd isotope record is a marked peak at  $\sim 6.8$  kyr BP ( $\epsilon_{Nd} = -5.8 \pm 0.2$ ) indicating substantial expansion of Pacific water masses into the Southern Ocean. In covariation with equatorward SWW intensification and paralleled by northward Pacific heat flux, the mid-Holocene expansion of deep Pacific water masses into the Southern Ocean was likely associated with intensified Pacific overturning. The implied Southern Ocean stratification probably contributed to a contemporaneous drop in atmospheric  $CO_2$ , and to the accelerated rise thereafter.

## 6.1. Introduction

The transformation of water masses in the Southern Ocean is closely linked to Southern Hemisphere atmospheric forcing, and as such, sensitive to climate change currently expressed in changes of heat, freshwater and carbon budgets in response to global warming (e.g., Gille, 2002; Oke and England, 2003; Böning et al., 2008; Ito et al., 2010). Mechanistically, Southern Hemisphere warming is associated with a tendency towards a positive Southern Annular Mode (SAM) describing the poleward intensification of the Southern Hemisphere westerly winds (SWW) (Kushner et al., 2001; Lamy et al., 2010). Such poleward intensification has been linked with rising atmospheric air temperatures in Antarctica, in particular in West Antarctica (Turner et al., 2005; Marshall et al., 2006b), and is likely to cause observed enhanced upwelling of relatively warm CDW on the Antarctic shelves (e.g., Thoma et al., 2008). Heat supply to the Antarctic shelves, induced by upwelling of warm CDW sourced from the Antarctic Circumpolar Current (ACC), can lead to subsurface melting of buttressing ice shelves. This drives intensified glacier retreat, particularly pronounced at the West Antarctic Ice Sheet (WAIS) (Cook et al., 2005; Pritchard et al., 2012; Rignot et al., 2013). Moreover, a poleward intensification of the SWW induces an asymmetric response to Surface Ocean mixing and a stronger meridional component in otherwise pre-dominant zonal air flow (Sallée et al., 2008, 2010). Under a warming scenario these processes can act in a positive feedback loop, scaled down by oceanic uptake of excess greenhouse gases, and in particular excess (e.g., anthropogenic) CO<sub>2</sub> of which about 40% are transferred into the ocean's interior during Southern Ocean water mass transformation (Sabine et al., 2004). The interaction of upwelling deep waters degassing old carbon into the atmosphere and the uptake by formation of intermediate waters is, however, crucial for the net flux (Le Quéré et al., 2007; Lovenduski et al., 2008).

As the dynamics of Southern Ocean water mass transformation are closely linked to momentum and buoyancy forcing, a poleward intensification of the SWW could impose substantial alteration of Southern Ocean dynamics progressing into the global overturning circulation system (e.g., Rahmstorf and England, 1997; Oke and England, 2003; Sijp and England, 2009), and expressed in the interhemispheric re-distribution of heat (e.g., Seidov and Maslin, 2001; Stocker and Johnsen, 2003). The global overturning circulation is currently dominated by water mass formation in the North Atlantic where North Atlantic Deep Water (NADW) forms from warm and saline surface water masses in the North Atlantic marginal Seas (Gascard, 1978; Schlitzer et al., 1991; Lilly et al., 1999; Ronski and Budéus, 2005; Fig. 6.1). At depth, the southward export of NADW is balanced by northward flow of Antarctic Intermediate and Bottom Water (AAIW and AABW, respectively) organised in shallow and deep meridional overturning cells, respectively, and referred to as Atlantic Meridional Overturning Circulation (AMOC) (e.g., Lumpkin and Speer, 2007; Talley, 2013). In the Southern Ocean, NADW joins the zonal flow of the ACC where it mixes with old, nutrient-rich and oxygen-poor water masses from the Indian and Pacific Ocean, i.e. Pacific Deep Water (PDW) and Indian Deep Water (IDW) to form Circumpolar Deep Water (CDW) (Reid and Lynn, 1971; Callahan,

1972; Talley, 2013; Fig. 6.1). Due to the higher density of NADW joining the zonal CDW flow the deeper levels of the ACC are characterised by a NADW-induced salinity maximum, oxygen and nutrient minima, whereas PDW and IDW cause relative minima in oxygen and salinity paired with maxima in nutrient content at mid-depth. Therefore, CDW is consequently sub-divided into upper and lower CDW, i.e. UCDW and LCDW, respectively (Reid and Lynn, 1971; Callahan, 1972; Fig. 6.1). Wind-induced upwelling of CDW into the Southern Ocean mixed layer feeds into the formation of AAIW which is subducted into the ocean interior north of the Polar Front (Piola and Georgi, 1982; Naveira Garabato et al., 2009; Bostock et al., 2013). Water masses of higher density upwell predominantly south of the Polar Front (e.g., Marshall and Speer, 2012; Talley, 2013), thereby supplying heat for the Antarctic continent and salt for the brine-induced AABW formation on the Antarctic shelves (Orsi et al., 1999; Fig. 6.1). This leads to NADW/LCDW feeding pre-dominantly into AABW formation and UCDW pre-dominantly into AAIW formation (e.g., Marshall and Speer, 2012; Talley, 2013; Fig. 6.1).

It has been shown that the modern Atlantic-dominated system is sensible to freshwater fluxes (e.g., Keigwin et al., 1991; Manabe and Stouffer, 1995; Seidov et al., 2001; Rahmstorf, 2002; McManus et al., 2004). A freshwater-induced reduction of Atlantic overturning may be partly compensated for by intensified overturning and deepening of water mass formation in the North Pacific (e.g., Okazaki et al., 2010; Rae et al., 2014) requiring, however, glacial boundary conditions, i.e. a closed Bering Strait (e.g., Hu et al., 2012). In order to assess the significance of Southern Ocean dynamics in the global climate system and projected future change, it is desirable to study intervals with boundary conditions similar to modern, such as the current interglacial, i.e. the Holocene (11.7 kyr BP to present). Early work described the Holocene as a relatively stable interval compared to the glacial-deglacial climate perturbations (e.g., Dansgaard et al., 1993). Subsequent studies identified significant climate cyclicity in analogy to millennial-scale glacial periodicity (Bond et al., 1997, 2001; Sarnthein et al., 2003). Although the postglacial sea-level rise induced flooding of the Bering Strait already ~13,000 years ago (Elias et al., 1997), about half of the postglacial sea-level rise and ice sheet decay occurred during the early to mid-Holocene (Fairbanks, 1987; Bard et al., 1996). This is believed to have influenced the formation regions of water masses feeding into NADW (Hillaire-Marcel et al., 2001; Solignac et al., 2004; Telesiński et al., 2014).

The Holocene Southern Ocean was exposed to substantial changes in the position/intensity of the SWW, imposing variability on mid-latitude air and sea surface temperatures associated with changes of the hydrological cycle and Antarctic sea ice extent (e.g., Lamy et al., 2010; Shevenell et al., 2011; Mulvaney et al., 2012). But the implications of such changes for processes of Holocene AAIW formation and the structure of the Holocene Southern Ocean water column are poorly constrained. We therefore target both branches of Southern Ocean water mass transformation, i.e. the changes in deep circulation feeding the mixed layer through upwelling and the formation of intermediate waters from such mixed layer water masses.

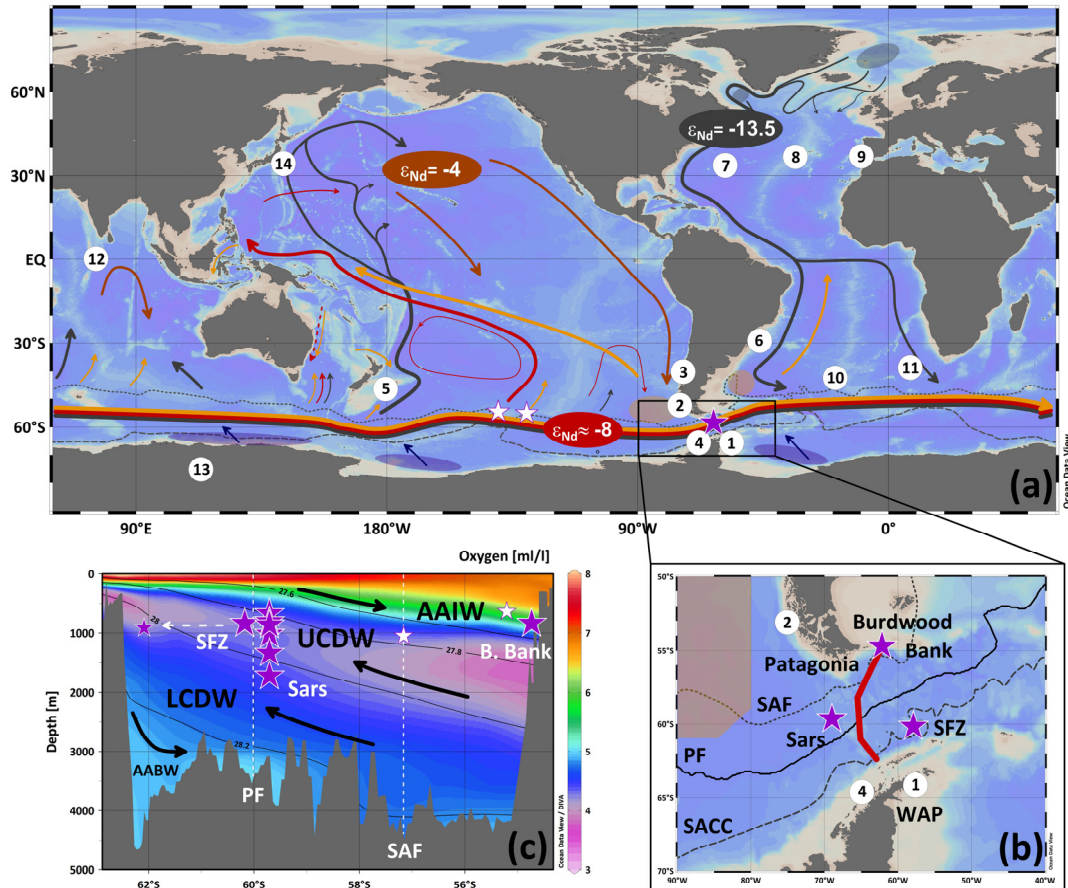


**Figure 6.1:** (a) Global map of simplified sub-surface ocean circulation (after Piola and Georgi, 1982; Talley and McCartney, 1982; Reid, 1989, 1994, 1997; McCartney, 1992; Mantyla and Reid, 1995; Orsi et al., 1999; Sokolov and Rintoul, 2000; Macdonald et al., 2009; Kawabe and Fujio, 2010; Bostock et al., 2013). Dark grey: North Atlantic Deep Water (NADW) and Lower Circumpolar Deep Water (LCDW); red: Upper Circumpolar Deep Water (UCDW); Red-brown: Pacific Deep Water (PDW) and Indian Deep Water (IDW); yellow: Antarctic Intermediate Water (AAIW). Hatched areas indicate main formation regions for NADW (grey), AABW (Antarctic Bottom Water; dark blue) and AAIW (yellow). Note that AABW fills the abyss of all major ocean basins (not shown here; see Orsi et al., 1999 and references therein) and that AAIW is also formed along the Antarctic Circumpolar Current (ACC) in all ocean basins (e.g., Piola and Georgi, 1982; Bostock et al., 2013). Stippled and dashed grey lines in the Southern Ocean indicate Subantarctic Front (SAF) and the southern ACC front (SACC), respectively (Orsi et al., 1995). Global seawater Nd isotope systematics represented by NADW ( $\epsilon_{Nd} \approx -13.5$ ; Piepgras and Wasserburg, 1987), PDW ( $\epsilon_{Nd} \approx -4$ ; Amakawa et al., 2009) and UCDW ( $\epsilon_{Nd} \approx -8$ ; Stichel et al., 2012; Chapter 3). Purple star with white line: deep-sea coral sampling locations in the Drake Passage (Table 6.1). White star with purple line: South Pacific corals (Table 6.1). White dots denote locations of data used in Figures 6.3 and 6.5. (1) James Ross Island deuterium ice core record (Mulvaney et al., 2012). (2) Accumulation rate of terrestrial organic carbon in Patagonian Fjord core TM1 (53°S; Lamy et al., 2010). (3) Southeast Pacific alkenone sea surface temperature (SST) (ODP 1233; Kaiser et al., 2005) and trace metal data from ODP sites 1233 (Mn) and 1234 (Re) (Muratli et al., 2010). (4) TEX<sub>86</sub> SST record from ODP 1098 located on the West Antarctic Peninsula (WAP) shelf (Shevenell et al., 2011). (5) Southwest Pacific alkenone SST record from core MD97-2120 (Pahnke and Sachs, 2006). (6) AAIW Nd isotope record from Brazilian margin core KNR159-5-36GGC (1238 m water depth) (Pahnke et al., 2008). (7) Bermuda Rise <sup>231</sup>Pa/<sup>230</sup>Th record from core OCE326-GGC5 (4550 m water depth) and Nd isotope record from core OCE326-GGC6 (4541 m water depth). (8) Mid-depth (2150 m) central North Atlantic <sup>231</sup>Pa/<sup>230</sup>Th record from core MD95-2037 (Gherardi et al., 2009). (9) Deep Iberian Margin (3135 m) <sup>231</sup>Pa/<sup>230</sup>Th record from core SU81-18 (Gherardi et al., 2005). (10) Deep South Atlantic (3770 m) Nd isotope data from core MD07-3076 (Skinner et al., 2013). (11) Deep Cape Basin (4981 m) Nd isotope data from core TNO57-21 (Piotrowski et al., 2012). (12) Deep Indian Ocean (3800 m) Nd isotope record from Chagos Trench core SK129-CR2 (Piotrowski et al., 2009). (13) EPICA Dome C carbon dioxide record (Monnin et al., 2001, 2004). (14) Northwest Pacific alkenone SST record from spliced cores KR02-06 St.A MC1, KR02-06 St.A GC and MD01-2421 (Isono et al., 2009). (b) Detailed map of Drake Passage coral sampling locations at Burdwood Bank, Sars seamount and Shackleton Fracture Zone (SFZ).

---

PF: Polar Front, other fronts and literature sample locations as in (a). WAP: West Antarctic Peninsula. Yellow hatched area indicates main AAIW formation area (see Bostock et al., 2013). Red line demarks oxygen section (WOA13: Garcia et al., 2013) shown in (c) where purple stars represent vertical distribution of sample locations across the Drake Passage. Thin black lines indicate surfaces of neutral density anomaly  $\gamma^n$  (Jackett and McDougall, 1997; in  $\text{kg/m}^3$ ). The neutral density at SFZ coral sampling depth of  $\sim 820$  m is  $\gamma^n \approx 28.05 \text{ kg/m}^3$ . The small purple star indicates the SFZ position in the section with respect to the density distribution relative to the PF. Similarly, South Pacific samples were translated into Drake Passage section density structure relative to the mean frontal positions (white stars with purple line). White stippled lines indicate mean positions of the SAF and PF (Orsi et al., 1995) as plotted in (b). Black arrows indicate the meridional components of Southern Ocean circulation, i.e. the direction of upwelling deep waters and downwelling of intermediate and bottom waters. Note the oxygen minimum in UCDW. Figures generated with ODV software (Schlitzer, 2012).

---

In order to reconstruct past water mass mixing, we here use the isotopes of rare earth element neodymium (Nd), shown to be a suitable proxy to trace water masses (von Blanckenburg, 1999) and mixing, e.g., in the Southern Ocean (Carter et al., 2012; Stichel et al., 2012; Garcia-Solsona et al., 2014; Basak et al., 2015). Water masses acquire their Nd isotope signature mainly in their source region which is in the ocean interior pre-dominantly altered by conservative mixing (Frank, 2002; Goldstein and Hemming, 2003; Carter et al., 2012). On a global scale, this leads to two source regions dominating the oceanic Nd distribution: the North Atlantic where NADW forms with  $\epsilon_{\text{Nd}} \approx -13.5$  (Piepgras and Wasserburg, 1987; Fig. 6.1) and the North Pacific where a volcanogenic signature of  $\epsilon_{\text{Nd}} \approx -4$  is imprinted on PDW (Amakawa et al., 2009; Fig. 6.1). The epsilon notation refers to the Nd isotopic composition, defined as  $\epsilon_{\text{Nd}} = ((^{143}\text{Nd}/^{144}\text{Nd}_{\text{sample}})/(^{143}\text{Nd}/^{144}\text{Nd}_{\text{CHUR}}) - 1) \times 10,000$  where CHUR is the chondritic uniform reservoir (Jacobsen and Wasserburg, 1980). Mixing of PDW and NADW in the Southern Ocean circumpolar flow leads to intermediate values of  $\epsilon_{\text{Nd}} = -7.6 \pm 0.2$  to  $\epsilon_{\text{Nd}} = -8.6 \pm 0.2$  for AAIW, UCDW and LCDW in the Drake Passage (Stichel et al., 2012; Chapter 3; Fig. 6.1). Despite strong isoneutral and dianeutral mixing in the lee of topography (St. Laurent et al., 2012; Thompson and Sallée, 2012; Watson et al., 2013), most tracers such as oxygen concentration resolve different Southern Ocean water masses in the Drake Passage (Fig. 6.1) and it remains unclear why Nd isotopes show relatively homogenous vertical distribution (see Chapter 3). This may simply result from Drake Passage water mass mixing incidentally involving Nd drawn to similar proportions from both ocean basins at respective density levels (cf. Sudre et al., 2011) as Nd isotope heterogeneity is resolved in other Southern Ocean locations (Carter et al., 2012; Stichel et al., 2012; Garcia-Solsona et al., 2014; Rickli et al., 2014; Basak et al., 2015).

We will therefore use our new Holocene Nd isotope data paired with existing radiocarbon data from absolutely dated Southern Ocean deep-sea corals to explore the history of water masses in the Drake Passage and evaluate the implications for the global overturning circulation.

## 6.2. Material and methods

### 6.2.1 Deep-sea corals samples

Deep-sea corals from the Southern Ocean have been collected from two locations. In the Drake Passage, a total of 24 specimens was raised by dredging and trawling during cruise NBP0805 from Burdwood Bank, Sars seamount and the Shackleton Fracture Zone (SFZ). Of the 24 individual corals, 23 are *D. dianthus* and one *B. malouinensis*. The depth interval of 695 to 1750 m covered by corals is pre-dominantly bathed by AAIW and UCDW (Table 6.1, Fig. 6.1). Due to the poleward steepening of isoneutrals samples from 695 m at Sars seamount are bathed by UCDW ( $27.6 \text{ kg/m}^3 < \gamma^n < 28.0 \text{ kg/m}^3$ ,  $\text{O}_2 \approx 4.2 \text{ ml/l}$ ; Sudre et al., 2011), whereas corals collected from 816 m water depth at Burdwood Bank are currently bathed by AAIW ( $27.35 \text{ kg/m}^3 < \gamma^n < 27.6 \text{ kg/m}^3$ ,  $\text{O}_2 \approx 6.5 \text{ ml/l}$ ; Sudre et al., 2011; Fig. 6.1). Additional three *D. dianthus* from the Smithsonian collection were processed for this study. They were collected by trawling during USAP expeditions 15 and 16 from average water depths of 1034 m ( $\sim 55^\circ\text{S}/130^\circ\text{W}$ ) and 465 m ( $\sim 54^\circ\text{S}/140^\circ\text{W}$ ) in the Pacific sector of the Southern Ocean (Table 6.1, Fig. 6.1). As such, these sampling locations are near the mean position of the Subantarctic Front (SAF) and currently bathed by AAIW and UCDW, respectively (Fig. 6.1).

### 6.2.2. Sample preparation and analytical procedures

The majority of Nd isotope analyses was carried out in the MAGIC laboratories at Imperial College London, following the approach outlined in Chapter 2. In brief, physically and chemically cleaned deep-sea coral samples were subjected to iron (Fe) co-precipitation to concentrate trace metals, to then separate uranium (U) and thorium (Th) for U-series dating (Burke and Robinson, 2012). The Nd fraction is collected during U-Th separation for purification during two-step column chemistry for TIMS Nd isotope analyses as  $\text{NdO}^+$ . Reported Nd concentration data was generated by doping with a  $^{150}\text{Nd}$  spike solution before Nd separation, and are hence minimum values not accounting for Nd loss during Fe co-precipitation and U-Th separation (Chapters 2 and 3).

Over a period of 26 months 5 and 15 ng loads of pure JNdi-1 were analysed ( $^{143}\text{Nd}/^{144}\text{Nd} = 0.512105 \pm 0.000009$ , 2SD,  $n = 110$ ) to monitor instrumental offset and normalise mass bias corrected  $^{143}\text{Nd}/^{144}\text{Nd}$  ratios of samples to the reference ratio of  $^{143}\text{Nd}/^{144}\text{Nd} = 0.512115 \pm 0.000007$  (Tanaka et al., 2000). BCR-2 rock reference material was processed with every batch of chemistry and yielded  $^{143}\text{Nd}/^{144}\text{Nd}$  ratios of  $0.512637 \pm 0.000011$  ( $2 \sigma$  SD;  $n = 32$ ) on loads of 10 and 30 ng Nd. A similar precision was obtained from replicate analyses of 10 and 30 ng Nd loads of our in-house coral reference material ( $^{143}\text{Nd}/^{144}\text{Nd} = 0.512336 \pm 0.000009$ ;  $n = 23$ ). Full procedural blanks of combined U, Th and Nd separation from aragonitic matrix ranged from 2 to 27 pg Nd ( $n = 20$ ). The Nd blank of the Nd chemistry alone ranged from 1 to 17 pg ( $n = 10$ ).

Neodymium isotope analyses of the South Pacific samples were carried out at Lamont-Doherty Earth Observatory (Table 6.1). These samples were subjected to similar physical and chemical cleaning procedures as outlined by van de Flierdt et al. (2006b, 2010), and subsequently

processed through anion exchange chemistry for U-series dating (Robinson et al., 2005, 2007; van de Flierdt et al., 2006b). In brief, after Fe co-precipitation the rare earth elements were separated with TRU spec<sup>®</sup> resin and Nd was subsequently isolated by  $\alpha$ -HIBA and cation exchange resin. Samples were loaded with Si gel for NdO<sup>+</sup> analyses on a VG Sector 54-30 thermal ionisation mass spectrometer using dynamic multicollection. Mass bias was corrected for by using  $^{146}\text{Nd}/^{144}\text{Nd} = 0.7219$ . All samples were and instrumental offset was corrected for by normalising to La Jolla nominal value of  $^{143}\text{Nd}/^{144}\text{Nd} = 0.511859 \pm 0.000007$  (Lugmair and Carlson, 1978). Repeated analyses of 5 and 35 ng La Jolla Nd standards resulted in average  $^{143}\text{Nd}/^{144}\text{Nd} = 0.511858 \pm 0.000016$  ( $n = 5$ ) and  $^{143}\text{Nd}/^{144}\text{Nd} = 0.511856 \pm 0.000020$  ( $n = 8$ ) for two analytical sessions applied as  $2\sigma$  external uncertainty. The internal  $2\sigma$  error is reported when the  $2\sigma$  external uncertainty was smaller (Table 6.1).

### 6.3. Results

Holocene Drake Passage Nd isotope results range from  $\epsilon_{\text{Nd}} = -5.8 \pm 0.2$  to  $\epsilon_{\text{Nd}} = -8.4 \pm 0.2$  over the past 11.8 kyr BP (i.e. thousand years before present, where present is 1950). This range includes three modern individuals from Chapter 3 omitting the result for *B. malouinensis* as it does not reliably record modern seawater (Chapter 3, Table 6.1). We grouped the results according to the neutral density ( $\gamma^n$ ) of the water depth they were collected from. Potential depth-dependent variability is subject to discussion below. Constructed time series of AAIW (Burdwood Bank) and UCDW (Sars seamount and Shackleton Fracture Zone; Table 6.1; Fig. 6.1) are presented in Figure 6.2 and are complemented by upstream samples from the subpolar South Pacific. The first observation is that there are pronounced trends in both, AAIW and UCDW history, throughout the Holocene. Starting with AAIW (water of  $\gamma^n < 27.6 \text{ kg/m}^3$ ), the onset of the Holocene features a significant Nd isotope shift from  $\epsilon_{\text{Nd}} = -7.3 \pm 0.2$  to  $\epsilon_{\text{Nd}} = -5.9 \pm 0.2$  followed by a gradual trend towards modern values (Table 6.1; Fig. 6.2). In contrast, the UCDW level ( $\gamma^n > 27.6 \text{ kg/m}^3$ ) recorded minor fluctuations around an average value of  $\epsilon_{\text{Nd}} \approx -7.8$  in the early Holocene, including two samples collected from locations close to the modern interface to LCDW  $\gamma^n > 28.0 \text{ kg/m}^3$  (Sudre et al., 2011; Table 6.1; Fig. 6.2). Large Nd isotope variability at the UCDW level is then evident during the following mid-Holocene. Maximum  $\epsilon_{\text{Nd}}$  values of  $-5.8 \pm 0.2$  are reached at 6.8 kyr BP followed by a decline to less radiogenic values between  $\epsilon_{\text{Nd}} = -7.4 \pm 0.2$  and  $\epsilon_{\text{Nd}} = -8.2 \pm 0.2$  during the late Holocene (Table 6.1; Fig. 6.2). It should be noted that rarely the exact same time interval is sampled by the corals from the two different density levels.

Table 6.1: Holocene deep-sea coral data.

| Coral ID  | Water depth (m) | Latitude | Longitude | Location | Species                | $^{238}\text{U}$ (ppb) | $^{232}\text{Th}$ (pg/g) | $^{234}\text{U}$ (ppb) | Age (kyr BP) | $^{235}\text{U}/^{238}\text{U}$ (ppb) | $^{143}\text{Nd}/^{144}\text{Nd}^b$ | 2SE   | $\epsilon_{\text{Nd}}$ <sup>c</sup> | 2SE      | $^{252}\text{D}$ (ng/g) | Nd (ng/g) | 2SE (ep) <sup>d</sup> |      |
|---|-----------------|----------|-----------|----------|------------------------|------------------------|--------------------------|------------------------|--------------|---------------------------------------|-------------------------------------|-------|-------------------------------------|----------|-------------------------|-----------|-----------------------|------|
| <i>UCDW (<math>V^0 &gt; 27.6 \text{ kg/m}^3</math>)</i> |                 |          |           |          |                        |                        |                          |                        |              |                                       |                                     |       |                                     |          |                         |           |                       |      |
| 441W ( $V^0 < 27.6 \text{ kg/m}^3$ )                    |                 |          |           |          |                        |                        |                          |                        |              |                                       |                                     |       |                                     |          |                         |           |                       |      |
| NBP0805-TB04-Dp-A-3*                                    | 816             | -54.734  | -62.216   | B. Bank  | <i>D. dianthus</i>     | 3088                   | 10                       | 43                     | 3            | 146.8                                 | 0.6                                 | 0.01  | 0.01                                | 0.512247 | 0.000006                | -7.63     | 0.11                  | 0.21 |
| NBP0805-TB04-Modern Flabellum*                          | 816             | -54.734  | -62.216   | B. Bank  | <i>F. curvatum</i>     | 4893                   | 15                       | 81                     | 3            | 146.5                                 | 0.6                                 | 0.01  | 0.01                                | 0.512248 | 0.000004                | -7.61     | 0.07                  | 0.21 |
| NBP0805-TB04-BigBeautyA*                                | 816             | -54.734  | -62.216   | B. Bank  | <i>D. dianthus</i>     | 4539                   | 14                       | 117                    | 2            | 145.9                                 | 0.6                                 | 0.41  | 0.01                                | 0.512248 | 0.000008                | -7.60     | 0.15                  | 0.21 |
| NBP0805-TB04-BigBeautyA Nd repl.*                       | 816             | -54.734  | -62.216   | B. Bank  | <i>D. dianthus</i>     |                        |                          |                        |              |                                       |                                     |       |                                     | 0.512252 | 0.000017                | -7.53     | 0.23                  | 0.23 |
| NBP0805-TB04-Dn-A-12                                    | 816             | -54.734  | -62.216   | B. Bank  | <i>D. dianthus</i>     | 3126                   | 10                       | 3237                   | 13           | 148.1                                 | 0.7                                 | 3.54  | 0.40                                | 0.512302 | 0.000017                | -6.56     | 0.13                  | 0.21 |
| NBP0805-TB04-Dn-A-11                                    | 816             | -54.734  | -62.216   | B. Bank  | <i>D. dianthus</i>     | 3646                   | 12                       | 784                    | 3            | 147.2                                 | 0.7                                 | 4.58  | 0.08                                | 0.512280 | 0.000003                | -6.98     | 0.07                  | 0.21 |
| NBP0805-TB04-Dn-A-13                                    | 816             | -54.734  | -62.216   | B. Bank  | <i>D. dianthus</i>     | 3921                   | 13                       | 175                    | 3            | 147.0                                 | 0.7                                 | 5.82  | 0.02                                | 0.512310 | 0.000007                | -6.40     | 0.13                  | 0.21 |
| NBP0805-TB04-Dn-B-6                                     | 816             | -54.734  | -62.216   | B. Bank  | <i>D. dianthus</i>     | 3744                   | 12                       | 186                    | 1            | 150.5                                 | 0.7                                 | 6.41  | 0.02                                | 0.512307 | 0.000004                | -6.46     | 0.07                  | 0.21 |
| NBP0805-TB04-Dn-B-4                                     | 816             | -54.734  | -62.216   | B. Bank  | <i>D. dianthus</i>     | 3920                   | 13                       | 629                    | 3            | 148.1                                 | 0.7                                 | 11.72 | 0.07                                | 0.512338 | 0.000006                | -5.86     | 0.11                  | 0.21 |
| NBP0805-TB04-Dn-E-3                                     | 816             | -54.734  | -62.216   | B. Bank  | <i>D. dianthus</i>     | 4727                   | 16                       | 181                    | 6            | 143.2                                 | 0.7                                 | 11.88 | 0.03                                | 0.512264 | 0.000007                | -7.30     | 0.13                  | 0.21 |
| <i>UCDW (<math>V^0 &gt; 27.6 \text{ kg/m}^3</math>)</i> |                 |          |           |          |                        |                        |                          |                        |              |                                       |                                     |       |                                     |          |                         |           |                       |      |
| NBP0805-DR40-Dc-A-1                                     | 1323            | -59.732  | -68.933   | Sars     | <i>D. dianthus</i>     | 3680                   | 11                       | 252                    | 2            | 145.1                                 | 0.7                                 | 1.08  | 0.03                                | 0.512219 | 0.000007                | -8.17     | 0.14                  | 0.21 |
| NBP0805-DR35-Dc-A-1                                     | 695             | -59.723  | -68.881   | Sars     | <i>D. dianthus</i>     | 3723                   | 14                       | 120                    | 2            | 146.0                                 | 0.8                                 | 1.65  | 0.01                                | 0.512250 | 0.000007                | -7.56     | 0.13                  | 0.21 |
| NBP0805-DR35-Dc-A-1 full repl.                          | 695             | -59.723  | -68.881   | Sars     | <i>D. dianthus</i>     | 4163                   | 27                       | 159                    | 1            | 145.8                                 | 1.3                                 | 1.69  | 0.02                                | 0.512260 | 0.000007                | -7.38     | 0.15                  | 0.21 |
| NBP0805-DR34-Dc-A-2                                     | 869             | -59.733  | -68.743   | Sars     | <i>D. dianthus</i>     | 4089                   | 22                       | 233                    | 1            | 149.4                                 | 1.1                                 | 5.76  | 0.03                                | 0.512315 | 0.000004                | -6.30     | 0.08                  | 0.21 |
| NBP0805-DR34-Dc-A-1                                     | 869             | -59.733  | -68.881   | Sars     | <i>D. dianthus</i>     | 3875                   | 12                       | 313                    | 1            | 150.9                                 | 0.7                                 | 6.80  | 0.03                                | 0.512341 | 0.000004                | -5.79     | 0.09                  | 0.21 |
| NBP0805-DR35-Dc-C-2                                     | 695             | -59.723  | -68.881   | Sars     | <i>D. dianthus</i>     | 4191                   | 19                       | 184                    | 1            | 153.3                                 | 1.0                                 | 7.64  | 0.03                                | 0.512269 | 0.000006                | -7.19     | 0.11                  | 0.21 |
| NBP0805-DR35-Dc-D-4                                     | 695             | -59.723  | -68.881   | Sars     | <i>D. dianthus</i>     | 4062                   | 13                       | 224                    | 1            | 150.5                                 | 0.7                                 | 10.08 | 0.03                                | 0.512250 | 0.000006                | -7.56     | 0.12                  | 0.21 |
| NBP0805-DR35-Dc-D-5                                     | 695             | -59.723  | -68.881   | Sars     | <i>D. dianthus</i>     | 3918                   | 14                       | 323                    | 4            | 150.6                                 | 0.8                                 | 10.20 | 0.04                                | 0.512250 | 0.000004                | -7.57     | 0.08                  | 0.21 |
| NBP0805-DR36-Dc-A-1                                     | 1750            | -59.707  | -69.008   | Sars     | <i>D. dianthus</i>     | 4057                   | 13                       | 207                    | 2            | 150.5                                 | 0.7                                 | 10.24 | 0.03                                | 0.512217 | 0.000005                | -8.21     | 0.09                  | 0.21 |
| NBP0805-DR35-Dc-D-1                                     | 695             | -59.723  | -68.881   | Sars     | <i>D. dianthus</i>     | 4506                   | 16                       | 157                    | 8            | 149.3                                 | 0.8                                 | 11.06 | 0.03                                | 0.512245 | 0.000008                | -7.66     | 0.15                  | 0.21 |
| NBP0805-DR35-Dc-D-3                                     | 695             | -59.723  | -68.881   | Sars     | <i>D. dianthus</i>     | 4312                   | 14                       | 226                    | 8            | 148.6                                 | 0.7                                 | 11.08 | 0.03                                | 0.512245 | 0.000004                | -7.67     | 0.09                  | 0.21 |
| NBP0805-DR35-Dc-B-1a                                    | 695             | -59.723  | -68.881   | Sars     | <i>D. dianthus</i>     | 5852                   | 21                       | 335                    | 2            | 147.8                                 | 0.8                                 | 11.32 | 0.04                                | 0.512216 | 0.000005                | -8.24     | 0.10                  | 0.21 |
| NBP0805-DR35-Dc-A-2c                                    | 695             | -59.723  | -68.881   | Sars     | <i>D. dianthus</i>     | 3887                   | 14                       | 551                    | 2            | 149.9                                 | 0.8                                 | 11.31 | 0.06                                | 0.512257 | 0.000005                | -7.79     | 0.09                  | 0.21 |
| NBP0805-DR35-Dc-B-1b full repl.                         | 695             | -59.723  | -68.881   | Sars     | <i>D. dianthus</i>     | 4713                   | 16                       | 393                    | 5            | 147.3                                 | 0.7                                 | 11.19 | 0.04                                | 0.512239 | 0.000005                | -7.43     | 0.09                  | 0.21 |
| NBP0805-DR35-Dc-C-1b chem. repl.                        | 695             | -59.723  | -68.881   | Sars     | <i>D. dianthus</i>     | 4259                   | 14                       | 302                    | 2            | 148.3                                 | 0.7                                 | 11.35 | 0.04                                | 0.512247 | 0.000005                | -7.62     | 0.09                  | 0.21 |
| NBP0805-DR35-Dc-C-1b                                    | 695             | -59.723  | -68.881   | Sars     | <i>D. dianthus</i>     | 4427                   | 16                       | 304                    | 1            | 147.2                                 | 0.8                                 | 11.40 | 0.04                                | 0.512247 | 0.000005                | -7.62     | 0.09                  | 0.21 |
| NBP0805-DR39-Dc-A-1                                     | 798             | -59.729  | -68.901   | Sars     | <i>D. dianthus</i>     | 6545                   | 27                       | 1040                   | 4            | 147.3                                 | 0.9                                 | 11.58 | 0.07                                | 0.512234 | 0.000006                | -7.89     | 0.12                  | 0.21 |
| NBP0805-DR38-Dc-A-1                                     | 978             | -59.743  | -68.898   | Sars     | <i>D. dianthus</i>     | 6026                   | 22                       | 916                    | 3            | 146.2                                 | 0.8                                 | 11.55 | 0.07                                | 0.512218 | 0.000005                | -8.20     | 0.09                  | 0.21 |
| NBP0805-DR35-Dc-E-1                                     | 695             | -59.723  | -68.881   | Sars     | <i>D. dianthus</i>     | 4234                   | 14                       | 788                    | 3            | 150.4                                 | 0.8                                 | 11.60 | 0.08                                | 0.512245 | 0.000005                | -7.66     | 0.10                  | 0.21 |
| NBP0805-DR35-Dc-E-1 chem. repl.                         | 695             | -59.723  | -68.881   | Sars     | <i>D. dianthus</i>     | 4949                   | 17                       | 650                    | 2            | 147.3                                 | 0.8                                 | 11.64 | 0.06                                | 0.512227 | 0.000009                | -8.02     | 0.18                  | 0.21 |
| NBP0805-DR35-Dc-E-1 Nd repl.                            | 695             | -59.723  | -68.881   | Sars     | <i>D. dianthus</i>     |                        |                          |                        |              |                                       |                                     |       |                                     | 0.512248 | 0.000007                | -7.61     | 0.13                  | 0.21 |
| NBP0805-DR23-Dc-A-7                                     | 819             | -60.182  | -57.834   | SFZ      | <i>D. dianthus</i>     | 4183                   | 14                       | 603                    | 2            | 149.1                                 | 0.7                                 | 11.85 | 0.06                                | 0.512208 | 0.000004                | -8.39     | 0.08                  | 0.21 |
| <i>Balanophyllia malouinensis</i>                       |                 |          |           |          |                        |                        |                          |                        |              |                                       |                                     |       |                                     |          |                         |           |                       |      |
| NBP1103-DH16-Bc-9                                       | 1418.5          | -54.808  | -62.119   | B. Bank  | <i>B. malouinensis</i> | 3748                   | 8                        | 2149                   | 9            | 143.6                                 | 0.4                                 | 11.73 | 0.45                                | 0.512277 | 0.000005                | -7.04     | 0.09                  | 0.21 |
| <i>South Pacific</i>                                    |                 |          |           |          |                        |                        |                          |                        |              |                                       |                                     |       |                                     |          |                         |           |                       |      |
| 47402   | 465             | -53.933  | -140.300  | S Pac    | <i>D. dianthus</i>     | 3879                   | 1                        | 245                    | 7            | 147.9                                 | 0.6                                 | 1.38  | 0.08                                | 0.512297 | 0.000022                | -6.65     | 0.86                  | 0.36 |
| 47406A  | 1034            | -54.842  | -129.783  | S Pac    | <i>D. dianthus</i>     | 3657                   | 1                        | 427                    | 6            | 150.1                                 | 0.5                                 | 2.83  | 0.15                                | 0.512236 | 0.000008                | -7.84     | 0.32                  | 0.36 |
| 47406B  | 1034            | -54.842  | -129.783  | S Pac    | <i>D. dianthus</i>     | 3864                   | 1                        | 209                    | 5            | 149.3                                 | 0.7                                 | 7.35  | 0.10                                | 0.512266 | 0.000009                | -7.25     | 0.34                  | 0.36 |

(a) 2SE is the analytical 2 $\sigma$  standard error.(b)  $^{143}\text{Nd}/^{144}\text{Nd}$  ratios were corrected for the offset of the measured  $^{143}\text{Nd}/^{144}\text{Nd}$  ratio of 0.512105  $\pm$  0.000009 ( $n = 110$ ) from the published value of 0.512115  $\pm$  0.000007 (Tanaka et al., 2000).(c)  $\epsilon_{\text{Nd}}$  was calculated using the present day CHUR value of  $^{143}\text{Nd}/^{144}\text{Nd} = 0.512638$  (Jacobsen and Wasserburg, 1980).(d) 2SD refers to the 2 $\sigma$  standard deviation derived from the long-term reproducibility of BCR-2 standards (see text). If the internal 2 $\sigma$  SE was larger than the external one, the internal error is reported.(e) 2SE (ep) is the propagated 2  $\sigma$  standard error of Nd concentrations determined by isotope dilution.

**Table 6.1:** Neodymium isotope and concentration results of deep-sea corals used for this study grouped by modern water mass and listed by their U-series age, which is expressed in thousand years before present (i.e. kyr BP where BP = 1950) (Burke and Robinson, 2012). Water depth is the depth of sample collection.

The South Pacific corals have been processed through different analytical procedures at LDEO (see section 6.2.2 and Chapter 5). Remaining samples were processed at Imperial College London and include minimum Nd concentration data (see Chapter 2). ‘Nd’ refers to the Nd concentration in the sample after co-precipitation and anion exchange chromatography for U-Series dating. Samples denoted ‘Nd repl.’ are re-sampled specimens processed for Nd isotope analyses only, ‘chem. repl.’ indicates samples processed through combined U-Th-Nd chemistry (Chapter 2) from poorly homogenised splits of the same sample and ‘full repl.’ denotes re-sampled coral processed through combined U-Th-Nd chemistry. Samples with asterisk are modern specimens from Chapter 3. *Balanophyllia malouinensis* listed individually as modern calibration revealed that this species is not a reliable recorder of ambient seawater (Chapter 3).

## 6.4. Discussion

### 6.4.1. Significance of the neodymium isotope signal recorded in deep-sea corals

It has been shown in Chapter 3 that the intra-skeletal Nd of aragonitic deep-sea corals is predominantly derived from seawater. We therefore aim to evaluate the nature of the recorded seawater signal with respect to changes in input, boundary exchange and water mass mixing ultimately acting to set the Nd isotope signature of seawater (e.g., Frank, 2002; Goldstein and Hemming; Lacan and Jeandel, 2005a). Figure 6.2 highlights that the majority of Holocene Southern Ocean Nd isotope signatures extracted from deep-sea corals plot outside the range of modern ACC seawater Nd isotopic composition, i.e. towards more radiogenic values. This result seems at odds with the common notion of relative water mass (and Nd isotope) stability throughout the Holocene (e.g., McManus et al., 2004; Piotrowski et al., 2004; Pahnke et al., 2008; Roberts et al., 2010). Therefore, we will first explore whether changes towards more radiogenic isotopes in AAIW and UCDW could be inflicted by the nearby land masses of Patagonia and the West Antarctic Peninsula (WAP) (volcanogenic rocks with  $\epsilon_{Nd} > \sim -5$ ; Hegner et al., 2007; Noble et al., 2012 and references therein).

In the North Atlantic, recent work indicates that ice-rafted detritus (IRD) release from drifting ice can cause Nd isotope staining of underlying water masses (Roberts and Piotrowski, 2015). While Patagonia is largely deglaciated during the Holocene (Sugden et al., 2009), the nearby WAP could supply IRD. However, the major iceberg route does not cross our sample locations, but enters the ACC downstream (Stuart and Long, 2011). Moreover, considering the high throughput of ACC flow (e.g., Cunningham et al., 2003) it may be speculated that armadas of icebergs would be required in order to release sufficient IRD and to significantly stain such vigorous water column. This renders local IRD input a highly unlikely source.

Another pathway for supplying continental Nd to the ocean is the input of dust (e.g., Tachikawa et al., 1999), even though its impact on the deeper water column seems limited (e.g., Greaves et al., 1999; Stichel et al., 2015). Nevertheless, dust has been inferred as a significant source of terrestrial input to the Scotia Sea (e.g., Weber et al., 2012). Comparison of our Nd isotope time series with magnetic susceptibility (MS) data from core MD07-3133, a recorder of the ferromagnetic

mineral input to the Scotia Sea, reveals a lack of correlation, rendering major dust influence unlikely (Fig. 6.2).

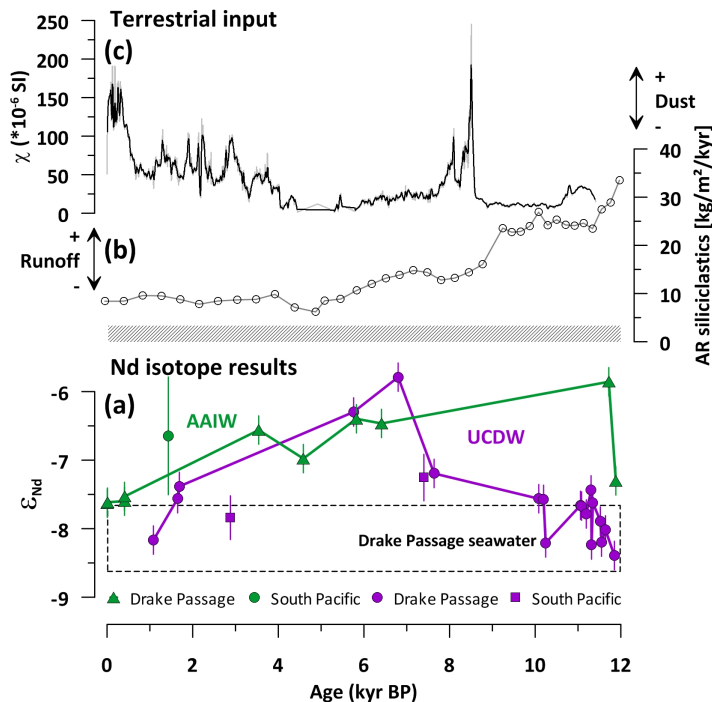


**Figure 6.2:** (a) Time series of Nd isotope results grouped by density class of seawater bathing the respective sampling site. Separation by isoneutral  $\gamma^n = 27.6 \text{ kg/m}^3$  (Sudre et al., 2011) translates roughly into separation between AAIW and underlying UCDW (Fig. 6.1). Subpolar South Pacific samples from same density class plotted separately. Modern Drake Passage seawater and coral samples (AAIW) from Chapter 3. Note that only one sample from SFZ contributes to the Drake Passage density class of  $\gamma^n > 27.6 \text{ kg/m}^3$ . (b) Accumulation rate of siliciclastic material at site TM1 driven by fluvial runoff from Patagonia (Lamy et al., 2010). (c) Magnetic susceptibility record from Scotia Sea core MD07-3134 serving as a proxy for (pre-dominant) dust input (Weber et al., 2012).

Freshwater runoff is another source considered to contribute in significant amounts to the marine Nd budget, despite the fact that most dissolved riverine Nd is scavenged upon mixing with seawater (Frank, 2002 and references therein). Nonetheless, a recent study by Rousseau et al. (2015) suggests that besides removal of  $\sim 71\%$  of dissolved riverine Nd in the low salinity zone by coagulation, dissolution of Nd in the mid to high salinity area of an estuary could contribute more Nd to the ocean than dust or dissolved riverine inputs. In the Drake Passage, terrestrial influence is reflected in aluminum and manganese seawater concentration data, but seems restricted to the Patagonian shelf (Middag et al., 2012). Comparison of our AAIW record to the accumulation rate of siliciclastic material in Patagonia (Lamy et al., 2010; Fig. 6.2) reveals some similarity in that both records show a decreasing trend throughout the Holocene. In detail, the Nd isotope record continues to evolve towards less radiogenic values in the mid to late Holocene, while the accumulation rate of siliciclastic material remains constant. In the UCDW depth range, maximum values are reached during the mid Holocene at a time of lower terrestrial inputs than the early Holocene. We hence conclude that changes in terrestrial inputs can possibly affect the source signature of locally formed AAIW, but are difficult to invoke for explaining the UCDW record.

#### 6.4.2. Formation of Antarctic Intermediate Water during the Holocene

Our new Drake Passage Nd isotope data from Holocene deep-sea corals, including one sample from the Pacific sector of the Southern Ocean, show intriguing differences to existing Holocene AAIW data from the Brazilian margin (Pahnke et al., 2008; Fig. 6.3), i.e. the pronounced shift at the

onset of the Holocene and the subsequent gradual Nd isotope trend towards modern values (Figs. 6.2 and 6.3). The abrupt nature of the initial shift covaries with indicators of SWW such as South Pacific SST (Kaiser et al., 2005; Pahnke and Sachs, 2006) and the accumulation rates of organic carbon in Chilean Fjords (Lamy et al., 2010; Fig. 6.3). The subsequent gradual trend of Drake Passage AAIW  $\epsilon_{\text{Nd}}$  is then paralleled by a wide range of proxies from the Holocene Southern Hemisphere, closely following Southern Hemisphere spring insolation (Laskar et al., 2004) and the mid-latitude ( $\sim 65^\circ\text{S}$ ) Antarctic ice core record from James Ross Island (JRI) (Mulvaney et al., 2012). Southern Hemisphere spring insolation has been argued to control austral summer duration (Huybers and Denton, 2008), and therefore sea-ice extent and upwelling of CDW onto the West Antarctic shelf (Shevenell et al., 2011; Fig. 6.3). In comparison with deep Nd isotope records from the South Atlantic (Skinner et al., 2013) and the northern Indian Ocean (Piotrowski et al., 2009), a strong gradient to overlying mid-depth and intermediate water masses is evident in the Drake Passage (Fig. 6.3). The trend towards unradiogenic Nd isotope signatures in the deep ocean has been ascribed to the deepening and/or intensification of NADW during the deglacial (Piotrowski et al., 2004, 2005; Skinner et al., 2013), consistent with the widely accepted picture of glacial-interglacial change in water mass geometry (e.g., Sarnthein et al., 1994; Curry and Oppo, 2005). During the Holocene, the UCDW and AAIW records change in opposite direction to deep ocean Nd isotope trends implying a deeply stratified water column. In the AAIW range, a pronounced shift from  $\epsilon_{\text{Nd}} = -7.3 \pm 0.2$  to  $\epsilon_{\text{Nd}} = -5.9 \pm 0.2$  is paralleled in underlying UCDW at, however, reduced amplitude precluding upward progression of the signal (Fig. 6.3). This AAIW Nd isotope shift of  $\sim 1.4$  epsilon units is accompanied by a  $\sim 40\%$  jump in  $\Delta\Delta^{14}\text{C}$  from  $\sim 130 \pm 11\%$  to  $\sim 90 \pm 14\%$  ( $\Delta\Delta^{14}\text{C} = \Delta^{14}\text{C}_{\text{coral}} - \Delta^{14}\text{C}_{\text{atmosphere}}$ ; contemporaneous  $\Delta^{14}\text{C}_{\text{atmosphere}}$  from Reimer et al., 2013), indicating better AAIW ventilation (Burke and Robinson, 2012). Similarly, enhanced AAIW ventilation during the earliest Holocene is evident from manganese data from the Chile margin (Muratli et al., 2010; Fig. 6.3), coincident with lateral AAIW expansion and enhanced intermediate-depth ventilation in the tropical Atlantic (Huang et al., 2014; Xie et al., 2014; Chen et al., 2015). The Nd isotope and  $\Delta\Delta^{14}\text{C}$  shifts in AAIW corals are accompanied by shifts towards warmer temperatures off Chile (Kaiser et al., 2005) and off New Zealand (Pahnke and Sachs, 2006), paired with enhanced accumulation rates of terrestrial organic matter in Chilean fjords (Lamy et al., 2010). Taken together, the proxy data indicate intriguing covariation of AAIW properties with the position and/or strength of the SWW defining the Holocene mean position of oceanic fronts, and therefore SST, as well as acting to control the Southern Hemisphere mid-latitude hydrological cycle (Jenny et al., 2003; Kaiser et al., 2005; Lamy et al., 2010). This is consistent with climate model outputs for Southern Hemisphere warming scenarios (e.g., Kushner et al., 2001; Delworth and Zeng, 2008) and recent observations (e.g., Gille, 2002; Böning et al., 2008). As the formation of AAIW in the modern Southern Ocean is linked to atmospheric forcing (e.g., Sloyan and Rintoul, 2001; Oke and England, 2004; Naveira Garabato et al., 2009; Close et al., 2013), and in the light of available robust Holocene literature data, we interpret the Drake Passage AAIW Nd isotope signal to be related to SWW dynamics through

wind-induced circulation changes. This raises the question of how the SWW can induce changes of the AAIW Nd isotopic composition given that underlying UCDW is less radiogenic and responds at smaller amplitude (Fig. 6.3).

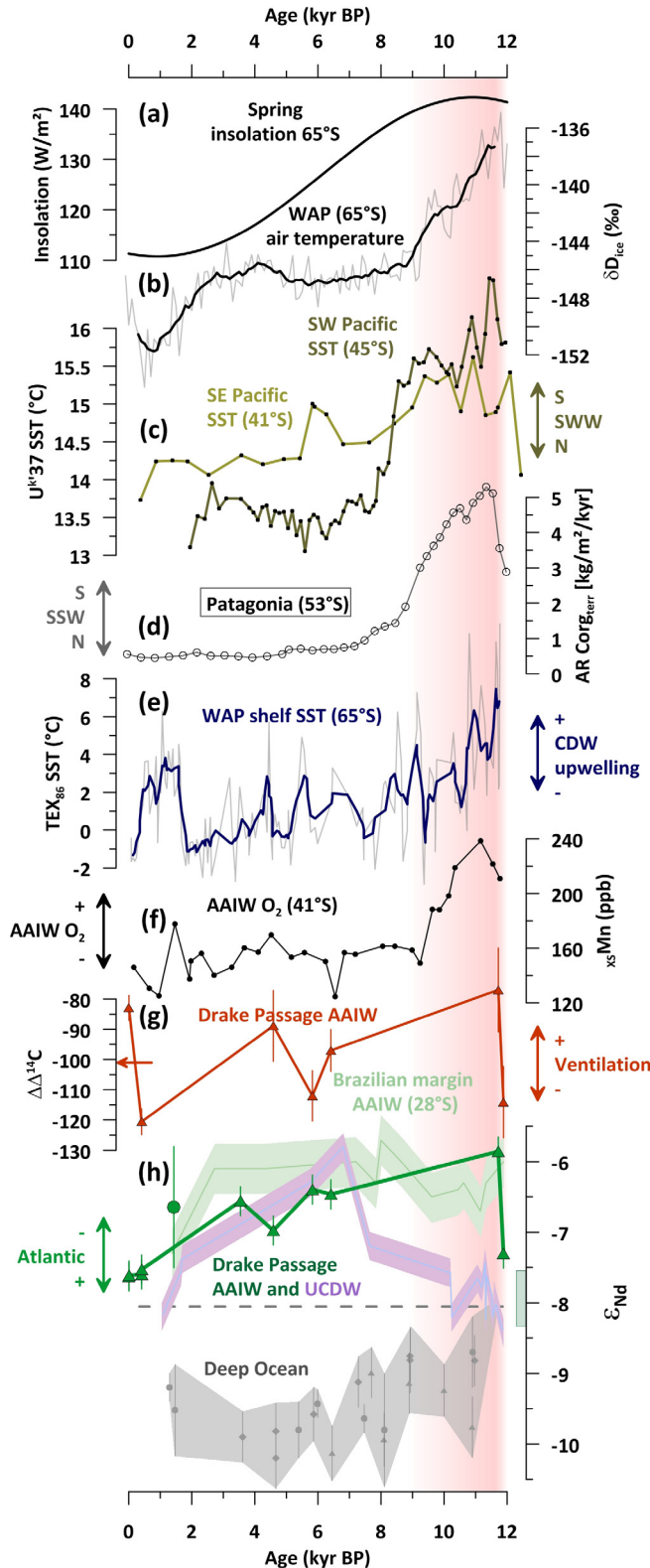


**Figure 6.3:** Holocene Southern Hemisphere atmosphere and ocean dynamics and their role in AAIW formation and ventilation. (a) Spring insolation at 65°S as an indicator for austral summer duration (Laskar et al., 2004; Huybers and Denton, 2008). (b) West Antarctic Peninsula (WAP)  $\delta D_{ice}$  ice core record from James Ross Island (JRI) ice core (Mulvaney et al., 2012). (c) Alkenone unsaturation index ( $U^{k37}$ ) sea surface temperature (SST) records from Southeast and Southwest Pacific used as first-order approximation of frontal and hence SWW position (Kaiser et al., 2005; Pahnke and Sachs, 2006). (d) Accumulation rate of terrestrial organic carbon in a Patagonian Fjord recording fluvial input, associated with SWW strength (Lamy et al., 2010). (e) WAP  $TEX_{86}$  shelf SST record, sensitive to upwelling of warm CDW onto the shelf and sea ice extent (Shevenell et al., 2011). (f) Oxygen content of AAIW in 835 m water depth off Chile reconstructed from excess manganese ( $_{XS}Mn$ ) concentrations in ODP core 1233.  $_{XS}Mn$  refers to the non-detrital component in the sediments. High values indicate high  $O_2$  content (Muratli et al., 2010). (g) Drake Passage AAIW radiocarbon record plotted as  $\Delta\Delta^{14}C = \Delta^{14}C_{coral} - \Delta^{14}C_{atmosphere}$  (Burke and Robinson, 2012). The atmospheric  $\Delta^{14}C$  used for subtraction was calculated as the average value of contemporaneous  $\Delta^{14}C$  (Reimer et al., 2013) averaged across  $2\sigma$  uncertainty range of uranium-series dating. Arrow indicates modern  $\Delta\Delta^{14}C_{AAIW}$  using pre-bomb  $\Delta^{14}C_{atmosphere}$  (Reimer et al., 2013) and natural  $\Delta^{14}C_{AAIW}$  from Key et al. (2004). (h) Drake Passage Nd isotope record from AAIW depth range (grass green) compared to Brazilian margin record (faded green) from Pahnke et al. (2008), underlying UCDW deep-coral Nd isotope data (pale purple) and stacked deep ocean time series (Piotrowski et al., 2009, 2012; Skinner et al., 2013). Dashed line indicates average Nd isotopic composition of seawater collected at coral sampling locations and green box represents seawater Nd isotopic composition of sample collected at depth of modern deep-sea corals calibrated in Chapter 3.

If it was boundary exchange (Lacan and Jeandel, 2005a; Carter et al., 2012; Rickli et al., 2014), it would be expected that underlying UCDW was similarly, if not more affected since UCDW would be forced towards the Antarctic margin (Fig. 6.1). Moreover, the Nd isotopic composition of modern seawater collected at the coral sampling locations shows no evidence in support of boundary exchange processes altering the Drake Passage seawater Nd isotope signature (Chapter 3, and see also Stichel et al., 2012).

Therefore, changing the Nd isotope signature of AAIW source waters through local fluxes is the most likely candidate. The Southeast Pacific is a main AAIW formation region (e.g., Bostock et al., 2013) so that input from Patagonia ( $\epsilon_{Nd} > -4$ ; Hegner et al., 2007 and references therein) could drive AAIW source waters towards more radiogenic values. Having said that, the Southeast Pacific AAIW formation area is east of Patagonia where strong westerly winds limit the westward flux of shelf water masses. Middag et al. (2012) showed that the extension of Patagonian shelf water masses carrying elevated trace metal concentrations from terrestrial input is largely restricted to the shelf. In the southern Drake Passage, they identified, however, a mid-depth plume of elevated trace metal concentrations reaching beyond the WAP shelf into the Drake Passage open ocean mixed layer (Middag et al., 2012). Terrestrial input from the WAP shelf is relatively radiogenic in nature ( $\epsilon_{Nd} > -4$ ; Hegner et al., 2007 and references therein; Noble et al., 2012). Carter et al. (2012) showed that water masses interacting with radiogenic Antarctic shelf sediments can carry their Nd isotope signature northwards into the Amundsen Sea surface ocean across the PF. In analogy, re-suspension and partial dissolution of sediments are likely to influence WAP shelf water masses (cf. Carter et al., 2012; Rickli et al., 2014). As the Drake Passage is a region of deep upwelling, such signal can only be transferred downward by water masses formed locally in the Southern Ocean, such as AAIW (cf. Piola and Georgi, 1982; Bostock et al., 2013).

We therefore propose that atmospheric forcing expressed in an abrupt southward shift of the SWW at the onset of the Holocene enhanced northward advection of (WAP) shelf (sub-) surface water masses. Such shelf water masses then supplied radiogenic Nd to the open ocean mixed layer, consequently feeding into AAIW. This scenario is consistent with modern observations showing that AAIW formation and properties are linked to Bellingshausen Sea subsurface water masses controlled by Southern Hemisphere atmospheric dynamics (Naveira Garabato et al., 2009). A poleward shift/intensification of the SWW is expressed in elevated air temperatures on the WAP shelf (Turner et al., 2005; Marshall et al., 2006b) and stronger upwelling of warm CDW on the Antarctic shelves (e.g., Thoma et al., 2008; Shevenell et al., 2011; Fig. 6.3). This heat supply, in particular from upwelling CDW, is capable to accelerate ice loss of buttressing ice shelves inducing thinning of grounded ice and hence glacier retreat of the modern (Cook et al., 2005; Pritchard et al., 2012) and early Holocene WAIS (Hillenbrand et al., 2012). Such retreat might further contribute to sediment-seawater interaction of shelf water masses, thereby supplying radiogenic Nd to WAP shelf water masses (indicated by dashed arrows in Fig. 6.4). The meridional (sub) surface water transport may further be

enhanced by stronger northward Ekman transport (Oke and England, 2003) and the asymmetric response of the surface ocean to atmospheric forcing, allowing meridional winds to cross the ACC more frequently (Sallée et al., 2008, 2010). Meridional winds west of the WAP are critical for the formation of AAIW in the Southeast Pacific (Naveira Garabato et al., 2009). Taken together, these processes could lead to the pronounced Nd isotope shift of 1.4 epsilon units in response to SWW forcing (Figs. 6.3 and 6.4). The contemporaneous  $\Delta\Delta^{14}\text{C}$  shift indicating better AAIW ventilation (Muratli et al., 2010; Fig. 6.3) would then result from higher AAIW formation rates (Oke and England, 2003) associated with stronger SWW-induced mixing (i.e. positive Southern Annular Mode case in Sallée et al., 2010) inducing better equilibration of upwelling deep water masses with atmospheric radiocarbon (Ito et al., 2004).

During the remainder of the Holocene, the Nd isotope trend covaries closely with proxies for atmospheric forcing. A gradual Nd isotope trend from  $\epsilon_{\text{Nd}} = -5.9 \pm 0.2$  at 11.7 kyr BP to modern values of  $\epsilon_{\text{Nd}} = -7.6 \pm 0.2$  in alive collected corals (Fig. 6.3) mimics a decrease in spring insolation/summer duration (Laskar et al., 2004), decreasing temperatures at JRI (Mulvaney et al., 2012), equatorward movement of the SWW (Kaiser et al., 2005; Pahnke et al., 2006; Lamy et al., 2010), paired with reduced upwelling of CDW and sea ice extension on the WAP shelf (Shevenell et al., 2011), and relatively poor AAIW ventilation in the Drake Passage (Burke and Robinson, 2012) and off Chile (Muratli et al., 2010; Fig. 6.3). This suggests that the progressive AAIW Nd isotope trend from the early Holocene to the present reflects the reduced incorporation of radiogenic shelf-derived water masses during AAIW formation due to the northward migration of the SWW. The above regional scenario shows that the Southern Hemisphere can drive climate processes with global significance due to Holocene teleconnections between high and low latitude atmospheric dynamics (Shevenell et al., 2011).

Such changes in AAIW formation have strong implications for the oceanic heat budget (Oke and England, 2003) and the oceanic uptake of carbon, which consequently influences atmospheric carbon concentration (Sabine et al., 2004; Le Quéré et al., 2007). Although the Southern Ocean can act as a net sink for excess carbon (Sabine et al., 2004), its efficiency may diminish during abrupt change to then turn into a net source of (natural) carbon (Le Quéré et al., 2007). More precisely, Southern Ocean northward Ekman drift and subduction of AAIW and its less dense companion SAMW (Subantarctic Mode Water) account for a significant amount of carbon uptake from the atmosphere (Ito et al., 2010), but enhanced wind-driven degassing of upwelling deep waters can act to release carbon to the atmosphere (Le Quéré et al., 2007; Lovenduski et al., 2008). Therefore, the formation of mode and intermediate waters in the Southern Ocean and their link to SWW dynamics seem crucial for the distribution of carbon between the ocean and the atmosphere. If SWW intensification, a projected future scenario under global warming (Yin, 2005; Fyfe and Saenko, 2006), is indeed accompanied by changes in formation rates and ventilation of AAIW as evident from our data, then the Southern Ocean may act as a net source of  $\text{CO}_2$ . This is due to enhanced deep upwelling paired

with increasing air-sea gas exchange of AAIW/SAMW source waters. This could then have contributed significantly to the accelerated early Holocene rise in atmospheric CO<sub>2</sub> (Monnin et al., 2001; 2004; Fig. 6.5).

Mechanistically, such enhanced formation rates of AAIW in the Southern Ocean need to be balanced for within the global overturning of the ocean. As noted above, deep ocean proxy data reflecting the strength of Atlantic overturning indicate indeed intensified NADW advection (McManus et al., 2004; Piotrowski et al., 2009, 2012; Gherardi et al., 2005; 2009; Roberts et al., 2010; Skinner et al., 2013, Fig. 6.5). In the section below, we will discuss the deep ocean signal in order to identify the processes causing deep chemical stratification in the Drake Passage and the implications for the global overturning circulation.

#### **6.4.3. Deep stratification of the Holocene Southern Ocean - implications for the global overturning circulation**

Our Drake Passage UCDW Nd isotope record (including one sample from the Pacific sector of the Southern Ocean) implies at a first glance a history for this water mass, decoupled from AAIW and Antarctic pacing (Figs. 6.3, 6.4 and 6.5). In detail, the UCDW data describe two domains when considered in  $\Delta\Delta^{14}\text{C}-\epsilon_{\text{Nd}}$  space (Fig. 6.4). During the earliest Holocene from  $\sim 11.8$  to  $\sim 11$  kyr BP, UCDW data is oriented in the similar direction to AAIW (Fig. 6.5). The implied mixing features, however, stronger influence of an unradiogenic and radiocarbon-depleted source ( $\epsilon_{\text{Nd}} = -8.4 \pm 0.2$  and  $\Delta\Delta^{14}\text{C} = -155 \pm 14\text{‰}$  at 11.8 kyr BP; Fig. 6.5). Such unradiogenic source was likely of Atlantic origin, probably a remnant of poorly ventilated glacial deep Atlantic water masses (e.g., Thornalley et al., 2011; Wilson et al., 2014; Chapter 4) exported south by AMOC resumption and deepening of NADW formation at the onset of the Holocene (Roberts et al., 2010; Gherardi et al., 2005, 2009; Fig. 6.5). Radiocarbon data show simultaneous and similar-magnitude shifts of both, UCDW (by  $\sim 50 \pm 20\text{‰}$ ) and AAIW (by  $\sim 40 \pm 20\text{‰}$ ), at the onset of the Holocene (Fig. 6.5). As UCDW is a major source for AAIW formation (e.g., Marshall and Speer, 2012), this implies that a shift in deep water ventilation occurred at the onset of the Holocene causing enhanced ventilation of the upper water column, expressed in Drake Passage  $\Delta\Delta^{14}\text{C}$  similar to pre-bomb values (i.e.  $\Delta\Delta^{14}\text{C}_{\text{AAIW}} \approx 105\text{‰}$  and  $\Delta\Delta^{14}\text{C}_{\text{UCDW}} \approx 115\text{‰}$ ; Key et al., 2004; Fig. 6.4). However, if the signal progressed upwards, one would expect a larger shift in UCDW Nd isotopes compared to AAIW. This is not the case. Figure 6.4 highlights, moreover, that the earliest Holocene composition of UCDW cannot be explained by upward mixing of well-ventilated deep water masses as this would require a yet unknown deep water mass to raise  $\Delta\Delta^{14}\text{C}_{\text{AAIW}}$  and the Nd isotopic composition simultaneously. Alternatively, very strong advection of extremely well-ventilated deep Pacific water masses would be required to mix into the UCDW range implying substantial spin-up of deep Pacific circulation and ventilation including export rates similar to modern NADW. This scenario seems unlikely given the size of the Pacific basin, resulting in long water mass transfer times and depleted background  $\Delta\Delta^{14}\text{C}$  (Key et al., 2004; Skinner

et al., 2015). Moreover there is no indication of such dramatic spin-up in North (Davies-Walczak et al., 2014) or South Pacific radiocarbon data (Sikes et al., 2000; Skinner et al., 2015).

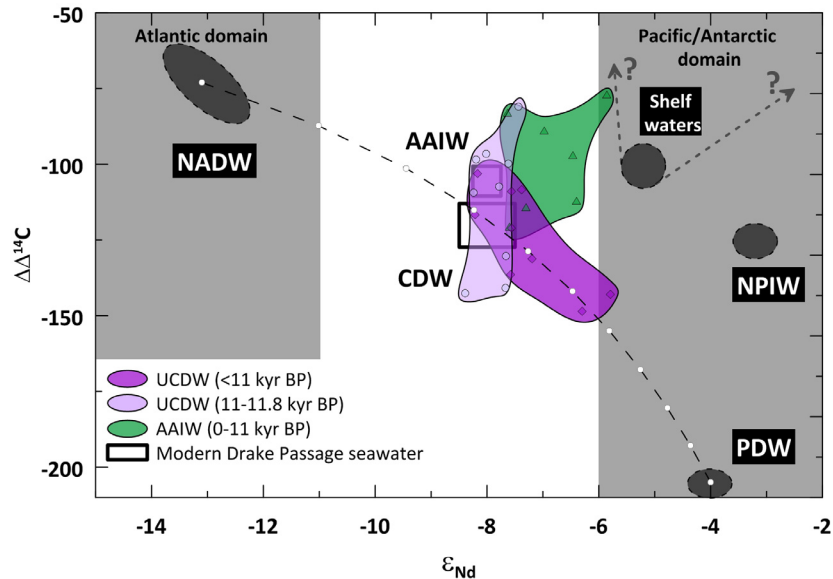


**Figure 6.4:** Drake Passage deep-sea coral data in radiocarbon-Nd-isotope space. Radiocarbon data for modern water masses taken from GLODAP data base natural seawater  $\Delta^{14}\text{C}$  reconstruction (Key et al., 2004). Modern (i.e. 1950)  $\Delta^{14}\text{C}_{\text{atmosphere}}$  (Reimer et al., 2013) used to generate seawater  $\Delta\Delta^{14}\text{C}$ . Coral  $\Delta\Delta^{14}\text{C}$  calculated with IntCal13 (Reimer et al., 2013; see also caption Fig. 6.3). Modern Nd isotope endmember data for western (Northwest Atl. AII 109-1 Stn30; Piepgras and Wasserburg, 1987) and eastern NADW (Ovide St. 15; Copard et al., 2011), central North Pacific PDW (BO-3; Amakawa et al., 2009), North Pacific Intermediate Water (NPIW) (Station 4; Zimmermann et al., 2009), Antarctic shelf waters (Carter et al., 2012), and modern UCDW and AAIW (Chapter 3). The arrows connected to modern West Antarctic shelf water masses indicate speculative extension of the range of shelf water mass properties (see discussion). The dashed line results from calculating conservative mixing between modern NADW and PDW where white dots indicate 0.1 fractions of mixing.

Therefore, we propose that increased ventilation recorded in UCDW corals during the earliest Holocene is induced by deepening and/or stronger mixing of UCDW with overlying mixed layer waters (i.e. the source waters which are ultimately subducted as AAIW; Piola and Georgi, 1982, Bostock et al., 2013). In detail, we interpret the early Holocene UCDW signal to be caused by deepening of the mixed layer depth (MLD) during a phase of maximum poleward intensification of the SWW (Lamy et al., 2010; Figs. 6.3 and 6.5). Such an interpretation is consistent with  $x_{\text{SRe}}$  data from ODP 1234 (1035 m bsl) off the Chile margin (Muratli et al., 2010). Rhenium is redox-sensitive so that changes in  $x_{\text{SRe}}$  can be interpreted in terms of changes in water oxygenation (Muratli et al., 2010). ODP 1234 is currently located at the interface of AAIW (high  $\text{O}_2$ ) and PDW (low  $\text{O}_2$ ; Fig. 6.2). Following the reasoning by Muratli et al. (2010), low  $x_{\text{SRe}}$  during the earliest Holocene indicates high presence of oxygenated AAIW, much in support of mixed layer deepening. This is particularly surprising as one coral with high  $\Delta\Delta^{14}\text{C} = -114 \pm 14\text{‰}$  is from 978 m water depth (Table 6.1, Fig. 6.5) implying substantial deepening of the MLD during the earliest Holocene. During this interval, the Nd isotopic composition of UCDW appears less sensitive than radiocarbon. We propose two potential explanations: either radiocarbon in the original mixed layer was better equilibrated with the

atmosphere than the final AAIW product. Or alternatively, enhanced peak SWW-induced mixing changed the  $\Delta\Delta^{14}\text{C}_{\text{AAIW}}$  due to intensified air-sea gas exchange whereas water mass mixing proportions recorded by Nd isotopes remain rather invariable. This remains, admittedly, speculative due to limited AAIW data coverage across the early Holocene interval (Figs. 6.3 and 6.5).

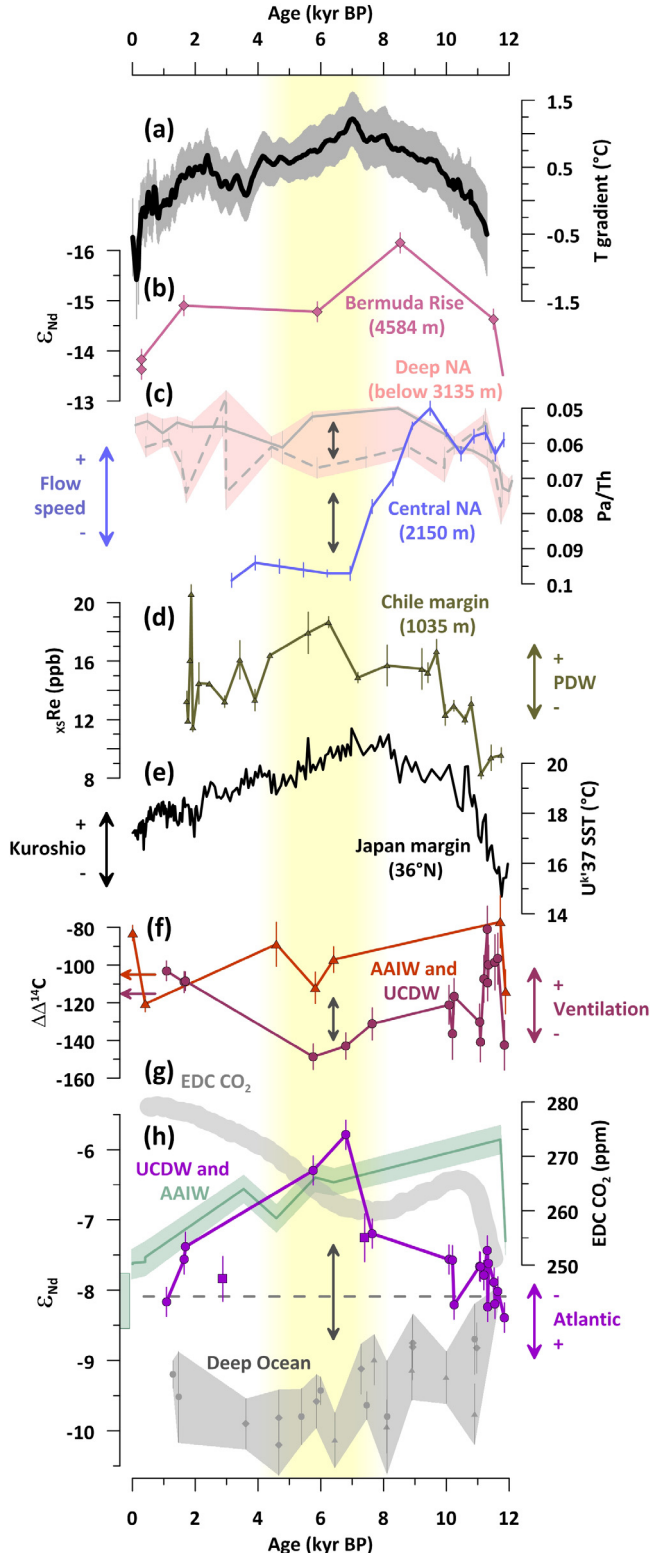


**Figure 6.5:** Global picture of overturning circulation changes during the Holocene. (a) Interhemispheric temperature gradient where positive values represent excess heat in the Northern Hemisphere and vice versa (Marcott et al., 2013 and references therein). (b) Bermuda Rise Nd isotope record (Roberts et al., 2010). (c)  $^{231}\text{Pa}/^{230}\text{Th}$  records from across the North Atlantic. Solid and dashed grey lines superimposed on rose polygon indicate deep western (4550 m) and eastern (3135 m) North Atlantic flow vigour, respectively (McManus et al., 2004; Gherardi et al., 2005). Mid-depth (2150 m) central North Atlantic  $^{231}\text{Pa}/^{230}\text{Th}$  record from Gherardi et al. (2009). (d) Excess rhenium ( $_{\text{xs}}\text{Re}$ ) from 1035 m water depth off Chile, located at hinge depth between high  $\text{O}_2$  (AAIW) and low  $\text{O}_2$  (PDW).  $_{\text{xs}}\text{Re}$  has an inverse relationship with oxygen content compared to  $_{\text{xs}}\text{Mn}$  (Fig. 6.4 caption). High  $_{\text{xs}}\text{Re}$  indicates low  $\text{O}_2$  content, but is insensitive in high oxygen environments (Muratli et al., 2010). (e) Alkenone unsaturation index ( $U^{\text{k}'37}$ ) record from off Japan recording northward extension of the Kuroshio Current (Isono et al., 2009). (f) Drake Passage deep-sea coral radiocarbon data from AAIW and UCDW depth range (Burke and Robinson, 2012). Modern values indicated by arrows in respective colors (Key et al., 2004; Reimer et al., 2013; see Fig. 6.3 caption for details). (g) 11-point running average of EPICA Dome C ice core carbon dioxide time series (Monnin et al., 2001, 2004). (h) Drake Passage Nd isotope record from UCDW highlighted and compared to overlying AAIW (translucent green) and stacked deep ocean time series (Piotrowski et al., 2009, 2012; Skinner et al., 2013). Dashed line and green box as in Fig. 6.3. Grey arrows indicate lateral inter-basin gradient in deep North Atlantic  $^{231}\text{Pa}/^{230}\text{Th}$ , otherwise vertical gradients in the water column.

Thereafter, from ~10 kyr BP our Nd isotope data evolves towards significantly more radiogenic Nd isotope signatures in UCDW depth range, peaking at 6.8 kyr BP at a value of  $\epsilon_{\text{Nd}} = -5.8 \pm 0.2$  paralleled by enhanced radiocarbon-depletion of  $\Delta\Delta^{14}\text{C}_{\text{UCDW}} = -160 \pm 9\text{‰}$  (Fig. 6.5). Hence, the relation between  $\Delta\Delta^{14}\text{C}_{\text{UCDW}}$  and UCDW Nd isotopes is, compared to the earliest Holocene interval, inverse (Fig. 6.5). This inverse relationship translates into a different mixing trend in  $\Delta\Delta^{14}\text{C}$ -Nd isotope space (Fig. 6.4) indicating a strong mid-Holocene contribution of radiocarbon-depleted, radiogenic PDW to UCDW. This was paralleled by reduced oxygenation of bottom waters at the Chilean margin indicating PDW expansion (AAIW shoaling) (Muratli et al., 2010; Fig. 6.5). The consistent change in both tracers renders non-conservative effects on endmembers and along the NADW and PDW flow paths unlikely so that the mid-Holocene UCDW ventilation and Nd isotope change translates into a ~40% reduction of NADW in UCDW, assuming similar-to-modern North Atlantic and North Pacific endmember properties (Piepgras and Wasserburg, 1987; Amakawa et al., 2009; Key et al., 2004; Fig. 6.4). Such strong and enduring (at least ~1000 years) interglacial reduction of NADW export raises obvious questions about the mechanism.

Mixing with deeper waters appears unlikely as underlying water masses are significantly less radiogenic during the mid-Holocene and evolve towards less radiogenic Nd isotope signatures of  $\epsilon_{\text{Nd}} \approx -9.5$  at the same time (Piotrowski et al., 2009, 2012; Skinner et al., 2013; Fig. 6.5). In the deep Northwest Atlantic, Nd isotope (Roberts et al., 2010) and  $^{231}\text{Pa}/^{230}\text{Th}$  data (McManus et al., 2004) from Bermuda Rise indicate consistently strong export of lower NADW (Fig. 6.5). In contrast,  $^{231}\text{Pa}/^{230}\text{Th}$  data suggest less vigorous flow during the mid-Holocene in the deep Northeastern Atlantic basin (Gherardi et al., 2005) and a dramatic reduction of mid-depth water mass export in the central North Atlantic around ~7 kyr BP (core MD95-2037 from 2150 m water depth; Gherardi et al., 2009). This depth range is today dominated by upper NADW carrying a strong Labrador Sea Water (LSW) component. Stable isotope and grain size analyses from the Northeast Atlantic suggest further that re-organisation of water masses allowed for intrusion of LSW into the deep Northeast Atlantic at ~6.5 kyr BP (Hoogakker et al., 2011). This is consistent with coarse fraction data from intermediate depths in the Southern Caribbean indicating stronger AAIW influence during the mid-Holocene (Xie et al., 2014) and enhanced ventilation at AAIW level in the tropical Atlantic (Chen et al., 2015), maybe in response to low mid-depth southward flow vigour (Gherardi et al., 2009). Therefore, it is suggested that the onset/intensification of Labrador Sea deep convection around 7 kyr BP (Solignac et al., 2004; Hoogakker et al., 2015) generated a higher density version of LSW penetrating pre-dominantly into lower NADW. Water masses exported from the Labrador Sea carry a distinct unradiogenic Nd isotope signature which is today resolved in less radiogenic values of upper NADW (Lambelet et al., accepted). If this pattern was reversed during the mid-Holocene, a vigorous deep southward flow would export very unradiogenic water masses at depth of which a high proportion could cross the ACC below the Drake Passage sill depth and upwell towards the Antarctic continent (Toggweiler and Samuels, 1995). It can be speculated that deepening of LSW could imply that more radiogenic (and

sluggish) upper NADW export mixes isoneutrally into the ACC at UCDW depths. This would explain both, the unradiogenic nature of the mid-Holocene deep ocean (Piotrowski et al., 2004, 2009, 2012; Roberts et al., 2010; Skinner et al., 2013) and deep Southern Ocean stratification (Fig. 6.5).

The North Atlantic processes of LSW formation, associated subpolar gyre dynamics and AMOC variability may all be driven by buoyancy forcing on the North Atlantic, and in particular over the Labrador Sea (Yeager and Danabasoglu, 2014). Regardless, a simple Nd isotope change of upper NADW driven by North Atlantic processes is unlikely to substantially influence the Drake Passage mixing equation. Mixing calculations reveal that upper NADW  $\epsilon_{Nd}$  of  $\sim -8$  would be required to drive a  $\sim 2$  epsilon unit change in Drake Passage UCDW (based on Piepgras and Wasserburg, 1987; Amakawa et al., 2009). This seems highly unlikely given reconstructions from the past mid-depth North Atlantic (Wilson et al., 2014; Chapter 5) rendering North Atlantic processes unsuitable to explain Drake Passage UCDW of  $\epsilon_{Nd} = -5.8 \pm 0.2$  at 6.8 kyr BP. Therefore, changes of the large scale overturning circulation, compensating for and/or independent of North Atlantic processes, are considered to explain mid-Holocene Drake Passage water mass mixing. Yeager and Danabasoglu (2014) showed that momentum (i.e. wind) forcing can account for substantial AMOC variability south of the equator, and it has been hypothesised that the position of the SWW acts to control the strength of overturning circulation and salinity stratification in the North Pacific (Sijp and England, 2009).

According to the scenario outlined by Sijp and England (2009) an equatorward shift of the SWW would induce a stratification breakdown in the North Pacific allowing for a deepening of convective processes. The SWW moved equatorward towards the mid-Holocene (Pahnke and Sachs, 2006; Lamy et al., 2010; Fig. 6.3), associated with a maximum in the extra-tropical interhemispheric temperature gradient (Marcott et al., 2013; Fig. 6.5). A substantial part of this Northern Hemisphere excess heat is presumably due to strong northward heat transport associated with intense deep water mass formation in the North Atlantic. However, a high resolution  $U^{k37}$  SST record from off Japan capturing the Kuroshio current (Isono et al., 2009) parallels the extra-tropical interhemispheric temperature gradient (Fig. 6.5). Paired with equatorward shifted SWW, this strongly suggests intensified mid-Holocene northward heat transport in the Pacific Ocean (Isono et al., 2009; Fig. 6.5). Such heat flux implies enhanced northward salinity flux via the Kuroshio Current (cf. Warren, 1983; Emile-Geay et al., 2003; Menviel et al., 2012) thus potentially inducing a proposed deepening of convective processes ventilating the North Pacific water column (cf. Sijp and England, 2009; Menviel et al., 2012). Indeed, radiocarbon reconstructions from the mid-depth Northwest (Rella and Uchida, 2014) and Northeast Pacific (Davies-Walczak et al., 2014) show indication for better ventilation during the mid-Holocene. These radiocarbon records were, however, generated from paired benthic-planktic  $^{14}C$  age differences which are sensitive to age model changes (see Davies-Walczak et al., 2014), and/or have been interpreted to monitor enhanced northward AAIW advection (Rella and Uchida, 2014). Stronger northwards advection of AAIW may indeed be a consequence of increased southward PDW export. Alternatively, deepening of North Pacific ventilation may occur away from

the Okhotsk Sea, which Rella and Uchida (2014) excluded as a source of deepened mid-Holocene ventilation based on proxy evidence. Either way, our data strongly suggest enhanced Pacific contribution to mid-Holocene Drake Passage UCDW, likely in response to a northward SWW shift (Kaiser et al., 2005; Pahnke and Sachs, 2006; Sijp and England, 2009; Lamy et al., 2010) and associated with fortified northward oceanic heat (and salinity) flux in the Pacific (Isono et al., 2009). Such link between North Pacific surface conditions and SWW intensity has been found in recent model simulations leading to enhanced mid-depth water mass export from the North Pacific (Menviel et al., 2012). The SWW-induced strengthening of the Pacific mid-depth circulation could have occurred well before Drake Passage UCDW properties changed. Regardless, the time scale of the shift itself is centennial, but may be further refined when more data becomes available for the critical interval between  $\sim 7.5$  and 6.8 kyr BP (Table 6.1, Fig. 6.5). In combination with processes acting to reduce mid-depth southward flow in the North Atlantic, our results render deepening of water mass formation in the mid-Holocene North Pacific likely. The implied expansion of PDW into the Southern Ocean involved deep and shallow stratification which, in turn, may then have played a critical role in the mid-Holocene drawdown of atmospheric  $\text{CO}_2$  and, through degassing, contributed to the accelerated rise thereafter (Fig. 6.6). In such a scenario, the ultimate controlling factor would be the position of the SWW mediating substantial re-organisation of mid-Holocene mid-depth circulation.

## 6.5. Conclusions

Our new Drake Passage Nd isotope data paired with existing radiocarbon data from the same corals reveal substantial oceanic re-organisation of the Holocene intermediate- and mid-depth circulation implying significant consequences for water column stratification and the structure of global meridional overturning circulation. A pronounced simultaneous shift of Nd isotopes and radiocarbon in AAIW depth range at the onset of the Holocene (11.7 kyr BP) can be tied to poleward intensification of the SWW. The AAIW Nd isotope signature is identified to result from mixing of upwelling deep waters with substantial contribution of shelf-derived water masses that were previously subjected to non-conservative exchange processes, likely sourced from the Westantarctic shelves. Better ventilation inferred from radiocarbon data indicates deepening of the mixed layer depth implying better equilibration of upwelling deep waters with the atmosphere, consequently leading to accelerated release of carbon dioxide into the atmosphere. The proposed vertical extension of the Early Holocene winter mixed layer can be traced down to  $\sim 1000$  m water depth in the Drake Passage rendering mixed layer deepening in response to poleward intensification of the SWW substantial.

From  $\sim 10$  kyr BP this effect ceased with the equatorward expansion of the SWW inducing substantial changes in mid-depth circulation. The mid-Holocene North Atlantic was characterised by buoyancy-driven reductions of mid-depth flow vigour and water mass export paired with strong southward flow at deep levels. These North Atlantic processes covary with a reduction of infiltration of Atlantic-like Nd isotope signatures and ventilation in Drake Passage UCDW. Simultaneously, sea

surface temperature data from the Northwest Pacific Ocean suggest intensified northward heat transport in the Kuroshio Current contributing to mid-Holocene Northern Hemisphere heat piracy. These combined effects lead us to conclude that the mid-Holocene (~6.8 to 5.8 kyr BP) domination of Pacific-derived water masses in Drake Passage UCDW was likely coupled with enhanced overturning in the Pacific. The recorded switch occurred on centennial time scale and was presumably associated with a contemporaneous drop in atmospheric CO<sub>2</sub>. Despite potential mid-depth water mass renewal in the Pacific Ocean, southward exported PDW would still carry high amounts of pre-formed properties, such as carbon, due to the nature of convective processes ventilating underlying old water masses. Hence, the mid-Holocene PDW expansion into the chemically stratified Southern Ocean water column was likely to play a key role in the contemporaneous drop in atmospheric CO<sub>2</sub> and then again, through degassing, during accelerated rise thereafter.

**Declaration:** I conducted the Nd isotope and concentration work presented in this chapter. The U-series and radiocarbon data were generated by Andrea Burke on samples provided by Laura Robinson.

## **Chapter 7**

### **Summary and general conclusions**

The aim of this work was to decipher past water mass mixing in the Southern Ocean in order to infer large-scale oceanic re-organisation during past intervals of climatic perturbations. A refined method of combined multi-element separation was used to minimise sample consumption, workload and uncertainty when comparing different geochemical parameters among each other.

Building upon previous studies, the global deep-sea coral Nd isotope calibration was extended, revealing that not all species are reliable recorders of ambient seawater. Exploring the nature of Nd in the coralline skeleton demonstrated that the skeletal Nd budget of most coral samples is dominated by seawater-derived phases, of which authigenic phosphate phases were identified as most likely phases to account for elevated intraskeletal Nd concentrations.

Based on above findings, the Nd isotopic composition of deep-sea corals was applied to reconstruct past oceanic Nd isotope variability. New data from the North Atlantic helped to constrain the Nd isotope evolution in this important source region. In comparison with available literature data, the results provide evidence that mid-depth waters exported from the North Atlantic were subject to significant isotopic variability, presumably due to changes in the relative proportions of source waters contributing to the exported intermediate to deep waters (Fig. 7.1).

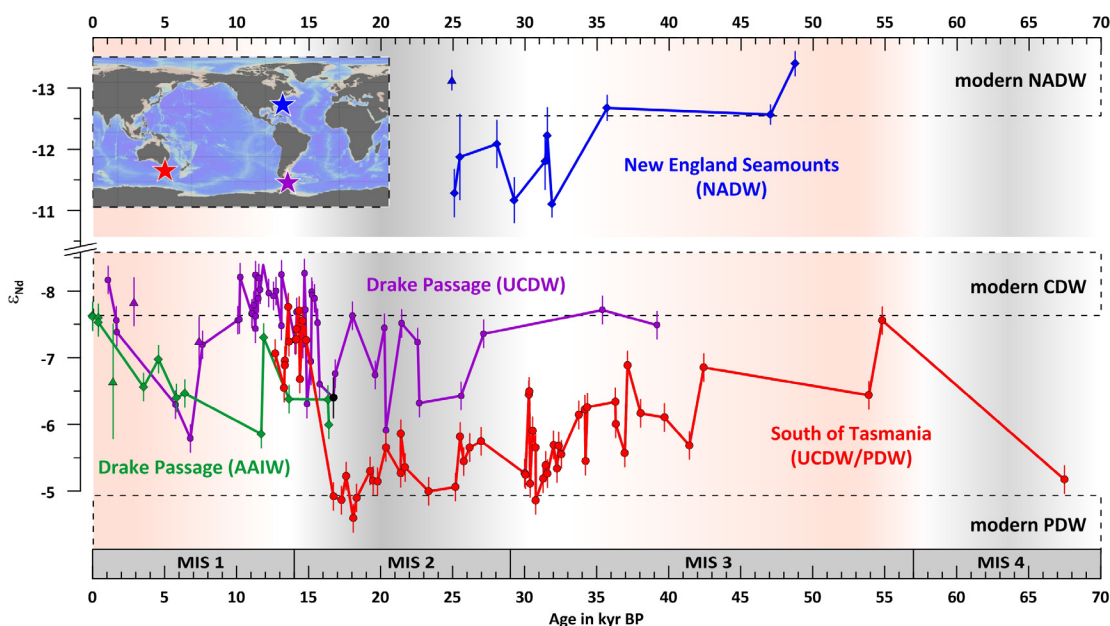


**Fig. 7.1:** Summary of the new deep-sea coral Nd isotope data from the New England Seamounts (NES), the Drake Passage and the Tasmanian margin (blue, purple and red stars on inset map, respectively). Water masses dominating at the coral sampling locations in the modern ocean are listed in brackets. The Tasmanian margin is dominated by UCDW, but also influenced by PDW (cf. Sokolov and Rintoul, 2000; Chapters 4 and 5). Data shown are based on successfully calibrated coral species only (see Chapter 3). The Drake Passage results include three samples from the South Pacific (triangles), and were grouped by modern water masses currently bathing the sampling sites. The oldest NES sample is from van de Flierdt et al. (2006b) and one Drake Passage sample (black dot) is from Robinson and van de Flierdt (2009). MIS: Marine Isotope Stage (after Lisiecki and Raymo, 2005), NADW: North Atlantic Deep Water, (U)CDW: (Upper) Circumpolar Deep Water, AAIW: Antarctic Intermediate Water, PDW: Pacific Deep Water. See discussion in Chapter 3 for references on seawater Nd isotopic composition. Inset base map generated with ODV software (Schlitzer, 2012).

In the Southern Ocean, abrupt variation superimposed on multi-millennial trends describe the character of Nd isotope variability in the Drake Passage and south of Tasmania over the last ~40,000 years (Fig. 7.1). Notably, whenever the time resolution (i.e. sampling density) is increased, deep-sea corals resolve (sub) centennial-scale variability previously barely identified in the Southern Ocean. The Nd isotope trends in both locations are remarkably different, suggesting that they record complementary features of past ocean circulation.

The Drake Passage Nd isotope signal, considered to monitor circumpolar water masses (i.e. UCDW), is relatively unradiogenic with a baseline similar to modern seawater ( $\epsilon_{\text{Nd}} \approx -7.5$ ). This indicates significant influence of Atlantic-derived water masses in the circumpolar flow throughout most of the last glacial. In contrast, the Tasmanian time series is characterised by a multi-millennial trend following Antarctica's climate beat (i.e. temperature and CO<sub>2</sub> records from Antarctic ice cores; e.g., EPICA community members, 2006, 2010; Ahn and Brook, 2008, 2014) with abrupt fluctuations superimposed. During glacial times, the Nd isotope signatures at the Tasmanian margin are significantly more radiogenic than contemporaneous UCDW (Fig. 7.1), indicating a stronger influence of Pacific waters at the location.

Based on the new coral data, a peak glacial circulation scenario is proposed, which is summarised and compared to the modern circulation in Figure 7.2. In the **modern ocean** (Fig. 7.2, panel A), NADW ( $\epsilon_{\text{Nd}} \approx -13$ ; Lambelet et al., accepted) is formed from surface waters in the marginal seas of the North Atlantic (blue circles with crosses) and then exported to the Southern Ocean at depth. In the open North Pacific, PDW ( $\epsilon_{\text{Nd}} \approx -4$ ; Amakawa et al., 2009) forms from deep and bottom waters by interior mixing (red circle with point; i.e. no active convection) and is exported into the Southern Ocean at mid-depth upon mixing with northward penetrating CDW (e.g., Macdonald et al., 2009; Kawabe and Fujio, 2010; Fig. 7.2, panels a-1 and a-2). The zonal flow of CDW is homogenous in its Nd isotopic composition ( $\epsilon_{\text{Nd}} \approx -8$ ; e.g., Carter et al., 2012; Stichel et al., 2012; Rickli et al., 2014; Basak et al., 2015). The Subantarctic Front (SAF, dashed line) and the Polar Front (PF, stippled line) are considered to represent most of the deep-reaching circumpolar flow (e.g., Cunningham et al., 2003). The main Southern Hemisphere westerly wind (SWW) forcing occurs slightly north of the SAF, in particular in the Drake Passage area (e.g., Kohfeld et al., 2013; Fig. 7.2, panels a-1 and a-2).

The **peak glacial** scenario (Fig. 7.2, panel B) shows major differences to the modern scenario. The new coral data illustrated in Figure 7.1 can only be explained by two Pacific-derived water masses mixing dynamically with an Atlantic-derived component in the circumpolar flow of UCDW. The North Atlantic source is represented by GNAIW ( $\epsilon_{\text{Nd}} \approx -12$ ; approximated from Huang et al., 2014; Wilson et al., 2014 and Chapter 5) and formed mainly south of Iceland (e.g., Ganopolski et al., 1998). The shoaled GNAIW export to the Southern Ocean precluded significant influence on the lower CDW range. Such reduced Atlantic influence was probably replaced by an old Pacific-derived water mass at the lower deep levels as part of a vertically expanded lower overturning circulation cell (dark grey)

(Matsumoto et al., 2002; Noble et al., 2013; Skinner et al., 2010, 2013, 2015; Fig. 7.2, panels b-1 and b-2). The overlying GNPIW, a water mass actively ventilated from the North Pacific during peak glacials (e.g., Keigwin, 1998; Matsumoto et al., 2002; Fig. 7.2, panel b-2), expanded southwards in the Pacific basin as documented by the Tasmanian margin data. As such, GNPIW probably occupied large parts of the glacial Pacific Ocean, which are dominated by UCDW in the modern ocean (Fig. 7.2).

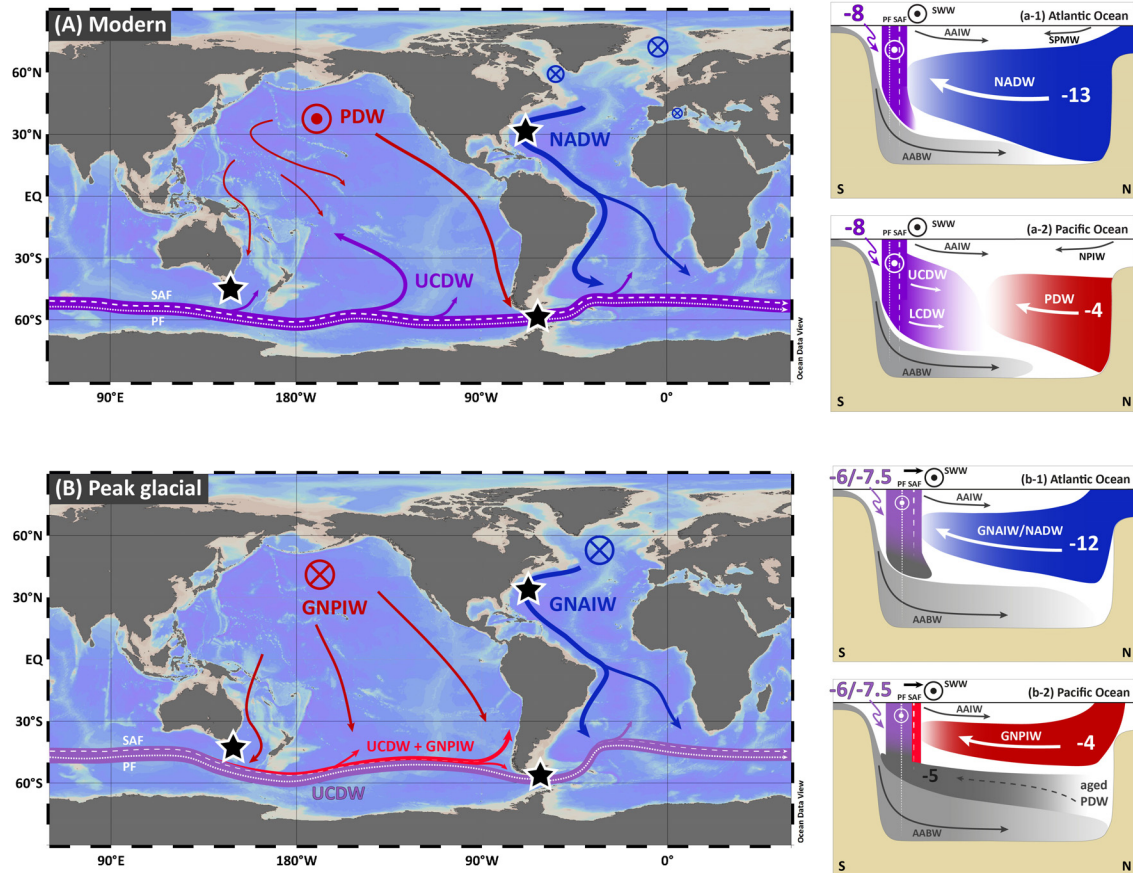


**Fig. 7.2:** Schematic of modern (A) and proposed peak glacial (B) mid-depth circulation, i.e. the depth range bathed by water masses of  $\gamma^{\text{N}} \approx 27.6 - 28.0$  in the modern ocean (see individual Chapters for more details). The coral sampling locations are indicated by the black stars. Circles with points indicate flow towards the reader, circles with crosses transport away from the reader. On the maps, this translates into upwelling and downwelling, respectively, whereas in the transect figures (a-1, a-2, b-1, b-2) this represents zonal transport. NADW: North Atlantic Deep Water ( $\epsilon_{\text{Nd}}$  from Lambelet et al., accepted); PDW: Pacific Deep Water (PDW;  $\epsilon_{\text{Nd}}$  from Amakawa et al., 2009); CDW: Circumpolar Deep Water (upper and lower;  $\epsilon_{\text{Nd}}$  based on Chapter 3 and references therein); AABW: Antarctic Bottom Water; AAIW: Antarctic Intermediate Water; NPIW: North Pacific Intermediate Water; SPMW: Subpolar Mode Water. The glacial analogue of SPMW is poorly constrained and hence not considered in the glacial scenario. GNPIW: Glacial North Pacific Intermediate Water ( $\epsilon_{\text{Nd}}$  inferred from Abouchami et al., 1997 and Amakawa et al., 2009); GNAIW: Glacial North Atlantic Intermediate Water (approximated from Huang et al., 2014; Wilson et al., 2014 and Chapter 5); PF: Polar Front (stippled line); SAF: Subantarctic Front (dashed line); SWW: Southern Hemisphere westerly winds. The peak glacial northward migration/expansion of Southern Ocean frontal zones is inferred from literature (Gersonde et al., 2005; Barrows and Juggins, 2005; Kohfeld et al., 2013; McCave et al., 2014; Lamy et al., 2015). In the transect figures, the white spaces between the major water masses are considered as mixing zones. The deep grey cell extending from the Southern Hemisphere shelves into the deep Northern Hemisphere oceans indicates the lower limb of the

---

overturning circulation, represented by AABW mixing into overlying water masses. The details of the deep level in the glacial transects is based on previous work (Matsumoto et al., 2002; Piotrowski et al., 2004, 2005, 2009, 2012; Anderson et al., 2009; Skinner et al., 2010, 2013, 2015; Noble et al., 2013; Ferrari et al., 2014). See text for further details. Base maps in (A) and (B) were generated with ODV software (Schlitzer, 2012).

---

It follows that northward deflection of GNPIW-influenced water masses off Chile likely reduced the lateral admixture of radiogenic GNPIW into the circumpolar flow during phases of unradiogenic Nd isotopic composition in glacial UCDW ( $\epsilon_{Nd} \approx -7.5$ ; recorded in the Drake Passage). The deflected GNPIW would consequently recirculate within the Pacific basin, but also be involved in AAIW formation. Likewise, vertical mixing with underlying deep waters was reduced, but did not cease in the Southern Ocean (Fig. 7.2, panels b-1 and b-2). In contrast, more radiogenic values ( $\epsilon_{Nd} \approx -6.0$ ) reflect stronger Pacific influence, dominated by enhanced mixing with deep water masses as indicated by comparison with available radiocarbon data (Burke et al., 2012; Chen et al., 2015; Chapter 4). Presumably, this occurred in response to redirection of SAF-bound flow into the Drake Passage enhancing turbulent mixing. Despite the continuous admixture of deep waters into glacial UCDW, the overall interaction between upper and lower circulation cells was, however, limited compared to the modern ocean. This is expressed in deeply stratified Southern Ocean water column (Fig. 7.2, panels b-1 and b-2), consistent with previous work (e.g., Matsumoto et al., 2002; Anderson et al., 2009; Ferrari et al., 2014).

The new deep-sea coral Nd isotope data hence confirm the idea proposed by Lamy et al. (2015) that a critical position of SWW-induced frontal movement in the Southeast Pacific could efficiently control the supply of Pacific-derived water masses to the Drake Passage (Fig. 2). This can explain the overall low fraction of GNPIW in glacial circumpolar flow and the SWW-related abrupt variation in deglacial Drake Passage water mass mixing (Fig. 7.1). Such changes imply a range of feedbacks and teleconnections, which can be subject to interoceanic and interhemispheric coupling often associated with oceanic seesawing (cf. e.g., WAIS Divide project members, 2015). The abrupt nature of change in the Drake Passage, but also south of Tasmania, suggests however that atmospheric signal propagation influenced Southern Ocean circulation patterns ultimately through changes in the position of the SWW.

This work highlights that the position of the SWW-controlled Southern Ocean fronts plays a pivotal role for the understanding of the global circulation, in particular for Southern Ocean mixing and lateral interoceanic water mass exchange. The significance of the SWW in controlling past Southern Ocean dynamics can be expected given the close relationship in the modern ocean. Nonetheless, the strong lateral component in Southern Ocean water mass mixing, in particular during the glacial-interglacial transition, is yet underrated in climatic reconstructions.

In order to substantiate the results and conclusions drawn from this work, it is suggested that future work should continue to focus on the nature of water mass exchange between the Pacific and

Atlantic Ocean from a Southern Ocean perspective. For this purpose, additional high resolution data from the Drake Passage and Tasmanian deep-sea coral sampling locations could help to explore such change in more detail, in particular during transient phases and across Heinrich intervals. In this context, deep-sea corals can also provide a suitable multi-proxy archive for high resolution reconstructions of past South Pacific water mass properties, a location where sedimentation rates are otherwise low and preclude sediment-based high resolution studies. Paired with improved constraints on past SWW dynamics this could help to better understand the interaction between the Southern Ocean and the Pacific Ocean, and hence the structure of the global overturning circulation during intervals of extreme climatic boundary conditions.

# **Bibliography**

- Abernathy, R., J. Marshall, M. Mazloff, and E. Shuckburgh (2010), Enhancement of Mesoscale Eddy Stirring at Steering Levels in the Southern Ocean, *Journal of Physical Oceanography*, **40**(1), 170–184, doi:10.1175/2009JPO4201.1.
- Abernathy, R. J. Marshall, and D. Ferreira (2011), The Dependence of Southern Ocean Meridional Overturning on Wind Stress, *Journal of Physical Oceanography*, **41**(12), 2261–2278, doi: <http://dx.doi.org/10.1175/JPO-D-11-023.1>.
- Abouchami, W., S. L. Goldstein, S. J. G. Gazer, A. Eisenhauer, and A. Mangini (1997), Secular changes of lead and neodymium in central Pacific seawater recorded by a Fe-Mn crust, *Geochimica et Cosmochimica Acta*, **61**(18), 3957–3974, doi:10.1016/S0016-7037(97)00218-4.
- Adkins, J. F., and E. A. Boyle (1997), Changing Atmospheric  $\Delta^{14}\text{C}$  and the Record of Deep Water Paleoveilations Ages, *Paleoceanography*, **12**(3), 337–344, doi:10.1029/97PA00379.
- Adkins, J. F., H. Cheng, E. A. Boyle, E. R. M. Druffel, and R. L. Edwards (1998), Deep-Sea Coral Evidence for Rapid Change in Ventilation of the Deep North Atlantic 15,400 Years Ago, *Science*, **280**(5364), 725–728, doi:10.1126/science.280.5364.725.
- Adkins, J. F., E. A. Boyle, W. B. Curry, and A. Lutring (2003), Stable isotopes in deep-sea corals and a new mechanism for “vital effects”, *Geochimica et Cosmochimica Acta*, **67**(6), 1129–1143, doi:10.1016/S0016-7037(02)01203-6.
- Adkins, J. F., G. M. Henderson, S.-L. Wang, S. O’Shea, and F. Mokadem (2004), Growth rates of the deep-sea scleractinia *Desmophyllum cristagalli* and *Enallopsammia rostrata*, *Earth and Planetary Science Letters*, **227**(3–4), 481–490, doi:10.1016/j.epsl.2004.08.022.
- Adkins, J. F. (2013), The role of deep ocean circulation in setting glacial climates, *Paleoceanography*, **28**(3), 539–561, doi:10.1002/palo.20046.
- Ahn, J., and E. J. Brook (2008), Atmospheric CO<sub>2</sub> and Climate on Millennial Time Scales During the Last Glacial Period, *Science*, **322**(5898), 83–85, doi:10.1126/science.1160832.
- Ahn, J., and E. J. Brook (2014), Siple Dome ice reveals two modes of millennial CO<sub>2</sub> change during the last ice age, *Nature Communications*, **5**. [online] Available from: <http://dx.doi.org/10.1038/ncomms4723>
- Akagi, T., Y. Hashimoto, F. F-F, H. Tsuno, H. Tao, and Y. Nakano (2004), Variation of the distribution coefficients of rare earth elements in modern coral-lattices: species and site dependencies, *Geochimica et Cosmochimica Acta*, **68**(10), 2265–2273, doi:10.1016/j.gca.2003.12.014.
- Allègre, C. J., O. Brevart, B. Dupre, and J.-F. Minster (1980), Isotopic and Chemical Effects Produced in a Continuously Differentiating Convecting Earth Mantle, *Philosophical Transactions of the Royal Society of London. Series A, Mathematical and Physical Sciences*, **297**(1431), 447–477, doi:10.1098/rsta.1980.0225.
- Alvarez-Solas, J., A. Robinson, M. Montoya, and C. Ritz (2013), Iceberg discharges of the last glacial period driven by oceanic circulation changes, *Proceedings of the National Academy of Sciences*, **110**(41), 16350–16354, doi:10.1073/pnas.1306622110.
- Amakawa, H., K. Sasaki, and M. Ebihara (2009), Nd isotopic composition in the central North Pacific, *Geochimica et Cosmochimica Acta*, **73**(16), 4705–4719, doi:10.1016/j.gca.2009.05.058.
- Amakawa, H., H. Tazoe, H. Obata, T. Gamo, Y. Sano, and C.-C. Shen (2013), Neodymium isotopic composition and concentration in the Southwest Pacific Ocean, *Geochemical Journal*, **47**(4), 409–422.
- Anagnostou, E., R. M. Sherrell, A. Gagnon, M. LaVigne, M. P. Field, and W. F. McDonough (2011), Seawater nutrient and carbonate ion concentrations recorded as P/Ca, Ba/Ca, and U/Ca in the deep-sea coral *Desmophyllum dianthus*, *Geochimica et Cosmochimica Acta*, **75**(9), 2529–2543.
- Andersen, K. K. et al. (2006), The Greenland Ice Core Chronology 2005, 15–42 ka. Part 1: constructing the time scale, *Quaternary Science Reviews*, **25**(23–24), 3246–3257, doi:10.1016/j.quascirev.2006.08.002.
- Andersen, M. B., C. H. Stirling, E.-K. Potter, A. N. Halliday, S. G. Blake, M. T. McCulloch, B. F. Ayling, and M. O’Leary (2008), High-precision U-series measurements of more than 500,000 year old fossil corals, *Earth and Planetary Science Letters*, **265**(1–2), 229–245, doi:10.1016/j.epsl.2007.10.010.

- Andersen, M. B., C. H. Stirling, B. Zimmermann, and A. N. Halliday (2010), Precise determination of the open ocean  $^{234}\text{U}/^{238}\text{U}$  composition, *Geochemistry, Geophysics, Geosystems*, **11**(12), Q12003, doi:10.1029/2010GC003318.
- Anderson, R. F., S. Ali, L. I. Bradtmiller, S. H. H. Nielsen, M. Q. Fleisher, B. E. Anderson, and L. H. Burckle (2009), Wind-Driven Upwelling in the Southern Ocean and the Deglacial Rise in Atmospheric  $\text{CO}_2$ , *Science*, **323**(5920), 1443–1448, doi:10.1126/science.1167441.
- Anderson, R. F., M. Q. Fleisher, L. F. Robinson, R. L. Edwards, J. A. Hoff, S. B. Moran, M. R. van der Loeff, A. L. Thomas, M. Roy-Barman, and R. Francois (2012), GEOTRACES intercalibration of  $^{230}\text{Th}$ ,  $^{232}\text{Th}$ ,  $^{231}\text{Pa}$ , and prospects for  $^{10}\text{Be}$ , *Limnology and Oceanography: Methods*, **10**(4), 179–213, doi:10.4319/lom.2012.10.179.
- Andreasen, R., and M. Sharma (2009), Fractionation and mixing in a thermal ionization mass spectrometer source: Implications and limitations for high-precision Nd isotope analyses, *International Journal of Mass Spectrometry*, **285**(1–2), 49–57, doi:10.1016/j.ijms.2009.04.004.
- Arsouze, T., J.-C. Dutay, F. Lacan, and C. Jeandel (2009), Reconstructing the Nd oceanic cycle using a coupled dynamical – biogeochemical model, *Biogeosciences*, **6**(12), 2829–2846, doi:10.5194/bg-6-2829-2009.
- Auro, M. E., L. F. Robinson, A. Burke, L. I. Bradtmiller, M. Q. Fleisher, and R. F. Anderson (2012), Improvements to  $^{232}\text{-thorium}$ ,  $^{230}\text{-thorium}$ , and  $^{231}\text{-protactinium}$  analysis in seawater arising from GEOTRACES intercalibration, *Limnology and Oceanography: Methods*, **10**(7), 464–474, doi:10.4319/lom.2012.10.464.
- Baldwin, M. P. (2001), Annular modes in global daily surface pressure, *Geophysical Research Letters*, **28**(21), 4115–4118, doi:10.1029/2001GL013564.
- Bard, E., B. Hamelin, M. Arnold, L. Montaggioni, G. Cabioch, G. Faure, and F. Rougerie (1996), Deglacial sea-level record from Tahiti corals and the timing of global meltwater discharge, *Nature*, **382**(6588), 241–244, doi:10.1038/382241a0.
- Bard, E., F. Rostek, J.-L. Turon, and S. Gendreau (2000), Hydrological Impact of Heinrich Events in the Subtropical Northeast Atlantic, *Science*, **289**(5483), 1321–1324, doi:10.1126/science.289.5483.1321.
- Barker, S., P. Diz, M. J. Vautravers, J. Pike, G. Knorr, I. R. Hall, and W. S. Broecker (2009), Interhemispheric Atlantic seesaw response during the last deglaciation, *Nature*, **457**(7233), 1097–1102, doi:10.1038/nature07770.
- Barker, S., G. Knorr, M. J. Vautravers, P. Diz, and L. C. Skinner (2010), Extreme deepening of the Atlantic overturning circulation during deglaciation, *Nature Geoscience*, **3**(8), 567–571, doi:10.1038/ngeo921.
- Barker, S., G. Knorr, R. L. Edwards, F. Parrenin, A. E. Putnam, L. C. Skinner, E. Wolff, and M. Ziegler (2011), 800,000 Years of Abrupt Climate Variability, *Science*, **334**(6054), 347–351, doi:10.1126/science.1203580.
- Barker, S., and P. Diz (2014), Timing of the descent into the last Ice Age determined by the bipolar seesaw, *Paleoceanography*, **29**(6), 2014PA002623, doi:10.1002/2014PA002623.
- Barker, S., J. Chen, X. Gong, L. Jonkers, G. Knorr, and D. Thornalley (2015), Icebergs not the trigger for North Atlantic cold events, *Nature*, **520**(7547), 333–336.
- Barrows, T. T., and S. Juggins (2005), Sea-surface temperatures around the Australian margin and Indian Ocean during the Last Glacial Maximum, *Quaternary Science Reviews*, **24**, 1017–1047, doi:10.1016/j.quascirev.2004.07.020.
- Basak, C., E. E. Martin, K. Horikawa, and T. M. Marchitto (2010), Southern Ocean source of  $^{14}\text{C}$ -depleted carbon in the North Pacific Ocean during the last deglaciation, *Nature Geoscience*, **3**(11), 770–773, doi:10.1038/ngeo987.
- Basak, C., K. Pahnke, M. Frank, F. Lamy, and R. Gersonde (2015), Neodymium isotopic characterization of Ross Sea Bottom Water and its advection through the southern South Pacific, *Earth and Planetary Science Letters*, **419**, 211–221, doi:10.1016/j.epsl.2015.03.011.
- Baturin, G. N. (2001), Uranium and Thorium in Phosphatic Bone Debris from the Ocean Bottom, *Lithology and Mineral Resources*, **36**(2), 99–108, doi:10.1023/A:1004866215497.

- Bau, M., A. Koschinsky, P. Dulski, and J. R. Hein (1996), Comparison of the partitioning behaviours of yttrium, rare earth elements, and titanium between hydrogenetic marine ferromanganese crusts and seawater, *Geochimica et Cosmochimica Acta*, **60**(10), 1709–1725, doi:10.1016/0016-7037(96)00063-4.
- Beal, L. M., W. P. M. De Ruijter, A. Biastock, R. Zahn, and SCOR/WCRP/IAPSO working group 136 (2011), On the role of the Agulhas system in oceanic circulation and climate, *Nature*, **472**, 429–436, doi:10.1038/nature09983.
- Bentsen, M., H. Drange, T. Furevik, and T. Zhou (2004), Simulated variability of the Atlantic meridional overturning circulation, *Climate Dynamics*, **22**(6-7), 701–720, doi:10.1007/s00382-004-0397-x.
- Berger, A., and M. F. Loutre (1991), Insolation values for the climate of the last 10 million years, *Quaternary Science Reviews*, **10**(4), 297–317, doi:10.1016/0277-3791(91)90033-Q.
- Biastock, A., C. W. Boning, F. U. Schwarzkopf, and J. R. E. Lutjeharms (2009), Increase in Agulhas leakage due to poleward shift of Southern Hemisphere westerlies, *Nature*, **462**, 495–499, doi:10.1038/nature08519.
- Blunier, T. et al. (1998), Asynchrony of Antarctic and Greenland climate change during the last glacial period, *Nature*, **394**(6695), 739–743, doi:10.1038/29447.
- Blunier, T., and E. J. Brook (2001), Timing of millennial-scale climate change in Antarctica and Greenland during the last glacial period, *Science*, **291**, 109–112, doi:10.1126/science.291.5501.109.
- Böhm, E., J. Lippold, M. Gutjahr, M. Frank, P. Blaser, B. Antz, J. Fohlmeister, N. Frank, M. B. Andersen, and M. Deininger (2015), Strong and deep Atlantic meridional overturning circulation during the last glacial cycle, *Nature*, **517**(7532), 73–76.
- Bond, G. C., and R. Lotti (1995), Iceberg Discharges into the North Atlantic on Millennial Time Scales During the Last Glaciation, *Science*, **267**(5200), 1005–1010, doi:10.1126/science.267.5200.1005.
- Bond, G., W. Showers, M. Cheseby, R. Lotti, P. Almasi, P. deMenocal, P. Priore, H. Cullen, I. Hajdas, and G. Bonani (1997), A Pervasive Millennial-Scale Cycle in North Atlantic Holocene and Glacial Climates, *Science*, **278**(5341), 1257–1266, doi:10.1126/science.278.5341.1257.
- Bond, G., B. Kromer, J. Beer, R. Muscheler, M. N. Evans, W. Showers, S. Hoffmann, R. Lotti-Bond, I. Hajdas, and G. Bonani (2001), Persistent Solar Influence on North Atlantic Climate During the Holocene, *Science*, **294**(5549), 2130–2136, doi:10.1126/science.1065680.
- Böning, C. W., A. Dispert, M. Visbeck, S. R. Rintoul, and F. U. Schwarzkopf (2008), The response of the Antarctic Circumpolar Current to recent climate change, *Nature Geoscience*, **1**(12), 864–869, doi:10.1038/ngeo362.
- Bostock, H. C., P. J. Sutton, M. J. M. Williams, and B. N. Opdyke (2013), Reviewing the circulation and mixing of Antarctic Intermediate Water in the South Pacific using evidence from geochemical tracers and Argo float trajectories, *Deep Sea Research Part I: Oceanographic Research Papers*, **73**, 84–98, doi:10.1016/j.dsr.2012.11.007.
- Brearley, J. A., K. L. Sheen, A. C. Naveira Garabato, D. A. Smeed, K. G. Speer, A. M. Thurnherr, M. P. Meredith, and S. Waterman (2014), Deep boundary current disintegration in Drake Passage, *Geophysical Research Letters*, **41**(1), 2013GL058617, doi:10.1002/2013GL058617.
- Broecker, W. S. (1982), Ocean chemistry during glacial time, *Geochimica et Cosmochimica Acta*, **46**(10), 1689–1705, doi:10.1016/0016-7037(82)90110-7.
- Broecker, W. S., M. Andree, G. Bonani, W. Wolfli, H. Oeschger, M. Klas, A. Mix, and W. Curry (1988), Preliminary estimates for the radiocarbon age of deep water in the glacial ocean, *Paleoceanography*, **3**(6), 659–669, doi:10.1029/PA003i006p00659.
- Broecker, W. S., and G. H. Denton (1989), The role of ocean-atmosphere reorganizations in glacial cycles, *Geochimica et Cosmochimica Acta*, **53**(10), 2465–2501, doi:10.1016/0016-7037(89)90123-3.
- Broecker, W. S., G. Bond, M. Klas, G. Bonani, and W. Wolfli (1990), A Salt Oscillator in the Glacial Atlantic? I. The Concept, *Paleoceanography*, **5**(4), 469–477, doi:10.1029/PA005i004p00469.
- Broecker, W. S. (1991), The Great Ocean Conveyor, *Oceanography*, **4**(2), 79–89.

- Broecker, W. S. (1998), Paleoocean Circulation during the Last Deglaciation: A Bipolar Seesaw?, *Paleoceanography*, **13**(2), 119–121, doi:10.1029/97PA03707.
- Broecker, W., and S. Barker (2007), A 190‰ drop in atmosphere's  $\Delta^{14}\text{C}$  during the “Mystery Interval” (17.5 to 14.5 kyr), *Earth and Planetary Science Letters*, **256**(1–2), 90–99, doi:10.1016/j.epsl.2007.01.015.
- Broecker, W., E. Clark, S. Barker, I. Hajdas, G. Bonani, and E. Moreno (2007), Radiocarbon age of late glacial deep water from the equatorial Pacific, *Paleoceanography*, **22**(2), PA2206, doi:10.1029/2006PA001359.
- Brook, E. J., S. Harder, J. Severinghaus, E. J. Steig, and C. M. Sucher (2000), On the origin and timing of rapid changes in atmospheric methane during the Last Glacial Period, *Global Biogeochem. Cycles*, **14**(2), 559–572, doi:10.1029/1999GB001182.
- Bryan, F. (1987), Parameter Sensitivity of Primitive Equation Ocean General Circulation Models, *Journal of Physical Oceanography*, **17**(7), 970–985, doi:10.1175/1520-0485(1987)017<0970:PSOPEO>2.0.CO;2.
- Bryan, S. P., T. M. Marchitto, and S. J. Lehman (2010), The release of  $^{14}\text{C}$ -depleted carbon from the deep ocean during the last deglaciation: Evidence from the Arabian Sea, *Earth and Planetary Science Letters*, **298**(1–2), 244–254, doi:10.1016/j.epsl.2010.08.025.
- Burke, A., L. F. Robinson, A. P. McNichol, W. J. Jenkins, K. M. Scanlon, and D. S. Gerlach (2010), Reconnaissance dating: A new radiocarbon method applied to assessing the temporal distribution of Southern Ocean deep-sea corals, *Deep Sea Research Part I: Oceanographic Research Papers*, **57**(11), 1510–1520, doi:10.1016/j.dsr.2010.07.010.
- Burke, A. (2012): *Constraining Circulation Changes Through the Last Deglaciation with Deep-sea Coral Radiocarbon and Sedimentary  $^{231}\text{Pa}/^{230}\text{Th}$* , PhD thesis, MIT/WHOI.
- Burke, A., and L. F. Robinson (2012), The Southern Ocean's Role in Carbon Exchange During the Last Deglaciation, *Science*, **335**(6068), 557–561, doi:10.1126/science.1208163.
- Burton, K. W., H.-F. Ling, and R. K. O'Nions (1997), Closure of the Central American Isthmus and its effect on deep-water formation in the North Atlantic, *Nature*, **386**(6623), 382–385, doi:10.1038/386382a0.
- Burton, K. W., and D. Vance (2000), Glacial-interglacial variations in the neodymium isotope composition of seawater in the Bay of Bengal recorded by planktonic foraminifera, *Earth and Planetary Science Letters*, **176**(3–4), 425–441, doi:doi: 10.1016/S0012-821X(00)00011-X.
- Byrne, R. H., and K.-H. Kim (1990), Rare earth element scavenging in seawater, *Geochimica et Cosmochimica Acta*, **54**(10), 2645–2656, doi:10.1016/0016-7037(90)90002-3.
- Byrne, R. H., and B. Li (1995), Comparative complexation behavior of the rare earths, *Geochimica et Cosmochimica Acta*, **59**(22), 4575–4589, doi:10.1016/0016-7037(95)00303-7.
- Cacho, I., J. O. Grimalt, F. J. Sierro, N. Shackleton, and M. Canals (2000), Evidence for enhanced Mediterranean thermohaline circulation during rapid climatic coolings, *Earth and Planetary Science Letters*, **183**(3–4), 417–429, doi:10.1016/S0012-821X(00)00296-X.
- Cairns, S. D. (1982), Antarctic and Subantarctic Scleractinia, in *Antarctic Research Series*, **34**, edited by L. S. Kornicker, pp. 1–74, American Geophysical Union, available from: <http://dx.doi.org/10.1029/AR034p0001>.
- Cairns, S. D. (2007), Deep-water corals: an overview with special reference to diversity and distribution of deep-water scleractinian corals, *Bulletin of Marine Science*, **81**(3), 311–322.
- Cairns, S. D., and M. V. Kitahara (2012), An illustrated key to the genera and subgenera of the recent azooxanthellate Scleractinia (Cnidaria, Anthozoa), with an attached glossary, *ZooKeys*, (227), 1–47, doi:10.3897/zookeys.227.3612.
- Callahan, J. E. (1972), The structure and circulation of deep water in the Antarctic, *Deep Sea Research and Oceanographic Abstracts*, **19**(8), 563–575, doi:10.1016/0011-7471(72)90040-X.
- Caniupán, M. et al. (2011), Millennial-scale sea surface temperature and Patagonian Ice Sheet changes off southernmost Chile (53°S) over the past ~60 kyr, *Paleoceanography*, **26**(3), PA3221, doi:10.1029/2010PA002049.
- Cantrell, K. J., and R. H. Byrne (1987), Rare earth element complexation by carbonate and oxalate ions, *Geochimica et Cosmochimica Acta*, **51**(3), 597–605, doi:10.1016/0016-7037(87)90072-X.

- Carlson, A. E., D. W. Oppo, R. E. Came, A. N. LeGrande, L. D. Keigwin, and W. B. Curry (2008), Subtropical Atlantic salinity variability and Atlantic meridional circulation during the last deglaciation, *Geology*, **36**(12), 991–994, doi:10.1130/G25080A.1.
- Carter, P., D. Vance, C. D. Hillenbrand, J. A. Smith, and D. R. Shoosmith (2012), The neodymium isotopic composition of water masses in the eastern Pacific sector of the Southern Ocean, *Geochimica et Cosmochimica Acta*, **79**, 41–59, doi:10.1016/j.gca.2011.11.034.
- Cerovečki, I., L. D. Talley, M. R. Mazloff, and G. Maze (2012), Subantarctic Mode Water Formation, Destruction, and Export in the Eddy-Permitting Southern Ocean State Estimate, *Journal of Physical Oceanography*, **43**(7), 1485–1511, doi:10.1175/JPO-D-12-0121.1.
- Chappellaz, J., T. Blunier, D. Raynaud, J. M. Barnola, J. Schwander, and B. Stauffert (1993), Synchronous changes in atmospheric CH<sub>4</sub> and Greenland climate between 40 and 8 kyr BP, *Nature*, **366**(6454), 443–445, doi:10.1038/366443a0.
- Charlier, B. L. A., C. Ginibre, D. Morgan, G. M. Nowell, D. G. Pearson, J. P. Davidson, and C. J. Ottley (2006), Methods for the microsampling and high-precision analysis of strontium and rubidium isotopes at single crystal scale for petrological and geochronological applications, *Chemical Geology*, **232**(3–4), 114–133, doi:10.1016/j.chemgeo.2006.02.015.
- Chen, T., L. F. Robinson, A. Burke, J. Southon, P. Spooner, P. J. Morris and H. C. Ng (2015): Synchronous Centennial Abrupt Events in the Ocean and Atmosphere during the Last Deglaciation, *Science*, **349**(6255), 1537–1541, doi: 10.1126/science.aac6159.
- Cheng, H., J. Adkins, R. L. Edwards, and E. A. Boyle (2000), U-Th dating of deep-sea corals, *Geochimica et Cosmochimica Acta*, **64**(14), 2401–2416, doi:10.1016/S0016-7037(99)00422-6.
- Clark, P. U., A. S. Dyke, J. D. Shakun, A. E. Carlson, J. Clark, B. Wohlfarth, J. X. Mitrovica, S. W. Hostetler, and A. M. McCabe (2009), The Last Glacial Maximum, *Science*, **325**(5941), 710–714, doi:10.1126/science.1172873.
- Close, S. E., A. C. Naveira Garabato, E. L. McDonagh, B. A. King, M. Biuw, and L. Boehme (2013), Control of Mode and Intermediate Water Mass Properties in Drake Passage by the Amundsen Sea Low, *Journal of Climate*, **26**(14), 5102–5123, doi:10.1175/JCLI-D-12-00346.1.
- Cohen, A. S., R. K. O’Nions, R. Siegenthaler, and W. L. Griffin (1988), Chronology of the pressure-temperature history recorded by a granulite terrain, *Contributions to Mineralogy and Petrology*, **98**(3), 303–311, doi:10.1007/BF00375181.
- Colin, C., N. Frank, K. Copard, and E. Douville (2010), Neodymium isotopic composition of deep-sea corals from the NE Atlantic: implications for past hydrological changes during the Holocene, *Quaternary Science Reviews*, **29**(19–20), 2509–2517, doi:10.1016/j.quascirev.2010.05.012.
- Cook, A. J., A. J. Fox, D. G. Vaughan, and J. G. Ferrigno (2005), Retreating Glacier Fronts on the Antarctic Peninsula over the Past Half-Century, *Science*, **308**(5721), 541–544, doi:10.1126/science.1104235.
- Cook, C. P. et al. (2013), Dynamic behaviour of the East Antarctic ice sheet during Pliocene warmth, *Nature Geoscience*, **6**(9), 765–769.
- Copard, K., C. Colin, E. Douville, A. Freiwald, G. Gudmundsson, B. De Mol, and N. Frank (2010), Nd isotopes in deep-sea corals in the North-eastern Atlantic, *Quaternary Science Reviews*, **29**(19–20), 2499–2508, doi:10.1016/j.quascirev.2010.05.025.
- Copard, K., C. Colin, N. Frank, C. Jeandel, J.-C. Montero-Serrano, G. Reverdin, and B. Ferron (2011), Nd isotopic composition of water masses and dilution of the Mediterranean outflow along the southwest European margin, *Geochemistry, Geophysics, Geosystems*, **12**(6), Q06020, doi:10.1029/2011GC003529.
- Copard, K., C., Colin, G. M., Henderson, J., Scholten, E., Douville, M.-A., Sicre, and N., Frank (2012), Late Holocene intermediate water variability in the northeastern Atlantic as recorded by deep-sea corals, *Earth and Planetary Science Letters*, **313–314**, 34–44.
- Crocket, K. C., D. Vance, M. Gutjahr, G. L. Foster, and D. A. Richards (2011), Persistent Nordic deep-water overflow to the glacial North Atlantic, *Geology*, **39**(6), 515–518, doi:10.1130/G31677.1.

- Crocket, K. C., M. Lambelet, T. van de Flierdt, M. Rehkämper, and L. F. Robinson (2014), Measurement of fossil deep-sea coral Nd isotopic compositions and concentrations by TIMS as NdO<sup>+</sup>, with evaluation of cleaning protocols, *Chemical Geology*, **374–375**, 128–140, doi:10.1016/j.chemgeo.2014.03.011.
- Cuif, J.-P., and Y. Dauphin (1998), Microstructural and physico-chemical characterization of ‘centers of calcification’ in septa of some recent scleractinian corals, *Paläontologische Zeitschrift*, **72(3-4)**, 257–269, doi:10.1007/BF02988357.
- Cuif, J.-P., Y. Dauphin, and P. Gautret (1999), Compositional diversity of soluble mineralizing matrices in some recent coral skeletons compared to fine-scale growth structures of fibres: discussion of consequences for biomineralization and diagenesis, *International Journal of Earth Sciences*, **88(3)**, 582–592, doi:10.1007/s005310050286.
- Cuif, J.-P., Y. Dauphin, J. Doucet, M. Salome, and J. Susini (2003), XANES mapping of organic sulfate in three scleractinian coral skeletons, *Geochimica et Cosmochimica Acta*, **67(1)**, 75–83, doi:10.1016/S0016-7037(02)01041-4.
- Cuif, J.-P., Y. Dauphin, P. Berthet, and J. Jegoudez (2004), Associated water and organic compounds in coral skeletons: Quantitative thermogravimetry coupled to infrared absorption spectrometry, *Geochemistry, Geophysics, Geosystems*, **5(11)**, Q11011, doi:10.1029/2004GC000783.
- Cuif, J. P., and Y. Dauphin (2005), The Environment Recording Unit in coral skeletons &ndash; a synthesis of structural and chemical evidences for a biochemically driven, stepping-growth process in fibres, *Biogeosciences*, **2(1)**, 61–73, doi:10.5194/bg-2-61-2005.
- Cunningham, S. A., S. G. Alderson, B. A. King, and M. A. Brandon (2003), Transport and variability of the Antarctic Circumpolar Current in Drake Passage, *Journal of Geophysical Research*, **108(C5)**, 8084, doi:10.1029/2001JC001147.
- Curry, W. B., and D. W. Oppo (2005), Glacial water mass geometry and the distribution of  $\delta^{13}\text{C}$  of  $\Sigma\text{CO}_2$  in the western Atlantic Ocean, *Paleoceanography*, **20(1)**, PA1017, doi:10.1029/2004PA001021.
- Dalziel, I. (2015), *Calibrated Hydrographic Data from Drake Passage acquired with a CTD during the Nathaniel B. Palmer expedition NBP0805 (2008)*, Integrated Earth Data Applications (IEDA), <http://doi.org/10.1594/IEDA/313716>.
- Dansgaard, W. et al. (1993), Evidence for general instability of past climate from a 250-kyr ice-core record, *Nature*, **364(6434)**, 218–220, doi:10.1038/364218a0.
- Dauphin, Y., J.-P. Cuif, and P. Massard (2006), Persistent organic components in heated coral aragonitic skeletons—Implications for palaeoenvironmental reconstructions, *Chemical Geology*, **231(1–2)**, 26–37, doi:10.1016/j.chemgeo.2005.12.010.
- Davies-Walczak, M., A. C. Mix, J. S. Stoner, J. R. Southon, M. Cheseby, and C. Xuan (2014), Late Glacial to Holocene radiocarbon constraints on North Pacific Intermediate Water ventilation and deglacial atmospheric CO<sub>2</sub> sources, *Earth and Planetary Science Letters*, **397**, 57–66, doi:10.1016/j.epsl.2014.04.004.
- De Baar, H. J. W., M. P. Bacon, P. G. Brewer, and K. W. Bruland (1985), Rare earth elements in the Pacific and Atlantic Oceans, *Geochimica et Cosmochimica Acta*, **49(9)**, 1943–1959, doi:10.1016/0016-7037(85)90089-4.
- Decloedt, T., and D. S. Luther (2010), On a Simple Empirical Parameterization of Topography-Catalyzed Diapycnal Mixing in the Abyssal Ocean, *Journal of Physical Oceanography*, **40(3)**, 487–508, doi:10.1175/2009JPO4275.1.
- De Deckker, P., M. Moros, K. Perner, and E. Jansen (2012), Influence of the tropics and southern westerlies on glacial interhemispheric asymmetry, *Nature Geoscience*, **5(4)**, 266–269, doi:10.1038/ngeo1431.
- Delworth, T. L., and F. Zeng (2008), Simulated impact of altered Southern Hemisphere winds on the Atlantic Meridional Overturning Circulation, *Geophysical Research Letters*, **35(20)**, L20708, doi:10.1029/2008GL035166.
- DePaolo, D. J. (1980), Crustal growth and mantle evolution: inferences from models of element transport and Nd and Sr isotopes, *Geochimica et Cosmochimica Acta*, **44(8)**, 1185–1196, doi:doi:10.1016/0016-7037(80)90072-1.

- Deplazes, G., A. Lückge, J.-B. W. Stuut, J. Pätzold, H. Kuhlmann, D. Husson, M. Fant, and G. H. Haug (2014), Weakening and strengthening of the Indian monsoon during Heinrich events and Dansgaard-Oeschger oscillations, *Paleoceanography*, **29**(2), 99–114, doi:10.1002/2013PA002509.
- De Pol-Holz, R., L. Keigwin, J. Southon, D. Hebbeln, and M. Mohtadi (2010), No signature of abyssal carbon in intermediate waters off Chile during deglaciation, *Nature Geoscience*, **3**(3), 192–195, doi:10.1038/ngeo745.
- Dickson, R., J. Lazier, J. Meincke, P. Rhines, and J. Swift (1996), Long-term coordinated changes in the convective activity of the North Atlantic, *Progress In Oceanography*, **38**(3), 241–295, doi:10.1016/S0079-6611(97)00002-5.
- Dulski, T. R. (1996), A Manual for the Chemical Analysis of Metals, *ASTM Manual Series*, **25**, ASTM, West Conshohocken, PA, doi: 10.1520/MNL25-EB.
- Duplessy, J.-C., L. Labeyrie, and C. Waelbroeck (2002), Constraints on the ocean oxygen isotopic enrichment between the Last Glacial Maximum and the Holocene: Paleoceanographic implications, *Quaternary Science Reviews*, **21**(1–3), 315–330, doi:10.1016/S0277-3791(01)00107-X.
- Durgadoo, J. V., B. R. Loveday, C. J. C. Reason, P. Penven, and A. Biastoch (2013), Agulhas Leakage Predominantly Responds to the Southern Hemisphere Westerlies, *Journal of Physical Oceanography*, **43**(10), 2113–2131, doi:10.1175/JPO-D-13-047.1.
- Dyez, K. A., R. Zahn, and I. R. Hall (2014), Multicentennial Agulhas leakage variability and links to North Atlantic climate during the past 80,000 years, *Paleoceanography*, **29**(12), 2014PA002698, doi:10.1002/2014PA002698.
- Edwards, R. ., J. H. Chen, and G. J. Wasserburg (1987), <sup>238</sup>U/<sup>234</sup>U/<sup>230</sup>Th/<sup>232</sup>Th systematics and the precise measurement of time over the past 500,000 years, *Earth and Planetary Science Letters*, **81**(2–3), 175–192, doi:10.1016/0012-821X(87)90154-3.
- Elderfield, H., and M. J. Greaves (1982), The rare earth elements in seawater, *Nature*, **296**(5854), 214–219, doi:10.1038/296214a0.
- Elderfield, H., and R. Pagett (1986), Rare earth elements in ichthyoliths: Variations with redox conditions and depositional environment, *Science of the Total Environment*, **49**, 175–197, doi:10.1016/0048-9697(86)90239-1.
- Elderfield, H., R. Upstill-Goddard, and E. R. Sholkovitz (1990), The rare earth elements in rivers, estuaries, and coastal seas and their significance to the composition of ocean waters, *Geochimica et Cosmochimica Acta*, **54**(4), 971–991, doi:10.1016/0016-7037(90)90432-K.
- Elderfield, H., P. Ferretti, M. Greaves, S. Crowhurst, I. N. McCave, D. Hodell, and A. M. Piotrowski (2012), Evolution of Ocean Temperature and Ice Volume Through the Mid-Pleistocene Climate Transition, *Science*, **337**(6095), 704–709, doi:10.1126/science.1221294.
- Elias, S. A., S. K. Short, and H. H. Birks (1997), Late Wisconsin environments of the Bering Land Bridge, *Palaeogeography, Palaeoclimatology, Palaeoecology*, **136**(1–4), 293–308, doi:10.1016/S0031-0182(97)00038-2.
- Eltgroth, S. F., J. F. Adkins, L. F. Robinson, J. Southon, and M. Kashgarian (2006), A deep-sea coral record of North Atlantic radiocarbon through the Younger Dryas: Evidence for intermediate water/deepwater reorganization, *Paleoceanography*, **21**(4), PA4207, doi:10.1029/2005PA001192.
- Emile-Geay, J., M. A. Cane, N. Naik, R. Seager, A. C. Clement, and A. van Geen (2003), Warren revisited: Atmospheric freshwater fluxes and “Why is no deep water formed in the North Pacific”, *Journal of Geophysical Research*, **108**(C6), 3178, doi:10.1029/2001JC001058.
- EPICA community members (2006), One-to-one coupling of glacial climate variability in Greenland and Antarctica, *Nature*, **444**, 195–198, doi:10.1038/nature05301.
- EPICA community members (2010): Stable oxygen isotopes of ice core EDML. doi:10.1594/PANGAEA.754444
- Fairbanks, R. G. (1989), A 17,000-year glacio-eustatic sea level record: influence of glacial melting rates on the Younger Dryas event and deep-ocean circulation, *Nature*, **342**(6250), 637–642, doi:10.1038/342637a0.

- Faris, J. P., and R. F. Buchanan (1964), Anion Exchange Characteristics of the Elements in Nitric Acid Medium, *Analytical Chemistry*, **36**(6), 1157–1158, doi:10.1021/ac60212a067.
- Feldberg, M. J., and A. C. Mix (2002), Sea-surface temperature estimates in the Southeast Pacific based on planktonic foraminiferal species; modern calibration and Last Glacial Maximum, *Marine Micropaleontology*, **44**(1–2), 1–29, doi:10.1016/S0377-8398(01)00035-4.
- Ferrari, R., M. F. Jansen, J. F. Adkins, A. Burke, A. L. Stewart, and A. F. Thompson (2014), Antarctic sea ice control on ocean circulation in present and glacial climates, *Proceedings of the National Academy of Sciences*, **111**(24), 8753–8758, doi:10.1073/pnas.1323922111.
- Fischer, H. et al. (2007), Reconstruction of millennial changes in dust emission, transport and regional sea ice coverage using the deep EPICA ice cores from the Atlantic and Indian Ocean sector of Antarctica, *Earth and Planetary Science Letters*, **260**(1–2), 340–354, doi:10.1016/j.epsl.2007.06.014.
- Flückiger, J., R. Knutti, and J. W. C. White (2006), Oceanic processes as potential trigger and amplifying mechanisms for Heinrich events, *Paleoceanography*, **21**(2), PA2014, doi:10.1029/2005PA001204.
- Foster, G. L., and D. Vance (2006), Negligible glacial-interglacial variation in continental chemical weathering rates, *Nature*, **444**(7121), 918–921, doi:10.1038/nature05365.
- Frank, M. (2002), Radiogenic isotopes: Tracers of past ocean circulation and erosional input, *Reviews of Geophysics*, **40**(1), 1001, doi:10.1029/2000RG000094.
- Frank, N., M. Paterne, L. Ayliffé, T. van Weering, J.-P. Henriot, and D. Blamart (2004), Eastern North Atlantic deep-sea corals: tracing upper intermediate water  $\Delta^{14}\text{C}$  during the Holocene, *Earth and Planetary Science Letters*, **219**(3–4), 297–309, doi:10.1016/S0012-821X(03)00721-0.
- Freeman, E., L. C. Skinner, A. Tisserand, T. Dokken, A. Timmermann, L. Menviel, and T. Friedrich (2015), An Atlantic–Pacific ventilation seesaw across the last deglaciation, *Earth and Planetary Science Letters*, **424**, 237–244, doi:10.1016/j.epsl.2015.05.032.
- Freiwald, A., J. H., Fosså, A. J. Grehan, T. Koslow and J. M. Roberts (2004), Cold-Water Coral Reefs, *UNEP-WCMC Biodiversity Series*, **22**, 1–85.
- Frost, C. D., and D. S. Coombs (1989), Nd isotope character of New Zealand sediments; implications for terrane concepts and crustal evolution, *American Journal of Science*, **289**(6), 744–770, doi:10.2475/ajs.289.6.744.
- Fusco, G., V. Artale, Y. Cotroneo, and G. Sannino (2008), Thermohaline variability of Mediterranean Water in the Gulf of Cadiz, 1948–1999, *Deep Sea Research Part I: Oceanographic Research Papers*, **55**(12), 1624–1638, doi:10.1016/j.dsr.2008.07.009.
- Fyfe, J. C., and O. A. Saenko (2006), Simulated changes in the extratropical Southern Hemisphere winds and currents, *Geophysical Research Letters*, **33**(6), L06701, doi:10.1029/2005GL025332.
- Ganachaud, A., and C. Wunsch (2000), Improved estimates of global ocean circulation, heat transport and mixing from hydrographic data, *Nature*, **408**(6811), 453–457, doi:10.1038/35044048.
- Ganopolski, A., S. Rahmstorf, V. Petoukhov, and M. Claussen (1998), Simulation of modern and glacial climates with a coupled global model of intermediate complexity, *Nature*, **391**(6665), 351–356, doi:10.1038/34839.
- Garcia, H. E., R. A. Locarnini, T. P. Boyer, J. I. Antonov, O. K. Baranova, M. M. Zweng, J. R. Reagan, D. R. Johnson, (2013), World Ocean Atlas 2013, Volume 3: Dissolved Oxygen, Apparent Oxygen Utilization, and Oxygen Saturation. Ed.: S. Levitus, Technical Ed.: A. Mishonov, *NOAA Atlas NESDIS 75*, 27 pp.
- Garcia-Solsona, E., C. Jeandel, M. Labatut, F. Lacan, D. Vance, V. Chavagnac, and C. Pradoux (2014), Rare earth elements and Nd isotopes tracing water mass mixing and particle-seawater interactions in the SE Atlantic, *Geochimica et Cosmochimica Acta*, **125**, 351–372, doi:10.1016/j.gca.2013.10.009.
- Gascard, J. C. (1978), Mediterranean deep-water formation baroclinic instability and oceanic eddies, *Oceanologica Acta*, **1**(3), 315–330.

- Gass, S. E., and J. M. Roberts (2006), The occurrence of the cold-water coral *Lophelia pertusa* (Scleractinia) on oil and gas platforms in the North Sea: Colony growth, recruitment and environmental controls on distribution, *Marine Pollution Bulletin.*, **52**(5), 549–559, doi:10.1016/j.marpolbul.2005.10.002.
- Gault-Ringold, M., and C. H. Stirling (2012), Anomalous isotopic shifts associated with organic resin residues during cadmium isotopic analysis by double spike MC-ICPMS, *Journal of Analytical Atomic Spectrometry*, **27**(3), 449–459, doi:10.1039/C2JA10360E.
- German, C. R., G. P. Klinkhammer, J. M. Edmond, A. Mura, and H. Elderfield (1990), Hydrothermal scavenging of rare-earth elements in the ocean, *Nature*, **345**(6275), 516–518, doi:10.1038/345516a0.
- Gersonde, R., X. Crosta, A. Abelmann, and L. Armand (2005), Sea-surface temperature and sea ice distribution of the Southern Ocean at the EPILOG Last Glacial Maximum—a circum-Antarctic view based on siliceous microfossil records, *Quaternary Science Reviews*, **24**(7–9), 869–896, doi:10.1016/j.quascirev.2004.07.015.
- Gherardi, J.-M., L. Labeyrie, J. F. McManus, R. Francois, L. C. Skinner, and E. Cortijo (2005), Evidence from the Northeastern Atlantic basin for variability in the rate of the meridional overturning circulation through the last deglaciation, *Earth and Planetary Science Letters*, **240**(3–4), 710–723, doi:10.1016/j.epsl.2005.09.061.
- Gherardi, J. -M., L. Labeyrie, S. Nave, R. Francois, J. F. McManus, and E. Cortijo (2009), Glacial-interglacial circulation changes inferred from <sup>231</sup>Pa/<sup>230</sup>Th sedimentary record in the North Atlantic region, *Paleoceanography*, **24**(2), PA2204, doi:10.1029/2008PA001696.
- Gibb, O. T., C. Hillaire-Marcel, and A. de Vernal (2014), Oceanographic regimes in the northwest Labrador Sea since Marine Isotope Stage 3 based on dinocyst and stable isotope proxy records, *Quaternary Science Reviews*, **92**, 269–279, doi:10.1016/j.quascirev.2013.12.010.
- Gille, S. T. (2002), Warming of the Southern Ocean Since the 1950s, *Science*, **295**(5558), 1275–1277, doi:10.1126/science.1065863.
- Gille, S. T. (2008), Decadal-Scale Temperature Trends in the Southern Hemisphere Ocean, *Journal of Climate*, **21**(18), 4749–4765, doi:10.1175/2008JCLI2131.1.
- Gingele, F. X., and P. De Deckker (2005), Clay mineral, geochemical and Sr–Nd isotopic fingerprinting of sediments in the Murray–Darling fluvial system, southeast Australia, *Australian Journal of Earth Sciences*, **52**, 965–974, doi: 10.1080/08120090500302301.
- Goddard, P. B., J. Yin, S. M. Griffies, and S. Zhang (2015), An extreme event of sea-level rise along the Northeast coast of North America in 2009–2010, *Nature Communications*, **6**.
- Goldstein, S. L., R. K. O’Nions, and P. J. Hamilton (1984), A Sm–Nd isotopic study of atmospheric dusts and particulates from major river systems, *Earth and Planetary Science Letters*, **70**(2), 221–236, doi: 10.1016/0012-821X(84)90007-4.
- Goldstein, S. J., and S. B. Jacobsen (1988), Nd and Sr isotopic systematics of river water suspended material: implications for crustal evolution, *Earth and Planetary Science Letters*, **87**(3), 249–265, doi: 10.1016/0012-821X(88)90013-1.
- Goldstein, S. J., D. W. Lea, S. Chakraborty, M. Kashgarian, and M. T. Murrell (2001), Uranium-series and radiocarbon geochronology of deep-sea corals: implications for Southern Ocean ventilation rates and the oceanic carbon cycle, *Earth and Planetary Science Letters*, **193**(1–2), 167–182, doi:10.1016/S0012-821X(01)00494-0.
- Goldstein, S. L., and S. R. Hemming (2003), Long-lived Isotopic Tracers in Oceanography, Paleoceanography, and Ice-sheet Dynamics, in *Treatise on Geochemistry*, vol. 6, edited by H. Elderfield, pp. 453–489, Elsevier, Pergamon, Oxford, doi: 10.1016/B0-08-043751-6/06179-X.
- Greaves, M. ., H. Elderfield, and E. . Sholkovitz (1999), Aeolian sources of rare earth elements to the Western Pacific Ocean, *Marine Chemistry*, **68**(1-2), 31–38, doi:doi: 10.1016/S0304-4203(99)00063-8.
- Grenier, M., C. Jeandel, F. Lacan, D. Vance, C. Venchiarutti, A. Cros, and S. Cravatte (2013), From the subtropics to the central equatorial Pacific Ocean: Neodymium isotopic composition and rare earth element concentration variations, *Journal of Geophysical Research - Oceans*, **118**(2), 592–618, doi:10.1029/2012JC008239.

- Gutjahr, M., M. Frank, C. H. Stirling, V. Klemm, T. van de Flierdt, and A. N. Halliday (2007), Reliable extraction of a deepwater trace metal isotope signal from Fe-Mn oxyhydroxide coatings of marine sediments, *Chemical Geology*, **242**(3-4), 351–370, doi:10.1016/j.chemgeo.2007.03.021.
- Hall, I. R., I. N. McCave, N. J. Shackleton, G. P. Weedon, and S. E. Harris (2001), Intensified deep Pacific inflow and ventilation in Pleistocene glacial times, *Nature*, **412**(6849), 809–812, doi:10.1038/35090552.
- Hall, A., and M. Visbeck (2002), Synchronous Variability in the Southern Hemisphere Atmosphere, Sea Ice, and Ocean Resulting from the Annular Mode, *Journal of Climate*, **15**(21), 3043–3057, doi:10.1175/1520-0442(2002)015<3043:SVITSH>2.0.CO;2.
- Halliday, A. N., J. P. Davidson, P. Holden, R. M. Owen, and A. M. Olivarez (1992), Metalliferous sediments and the scavenging residence time of Nd near hydrothermal vents, *Geophysical Research Letters*, **19**(8), 761–764, doi:10.1029/92GL00393.
- Hanebuth, T. J. J., W. Zhang, A. L. Hofmann, L. A. Löwemark, and T. Schwenk (2015), Oceanic density fronts steering bottom-current induced sedimentation deduced from a 50 ka contourite-drift record and numerical modeling (off NW Spain), *Quaternary Science Reviews*, **112**, 207–225, doi:10.1016/j.quascirev.2015.01.027.
- Hathorne, E. C., T. Stichel, B. Brück, and M. Frank (2015), Rare earth element distribution in the Atlantic sector of the Southern Ocean: The balance between particle scavenging and vertical supply, *Marine Chemistry*, **177**(1), 157–171, doi:10.1016/j.marchem.2015.03.011. [online] Available from: <http://www.sciencedirect.com/science/article/pii/S0304420315000651>
- Hays, J. D., J. Imbrie, and N. J. Shackleton (1976), Variations in the Earth's Orbit: Pacemaker of the Ice Ages, *Science*, **194**(4270), 1121–1132, doi:10.1126/science.194.4270.1121.
- Heath, R. A. (1981), Oceanic fronts around southern New Zealand, *Deep Sea Research Part A. Oceanographic Research Papers*, **28**(6), 547–560, doi:10.1016/0198-0149(81)90116-3.
- Hebbeln, D., M. Marchant, and G. Wefer (2002), Paleoproductivity in the southern Peru–Chile Current through the last 33000 yr, *Marine Geology*, **186**(3–4), 487–504, doi:10.1016/S0025-3227(02)00331-6.
- Hegner, E., H. J. Dauelsberg, M. M. Rutgers van der Loeff, C. Jeandel, and H. J. W. de Baar (2007), Nd isotopic constraints on the origin of suspended particles in the Atlantic Sector of the Southern Ocean, *Geochemistry Geophysics Geosystems*, **8**(10), Q10008, doi:10.1029/2007GC001666.
- Hemming, S. R. (2004), Heinrich events: Massive late Pleistocene detritus layers of the North Atlantic and their global climate imprint, *Reviews of Geophysics*, **42**(1), RG1005, doi:10.1029/2003RG000128.
- Henderson, G. M., and R. F. Anderson (2003), The U-series Toolbox for Paleoceanography, *Reviews in Mineralogy and Geochemistry*, **52**(1), 493–531, doi:10.2113/0520493.
- Henry, L.-A. et al. (2014), Global ocean conveyor lowers extinction risk in the deep sea, *Deep Sea Research Part I: Oceanographic Research Papers*, **88**, 8–16, doi:10.1016/j.dsr.2014.03.004.
- Hillaire-Marcel, C., A. de Vernal, G. Bilodeau, and A. J. Weaver (2001), Absence of deep-water formation in the Labrador Sea during the last interglacial period, *Nature*, **410**(6832), 1073–1077, doi:10.1038/35074059.
- Hillaire-Marcel, C., A. de Vernal, and J. McKay (2011), Foraminifer isotope study of the Pleistocene Labrador Sea, northwest North Atlantic (IODP Sites 1302/03 and 1305), with emphasis on paleoceanographical differences between its “inner” and “outer” basins, *Marine Geology*, **279**(1–4), 188–198, doi:10.1016/j.margeo.2010.11.001.
- Hillenbrand, C.-D. et al. (2012), Grounding-line retreat of the West Antarctic Ice Sheet from inner Pine Island Bay, *Geology*, **41**(1), 35–38, doi:10.1130/G33469.1.
- Hines, S. K. V., J. R. Southon, and J. F. Adkins (2015), A high-resolution record of Southern Ocean intermediate water radiocarbon over the past 30,000 years, *Earth and Planetary Science Letters*, **432**, 46–58, doi:10.1016/j.epsl.2015.09.038.
- Hodell, D. A., K. A. Venz, C. D. Charles, and U. S. Ninnemann (2003), Pleistocene vertical carbon isotope and carbonate gradients in the South Atlantic sector of the Southern Ocean, *Geochemistry Geophysics Geosystems*, **4**(1), 1004, doi:10.1029/2002GC000367.

- Holland, P. R., A. Jenkins, and D. M. Holland (2010), Ice and ocean processes in the Bellingshausen Sea, Antarctica, *Journal of Geophysical Research*, **115**(C5), C05020, doi:10.1029/2008JC005219.
- Hoogakker, B. A. A., M. R. Chapman, I. N. McCave, C. Hillaire-Marcel, C. R. W. Ellison, I. R. Hall, and R. J. Telford (2011), Dynamics of North Atlantic Deep Water masses during the Holocene, *Paleoceanography*, **26**(4), PA4214, doi:10.1029/2011PA002155.
- Hoogakker, B. A. A., I. N. McCave, H. Elderfield, C. Hillaire-Marcel, and J. Simstich (2015), Holocene climate variability in the Labrador Sea, *Journal of the Geological Society*, **172**(2), 272–277, doi:10.1144/jgs2013-097.
- Horwitz, E. P., R. Chiarizia, M. L. Dietz, H. Diamond, and D. M. Nelson (1993), Separation and preconcentration of actinides from acidic media by extraction chromatography, *Analytica Chimica Acta*, **281**(2), 361–372, doi:10.1016/0003-2670(93)85194-O.
- Hoy, S. K., L. F. Robinson, K. M. Scanlon, and R. G. Waller, (2015): *Processed EM-120 multibeam swath bathymetry collected during Nathaniel B. Palmer cruises NBP08-05 and NBP11-03 (grids and associated navigation)*, School of Earth Sciences, University of Bristol, doi:10.1594/PANGAEA.848195.
- Hu, A., G. A. Meehl, W. Han, A. Abe-Ouchi, C. Morrill, Y. Okazaki, and M. O. Chikamoto (2012), The Pacific-Atlantic seesaw and the Bering Strait, *Geophysical Research Letters*, **39**(3), L03702, doi:10.1029/2011GL050567.
- Huang, K.-F., D. W. Oppo, and W. B. Curry (2014), Decreased influence of Antarctic intermediate water in the tropical Atlantic during North Atlantic cold events, *Earth and Planetary Science Letters*, **389**, 200–208, doi:10.1016/j.epsl.2013.12.037.
- Huff, E. A., and D. R. Huff (1993), TRU-Spec and RE-Spec Chromatography: Basic Studies and Applications, *34th ORNL/DOE Conference on Analytical Chemistry in Energy Technology*, Gatlinburg, TN, , published by ORNL, TN and US DOE, Washington, D.C.
- Hughes, C. W., P. L. Woodworth, M. P. Meredith, V. Stepanov, T. Whitworth, and A. R. Pyne (2003), Coherence of Antarctic sea levels, Southern Hemisphere Annular Mode, and flow through Drake Passage, *Geophysical Research Letters*, **30**(9), 1464, doi:10.1029/2003GL017240.
- Huhn, O., W. Roether, and R. Steinfeldt (2008), Age spectra in North Atlantic Deep Water along the South American continental slope, 10°N–30°S, based on tracer observations, *Deep Sea Research Part I: Oceanographic Research Papers*, **55**(10), 1252–1276, doi:10.1016/j.dsr.2008.05.016.
- Huybers, P., and G. Denton (2008), Antarctic temperature at orbital timescales controlled by local summer duration, *Nature Geoscience*, **1**(11), 787–792, doi:10.1038/ngeo311.
- Huybers, P. (2009), Antarctica's Orbital Beat, *Science*, **325**(5944), 1085–1086, doi:10.1126/science.1176186.
- Imbrie, J. et al. (1992), On the Structure and Origin of Major Glaciation Cycles 1. Linear Responses to Milankovitch Forcing, *Paleoceanography*, **7**(6), 701–738, doi:10.1029/92PA02253.
- Imbrie, J. et al. (1993), On the structure and origin of major glaciation cycles 2. The 100,000-year cycle, *Paleoceanography*, **8**(6), 699–735, doi:10.1029/93PA02751.
- IPCC (2013), *Climate Change 2013: The Physical Science Basis. Contribution of Working Group I to the Fifth Assessment Report of the Intergovernmental Panel on Climate Change*, Stocker, T.F., D. Qin, G.-K. Plattner, M. Tignor, S.K. Allen, J. Boschung, A. Nauels, Y. Xia, V. Bex and P.M. Midgley (eds.), Cambridge University Press, Cambridge, United Kingdom and New York, NY, USA, 1535 pp.
- Isono, D., M. Yamamoto, T. Irino, T. Oba, M. Murayama, T. Nakamura, and H. Kawahata (2009), The 1500-year climate oscillation in the midlatitude North Pacific during the Holocene, *Geology*, **37**(7), 591–594, doi:10.1130/G25667A.1.
- Ito, T., J. Marshall, and M. Follows (2004), What controls the uptake of transient tracers in the Southern Ocean?, *Global Biogeochemical Cycles*, **18**(2), GB2021, doi:10.1029/2003GB002103.
- Ito, T., M. Woloszyn, and M. Mazloff (2010), Anthropogenic carbon dioxide transport in the Southern Ocean driven by Ekman flow, *Nature*, **463**(7277), 80–83, doi:10.1038/nature08687.

- IUPAC (2014): Compendium of Chemical Terminology, 2<sup>nd</sup> ed. (the "Gold Book"). Compiled by A. D. McNaught and A. Wilkinson. Blackwell Scientific Publications, Oxford (1997). XML on-line corrected version 2.3.3 (2014-02-24): <http://goldbook.iupac.org> (2006-) created by M. Nic, J. Jirat, B. Kosata; updates compiled by A. Jenkins, ISBN 0-9678550-9-8, doi:10.1351/goldbook.
- Jackett, D. R., and T. J. M. McDougall (1997), A Neutral Density Variable for the World's Oceans, *Journal of Physical Oceanography*, **27**(2), 237–263, doi: [http://dx.doi.org/10.1175/1520-0485\(1997\)027<0237:ANDVFT>2.0.CO;2](http://dx.doi.org/10.1175/1520-0485(1997)027<0237:ANDVFT>2.0.CO;2).
- Jacobsen, S. B., and G. J. Wasserburg (1980), Sm-Nd isotopic evolution of chondrites, *Earth and Planetary Science Letters*, **50**(1), 139–155, doi: 10.1016/0012-821X(80)90125-9.
- Jeandel, C. (1993), Concentration and isotopic composition of Nd in the South Atlantic Ocean, *Earth and Planetary Science Letters*, **117**(3-4), 581–591, doi:doi: 10.1016/0012-821X(93)90104-H.
- Jeandel, C., J. K. Bishop, and A. Zindler (1995), Exchange of neodymium and its isotopes between seawater and small and large particles in the Sargasso Sea, *Geochimica et Cosmochimica Acta*, **59**(3), 535–547, doi:10.1016/0016-7037(94)00367-U.
- Jeandel, C., T. Arsouze, F. Lacan, P. Téchiné, and J.-C. Dutay (2007), Isotopic Nd compositions and concentrations of the lithogenic inputs into the ocean: A compilation, with an emphasis on the margins, *Chemical Geology*, **239**(1–2), 156–164, doi:10.1016/j.chemgeo.2006.11.013.
- Jeandel, C., C. Venchiarutti, M. Bourquin, C. Pradoux, F. Lacan, P. van Beek, and J. Riotte (2011), Single Column Sequential Extraction of Ra, Nd, Th, Pa and U from a Natural Sample, *Geostandards and Geoanalytical Research*, **35**(4), 449–459, doi:10.1111/j.1751-908X.2010.00087.x.
- Jenkins, W. J., W. M. Smethie Jr., E. A. Boyle, and G. A. Cutter (2015), Water mass analysis for the U.S. GEOTRACES (GA03) North Atlantic sections, *Deep Sea Research Part II: Topical Studies in Oceanography*, **116**, 6–20, doi:10.1016/j.dsr2.2014.11.018.
- Jenny, B., D. Wilhelm, and B. Valero-Garcés (2003), The Southern Westerlies in Central Chile: Holocene precipitation estimates based on a water balance model for Laguna Aculeo (33°50'S), *Climate Dynamics*, **20**(2-3), 269–280, doi:10.1007/s00382-002-0267-3.
- Jones, C. E., A. N. Halliday, D. K. Rea, and R. M. Owen (1994), Neodymium isotopic variations in North Pacific modern silicate sediment and the insignificance of detrital REE contributions to seawater, *Earth and Planetary Science Letters*, **127**(1), 55–66, doi:10.1016/0012-821X(94)90197-X.
- Jonkers, L., R. Zahn, A. Thomas, G. Henderson, W. Abouchami, R. François, P. Masque, I. R. Hall, and T. Bickert (2015), Deep circulation changes in the central South Atlantic during the past 145 kyrs reflected in a combined <sup>231</sup>Pa/<sup>230</sup>Th, Neodymium isotope and benthic record, *Earth and Planetary Science Letters*, **419**, 14–21, doi:10.1016/j.epsl.2015.03.004.
- Joughin, I., R. B. Alley, and D. M. Holland (2012), Ice-Sheet Response to Oceanic Forcing, *Science*, **338**(6111), 1172–1176, doi:10.1126/science.1226481.
- Kaiser, J., F. Lamy, and D. Hebbeln (2005), A 70-kyr sea surface temperature record off southern Chile (Ocean Drilling Program Site 1233), *Paleoceanography*, **20**(4), PA4009, doi:10.1029/2005PA001146.
- Kaiser, J., and F. Lamy (2010), Links between Patagonian Ice Sheet fluctuations and Antarctic dust variability during the last glacial period (MIS 4-2), *Quaternary Science Reviews*, **29**(11–12), 1464–1471, doi:10.1016/j.quascirev.2010.03.005.
- Kawabe, M., and S. Fujio (2010), Pacific ocean circulation based on observation, *Journal of Oceanography*, **66**(3), 389–403, doi:10.1007/s10872-010-0034-8.
- Keigwin, L. D. (1998), Glacial-age hydrography of the far northwest Pacific Ocean, *Paleoceanography*, **13**(4), 323–339, doi:10.1029/98PA00874.
- Keller, N. B. (1976), The deep-sea madreporarian corals of the genus *Fungiacyathus* from the Kurile-Kamchatka, Aleutian Trenches and other regions of the world oceans, *Trudy Instituta Okeanologii*, **99**, 31-44.

- Kempton, P. D., J. G. Fitton, A. D. Saunders, G. M. Nowell, R. N. Taylor, B. S. Hardarson, and G. Pearson (2000), The Iceland plume in space and time: a Sr-Nd-Pb-Hf study of the North Atlantic rifted margin, *Earth and Planetary Science Letters*, **177**(3-4), 255–271, doi:10.1016/S0012-821X(00)00047-9.
- Kennett, J. P. (1977), Cenozoic evolution of Antarctic glaciation, the circum-Antarctic Ocean, and their impact on global paleoceanography, *Journal of Geophysical Research*, **82**(27), 3843–3860, doi:10.1029/JC082i027p03843.
- Key, R. M., A. Kozyr, C. L. Sabine, K. Lee, R. Wanninkhof, J. L. Bullister, R. A. Feely, F. J. Millero, C. Mordy, and T.-H. Peng (2004), A global ocean carbon climatology: Results from Global Data Analysis Project (GLODAP), *Global Biogeochemical Cycles*, **18**(4), GB4031, doi:10.1029/2004GB002247.
- Kiefer, T., M. Sarnthein, H. Erlenkeuser, P. M. Grootes, and A. P. Roberts (2001), North Pacific response to millennial-scale changes in ocean circulation over the last 60 kyr, *Paleoceanography*, **16**(2), 179–189, doi:10.1029/2000PA000545.
- Knox, F., and M. B. McElroy (1984), Changes in atmospheric CO<sub>2</sub>: Influence of the marine biota at high latitude, *Journal of Geophysical Research*, **89**(D3), 4629–4637, doi:10.1029/JD089iD03p04629.
- Koepfenkastrof, D., and E. H. De Carlo (1992), Sorption of rare-earth elements from seawater onto synthetic mineral particles: An experimental approach, *Chemical Geology*, **95**(3–4), 251–263, doi:10.1016/0009-2541(92)90015-W.
- Kohfeld, K. E., R. M. Graham, A. M. de Boer, L. C. Sime, E. W. Wolff, C. Le Quéré, and L. Bopp (2013), Southern Hemisphere westerly wind changes during the Last Glacial Maximum: paleo-data synthesis, *Quaternary Science Reviews*, **68**, 76–95, doi:10.1016/j.quascirev.2013.01.017.
- Kraus, K. A., G. E. Moore, and F. Nelson (1956), Anion-exchange Studies. XXI. Th(IV) and U(IV) in Hydrochloric Acid. Separation of Thorium, Protactinium and Uranium<sup>1,2</sup>, *Journal of the American Chemical Society*, **78**(12), 2692–2695, doi:10.1021/ja01593a010.
- Kraus, K. A., and F. Nelson (1958), Metal separations by anion exchange, in *Ion Exchange and Chromatography in Analytical Chemistry*, *ASTM Special Technical Publications* 195, edited by American Society for Testing and Materials, pp. 27–57, ASTM, Philadelphia.
- Kuhlbrodt, T., A. Griesel, M. Montoya, A. Levermann, M. Hofmann, and S. Rahmstorf (2007), On the driving processes of the Atlantic meridional overturning circulation, *Reviews of Geophysics*, **45**(2), RG2001, doi:10.1029/2004RG000166.
- Kushner, P. J., I. M. Held, and T. L. Delworth (2001), Southern Hemisphere Atmospheric Circulation Response to Global Warming, *Journal of Climate*, **14**(10), 2238–2249, doi:10.1175/1520-0442(2001)014<0001:SHACRT>2.0.CO;2.
- Lacan, F., and C. Jeandel (2004a), Subpolar Mode Water formation traced by neodymium isotopic composition, *Geophysical Research Letters*, **31**(14), L14306, doi:10.1029/2004GL019747.
- Lacan, F., and C. Jeandel (2004b), Neodymium isotopic composition and rare earth element concentrations in the deep and intermediate Nordic Seas: Constraints on the Iceland Scotland Overflow Water signature, *Geochemistry Geophysics Geosystems*, **5**(11), Q11006, doi:10.1029/2004GC000742.
- Lacan, F., and C. Jeandel (2005a), Neodymium isotopes as a new tool for quantifying exchange fluxes at the continent–ocean interface, *Earth and Planetary Science Letters*, **232**(3–4), 245–257, doi:10.1016/j.epsl.2005.01.004.
- Lacan, F., and C. Jeandel (2005b), Acquisition of the neodymium isotopic composition of the North Atlantic Deep Water, *Geochemistry, Geophysics, Geosystems*, **6**(12), Q12008, doi:10.1029/2005GC000956.
- Lacan, F., K. Tachikawa, and C. Jeandel (2012), Neodymium isotopic composition of the oceans: A compilation of seawater data, *Chemical Geology*, **300–301**, 177–184, doi:10.1016/j.chemgeo.2012.01.019.
- Lagabriele, Y., Y. Goddérès, Y. Donnadieu, J. Malavieille, and M. Suarez (2009), The tectonic history of Drake Passage and its possible impacts on global climate, *Earth and Planetary Science Letters*, **279**(3-4), 197–211, doi:10.1016/j.epsl.2008.12.037.

- Laj, C., C. Kissel, A. Mazaud, E. Michel, R. Muscheler, and J. Beer (2002), Geomagnetic field intensity, North Atlantic Deep Water circulation and atmospheric  $\Delta^{14}\text{C}$  during the last 50 kyr, *Earth and Planetary Science Letters*, **200**(1–2), 177–190, doi:10.1016/S0012-821X(02)00618-0.
- Lambelet, M. L., T. van de Flierdt, K. Crocket, M. Rehkämper, K. Kreissig, B. Coles, M. J. A. Rijkenberg, L. J. A. Gerringa, H. J. W. de Baar and R. Steinfeldt (accepted), Neodymium isotopic composition and concentration in the western North Atlantic Ocean: results from the GEOTRACES GA02 section, *Geochimica et Cosmochimica Acta*.
- Lamy, F., R. Kilian, H. W. Arz, J.-P. Francois, J. Kaiser, M. Prange, and T. Steinke (2010), Holocene changes in the position and intensity of the southern westerly wind belt, *Nature Geoscience*, **3**(10), 695–699, doi:10.1038/ngeo959.
- Lamy, F., R. Gersonde, G. Winckler, O. Esper, A. Jaeschke, G. Kuhn, J. Ullermann, A. Martinez-Garcia, F. Lambert, and R. Kilian (2014), Increased Dust Deposition in the Pacific Southern Ocean During Glacial Periods, *Science*, **343**(6169), 403–407, doi:10.1126/science.1245424.
- Lamy, F., H. Arz, R. Kilian, C. Lange, L. Lembke, M. Wengler, J. Kaiser, O. Baeza Urrea, I. Hall, N. Harada, and R. Tiedemann (2015), Glacial reduction in Drake Passage throughflow and millennial-scale variations, *Geophysical Research Abstracts*, **17**, EGU2015-10423, EGU General Assembly 2015.
- Langlais, C. E., S. R. Rintoul, and J. D. Zika (2015), Sensitivity of Antarctic Circumpolar Current Transport and Eddy Activity to Wind Patterns in the Southern Ocean, *Journal of Physical Oceanography*, **45**(4), 1051–1067, doi:10.1175/JPO-D-14-0053.1.
- Laskar, J., P. Robutel, F. Joutel, M. Gastineau, A. C. M. Correia, and B. Levrard (2004), A long-term numerical solution for the insolation quantities of the Earth, *Astronomy & Astrophysics*, **428**(1), 261–285, doi:10.1051/0004-6361:20041335.
- Lawver, L. A., and L. M. Gahagan (2003), Evolution of Cenozoic seaways in the circum-Antarctic region, *Palaeogeography, Palaeoclimatology, Palaeoecology*, **198**(1–2), 11–37, doi:10.1016/S0031-0182(03)00392-4.
- Ledwell, J. R., L. C. St. Laurent, J. B. Girton, and J. M. Toole (2011), Diapycnal Mixing in the Antarctic Circumpolar Current. *Journal of Physical Oceanography*, **41**(1), 241–246, doi: http://dx.doi.org/10.1175/2010JPO4557.1.
- Lee, J. H., and R. H. Byrne (1993), Complexation of trivalent rare earth elements (Ce, Eu, Gd, Tb, Yb) by carbonate ions, *Geochimica et Cosmochimica Acta*, **57**(2), 295–302, doi:10.1016/0016-7037(93)90432-V.
- Le Quéré, C. et al. (2007), Saturation of the Southern Ocean CO<sub>2</sub> Sink Due to Recent Climate Change, *Science*, **316**(5832), 1735–1738, doi:10.1126/science.1136188.
- Lilly, J. M., P. B. Rhines, M. Visbeck, R. Davis, J. R. N. Lazier, F. Schott, and D. Farmer (1999), Observing Deep Convection in the Labrador Sea during Winter 1994/95, *Journal of Physical Oceanography*, **29**(8), 2065–2098, doi:doi: 10.1175/1520-0485(1999)029<2065:ODCITL>2.0.CO;2.
- Limpasuvan, V., and D. L. Hartmann (1999), Eddies and the annular modes of climate variability, *Geophysical Research Letters*, **26**(20), 3133–3136, doi:10.1029/1999GL010478.
- Lisiecki, L. E., and M. E. Raymo (2005), A Pliocene-Pleistocene stack of 57 globally distributed benthic  $\delta^{18}\text{O}$  records, *Paleoceanography*, **20**(1), PA1003, doi:10.1029/2004PA001071.
- Liu, W., and A. Hu (2015), The role of the PMOC in modulating the deglacial shift of the ITCZ, *Climate Dynamics*, 1–16, doi:10.1007/s00382-015-2520-6.
- Locarnini, R. A., A. V. Mishonov, J. I. Antonov, T. P. Boyer, H. E. Garcia, O. K. Baranova, M. M. Zweng, C. R. Paver, J. R. Reagan, D. R. Johnson, M. Hamilton, and D. Seidov, 2013. *World Ocean Atlas 2013, Volume 1: Temperature*. S. Levitus, Ed., A. Mishonov Technical Ed.; NOAA Atlas NESDIS **73**, 40 pp.
- López Correa, M., P. Montagna, N. Joseph, A. Rüggeberg, J. Fietzke, S. Flögel, B. Dorschel, S. L. Goldstein, A. Wheeler, and A. Freiwald (2012), Preboreal onset of cold-water coral growth beyond the Arctic Circle revealed by coupled radiocarbon and U-series dating and neodymium isotopes, *Quaternary Science Reviews*, **34**, 24–43, doi:10.1016/j.quascirev.2011.12.005.

- Lovenduski, N. S., and N. Gruber (2005), Impact of the Southern Annular Mode on Southern Ocean circulation and biology, *Geophysical Research Letters*, **32**(11), L11603, doi:10.1029/2005GL022727.
- Lovenduski, N. S., N. Gruber, and S. C. Doney (2008), Toward a mechanistic understanding of the decadal trends in the Southern Ocean carbon sink, *Global Biogeochemical Cycles*, **22**(3), GB3016, doi:10.1029/2007GB003139.
- Lugmair, G. W. and R. W. Carlson (1978), The Sm-Nd history of KREEP, In: *Lunar and Planetary Science Conference, 9<sup>th</sup>* (1978), Proceedings, **1**, 689-704, New York, Pergamon Press.
- Lumpkin, R., and K. Speer (2007), Global Ocean Meridional Overturning, *Journal of Physical Oceanography*, **37**(10), 2550–2562, doi:10.1175/JPO3130.1.
- Lund, D. C., A. C. Tessin, J. L. Hoffman, and A. Schmittner (2015), Southwest Atlantic water mass evolution during the last deglaciation, *Paleoceanography*, **30**(5), 2014PA002657, doi:10.1002/2014PA002657.
- Macdonald, A. M., S. Mecking, P. E. Robbins, J. M. Toole, G. C. Johnson, L. Talley, M. Cook, and S. E. Wijffels (2009), The WOCE-era 3-D Pacific Ocean circulation and heat budget, *Progress in Oceanography*, **82**(4), 281–325, doi:10.1016/j.pocean.2009.08.002.
- Manabe, S., and R. J. Stouffer (1995), Simulation of abrupt climate change induced by freshwater input to the North Atlantic Ocean, *Nature*, **378**(6553), 165–167, doi:10.1038/378165a0.
- Mangini, A., J. M. Godoy, M. L. Godoy, R. Kowsmann, G. M. Santos, M. Ruckelshausen, A. Schroeder-Ritzrau, and L. Wacker (2010), Deep sea corals off Brazil verify a poorly ventilated Southern Pacific Ocean during H2, H1 and the Younger Dryas, *Earth and Planetary Science Letters*, **293**(3–4), 269–276, doi:10.1016/j.epsl.2010.02.041.
- Mantyla, A. W., and J. L. Reid (1995), On the origins of deep and bottom waters of the Indian Ocean, *Journal of Geophysical Research*, **100**(C2), 2417–2439, doi:10.1029/94JC02564.
- Marchitto, T. M., S. J. Lehman, J. D. Ortiz, J. Flückiger, and A. van Geen (2007), Marine Radiocarbon Evidence for the Mechanism of Deglacial Atmospheric CO<sub>2</sub> Rise, *Science*, **316**(5830), 1456 – 1459, doi:10.1126/science.1138679.
- Marcott, S. A. et al. (2011), Ice-shelf collapse from subsurface warming as a trigger for Heinrich events, *Proceedings of the National Academy of Sciences*, **108**(33), 13415–13419, doi:10.1073/pnas.1104772108.
- Marcott, S. A., J. D. Shakun, P. U. Clark, and A. C. Mix (2013), A Reconstruction of Regional and Global Temperature for the Past 11,300 Years, *Science*, **339**(6124), 1198–1201, doi:10.1126/science.1228026.
- Marcott, S. A. et al. (2014), Centennial-scale changes in the global carbon cycle during the last deglaciation, *Nature*, **514**(7524), 616–619.
- Margolin, A. R., L. F. Robinson, A. Burke, R. G. Waller, K. M. Scanlon, M. L. Roberts, M. E. Auro, and T. van de Flierdt (2014), Temporal and spatial distributions of cold-water corals in the Drake Passage: Insights from the last 35,000 years, *Deep Sea Research Part II: Topical Studies in Oceanography*, **99**, 237–248, doi:10.1016/j.dsr2.2013.06.008.
- Marini, C., C. Frankignoul, and J. Mignot (2010), Links between the Southern Annular Mode and the Atlantic Meridional Overturning Circulation in a Climate Model, *Journal of Climate*, **24**(3), 624–640, doi:10.1175/2010JCLI3576.1.
- Marshall, J., and T. Radko (2003), Residual-Mean Solutions for the Antarctic Circumpolar Current and Its Associated Overturning Circulation, *Journal of Physical Oceanography*, **33**(11), 2341–2354, doi:10.1175/1520-0485(2003)033<2341:RSFTAC>2.0.CO;2.
- Marshall, J., E. Shuckburgh, H. Jones, and C. Hill (2006a), Estimates and Implications of Surface Eddy Diffusivity in the Southern Ocean Derived from Tracer Transport, *Journal of Physical Oceanography*, **36**(9), 1806–1821, doi:10.1175/JPO2949.1.
- Marshall, J., and K. Speer (2012), Closure of the meridional overturning circulation through Southern Ocean upwelling, *Nature Geoscience*, **5**(3), 171–180, doi:10.1038/ngeo1391.
- Marshall, G. J., A. Orr, N. P. M. van Lipzig, and J. C. King (2006b), The Impact of a Changing Southern Hemisphere Annular Mode on Antarctic Peninsula Summer Temperatures, *Journal of Climate*, **19**(20), 5388–5404, doi:10.1175/JCLI3844.1.

- Marshall, J., and K. Speer (2012), Closure of the meridional overturning circulation through Southern Ocean upwelling, *Nature Geoscience*, **5**(3), 171–180, doi:10.1038/ngeo1391.
- Martin, E. E., and H. D. Scher (2004), Preservation of seawater Sr and Nd isotopes in fossil fish teeth: bad news and good news, *Earth and Planetary Science Letters*, **220**(1-2), 25–39, doi:10.1016/S0012-821X(04)00030-5.
- Martin, E. E., S. W. Blair, G. D. Kamenov, H. D. Scher, E. Bourbon, C. Basak, and D. N. Newkirk (2010), Extraction of Nd isotopes from bulk deep sea sediments for paleoceanographic studies on Cenozoic time scales, *Chemical Geology*, **269**(3–4), 414–431, doi:10.1016/j.chemgeo.2009.10.016.
- Martínez-Botí, M. A., D. Vance, and P. G. Mortyn (2009), Nd/Ca ratios in plankton-towed and core top foraminifera: Confirmation of the water column acquisition of Nd, *Geochemistry, Geophysics, Geosystems*, **10**(8), Q08018, doi:10.1029/2009GC002701.
- Martinez-Boti, M. A., G. Marino, G. L. Foster, P. Ziveri, M. J. Henehan, J. W. B. Rae, P. G. Mortyn, and D. Vance (2015), Boron isotope evidence for oceanic carbon dioxide leakage during the last deglaciation, *Nature*, **518**(7538), 219–222.
- Masarik, J., and J. Beer (1999), Simulation of particle fluxes and cosmogenic nuclide production in the Earth's atmosphere, *Journal of Geophysical Research*, **104**(D10), 12099–12111, doi:10.1029/1998JD200091.
- Mason, H. E., P. Montagna, L. Kubista, M. Taviani, M. McCulloch, and B. L. Phillips (2011), Phosphate defects and apatite inclusions in coral skeletal aragonite revealed by solid-state NMR spectroscopy, *Geochimica et Cosmochimica Acta*, **75**(23), 7446–7457, doi:10.1016/j.gca.2011.10.002.
- Matsumoto, K., and J. Lynch-Stieglitz (1999), Similar glacial and Holocene deep water circulation inferred from southeast Pacific benthic foraminiferal carbon isotope composition, *Paleoceanography*, **14**(2), 149–163, doi:10.1029/1998PA900028.
- Matsumoto, K., T. Oba, J. Lynch-Stieglitz, and H. Yamamoto (2002): Interior hydrography and circulation of the glacial Pacific Ocean, *Quaternary Science Reviews*, **21**(14-15), 1693-1704, doi:10.1016/S0277-3791(01)00142-1.
- Matsumoto, K. (2007), Radiocarbon-based circulation age of the world oceans, *Journal of Geophysical Research*, **112**(C9), C09004, doi:10.1029/2007JC004095.
- Max, L., L. Lembke-Jene, J.-R. Riethdorf, R. Tiedemann, D. Nürnberg, H. Kühn, and A. Mackensen (2014), Pulses of enhanced North Pacific Intermediate Water ventilation from the Okhotsk Sea and Bering Sea during the last deglaciation, *Climate of the Past*, **10**(2), 591–605, doi:10.5194/cp-10-591-2014.
- Mayewski, P. A. et al. (1994), Changes in Atmospheric Circulation and Ocean Ice Cover over the North Atlantic During the Last 41,000 Years, *Science*, **263**(5154), 1747–1751, doi:10.1126/science.263.5154.1747.
- McCartney, M. S., and L. D. Talley (1982), The Subpolar Mode Water of the North Atlantic Ocean, *Journal of Physical Oceanography*, **12**(11), 1169–1188, doi:10.1175/1520-0485(1982)012<1169:TSMWOT>2.0.CO;2.
- McCartney, M. S. (1992), Recirculating components to the deep boundary current of the northern North Atlantic, *Progress in Oceanography*, **29**(4), 283–383, doi:10.1016/0079-6611(92)90006-L.
- McCave, I. N., S. J. Crowhurst, G. Kuhn, C.-D. Hillenbrand, and M. P. Meredith (2014), Minimal change in Antarctic Circumpolar Current flow speed between the last glacial and Holocene, *Nature Geoscience*, **7**(2), 113–116.
- McIntyre, C. P., M. L. Roberts, J. R. Burton, A. P. McNichol, A. Burke, L. F. Robinson, K. F. von Reden, and W. J. Jenkins (2011), Rapid radiocarbon (<sup>14</sup>C) analysis of coral and carbonate samples using a continuous-flow accelerator mass spectrometry (CFAMS) system, *Paleoceanography*, **26**(4), PA4212.
- McManus, J. F., R. Francois, J.-M. Gherardi, L. D. Keigwin, and S. Brown-Leger (2004), Collapse and rapid resumption of Atlantic meridional circulation linked to deglacial climate changes, *Nature*, **428**(6985), 834–837, doi:10.1038/nature02494.

- Menviel, L., A. Timmermann, O. Elison Timm, and A. Mouchet (2011): Deconstructing the Last Glacial termination: the role of millennial and orbital-scale forcings, *Quaternary Science Reviews*, **30**(9-10), 1155-1172.
- Menviel, L., A. Timmermann, O. Elison Timm, A. Mouchet, A. Abe-Ouchi, M. O. Chikamoto, N. Harada, R. Ohgaito, and Y. Okazaki (2012): Removing the North Pacific halocline: Effects on global climate, ocean circulation and the carbon cycle, *Deep-Sea Research II*, **61-64**, 106-113.
- Menviel, L., M. H. England, K. J. Meissner, A. Mouchet, and J. Yu (2014), Atlantic-Pacific seesaw and its role in outgassing CO<sub>2</sub> during Heinrich events, *Paleoceanography*, **29**(1), 58–70, doi:10.1002/2013PA002542.
- Mercer, J. H. (1984), Simultaneous Climatic Change in Both Hemispheres and Similar Bipolar Interglacial Warming: Evidence and Implications, in *Climate Processes and Climate Sensitivity*, pp. 307–313, American Geophysical Union.
- Meredith, M. P., A. C. Naveira Garabato, A. M. Hogg, and R. Farneti (2012), Sensitivity of the Overturning Circulation in the Southern Ocean to Decadal Changes in Wind Forcing, *Journal of Climate*, **25**(1), 99–110, doi:10.1175/2011JCLI4204.1.
- Middag, R., H. J. W. de Baar, P. Laan, and O. Huhn (2012), The effects of continental margins and water mass circulation on the distribution of dissolved aluminum and manganese in Drake Passage, *Journal of Geophysical Research*, **117**(C1), C01019, doi:10.1029/2011JC007434.
- Mienert, J., and J. Chi (1995), Astronomical time-scale for physical property records from Quaternary sediments of the northern North Atlantic, *Geologische Rundschau*, **84**(1), 67–88, doi:10.1007/BF00192243.
- Milankovitch, M. (1941), *Kanon der Erdbestrahlung und seine Anwendung auf das Eiszeiten-problem*. Belgrad.
- Mohtadi, M., P. Rossel, C. B. Lange, S. Pantoja, P. Böning, D. J. Repeta, M. Grunwald, F. Lamy, D. Hebbeln, and H.-J. Brumsack (2008), Deglacial pattern of circulation and marine productivity in the upwelling region off central-south Chile, *Earth and Planetary Science Letters*, **272**(1–2), 221–230, doi:10.1016/j.epsl.2008.04.043.
- Monnin, E., A. Indermühle, A. Dällenbach, J. Flückiger, B. Stauffer, T. F. Stocker, D. Raynaud, and J.-M. Barnola (2001), Atmospheric CO<sub>2</sub> Concentrations over the Last Glacial Termination, *Science*, **291**(5501), 112–114, doi:10.1126/science.291.5501.112.
- Monnin, E. et al. (2004), Evidence for substantial accumulation rate variability in Antarctica during the Holocene, through synchronization of CO<sub>2</sub> in the Taylor Dome, Dome C and DML ice cores, *Earth and Planetary Science Letters*, **224**(1–2), 45–54, doi:10.1016/j.epsl.2004.05.007.
- Montagna, P., M. McCulloch, M. Taviani, C. Mazzoli, and B. Vendrell (2006), Phosphorus in Cold-Water Corals as a Proxy for Seawater Nutrient Chemistry, *Science*, **312**(5781), 1788–1791, doi:10.1126/science.1125781.
- Montero-Serrano, J.-C., N. Frank, C. Colin, C. Wienberg, and M. Eisele (2011), The climate influence on the mid-depth Northeast Atlantic gyres viewed by cold-water corals, *Geophysical Research Letters*, **38**(19), L19604, doi:10.1029/2011GL048733.
- Montero-Serrano, J.-C. et al. (2013), Decadal changes in the mid-depth water mass dynamic of the Northeastern Atlantic margin (Bay of Biscay), *Earth and Planetary Science Letters*, **364**, 134–144, doi:10.1016/j.epsl.2013.01.012.
- Morrison, A. K., and Andrew McC. Hogg (2013), On the Relationship between Southern Ocean Overturning and ACC Transport. *Journal of Physical Oceanography*, **43**(1), 140–148, doi: http://dx.doi.org/10.1175/JPO-D-12-057.1.
- Mulvaney, R., N. J. Abram, R. C. A. Hindmarsh, C. Arrowsmith, L. Fleet, J. Triest, L. C. Sime, O. Alemany, and S. Foord (2012), Recent Antarctic Peninsula warming relative to Holocene climate and ice-shelf history, *Nature*, **489**(7414), 141–144, doi:10.1038/nature11391.
- Munday, D. R., H. L. Johnson, and D. P. Marshall (2013), Eddy Saturation of Equilibrated Circumpolar Currents, *Journal of Physical Oceanography*, **43**(3), 507–532, doi:10.1175/JPO-D-12-095.1.
- Munk, W. H. (1966), Abyssal recipes, *Deep Sea Research and Oceanographic Abstracts*, **13**(4), 707–730, doi:10.1016/0011-7471(66)90602-4.

- Munk, W., and C. Wunsch (1998), Abyssal recipes II: energetics of tidal and wind mixing, *Deep Sea Research Part I: Oceanographic Research Papers*, **45**(12), 1977–2010, doi:10.1016/S0967-0637(98)00070-3.
- Muratli, J. M., Z. Chase, A. C. Mix, and J. McManus (2010), Increased glacial-age ventilation of the Chilean margin by Antarctic Intermediate Water, *Nature Geoscience*, **3**(1), 23–26, doi:10.1038/ngeo715.
- Murphy, K., M. Rehkämper, K. Kreissig, B. Coles, and T. van de Flierdt (2015), Improvements in Cd stable isotope analysis achieved through use of liquid-liquid extraction to remove organic residues from Cd separates obtained by extraction chromatography, *Journal of Analytical Atomic Spectrometry*, doi:10.1039/C5JA00115C.
- Muscheler, R., J. Beer, G. Wagner, C. Laj, C. Kissel, G. M. Raisbeck, F. Yiou, and P. W. Kubik (2004), Changes in the carbon cycle during the last deglaciation as indicated by the comparison of  $^{10}\text{Be}$  and  $^{14}\text{C}$  records, *Earth and Planetary Science Letters*, **219**(3–4), 325–340, doi:10.1016/S0012-821X(03)00722-2.
- Naveira Garabato, A. C., D. P. Stevens, and K. J. Heywood (2003), Water Mass Conversion, Fluxes, and Mixing in the Scotia Sea Diagnosed by an Inverse Model, *Journal of Physical Oceanography*, **33**(12), 2565–2587, doi:10.1175/1520-0485(2003)033<2565:WMCFAM>2.0.CO;2.
- Naveira Garabato, A. C., L. Jullion, D. P. Stevens, K. J. Heywood, and B. A. King (2009), Variability of Subantarctic Mode Water and Antarctic Intermediate Water in the Drake Passage during the Late-Twentieth and Early-Twenty-First Centuries, *Journal of Climate*, **22**(13), 3661–3688, doi:10.1175/2009JCLI2621.1.
- Naveira Garabato, A. C., R. Ferrari, and K. L. Polzin (2011), Eddy stirring in the Southern Ocean, *Journal of Geophysical Research*, **116**(C9), C09019, doi:10.1029/2010JC006818.
- Neil, H. L., L. Carter, and M. Y. Morris (2004), Thermal isolation of Campbell Plateau, New Zealand, by the Antarctic Circumpolar Current over the past 130 kyr, *Paleoceanography*, **19**(4), PA4008, doi:10.1029/2003PA000975.
- Nelson, F., T. Murase, and K. A. Kraus (1964), Ion exchange procedures: I. Cation exchange in concentration HCl and HClO<sub>4</sub> solutions, *Journal of Chromatography A*, **13**, 503–535, doi:10.1016/S0021-9673(01)95146-5.
- Noble, T. L., A. M. Piotrowski, L. F. Robinson, J. F. McManus, C.-D. Hillenbrand, and A. J.-M. Bory (2012), Greater supply of Patagonian-sourced detritus and transport by the ACC to the Atlantic sector of the Southern Ocean during the last glacial period, *Earth and Planetary Science Letters*, **317–318**, 374–385, doi:10.1016/j.epsl.2011.10.007.
- Noble, T. L., A. M. Piotrowski, and I. N. McCave (2013), Neodymium isotopic composition of intermediate and deep waters in the glacial southwest Pacific, *Earth and Planetary Science Letters*, **384**, 27–36, doi:10.1016/j.epsl.2013.10.010.
- North Greenland Ice Core Project members (2004), High-resolution record of Northern Hemisphere climate extending into the last interglacial period, *Nature*, **431**(7005), 147–151, doi:10.1038/nature02805.
- Nürnberg, D., N. Brughmans, J. Schönfeld, U. Ninnemann, and C. Dullo (2004), Paleo-Export Production, Terrigenous Flux and Sea Surface Temperatures Around Tasmania: Implications for Glacial/Interglacial Changes in the Subtropical Convergence Zone, in *The Cenozoic Southern Ocean: Tectonics, Sedimentation, and Climate Change Between Australia and Antarctica*, pp. 291–318, American Geophysical Union.
- Nürnberg, D., and J. Groeneveld (2006), Pleistocene variability of the Subtropical Convergence at East Tasman Plateau: Evidence from planktonic foraminiferal Mg/Ca (ODP Site 1172A), *Geochemistry Geophysics Geosystems*, **7**(4), Q04P11, doi:10.1029/2005GC000984.
- OBIS (2015), Global distribution of deep-sea corals below 100 m water depth, *Ocean Biogeographic Information System*, Intergovernmental Oceanographic Commission of UNESCO, available online: <http://www.iobis.org>, accessed: 2015-09-02.
- Ohshima, K. I. et al. (2013), Antarctic Bottom Water production by intense sea-ice formation in the Cape Darnley polynya, *Nature Geoscience*, **6**(3), 235–240, doi:10.1038/ngeo1738.

- Oka, A., H. Hasumi, N. Okada, T. T. Sakamoto, and T. Suzuki (2006), Deep convection seesaw controlled by freshwater transport through the Denmark Strait, *Ocean Modelling*, **15**(3–4), 157–176, doi:10.1016/j.ocemod.2006.08.004.
- Okazaki, Y., A. Timmermann, L. Menviel, N. Harada, A. Abe-Ouchi, M. O. Chikamoto, A. Mouchet, and H. Asahi (2010), Deepwater Formation in the North Pacific During the Last Glacial Termination, *Science*, **329**(5988), 200–204, doi:10.1126/science.1190612.
- Oke, P. R., and M. H. England (2004), Oceanic Response to Changes in the Latitude of the Southern Hemisphere Subpolar Westerly Winds, *Journal of Climate*, **17**(5), 1040–1054, doi:10.1175/1520-0442(2004)017<1040:ORTCIT>2.0.CO;2.
- O’Nions, R. K., N. M. Evensen, and P. J. Hamilton (1979), Geochemical modeling of mantle differentiation and crustal growth, *Journal of Geophysical Research: Solid Earth*, **84**(B11), 6091–6101, doi:10.1029/JB084iB11p06091.
- Oppo, D. W., J. F. McManus, and J. L. Cullen (2006), Evolution and demise of the Last Interglacial warmth in the subpolar North Atlantic, *Quaternary Science Reviews*, **25**(23–24), 3268–3277, doi:10.1016/j.quascirev.2006.07.006.
- Orejas, C., A. Gori, and J. M. Gili (2008), Growth rates of live *Lophelia pertusa* and *Madrepora oculata* from the Mediterranean Sea maintained in aquaria, *Coral Reefs*, **27**(2), 255–255, doi:10.1007/s00338-007-0350-7.
- Orsi, A. H., T. Whitworth III, and W. D. Nowlin Jr. (1995), On the meridional extent and fronts of the Antarctic Circumpolar Current, *Deep Sea Research Part I: Oceanographic Research Papers*, **42**(5), 641–673, doi:10.1016/0967-0637(95)00021-W.
- Orsi, A. H., G. C. Johnson, and J. L. Bullister (1999), Circulation, mixing, and production of Antarctic Bottom Water, *Progress In Oceanography*, **43**(1), 55–109, doi:10.1016/S0079-6611(99)00004-X.
- Pahnke, K., and R. Zahn (2005), Southern Hemisphere Water Mass Conversion Linked with North Atlantic Climate Variability, *Science*, **307**(5716), 1741–1746, doi:10.1126/science.1102163.
- Pahnke, K., and J. P. Sachs (2006), Sea surface temperatures of southern midlatitudes 0–160 kyr B.P., *Paleoceanography*, **21**(2), PA2003, doi:10.1029/2005PA001191.
- Pahnke, K., S. L. Goldstein, and S. R. Hemming (2008), Abrupt changes in Antarctic Intermediate Water circulation over the past 25,000[thinsp]years, *Nature Geoscience*, **1**(12), 870–874, doi:10.1038/ngeo360.
- Pearce, C. R., M. T. Jones, E. H. Oelkers, C. Pradoux, and C. Jeandel (2013), The effect of particulate dissolution on the neodymium (Nd) isotope and Rare Earth Element (REE) composition of seawater, *Earth and Planetary Science Letters*, **369–370**, 138–147, doi:10.1016/j.epsl.2013.03.023.
- Petherick, L. et al. (2013), Climatic records over the past 30 ka from temperate Australia – a synthesis from the Oz-INTIMATE workgroup, *Quaternary Science Reviews*, **74**, 58–77, doi:10.1016/j.quascirev.2012.12.012.
- Petit, J. R. et al. (1999), Climate and atmospheric history of the past 420,000 years from the Vostok ice core, Antarctica, *Nature*, **399**(6735), 429–436, doi:10.1038/20859.
- Piepgras, D. J., and G. J. Wasserburg (1982), Isotopic Composition of Neodymium in Waters from the Drake Passage, *Science*, **217**(4556), 207–214, doi:10.1126/science.217.4556.207.
- Piepgras, D., and G. Wasserburg (1987), Rare earth element transport in the western North Atlantic inferred from Nd isotopic observations, *Geochimica et Cosmochimica Acta*, **51**(5), 1257–1271, doi:doi: 10.1016/0016-7037(87)90217-1.
- Piepgras, D. J., and S. B. Jacobsen (1988), The isotopic composition of neodymium in the North Pacific, *Geochimica et Cosmochimica Acta*, **52**(6), 1373–1381, doi:10.1016/0016-7037(88)90208-6.
- Pin, C., and J. S. Zalduegui (1997), Sequential separation of light rare-earth elements, thorium and uranium by miniaturized extraction chromatography: Application to isotopic analyses of silicate rocks, *Analytica Chimica Acta*, **339**(1–2), 79–89, doi:10.1016/S0003-2670(96)00499-0.
- Piola, A. R., and D. T. Georgi (1982), Circumpolar properties of Antarctic intermediate water and Subantarctic Mode Water, *Deep Sea Research Part A. Oceanographic Research Papers*, **29**(6), 687–711, doi:10.1016/0198-0149(82)90002-4.

- Piotrowski, A. M., S. L. Goldstein, S. R. Hemming, and R. G. Fairbanks (2004), Intensification and variability of ocean thermohaline circulation through the last deglaciation, *Earth and Planetary Science Letters*, **225**(1–2), 205–220, doi:10.1016/j.epsl.2004.06.002.
- Piotrowski, A. M., S. L. Goldstein, S. R. Hemming, and R. G. Fairbanks (2005), Temporal Relationships of Carbon Cycling and Ocean Circulation at Glacial Boundaries, *Science*, **307**(5717), 1933–1938, doi:10.1126/science.1104883.
- Piotrowski, A. M., S. L. Goldstein, H. R., R. G. Fairbanks, and D. R. Zylberberg (2008), Oscillating glacial northern and southern deep water formation from combined neodymium and carbon isotopes, *Earth and Planetary Science Letters*, **272**(1-2), 394–405, doi:doi:10.1016/j.epsl.2008.05.011.
- Piotrowski, A. M., V. K. Banakar, A. E. Scrivner, H. Elderfield, A. Galy, and A. Dennis (2009), Indian Ocean circulation and productivity during the last glacial cycle, *Earth and Planetary Science Letters*, **285**(1–2), 179–189, doi:10.1016/j.epsl.2009.06.007.
- Piotrowski, A. M., A. Galy, J. A. L. Nicholl, N. Roberts, D. J. Wilson, J. A. Clegg, and J. Yu (2012), Reconstructing deglacial North and South Atlantic deep water sourcing using foraminiferal Nd isotopes, *Earth and Planetary Science Letters*, **357–358**, 289–297, doi:10.1016/j.epsl.2012.09.036.
- Polzin, K. L., J. M. Toole, J. R. Ledwell, and R. W. Schmitt (1997), Spatial Variability of Turbulent Mixing in the Abyssal Ocean, *Science*, **276**(5309), 93–96, doi:10.1126/science.276.5309.93.
- Pritchard, H. D., S. R. M. Ligtenberg, H. A. Fricker, D. G. Vaughan, M. R. van den Broeke, and L. Padman (2012), Antarctic ice-sheet loss driven by basal melting of ice shelves, *Nature*, **484**(7395), 502–505, doi:10.1038/nature10968.
- Przenioslo, R., J. Stolarski, M. Mazur, and M. Brunelli (2008), Hierarchically structured scleractinian coral biocrystals, *Journal of Structural Biology*, **161**(1), 74–82, doi:10.1016/j.jsb.2007.09.020.
- Putnam, A. E., G. H. Denton, J. M. Schaefer, D. J. A. Barrell, B. G. Andersen, R. C. Finkel, R. Schwartz, A. M. Doughty, M. R. Kaplan, and C. Schluchter (2010), Glacier advance in southern middle-latitudes during the Antarctic Cold Reversal, *Nature Geoscience*, **3**(10), 700–704, doi:10.1038/ngeo962.
- Rae, J. W. B., M. Sarnthein, G. L. Foster, A. Ridgwell, P. M. Grootes, and T. Elliott (2014), Deep water formation in the North Pacific and deglacial CO<sub>2</sub> rise, *Paleoceanography*, **29**(6), 2013PA002570, doi:10.1002/2013PA002570.
- Rahmstorf, S., and M. H. England (1997), Influence of Southern Hemisphere Winds on North Atlantic Deep Water Flow, *Journal of Physical Oceanography*, **27**(9), 2040–2054, doi:10.1175/1520-0485(1997)027<2040:IOSHWO>2.0.CO;2.
- Rahmstorf, S. (2002), Ocean circulation and climate during the past 120,000 years, *Nature*, **419**(6903), 207–214, doi:10.1038/nature01090.
- Rasmussen, T. L., D. W. Oppo, E. Thomsen, and S. J. Lehman (2003), Deep sea records from the southeast Labrador Sea: Ocean circulation changes and ice-rafting events during the last 160,000 years, *Paleoceanography*, **18**(1), 1018, doi:10.1029/2001PA000736.
- Reeves, J. M. et al. (2013), Climate variability over the last 35,000 years recorded in marine and terrestrial archives in the Australian region: an OZ-INTIMATE compilation, *Quaternary Science Reviews*, **74**, 21–34, doi:10.1016/j.quascirev.2013.01.001.
- Reid, J. L., and R. J. Lynn (1971), On the influence of the Norwegian-Greenland and Weddell seas upon the bottom waters of the Indian and Pacific oceans, *Deep Sea Research and Oceanographic Abstracts*, **18**(11), 1063–1088, doi:10.1016/0011-7471(71)90094-5.
- Reid, J. L. (1989), On the total geostrophic circulation of the South Atlantic Ocean: Flow patterns, tracers, and transports, *Progress in Oceanography*, **23**(3), 149–244, doi:10.1016/0079-6611(89)90001-3.
- Reid, J. L. (1994), On the total geostrophic circulation of the North Atlantic Ocean: Flow patterns, tracers, and transports, *Progress in Oceanography*, **33**(1), 1–92, doi:10.1016/0079-6611(94)90014-0.
- Reid, J. L. (1997), On the total geostrophic circulation of the Pacific Ocean: flow patterns, tracers, and transports, *Progress in Oceanography*, **39**(4), 263–352, doi:10.1016/S0079-6611(97)00012-8.

- Reimer, P. J. et al. (2009), IntCal09 and Marine09 Radiocarbon Age Calibration Curves, 0-50,000 Years cal BP, *Radiocarbon*, **51**(4), [online] available from: <https://journals.uair.arizona.edu/index.php/radiocarbon/article/view/3569>.
- Reimer, P. J. et al. (2013), IntCal13 and Marine13 Radiocarbon Age Calibration Curves 0–50,000 Years cal BP, *Radiocarbon*, **55**(4), [online] Available from: <https://journals.uair.arizona.edu/index.php/radiocarbon/article/view/16947>.
- Rella, S. F., and M. Uchida (2014), A Southern Ocean trigger for Northwest Pacific ventilation during the Holocene?, *Science Reports*, **4**, [online] Available from: <http://dx.doi.org/10.1038/srep04046>
- Renssen, H., H. Goosse, and T. Fichefet (2005), Contrasting trends in North Atlantic deep-water formation in the Labrador Sea and Nordic Seas during the Holocene, *Geophysical Research Letters*, **32**(8), L08711, doi:10.1029/2005GL022462.
- Reynard, B., C. Lécuyer, and P. Grandjean (1999), Crystal-chemical controls on rare-earth element concentrations in fossil biogenic apatites and implications for paleoenvironmental reconstructions, *Chemical Geology*, **155**(3–4), 233–241, doi:10.1016/S0009-2541(98)00169-7.
- Rhodes, R. H., E. J. Brook, J. C. H. Chiang, T. Blunier, O. J. Maselli, J. R. McConnell, D. Romanini, and J. P. Severinghaus (2015), Enhanced tropical methane production in response to iceberg discharge in the North Atlantic, *Science*, **348**(6238), 1016–1019, doi:10.1126/science.1262005.
- Rickli, J., M. Gutjahr, D. Vance, M. Fischer-Gödde, C.-D. Hillenbrand, and G. Kuhn (2014), Neodymium and hafnium boundary contributions to seawater along the West Antarctic continental margin, *Earth and Planetary Science Letters*, **394**, 99–110, doi:10.1016/j.epsl.2014.03.008.
- Rignot, E., G. Casassa, P. Gogineni, W. Krabill, A. Rivera, and R. Thomas (2004), Accelerated ice discharge from the Antarctic Peninsula following the collapse of Larsen B ice shelf, *Geophysical Research Letters*, **31**(18), L18401, doi:10.1029/2004GL020697.
- Rignot, E., S. Jacobs, J. Mouginot, and B. Scheuchl (2013), Ice-Shelf Melting Around Antarctica, *Science*, **341**(6143), 266–270, doi:10.1126/science.1235798.
- Rignot, E., I. Fenty, Y. Xu, C. Cai, and C. Kemp (2015), Undercutting of marine-terminating glaciers in West Greenland, *Geophysical Research Letters*, 2015GL064236, doi:10.1002/2015GL064236.
- Rintoul, S. R., J. R. Donguy, and D. H. Roemmich (1997), Seasonal evolution of upper ocean thermal structure between Tasmania and Antarctica, *Deep Sea Research Part I: Oceanographic Research Papers*, **44**(7), 1185–1202, doi:10.1016/S0967-0637(96)00125-2.
- Rintoul, S. R., and J. L. Bullister (1999), A late winter hydrographic section from Tasmania to Antarctica, *Deep Sea Research Part I: Oceanographic Research Papers*, **46**(8), 1417–1454, doi:10.1016/S0967-0637(99)00013-8.
- Risk, M. J., J. M. Heikoop, M. G. Snow, and R. Beukens (2002), Lifespans and growth patterns of two deep-sea corals: *Primnoa resedaeformis* and *Desmophyllum cristagalli*, *Hydrobiologia*, **471**(1–3), 125–131, doi:10.1023/A:1016557405185.
- Roberts, J. M., A. J. Wheeler, and A. Freiwald (2006), Reefs of the Deep: The Biology and Geology of Cold-Water Coral Ecosystems, *Science*, **312**(5773), 543–547, doi:10.1126/science.1119861.
- Roberts, N. L., A. M. Piotrowski, J. F. McManus, and L. D. Keigwin (2010), Synchronous Deglacial Overturning and Water Mass Source Changes, *Science*, **327**(5961), 75–78, doi:10.1126/science.1178068.
- Roberts, N. L., and A. M. Piotrowski (2015), Radiogenic Nd isotope labeling of the northern NE Atlantic during MIS 2, *Earth and Planetary Science Letters*, **423**, 125–133, doi:10.1016/j.epsl.2015.05.011.
- Robinson, L. F., J. F. Adkins, L. D. Keigwin, J. Southon, D. P. Fernandez, S.-L. Wang, and D. S. Scheirer (2005), Radiocarbon Variability in the Western North Atlantic During the Last Deglaciation, *Science*, **310**(5753), 1469–1473, doi:10.1126/science.1114832.
- Robinson, L. F., J. F. Adkins, D. P. Fernandez, D. S. Burnett, S.-L. Wang, A. C. Gagnon, and N. Krakauer (2006), Primary U distribution in scleractinian corals and its implications for U series dating, *Geochemistry, Geophysics, Geosystems*, **7**(5), Q05022, doi:10.1029/2005GC001138.

- Robinson, L. F., J. F. Adkins, D. S. Scheirer, D. P. Fernandez, A. Gagnon, and R. G. Waller (2007), Deep-sea scleractinian coral age and depth distributions in the northwest Atlantic for the last 225,000 years, *Bulletin of Marine Science*, **81**(3), 371–391.
- Robinson, L. F., and T. van de Flierdt (2009), Southern Ocean evidence for reduced export of North Atlantic Deep Water during Heinrich event 1, *Geology*, **37**(3), 195–198, doi:10.1130/G25363A.1.
- Robinson, L. F., J. F. Adkins, N. Frank, A. C. Gagnon, N. G. Prouty, E. Brendan Roark, and T. van de Flierdt (2014), The geochemistry of deep-sea coral skeletons: A review of vital effects and applications for palaeoceanography, *Deep-Sea Research Part II: Topical Studies in Oceanography*, **99**, 184–198, doi:10.1016/j.dsr2.2013.06.005.
- Rohling, E. J., Q. S. Liu, A. P. Roberts, J. D. Stanford, S. O. Rasmussen, P. L. Langen, and M. Siddall (2009), Controls on the East Asian monsoon during the last glacial cycle, based on comparison between Hulu Cave and polar ice-core records, *Quaternary Science Reviews*, **28**(27–28), 3291–3302, doi:10.1016/j.quascirev.2009.09.007.
- Ronge, T. A., S. Steph, R. Tiedemann, M. Prange, U. Merkel, D. Nürnberg, and G. Kuhn (2015), Pushing the boundaries: Glacial/interglacial variability of intermediate and deep waters in the southwest Pacific over the last 350,000 years, *Paleoceanography*, **30**(2), 2014PA002727, doi:10.1002/2014PA002727.
- Ronski, S., and G. Budéus (2005), Time series of winter convection in the Greenland Sea, *Journal of Geophysical Research*, **110**(C4), C04015, doi:10.1029/2004JC002318.
- Rother, H., D. Fink, J. Shulmeister, C. Mifsud, M. Evans, and J. Pugh (2014), The early rise and late demise of New Zealand's last glacial maximum, *Proceedings of the National Academy of Sciences*, **111**(32), 11630–11635, doi:10.1073/pnas.1401547111.
- Rousseau, T. C. C., J. E. Sonke, J. Chmeleff, P. van Beek, M. Souhaut, G. Boaventura, P. Seyler, and C. Jeandel (2015), Rapid neodymium release to marine waters from lithogenic sediments in the Amazon estuary, *Nature Communications*, **6**. [online] Available from: <http://dx.doi.org/10.1038/ncomms8592>.
- Ryan, W. B. F. et al. (2009), Global Multi-Resolution Topography synthesis, *Geochemistry, Geophysics, Geosystems*, **10**(3), Q03014, doi:10.1029/2008GC002332.
- Sabatier, P., J.-L. Reyss, J. M. Hall-Spencer, C. Colin, N. Frank, N. Tisnérat-Laborde, L. Bordier, and E. Douville (2012), 210Pb-226Ra chronology reveals rapid growth rate of *Madrepora oculata* and *Lophelia pertusa* on world's largest cold-water coral reef, *Biogeosciences*, **9**(3), 1253–1265, doi:10.5194/bg-9-1253-2012.
- Sabine, C. L. et al. (2004), The Oceanic Sink for Anthropogenic CO<sub>2</sub>, *Science*, **305**(5682), 367–371, doi:10.1126/science.1097403.
- Saenko, O. A., A. Schmittner, and A. J. Weaver (2004), The Atlantic–Pacific Seesaw, *Journal of Climate*, **17**(11), 2033–2038, doi:10.1175/1520-0442(2004)017<2033:TAS>2.0.CO;2.
- Saenko, O. A. (2006), The Effect of Localized Mixing on the Ocean Circulation and Time-Dependent Climate Change, *Journal of Physical Oceanography*, **36**(1), 140–160, doi:10.1175/JPO2839.1.
- Sallée, J. B., K. Speer, and R. Morrow (2008), Response of the Antarctic Circumpolar Current to Atmospheric Variability, *Journal of Climate*, **21**(12), 3020–3039, doi:10.1175/2007JCLI1702.1.
- Sallée, J. B., K. G. Speer, and S. R. Rintoul (2010), Zonally asymmetric response of the Southern Ocean mixed-layer depth to the Southern Annular Mode, *Nature Geoscience*, **3**(4), 273–279, doi:10.1038/ngeo812.
- Sallée, J. B., K. Speer, and S. R. Rintoul (2011), Mean-flow and topographic control on surface eddy-mixing in the Southern Ocean, *Journal of Marine Research*, **69**(4–5), 753–777, doi:10.1357/002224011799849408.
- Sarmiento, J. L., and J. R. Toggweiler (1984), A new model for the role of the oceans in determining atmospheric PCO<sub>2</sub>, *Nature*, **308**(5960), 621–624, doi:10.1038/308621a0.
- Sarnthein, M., K. Winn, S. J. A. Jung, J.-C. Duplessy, L. Labeyrie, H. Erlenkeuser, and G. Ganssen (1994), Changes in East Atlantic Deepwater Circulation Over the Last 30,000 years: Eight Time Slice Reconstructions, *Paleoceanography*, **9**(2), 209–267, doi:10.1029/93PA03301.

- Sarnthein, M., S. van Kreveld, H. Erlenkeuser, P. M. Grootes, M. Kucera, U. Pflaumann, and M. Schulz (2003), Centennial-to-millennial-scale periodicities of Holocene climate and sediment injections off the western Barents shelf, 75°N, *Boreas*, **32**(3), 447–461, doi:10.1111/j.1502-3885.2003.tb01227.x.
- Schlitzer, R., W. Roether, H. Oster, H.-G. Junghans, M. Hausmann, H. Johannsen, and A. Michelato (1991), Chlorofluoromethane and oxygen in the Eastern Mediterranean, *Deep Sea Research Part A. Oceanographic Research Papers*, **38**(12), 1531–1551, doi:10.1016/0198-0149(91)90088-W.
- Schlitzer, R. (2012), Ocean Data View, <http://odv.awi.de>.
- Schmidt, M. W., H. J. Spero, and D. W. Lea (2004), Links between salinity variation in the Caribbean and North Atlantic thermohaline circulation, *Nature*, **428**(6979), 160–163, doi:10.1038/nature02346.
- Schmitt, J. et al. (2012), Carbon Isotope Constraints on the Deglacial CO<sub>2</sub> Rise from Ice Cores, *Science*, **336**(6082), 711–714, doi:10.1126/science.1217161.
- Schmittner, A., O. A. Saenko, and A. J. Weaver (2003), Coupling of the hemispheres in observations and simulations of glacial climate change, *Quaternary Science Reviews*, **22**(5–7), 659–671, doi:10.1016/S0277-3791(02)00184-1.
- SCOR Working Group (2007), GEOTRACES – An international study of the global marine biogeochemical cycles of trace elements and their isotopes, *Chemie der Erde – Geochemistry*, **67**(2), 85–131, doi:10.1016/j.chemer.2007.02.001.
- Seidov, D., and M. Maslin (2001), Atlantic ocean heat piracy and the bipolar climate see-saw during Heinrich and Dansgaard–Oeschger events, *Journal of Quaternary Science*, **16**(4), 321–328, doi:10.1002/jqs.595.
- Seidov, D., E. Barron, and B. J. Haupt (2001), Meltwater and the global ocean conveyor: northern versus southern connections, *Global and Planetary Change*, **30**(3–4), 257–270, doi:10.1016/S0921-8181(00)00087-4.
- Shackleton, N. J., J.-C. Duplessy, M. Arnold, P. Maurice, M. A. Hall, and J. Cartlidge (1988), Radiocarbon age of last glacial Pacific deep water, *Nature*, **335**(6192), 708–711, doi:10.1038/335708a0.
- Shaffer, G., S. M. Olsen, and C. J. Bjerrum (2004), Ocean subsurface warming as a mechanism for coupling Dansgaard–Oeschger climate cycles and ice-rafting events, *Geophysical Research Letters*, **31**(24), L24202, doi:10.1029/2004GL020968.
- Shakun, J. D., P. U. Clark, F. He, S. A. Marcott, A. C. Mix, Z. Liu, B. Otto-Bliesner, A. Schmittner, and E. Bard (2012), Global warming preceded by increasing carbon dioxide concentrations during the last deglaciation, *Nature*, **484**(7392), 49–54, doi:10.1038/nature10915.
- Shaw, H., and G. Wasserburg (1985), Sm–Nd in marine carbonates and phosphates: Implications for Nd isotopes in seawater and crustal ages, *Geochimica et Cosmochimica Acta*, **49**(2), 503–518, doi:10.1016/0016-7037(85)90042-0.
- Sheen, K. L. et al. (2014), Eddy-induced variability in Southern Ocean abyssal mixing on climatic timescales, *Nature Geoscience*, **7**(8), 577–582.
- Shevenell, A. E., A. E. Ingalls, E. W. Domack, and C. Kelly (2011), Holocene Southern Ocean surface temperature variability west of the Antarctic Peninsula, *Nature*, **470**(7333), 250–254, doi:10.1038/nature09751.
- Sholkovitz, E. R., W. M. Landing, and B. L. Lewis (1994), Ocean particle chemistry: The fractionation of rare earth elements between suspended particles and seawater, *Geochimica et Cosmochimica Acta*, **58**(6), 1567–1579, doi:10.1016/0016-7037(94)90559-2.
- Sholkovitz, E., and G. T. Shen (1995), The incorporation of rare earth elements in modern coral, *Geochimica et Cosmochimica Acta*, **59**(13), 2749–2756, doi:10.1016/0016-7037(95)00170-5.
- Siddall, M., S. Khatiwala, T. van de Flierdt, K. Jones, S. L. Goldstein, S. Hemming, and R. F. Anderson (2008), Towards explaining the Nd paradox using reversible scavenging in an ocean general circulation model, *Earth and Planetary Science Letters*, **274**(3–4), 448–461, doi:10.1016/j.epsl.2008.07.044.

- Siegenthaler, U., and T. Wenk (1984), Rapid atmospheric CO<sub>2</sub> variations and ocean circulation, *Nature*, **308**(5960), 624–626, doi:10.1038/308624a0.
- Sievers, H. A., and W. D. Nowlin (1984), The stratification and water masses at Drake Passage, *Journal of Geophysical Research*, **89**(C6), 10489–10514, doi:10.1029/JC089iC06p10489.
- Sigman, D. M., M. P. Hain, and G. H. Haug (2010), The polar ocean and glacial cycles in atmospheric CO<sub>2</sub> concentration, *Nature*, **466**(7302), 47–55, doi:10.1038/nature09149.
- Sijp, W. P., and M. H. England (2004), Effect of the Drake Passage Throughflow on Global Climate, *Journal of Physical Oceanography*, **34**(5), 1254–1266, doi:10.1175/1520-0485(2004)034<1254:EOTDPT>2.0.CO;2.
- Sijp, W. P., and M. H. England (2009), Southern Hemisphere Westerly Wind Control over the Ocean's Thermohaline Circulation, *Journal of Climate*, **22**(5), 1277–1286, doi:10.1175/2008JCLI2310.1.
- Sikes, E. L., C. R. Samson, T. P. Guilderson, and W. R. Howard (2000), Old radiocarbon ages in the southwest Pacific Ocean during the last glacial period and deglaciation, *Nature*, **405**(6786), 555–559, doi:10.1038/35014581.
- Skinner, L. C., S. Fallon, C. Waelbroeck, E. Michel, and S. Barker (2010), Ventilation of the Deep Southern Ocean and Deglacial CO<sub>2</sub> Rise, *Science*, **328**(5982), 1147–1151, doi:10.1126/science.1183627.
- Skinner, L. C., A. E. Scrivner, D. Vance, S. Barker, S. Fallon, and C. Waelbroeck (2013), North Atlantic versus Southern Ocean contributions to a deglacial surge in deep ocean ventilation, *Geology*, **41**(6), 667–670, doi:10.1130/G34133.1.
- Skinner, L. C., C. Waelbroeck, A. E. Scrivner, and S. J. Fallon (2014), Radiocarbon evidence for alternating northern and southern sources of ventilation of the deep Atlantic carbon pool during the last deglaciation, *Proceedings of the National Academy of Sciences*, **111**(15), 5480–5484, doi:10.1073/pnas.1400668111.
- Skinner, L., I. N. McCave, L. Carter, S. Fallon, A. E. Scrivner, and F. Primeau (2015), Reduced ventilation and enhanced magnitude of the deep Pacific carbon pool during the last glacial period, *Earth and Planetary Science Letters*, **411**, 45–52, doi:10.1016/j.epsl.2014.11.024.
- Sloyan, B. M., and S. R. Rintoul (2001), Circulation, Renewal, and Modification of Antarctic Mode and Intermediate Water, *Journal of Physical Oceanography*, **31**(4), 1005–1030, doi:10.1175/1520-0485(2001)031<1005:CRAMOA>2.0.CO;2.
- Smith, K. S., and J. Marshall (2009), Evidence for Enhanced Eddy Mixing at Middepth in the Southern Ocean. *Journal of Physical Oceanography*, **39**(1), 50–69.
- Sokolov, S., and S. Rintoul (2000), Circulation and water masses of the southwest Pacific: WOCE Section P11, Papua New Guinea to Tasmania, *Journal of Marine Research*, **58**(2), 223–268, doi:10.1357/002224000321511151.
- Solignac, S., A. de Vernal, and C. Hillaire-Marcel (2004), Holocene sea-surface conditions in the North Atlantic—contrasted trends and regimes in the western and eastern sectors (Labrador Sea vs. Iceland Basin), *Quaternary Science Reviews*, **23**(3–4), 319–334, doi:10.1016/j.quascirev.2003.06.003.
- Squires, D.F. (1961), Deep sea corals collected by the Lamont Geological Observatory, 2, Scotia Sea corals, *American Museum Novitates.*, **2046**, 1–48, URI: <http://hdl.handle.net/2246/3482>.
- St. Laurent, L., A. C. Naveira Garabato, J. R. Ledwell, A. M. Thurnherr, J. M. Toole, and A. J. Watson (2012), Turbulence and Diapycnal Mixing in Drake Passage, *Journal of Physical Oceanography*, **42**(12), 2143–2152, doi:10.1175/JPO-D-12-027.1.
- Stanley, G. D. and S. D. Cairns (1988), Constructional azooxanthellate coral communities; an overview with implications for the fossil records, *Palaios*, **3**(2), 233.
- Steig, E. J., and R. B. Alley (2002), Phase relationships between Antarctic and Greenland climate records, *Annals of Glaciology*, **35**(1), 451–456, doi:10.3189/172756402781817211.
- Stichel, T., M. Frank, J. Rickli, and B. A. Haley (2012), The hafnium and neodymium isotope composition of seawater in the Atlantic sector of the Southern Ocean, *Earth and Planetary Science Letters*, **317–318**, 282–294, doi:10.1016/j.epsl.2011.11.025.

- Stichel, T., A. E. Hartman, B. Duggan, S. L. Goldstein, H. Scher, and K. Pahnke (2015), Separating biogeochemical cycling of neodymium from water mass mixing in the Eastern North Atlantic, *Earth and Planetary Science Letters*, **412**, 245–260, doi:10.1016/j.epsl.2014.12.008.
- Stocker, T. F., and D. G. Wright (1991), Rapid transitions of the ocean's deep circulation induced by changes in surface water fluxes, *Nature*, **351**(6329), 729–732, doi:10.1038/351729a0.
- Stocker, T. F., and S. J. Johnsen (2003), A minimum thermodynamic model for the bipolar seesaw, *Paleoceanography*, **18**(4), 1087, doi:10.1029/2003PA000920.
- Stommel, H. (1958), The abyssal circulation, *Deep Sea Research (1953)*, **5**(1), 80–82, doi:10.1016/S0146-6291(58)80014-4.
- Stommel, H. (1961), Thermohaline Convection with Two Stable Regimes of Flow, *Tellus*, **13**(2), 224–230, doi:10.1111/j.2153-3490.1961.tb00079.x.
- Stott, L., J. Southon, A. Timmermann, and A. Koutavas (2009), Radiocarbon age anomaly at intermediate water depth in the Pacific Ocean during the last deglaciation, *Paleoceanography*, **24**(2), PA2223, doi:10.1029/2008PA001690.
- Stouffer, R. J., D. Seidov, and B. J. Haupt (2007), Climate Response to External Sources of Freshwater: North Atlantic versus the Southern Ocean, *Journal of Climate*, **20**(3), 436–448, doi:10.1175/JCLI4015.1.
- Stramma, L., and M. England (1999), On the water masses and mean circulation of the South Atlantic Ocean, *Journal of Geophysical Research*, **104**(C9), 20863–20883, doi:10.1029/1999JC900139.
- Strelow, F. W. E. (1960), An Ion Exchange Selectivity Scale of Cations Based on Equilibrium Distribution Coefficients, *Analytical Chemistry*, **32**(9), 1185–1188, doi:10.1021/ac60165a042.
- Strelow, F. W. E., R. Rethemeyer, and C. J. C. Bothma (1965), Ion Exchange Selectivity Scales for Cations in Nitric Acid and Sulfuric Acid Media with a Sulfonated Polystyrene Resin., *Analytical Chemistry*, **37**(1), 106–111, doi:10.1021/ac60220a027.
- Strikis, N. M. et al. (2015), Timing and structure of Mega-SACZ events during Heinrich Stadial 1, *Geophysical Research Letters*, 2015GL064048, doi:10.1002/2015GL064048.
- Stuart, K. M., and D. G. Long (2011), Tracking large tabular icebergs using the SeaWinds Ku-band microwave scatterometer, *Deep Sea Research Part II: Topical Studies in Oceanography*, **58**(11–12), 1285–1300, doi:10.1016/j.dsr2.2010.11.004.
- Sudre, J., V. Garçon, C. Provost, N. Sennéchaël, O. Huhn, and M. Lacombe (2011), Short-term variations of deep water masses in Drake Passage revealed by a multiparametric analysis of the ANT-XXIII/3 bottle data, *Deep Sea Research Part II: Topical Studies in Oceanography*, **58**(25–26), 2592–2612, doi:10.1016/j.dsr2.2011.01.005.
- Sugden, D. E., R. D. McCulloch, A. J.-M. Bory, and A. S. Hein (2009), Influence of Patagonian glaciers on Antarctic dust deposition during the last glacial period, *Nature Geoscience*, **2**(4), 281–285, doi:10.1038/ngeo474.
- Svensson, A. et al. (2006), The Greenland Ice Core Chronology 2005, 15–42 ka. Part 2: comparison to other records, *Quaternary Science Reviews*, **25**(23–24), 3258–3267, doi:10.1016/j.quascirev.2006.08.003.
- Svensson, A. et al. (2008), A 60 000 year Greenland stratigraphic ice core chronology, *Climate of the Past*, **4**(1), 47–57, doi:10.5194/cp-4-47-2008.
- Sverdrup, H. U. (1940), Hydrology, Section 2, discussion, in: *Report British, Australian, New Zealand Antarctic Research Expedition 1921-31*, Series A, **3**, pp.88-126, Oceanography, Part 2, Section 2.
- Tachikawa, K., C. Handel, and B. Dupré (1997), Distribution of rare earth elements and neodymium isotopes in settling particulate material of the tropical Atlantic Ocean (EUMELI site), *Deep Sea Research Part I: Oceanographic Research Papers*, **44**(11), 1769–1792, doi:doi:10.1016/S0967-0637(97)00057-5.
- Tachikawa, K., C. Jeandel, and M. Roy-Barman (1999), A new approach to the Nd residence time in the ocean: the role of atmospheric inputs, *Earth and Planetary Science Letters*, **170**(4), 433–446, doi:doi:10.1016/S0012-821X(99)00127-2.

- Tachikawa, K., V. Athias, and C. Jeandel (2003), Neodymium budget in the modern ocean and paleo-oceanographic implications, *Journal of Geophysical Research*, **108**(C8), 3254, doi:10.1029/1999JC000285.
- Tachikawa, K., M. Roy-Barman, A. Michard, D. Thouron, D. Yeghicheyan, and C. Jeandel (2004), Neodymium isotopes in the Mediterranean Sea: comparison between seawater and sediment signals, *Geochimica et Cosmochimica Acta*, **68**(14), 3095–3106, doi:10.1016/j.gca.2004.01.024.
- Talley, L. D., and M. S. McCartney (1982), Distribution and Circulation of Labrador Sea Water, *Journal of Physical Oceanography*, **12**(11), 1189–1205, doi:10.1175/1520-0485(1982)012<1189:DACOLS>2.0.CO;2.
- Talley, L. D. (1996), Antarctic Intermediate Water in the South Atlantic, in: *The South Atlantic: Present and Past Circulation*, Eds. G. Wefer et al., pp. 219–238, Springer Berlin, Heidelberg, [http://dx.doi.org/10.1007/978-3-642-80353-6\\_11](http://dx.doi.org/10.1007/978-3-642-80353-6_11)
- Talley, L. D. (2013), Closure of the global overturning circulation through the Indian, Pacific, and Southern Oceans: Schematics and transports, *Oceanography*, **26**(1), 80–97.
- Tanaka, T. et al. (2000), JNdi-1: A neodymium isotopic reference in consistency with LaJolla neodymium, *Chemical Geology*, **168**(3–4), 279–281, doi:10.1016/S0009-2541(00)00198-4.
- Taylor, S. R., and S. M. McLennan (1985), *The continental crust: Its composition and evolution*, Blackwell Scientific Pub., Palo Alto, CA.
- Telesiński, M. M., R. F. Spielhagen, and H. A. Bauch (2014), Water mass evolution of the Greenland Sea since late glacial times, *Climate of the Past*, **10**(1), 123–136, doi:10.5194/cp-10-123-2014.
- Terakado, Y., and A. Masuda (1988), The coprecipitation of rare-earth elements with calcite and aragonite, *Chemical Geology*, **69**(1–2), 103–110, doi:10.1016/0009-2541(88)90162-3.
- Thiagarajan, N., D. Gerlach, M. L. Roberts, A. Burke, A. McNichol, W. J. Jenkins, A. V. Subhas, R. E. Thresher, and J. F. Adkins (2013), Movement of deep-sea coral populations on climatic timescales, *Paleoceanography*, **28**(2), 227–236, doi:10.1002/palo.20023.
- Thiagarajan, N., A. V. Subhas, J. R. Southon, J. M. Eiler, and J. F. Adkins (2014), Abrupt pre-Bolling-Allerod warming and circulation changes in the deep ocean, *Nature*, **511**(7507), 75–78.
- Thoma, M., A. Jenkins, D. Holland, and S. Jacobs (2008), Modelling Circumpolar Deep Water intrusions on the Amundsen Sea continental shelf, Antarctica, *Geophysical Research Letters*, **35**(18), L18602, doi:10.1029/2008GL034939.
- Thompson, A. F., and J.-B. Sallée (2012), Jets and Topography: Jet Transitions and the Impact on Transport in the Antarctic Circumpolar Current, *Journal of Physical Oceanography*, **42**(6), 956–972, doi:10.1175/JPO-D-11-0135.1.
- Thornalley, D. J. R., I. N. McCave, and H. Elderfield (2010), Freshwater input and abrupt deglacial climate change in the North Atlantic, *Paleoceanography*, **25**(1), PA1201, doi:10.1029/2009PA001772.
- Thornalley, D. J. R., S. Barker, W. S. Broecker, H. Elderfield, and I. N. McCave (2011), The Deglacial Evolution of North Atlantic Deep Convection, *Science*, **331**(6014), 202–205, doi:10.1126/science.1196812.
- Thornalley, D. J. R., S. Barker, J. Becker, I. R. Hall, and G. Knorr (2013), Abrupt changes in deep Atlantic circulation during the transition to full glacial conditions, *Paleoceanography*, **28**(2), 253–262, doi:10.1002/palo.20025.
- Thornalley, D. J. R., H. A. Bauch, G. Gebbie, W. Guo, M. Ziegler, S. M. Bernasconi, S. Barker, L. C. Skinner, and J. Yu (2015), A warm and poorly ventilated deep Arctic Mediterranean during the last glacial period, *Science*, **349**(6249), 706–710, doi:10.1126/science.aaa9554.
- Tiedemann, R., T. A. Ronge, F. Lamy, P. Köhler, M. Frische, R. De Pol-Holz, K. Pahnke, B. V. Alloway, L. Wacker, and J. Southon (2015), New Constraints on the Glacial Extent of the Pacific Carbon Pool and its Deglacial Outgassing, *Nova Acta Leopoldina NF* **121**(408), 229–233.

- Toggweiler, J. R., and B. Samuels (1993), Is the Magnitude of the Deep Outflow from the Atlantic Ocean Actually Governed by Southern Hemisphere Winds?, *The Global Carbon Cycle*, **15**, (ed.) M. Heimann, pp. 303–331, Springer Berlin Heidelberg, available from: [http://dx.doi.org/10.1007/978-3-642-84608-3\\_13](http://dx.doi.org/10.1007/978-3-642-84608-3_13)
- Toggweiler, J. R., and B. Samuels (1995), Effect of drake passage on the global thermohaline circulation, *Deep Sea Research Part I: Oceanographic Research Papers*, **42**(4), 477–500, doi:10.1016/0967-0637(95)00012-U.
- Toggweiler, J. R., and B. Samuels (1998), On the Ocean's Large-Scale Circulation near the Limit of No Vertical Mixing, *Journal of Physical Oceanography*, **28**(9), 1832–1852, doi:10.1175/1520-0485(1998)028<1832:OTOSLS>2.0.CO;2.
- Toggweiler, J. R. (1999), Variation of atmospheric CO<sub>2</sub> by ventilation of the ocean's deepest water, *Paleoceanography*, **14**(5), 571–588, doi:10.1029/1999PA900033.
- Toggweiler, J. R., J. L. Russell, and S. R. Carson (2006), Midlatitude westerlies, atmospheric CO<sub>2</sub>, and climate change during the ice ages, *Paleoceanography*, **21**(2), PA2005, doi:10.1029/2005PA001154.
- Tulloch, R., R. Ferrari, O. Jahn, A. Klocker, J. LaCasce, J. R. Ledwell, J. Marshall, M.-J. Messias, K. Speer, and A. Watson (2014), Direct Estimate of Lateral Eddy Diffusivity Upstream of Drake Passage, *Journal of Physical Oceanography*, **44**(10), 2593–2616, doi: <http://dx.doi.org/10.1175/JPO-D-13-0120.1>.
- Turner, J., S. R. Colwell, G. J. Marshall, T. A. Lachlan-Cope, A. M. Carleton, P. D. Jones, V. Lagun, P. A. Reid, and S. Iagovkina (2005), Antarctic climate change during the last 50 years, *International Journal of Climatology*, **25**(3), 279–294, doi:10.1002/joc.1130.
- Upton, P., A. J. Kettner, B. Gomez, A. R. Orpin, N. Litchfield, and M. J. Page (2013), Simulating post-LGM riverine fluxes to the coastal zone: The Waipaoa River System, New Zealand, *Computers & Geosciences*, **53**, 48–57, doi:10.1016/j.cageo.2012.02.001.
- Vance, D., and K. Burton (1999), Neodymium isotopes in planktonic foraminifera: a record of the response of continental weathering and ocean circulation rates to climate change, *Earth and Planetary Science Letters*, **173**(4), 365–379, doi:10.1016/S0012-821X(99)00244-7.
- Vance, D., A. E. Scrivner, P. Beney, M. Staubwasser, G. M. Henderson, and N. C. Slowey (2004), The use of foraminifera as a record of the past neodymium isotope composition of seawater, *Paleoceanography*, **19**(2), PA2009, doi:10.1029/2003PA000957.
- van de Flierdt, T., S. R. Hemming, S. L. Goldstein, and W. Abouchami (2006a), Radiogenic isotope fingerprint of Wilkes Land–Adélie Coast Bottom Water in the circum-Antarctic Ocean, *Geophysical Research Letters*, **33**(12), L12606, doi:10.1029/2006GL026020.
- van de Flierdt, T., L. F. Robinson, J. F. Adkins, S. R. Hemming, and S. L. Goldstein (2006b), Temporal stability of the neodymium isotope signature of the Holocene to glacial North Atlantic, *Paleoceanography*, **21**(4), PA4102, doi:10.1029/2006PA001294.
- van de Flierdt, T., and M. Frank (2010), Neodymium isotopes in paleoceanography, *Quaternary Science Reviews*, **29**(19–20), 2439–2441, doi:10.1016/j.quascirev.2010.07.001.
- van de Flierdt, T., L. F. Robinson, and J. F. Adkins (2010), Deep-sea coral aragonite as a recorder for the neodymium isotopic composition of seawater, *Geochimica et Cosmochimica Acta*, **74**(21), 6014–6032, doi:10.1016/j.gca.2010.08.001.
- van de Flierdt, T. et al. (2012), GEOTRACES intercalibration of neodymium isotopes and rare earth element concentrations in seawater and suspended particles. Part 1: reproducibility of results for the international intercomparison, *Limnology and Oceanography: Methods*, **10**(4), 234–251, doi:10.4319/lom.2012.10.234.
- Viebahn, J., and C. Eden (2010), Towards the impact of eddies on the response of the Southern Ocean to climate change, *Ocean Modelling*, **34**(3–4), 150–165, doi:10.1016/j.ocemod.2010.05.005.
- Voelker, A. H. L., S. M. Lebreiro, J. Schönfeld, I. Cacho, H. Erlenkeuser, and F. Abrantes (2006), Mediterranean outflow strengthening during northern hemisphere coolings: A salt source for the glacial Atlantic?, *Earth and Planetary Science Letters*, **245**(1–2), 39–55, doi:10.1016/j.epsl.2006.03.014.

- Voelker, A. H. L., and H. Haflidason (2015), Refining the Icelandic tephrochronology of the last glacial period – The deep-sea core PS2644 record from the southern Greenland Sea, *Global and Planetary Change*, **131**, 35–62, doi:10.1016/j.gloplacha.2015.05.001.
- von Blanckenburg, F. (1999), Tracing Past Ocean Circulation?, *Science*, **286**(5446), 1862–1863, doi:10.1126/science.286.5446.1862b.
- Wainer, I., M. Goes, L. N. Murphy, and E. Brady (2012), Changes in the intermediate water mass formation rates in the global ocean for the Last Glacial Maximum, mid-Holocene and pre-industrial climates, *Paleoceanography*, **27**(3), PA3101, doi:10.1029/2012PA002290.
- WAIS Divide project members (2013), Onset of deglacial warming in West Antarctica driven by local orbital forcing, *Nature*, **500**(7463), 440–444.
- WAIS Divide project members (2015), Precise inter-polar phasing of abrupt climate change during the last ice age, *Nature*, **520**(7549), 661–665, doi:10.1038/nature14401.
- Walter, H., E. Hegner, B. Diekmann, G. Kuhn, and M. Rutgers van der loeff (2000), Provenance and transport of terrigenous sediment in the south Atlantic Ocean and their relations to glacial and interglacial cycles: Nd and Sr isotopic evidence, *Geochimica et Cosmochimica Acta*, **64**(22), 3813–3827, doi:10.1016/S0016-7037(00)00476-2.
- Wang, Y. J., H. Cheng, R. L. Edwards, Z. S. An, J. Y. Wu, C.-C. Shen, and J. A. Dorale (2001), A High-Resolution Absolute-Dated Late Pleistocene Monsoon Record from Hulu Cave, China, *Science*, **294**(5550), 2345–2348, doi:10.1126/science.1064618.
- Wang, Z., X. Zhang, Z. Guan, B. Sun, X. Yang, and C. Liu (2015), An atmospheric origin of the multi-decadal bipolar seesaw, *Nature Scientific Reports*, **5**(8909), 1–6, doi: 10.1038/srep08909.
- Warren, B. A. (1983), Why is no deep water formed in the North Pacific?, *Journal of Marine Research*, **41**(2), 327–347, doi:10.1357/002224083788520207.
- Watson, A. J., J. R. Ledwell, M.-J. Messias, B. A. King, N. Mackay, M. P. Meredith, B. Mills, and A. C. Naveira Garabato (2013), Rapid cross-density ocean mixing at mid-depths in the Drake Passage measured by tracer release, *Nature*, **501**(7467), 408–411.
- Webb, G. E., L. D. Nothdurft, B. S. Kamber, J. T. Kloprogge, and J.-X. Zhao (2009), Rare earth element geochemistry of scleractinian coral skeleton during meteoric diagenesis: a sequence through neomorphism of aragonite to calcite, *Sedimentology*, **56**(5), 1433–1463, doi:10.1111/j.1365-3091.2008.01041.x.
- Weber, M. E., L. A. Mayer, C. Hillaire-Marcel, G. Bilodeau, F. Rack, R. N. Hiscott, and A. E. Aksu (2001), Derivation of  $\delta^{18}\text{O}$  from sediment core log data: Implications for millennial-scale climate change in the Labrador Sea, *Paleoceanography*, **16**(5), 503–514, doi:10.1029/2000PA000560.
- Weber, M. E., G. Kuhn, D. Sprenk, C. Rolf, C. Ohlwein, and W. Ricken (2012), Dust transport from Patagonia to Antarctica – A new stratigraphic approach from the Scotia Sea and its implications for the last glacial cycle, *Quaternary Science Reviews*, **36**, 177–188, doi:10.1016/j.quascirev.2012.01.016.
- Weis, D. et al. (2006), High-precision isotopic characterization of USGS reference materials by TIMS and MC-ICP-MS, *Geochemistry Geophysics Geosystems*, **7**(8), Q08006, doi:10.1029/2006GC001283.
- Well, R., W. Roether, and D. P. Stevens (2003), An additional deep-water mass in Drake Passage as revealed by  $^3\text{He}$  data, *Deep Sea Research Part I: Oceanographic Research Papers*, **50**(9), 1079–1098, doi:10.1016/S0967-0637(03)00050-5.
- Whittaker, T. E., C. H. Hendy, and J. C. Hellstrom (2011), Abrupt millennial-scale changes in intensity of Southern Hemisphere westerly winds during marine isotope stages 2–4, *Geology*, **39**(5), 455–458, doi:10.1130/G31827.1.
- Williams, P. W., D. N. T. King, J.-X. Zhao, and K. D. Collerson (2005), Late Pleistocene to Holocene composite speleothem  $^{18}\text{O}$  and  $^{13}\text{C}$  chronologies from South Island, New Zealand—did a global Younger Dryas really exist?, *Earth and Planetary Science Letters*, **230**(3–4), 301–317, doi:10.1016/j.epsl.2004.10.024.
- Wilson, S.A. (1997), The collection, preparation and testing of USGS reference material BCR-2, Columbia River, Basalt, *U.S. Geological Survey Open-File Report*, 98-00x.

- Wilson, D. J., A. M. Piotrowski, A. Galy, and I. N. McCave (2012), A boundary exchange influence on deglacial neodymium isotope records from the deep western Indian Ocean, *Earth and Planetary Science Letters*, **341–344**, 35–47, doi:10.1016/j.epsl.2012.06.009.
- Wilson, D. J., K. C. Crocket, T. van de Flierdt, L. F. Robinson, and J. F. Adkins (2014), Dynamic intermediate ocean circulation in the North Atlantic during Heinrich Stadial 1: A radiocarbon and neodymium isotope perspective, *Paleoceanography*, **29**(11), 1072–1093, doi:10.1002/2014PA002674.
- Wunsch, C. (2002), What Is the Thermohaline Circulation?, *Science*, **298**(5596), 1179–1181, doi:10.1126/science.1079329.
- Wyndham, T., M. McCulloch, S. Fallon, and C. Alibert (2004), High-resolution coral records of rare earth elements in coastal seawater: biogeochemical cycling and a new environmental proxy, *Geochimica et Cosmochimica Acta*, **68**(9), 2067–2080, doi:10.1016/j.gca.2003.11.004.
- Wyrski, K. (1961), The thermohaline circulation in relation to the general circulation in the oceans, *Deep Sea Research (1953)*, **8**(1), 39–64, doi:10.1016/0146-6313(61)90014-4.
- Xie, R. C., F. Marcantonio, and M. W. Schmidt (2012), Deglacial variability of Antarctic Intermediate Water penetration into the North Atlantic from authigenic neodymium isotope ratios, *Paleoceanography*, **27**(3), PA3221, doi:10.1029/2012PA002337.
- Xie, R. C., F. Marcantonio, and M. W. Schmidt (2014), Reconstruction of intermediate water circulation in the tropical North Atlantic during the past 22,000 years, *Geochimica et Cosmochimica Acta*, **140**, 455–467, doi:10.1016/j.gca.2014.05.041.
- Xu, X., W. J. Schmitz, H. E. Hurlburt, P. J. Hogan, and E. P. Chassignet (2010), Transport of Nordic Seas overflow water into and within the Irminger Sea: An eddy-resolving simulation and observations, *Journal of Geophysical Research*, **115**(C12), C12048, doi:10.1029/2010JC006351.
- Yashayaev, I., M. Bersch, and H. M. van Aken (2007), Spreading of the Labrador Sea Water to the Irminger and Iceland basins, *Geophysical Research Letters*, **34**(10), L10602, doi:10.1029/2006GL028999.
- Yeager, S., and G. Danabasoglu (2014), The Origins of Late-Twentieth-Century Variations in the Large-Scale North Atlantic Circulation, *Journal of Climate*, **27**(9), 3222–3247, doi:10.1175/JCLI-D-13-00125.1.
- Yihui, D., and J. C. L. Chan (2005), The East Asian summer monsoon: an overview, *Meteorology and Atmospheric Physics*, **89**(1–4), 117–142, doi:10.1007/s00703-005-0125-z.
- Yin, J. H. (2005), A consistent poleward shift of the storm tracks in simulations of 21st century climate, *Geophysical Research Letters*, **32**(18), L18701, doi:10.1029/2005GL023684.
- Zahn, R., J. Schönfeld, H.-R. Kudrass, M.-H. Park, H. Erlenkeuser, and P. Grootes (1997), Thermohaline instability in the North Atlantic during meltwater events: Stable isotope and ice-rafted detritus records from Core SO75-26KL, Portuguese Margin, *Paleoceanography*, **12**(5), 696–710, doi:10.1029/97PA00581.
- Zarriess, M. (2011), Bipolar seesaw in the northeastern tropical Atlantic during Heinrich stadials, *Geophysical Research Letters*, **38**, L04706, doi:10.1029/2010GL046070.
- Zhai, X., and D. R. Munday (2014), Sensitivity of Southern Ocean overturning to wind stress changes: Role of surface restoring time scales, *Ocean Modelling*, **84**, 12–25, doi:10.1016/j.ocemod.2014.09.004.
- Zimmermann, B., D. Porcelli, M. Frank, J. Rickli, D.-C. Lee, and A. N. Halliday (2009), The hafnium isotope composition of Pacific Ocean water, *Geochimica et Cosmochimica Acta*, **73**(1), 91–101, doi:10.1016/j.gca.2008.09.033.
- Zweng, M. M., J. R. Reagan, J. I. Antonov, R. A. Locarnini, A. V. Mishonov, T. P. Boyer, H. E. Garcia, O. K. Baranova, D. R. Johnson, D. Seidov and M. M. Biddle (2013), World Ocean Atlas 2013, Volume 2: Salinity. Ed.: S. Levitus, Technical Ed.: A. Mishonov; *NOAA Atlas NESDIS 74*, 39 pp.

# Appendix

## Appendix Table:

Neodymium isotope and concentration results of deep-sea corals not used for paleoceanographic interpretation. Coral species termed 'colonial' are unidentified colonial scleractinian corals. Drake Passage Stylasterids from Interim seamount show open U-system behavior. Ages reported in kyr BP, which is expressed in thousand years before present (i.e. 1950). Water depth is the depth of sample collection.

Samples were processed from U-Th chemistry wash fractions at Imperial College London, Nd concentrations are hence minimum values (underestimated by ~10%; see Chapter 2). Uranium-series data from Burke (2012). See main text for details about North Atlantic and Drake Passage sampling locations.

## Appendix: Deep-sea coral results from Galapagos, Interim, seamount and Reykjanes Ridge

| Cruise                                      | Event | Sample  | Species             | Location   | Latitude | Longitude | Water depth (m) | Sample mass (g) | Age (kyr BP) | $^{238}\text{U}$ (ng/g) | $^{232}\text{Th}$ (pg/g) | $^{238}\text{U}$ ZSE | $^{232}\text{Th}$ ZSE | $^{238}\text{U}$ ZSE | $^{232}\text{Th}$ ZSE | $^{238}\text{U}$ ZSE | $^{232}\text{Th}$ ZSE | $^{143}\text{Nd}/^{144}\text{Nd}$ | ZSE    | $\epsilon_{\text{Nd}}$ | ZSE  | $^{238}\text{U}$ ZSE | $^{232}\text{Th}$ ZSE | $^{143}\text{Nd}/^{144}\text{Nd}$ ZSE | $\epsilon_{\text{Nd}}$ ZSE | $\text{Nd}_{\text{coral}}$ (ng/g) | 2SE (ep) <sup>a</sup> |  |  |  |
|---|-------|---------|---------------------|------------|----------|-----------|-----------------|-----------------|--------------|-------------------------|--------------------------|----------------------|-----------------------|----------------------|-----------------------|----------------------|-----------------------|-----------------------------------|--------|------------------------|------|----------------------|-----------------------|---------------------------------------|----------------------------|-----------------------------------|-----------------------|--|--|--|
| <i>Galapagos</i>                            |       |         |                     |            |          |           |                 |                 |              |                         |                          |                      |                       |                      |                       |                      |                       |                                   |        |                        |      |                      |                       |                                       |                            |                                   |                       |  |  |  |
| WV1007                                      | D03   | 1-2     | colonial            | Galapagos  | 0.46     | -90.71    | 610             | 0.31503         | 36.72        | 0.18                    | 4370.8                   | 14.3                 | 32.5                  | 5.6                  | 140.7                 | 0.7                  | 0.512623              | 0.000009                          | -0.30  | 0.17                   | 0.21 | 8.2                  | 0.0003                |                                       |                            |                                   |                       |  |  |  |
| WV1007                                      | D03   | 1-3     | colonial            | Galapagos  | 0.46     | -90.71    | 610             | 0.33573         | 35.10        | 0.17                    | 3861.5                   | 12.4                 | 45.0                  | 4.0                  | 144.2                 | 0.7                  | 0.512544              | 0.000011                          | -1.83  | 0.22                   | 0.21 | 4.8                  | 0.0003                |                                       |                            |                                   |                       |  |  |  |
| WV1007                                      | D03   | 4-11    | colonial            | Galapagos  | 0.46     | -90.71    | 610             | 0.27059         | 36.92        | 0.18                    | 4126.4                   | 13.5                 | 107.1                 | 3.0                  | 145.4                 | 0.8                  | 0.512574              | 0.000011                          | -1.25  | 0.21                   | 0.21 | 5.6                  | 0.0004                |                                       |                            |                                   |                       |  |  |  |
| WV1007                                      | D09   | 17      | colonial            | Galapagos  | 0.79     | -91.30    | 495             | 0.64770         | -0.01        | 0.00                    | 3985.4                   | 13.9                 | 7.0                   | 4.2                  | 147.0                 | 0.7                  | 0.512585              | 0.000009                          | -1.03  | 0.17                   | 0.21 | 4.9                  | 0.0002                |                                       |                            |                                   |                       |  |  |  |
| WV1007                                      | D09   | 12      | colonial            | Galapagos  | 0.79     | -91.30    | 495             | 0.71538         | -0.05        | 0.01                    | 3384.8                   | 11.9                 | 6.7                   | 3.7                  | 147.1                 | 0.7                  | 0.512586              | 0.000010                          | -1.01  | 0.19                   | 0.21 | 4.4                  | 0.0002                |                                       |                            |                                   |                       |  |  |  |
| <i>Drake Passage (Stylasterid)</i>          |       |         |                     |            |          |           |                 |                 |              |                         |                          |                      |                       |                      |                       |                      |                       |                                   |        |                        |      |                      |                       |                                       |                            |                                   |                       |  |  |  |
| NBP1103                                     | DH78  | Stc-2-1 | <i>Stylasterid</i>  | Interim    | -60.642  | -66.044   | 1545            | 0.1335          | 9.74         | 1.93                    | 94                       | 0                    | 218.6                 | 1.6                  | 151.7                 | 2.0                  | 0.512201              | 0.000006                          | -8.53  | 0.11                   | 0.21 | 94.2                 | 0.00075               |                                       |                            |                                   |                       |  |  |  |
| NBP1103                                     | DH83  | St-3    | <i>Stylasterid</i>  | Interim    | -60.686  | -66.057   | 1811            | 0.5447          | 57.96        | 6.08                    | 96                       | 0                    | 716.0                 | 2.9                  | 183.7                 | 3.7                  | 0.512197              | 0.000005                          | -8.61  | 0.11                   | 0.21 | 441.1                | 0.03270               |                                       |                            |                                   |                       |  |  |  |
| <i>Northeast Atlantic (solitary corals)</i> |       |         |                     |            |          |           |                 |                 |              |                         |                          |                      |                       |                      |                       |                      |                       |                                   |        |                        |      |                      |                       |                                       |                            |                                   |                       |  |  |  |
| CE0806                                      | Dr29  | 3       | <i>Flabellum</i>    | Rey. Ridge | 61.407   | 27.856    | 994             | 0.66445         | 1.08         | 0.05                    | 4082                     | 15                   | 255                   | 1                    | 147.5                 | 0.8                  | 0.512013              | 0.000006                          | -12.19 | 0.20                   | 0.21 | 38.3                 | 0.0007                |                                       |                            |                                   |                       |  |  |  |
| CE0806                                      | Dr26A | 1       | <i>D. dianthus</i>  | Rey. Ridge | 60.738   | 29.444    | 1141.5          | 0.40836         | 4.41         | 0.08                    | 4730                     | 16                   | 502                   | 2                    | 146.2                 | 0.7                  | 0.512120              | 0.000006                          | -10.11 | 0.20                   | 0.21 | 46.7                 | 0.0009                |                                       |                            |                                   |                       |  |  |  |
| CE0806                                      | Dr31A | 1       | <i>Caryophyllia</i> | Rey. Ridge | 61.872   | 27.008    | 768             | 0.64196         | 9.53         | 0.23                    | 3267                     | 11                   | 965                   | 3                    | 148.2                 | 0.8                  | 0.511925              | 0.000005                          | -13.91 | 0.20                   | 0.21 | 67.4                 | 0.0005                |                                       |                            |                                   |                       |  |  |  |
| CE0806                                      | Dr25  | 7       | <i>Flabellum</i>    | Rey. Ridge | 60.685   | 29.211    | 1416            | 0.27336         | 14.45        | 0.08                    | 4458                     | 15                   | 224                   | 2                    | 150.1                 | 0.7                  | 0.512156              | 0.000007                          | -9.41  | 0.20                   | 0.21 | 40.6                 | 0.0008                |                                       |                            |                                   |                       |  |  |  |
| CE0806                                      | Dr29  | 2       | <i>D. dianthus</i>  | Rey. Ridge | 61.407   | 27.856    | 994             | 0.05363         | 14.56        | 0.12                    | 4350                     | 16                   | 99                    | 63                   | 149.7                 | 0.8                  | 0.512187              | 0.000012                          | -8.80  | 0.24                   | 0.24 | 20.5                 | 0.0170                |                                       |                            |                                   |                       |  |  |  |
| <i>Northeast Atlantic (colonial corals)</i> |       |         |                     |            |          |           |                 |                 |              |                         |                          |                      |                       |                      |                       |                      |                       |                                   |        |                        |      |                      |                       |                                       |                            |                                   |                       |  |  |  |
| CE0806                                      | Dr27  | 4       | colonial            | Rey. Ridge | 61.187   | 28.874    | 1313.5          | 0.91496         | 0.39         | 0.11                    | 3441                     | 11                   | 478                   | 2                    | 147.0                 | 0.7                  | 0.512038              | 0.000008                          | -11.71 | 0.20                   | 0.21 | 19.3                 | 0.0003                |                                       |                            |                                   |                       |  |  |  |
| CE0805                                      | Dr27  | 3       | colonial            | Rey. Ridge | 61.187   | 28.874    | 1313.5          | 0.72412         | 4.18         | 0.14                    | 3221                     | 10                   | 570                   | 2                    | 151.9                 | 0.7                  | 0.511977              | 0.000006                          | -12.89 | 0.20                   | 0.21 | 88.7                 | 0.0033                |                                       |                            |                                   |                       |  |  |  |
| CE0806                                      | Dr19B | 5       | colonial            | Rey. Ridge | 58.947   | 32.164    | 1429            | 0.30741         | 9.08         | 0.17                    | 3731                     | 12                   | 810                   | 3                    | 147.6                 | 0.8                  | 0.511888              | 0.000005                          | -14.62 | 0.20                   | 0.21 | 25.8                 | 0.0007                |                                       |                            |                                   |                       |  |  |  |

(a) ZSE is the analytical 2 $\sigma$  standard error.(b)  $^{143}\text{Nd}/^{144}\text{Nd}$  ratios were corrected for the offset of the measured  $\text{Nd}_{\text{coral}}$  ratio of  $0.512105 \pm 0.000009$  ( $n = 110$ ) from the published value of  $0.512115 \pm 0.000007$  (Tanaka et al., 2000).(c)  $\epsilon_{\text{Nd}}$  was calculated using the present day CHUR value of  $^{143}\text{Nd}/^{144}\text{Nd} = 0.512638$  (Jacobsen and Wasserburg, 1980).(d) 2SD refers to the 2 $\sigma$  standard deviation derived from the longterm reproducibility (see main text). If the internal 2 $\sigma$  SE was larger than the external one, the internal error is reported.(e) ZSE (ep) is the propagated 2 $\sigma$  standard error of Nd concentrations determined by isotope dilution.